Terrestrial and Astronomical Applications of Uncooled Infrared Technology

Maisie Frances Rashman

A thesis submitted in partial fulfilment of the requirements of
Liverpool John Moores University for the degree of Doctor of Philosophy

March 2020

Declaration

The work presented in this thesis was carried out at the Astrophysics Research Institute, Liverpool John Moores University. Unless otherwise stated, it is the original work of the author.

While registered as a candidate for the degree of Doctor of Philosophy, for which submission is now made, the author has not been registered as a candidate for any other award. This thesis has not been submitted in whole, or in part, for any other degree.

Maisie Rashman
Astrophysics Research Institute
Liverpool John Moores University
IC2
146 Brownlow Hill
Liverpool
L3 5RF
UK

June 2020

Abstract

This thesis provides an account of the application of uncooled microbolometer technology in two different fields; astronomy and conservation ecology. Uncooled microbolometers are readily available as low-cost, commercial detectors for imaging in the $7.5 - 13.5\mu$m spectral region. Their affordable price and coverage of the wavelengths at which the the spectral energy distribution of animals that use metabolic heat to maintain a stable internal temperature peaks, has popularised these systems for use in ecology. However, their use as the primary detectors in conservation surveys suffers from a data analysis bottleneck due to the large volumes of data and the manual approach to detecting and identifying animal species. As a result, the efficiency and efficacy of these systems is limited by the volume of data and the lack of resources and experience in handling infrared imagery.

In contrast, astronomical techniques are well developed for infrared wavelengths and the analysis of large quantities of data has been successfully automated for many years. Apart from observations of solar system objects with very small (<200mm aperture) telescopes and some high altitude experiments, microbolometers have not been deployed in astronomy for ground-based observing. Although observing in this spectral region is key to understanding the cold, dusty and distant universe, resources for mid-IR observing are not as readily available as those for other wavelengths due to the very high thermal background and the requirement for specialist detector systems. Through our work, we attempt to discern whether microbolometers, and standard astronomical infrared observing and data analysis techniques, can be applied successfully in these two fields.

In part I three analogous, standard astronomical instrumentation techniques are applied

to characterise the random and spatial noise present in a FLIR Tau 2 Core microbolometer to determine the systematics and sources of statistical noise that limit read-out accuracy. Flat fielding, stacking and binning are used to determine that the focal plane array is dominated by large structure noise, and demonstrate how this can be corrected. An NEdT of < 60mK is isolated and recorded for the system.

Part II introduces Astro-Ecology, a field that couples microbolometers and astronomy instrumentation techniques for application in conservation biology to monitor vulnerable species. Several investigations are presented to determine the feasibility of developing an astronomy based, fully automated reduction pipeline for mid-IR data collected using unmanned aerial vehicle (UAV) technology From these investigations the efficacy of microbolometers for animal surveys was found to be highly dependent on ground and ambient air temperatures, and to fully automate a pipeline would require more than standard astronomical techniques and software.

In part III, a small, passively cooled, prototype, N-band ($\sim 10\mu$m) instrument is developed and tested. The optical and mechanical design of the instrument is described, with the instrument constructed from commercially available components and an uncooled microbolometer focal-plane array. The incorporation of adjustable germanium reimaging optics rescale the image to the appropriate plate scale for the 2-m diameter Liverpool Telescope on La Palma. A week-long programme of observations was conducted to test the system sensitivity and stability, and the feasibility of using this technology in 'facility' class instruments for small telescopes. From observations of bright solar system and stellar sources, a plate scale of $0.75''$ per pixel is measured, with this confirming that the optical design allows diffraction limited imaging. A photometric stability of $\sim 10\%$ is recorded with this largely due to sky variability. A 3σ sensitivity of 7×10^3 Jy for a single, ~ 0.11 second exposure is measured, which corresponds to a sensitivity limit of 3×10^2 Jy for a 60 second total integration.

Recognising the need for improved sensitivity, the instrument was upgraded to be optimised for mid-IR observations using a chopping system. The instrument was deployed for a week on the 1.52m Carlos Sanchez Telescope on Tenerife alongside a regime of chopping and nodding. Observations of several very bright mid-IR sources with catalogue fluxes down to ~ 600 Jy are presented. A sensitivity improvement of ~ 4 magnitudes over previous unchopped observations is recorded, in line with sensitivity predictions.

Publications

In the course of completing the work presented in this thesis, the contents of Chapter 4 have been submitted and accepted for publication in a refereed journal:

Rashman, M. F.; Steele, I. A.; Bates, S. D.; Copley, D.; Longmore S. N. (2020) "Uncooled microbolometer arrays for ground-based astronomy," *Monthly Notices of the Royal Astronomical Society*, Volume 492, Issue 1, Pages 480–487

The contents of Chapter 5 have been submitted for publication in Experimental Astronomy, pending review. The contents of Chapter 2 have been presented, submitted and accepted for publication in the conference proceedings:

Rashman, M. F.; Steele, I. A.; Burke, C.; Longmore, S.N.; Wich, S. (2018) "Adapting thermal-infrared technology and astronomical techniques for use in conservation biology," *Proc. SPIE 10709, High Energy, Optical, and Infrared Detectors for Astronomy VIII*, 107092S

The following are papers on which I have been a contributing author and my contribution to each is presented in Chapter 3:

Burke, C.; Rashman, M.F.; Longmore, S.N.; McAree, O.; Clover-Kapfer, P.; Ancrenaz, M; Wich, S.A. (2019) "Successful observation of orangutans in the wild with thermal-equipped drones," *Journal of Unmanned Vehicle Systems*, 7, 3

Burke, C.; Rashman, M.F.; Wich, S.A.; Symons, A.; Theron, C.; Longmore, S.N. (2018) "Optimising observing strategies for monitoring animals using drone-mounted thermal infrared cameras," *International Journal of Remote Sensing*, 40:2, 439-467.

Burke, C.; Rashman, M; McAree, O.; Hambrecht, L.; Longmore, S.N; Piel, A.K.; Wich, S. (2018) "Addressing environmental and atmospheric challenges for capturing high-precision thermal infrared data in the field of astro-ecology," *Proc. SPIE 10709, High Energy, Optical, and Infrared Detectors for Astronomy VIII*, 107091O

Acknowledgements

This thesis is dedicated in thanks to so many people who offered advice, support, feedback and friendship in the time it took for me to get here. But in particular:

For the Rashmans; Elliot, Michele and Felix, and for Bracken Harper and JP Walker. It goes without saying that the contributions of my family and my partner have been invaluable and without them, this thesis would not exist.

For Kate Furnell and Danielle Coogan, whose unwavering support and care has kept me going, and to who I am forever indebted. I could not have asked for better friends.

For Alison Keen and the NSO team, who provide an invaluable contribution to astronomy outreach and who have helped me in more ways than they realise.

For Stuart Bates and the LT and NRT groups, who gracefully allowed me to invade their spaces, use their resources and utilise their expertise in all aspects of astronomical instrumentation.

And finally, for Iain Steele who has the patience of a saint and who never once made me feel dumb (even when I was being dumb). His boundless ideas and tremendous knowledge are the reason I have a thesis I can be proud of.

Thank you.

Maisie Frances Rashman June 2020

"Do not go gentle into that good night. Rage, rage against the dying of the light."

Dylan Thomas

Contents

List of Figures

List of Tables

Physical Constants

Speed of Light	c	$=$	3.00×10^{8} ms^{-1}
Planck's Constant	h	$=$	6.63×10^{-34} Js
Boltzmann Constant	k	$=$	1.38×10^{-23} JK^{-1}
Stefan Boltzmann Constant	σ	$=$	5.67×10^{-8} Js^{-1}m^{-2}K^{-4}

Chapter 1

Introduction

This chapter presents a brief overview of infrared theory and how a small spectral region within the infrared can be applied in two different fields; astronomy and ecology. An introduction to infrared radiation, the mid-infrared (mid-IR) spectral region and radiation theory is provided. The theory behind microbolometers, a type of low cost and commercially available detector for the mid-IR, is briefly introduced and discussed. This is followed by a short description of mid-IR astronomy, covering the topics of observing history, limitations and applications. This precedes a section describing the need for, and theory behind, mid-IR observing in conservation ecology. The Chapter concludes with a discussion of the central motivations of this thesis.

1.1 Infrared Radiation

Infrared (from the Latin word 'infra' meaning 'below') radiation was discovered by Frederick William Herschel (1738 - 1822) in 1800 (Herschel, 1800). With his interest piqued by the desire to observe sunspots without suffering permanent eye damage (historical review by Barr, 1961), Herschel used a prism to observe a solar spectrum and measured the temperature of each colour relative to a control thermometer. From these studies he confirmed that radiant energy is present in all parts of the visible spectrum. However, his observations led him to the conclusion that the maximum of the energy distribution lay in an un-observed part of the spectra; just beyond the red. The infrared is now considered to cover wavelengths from $\sim$ 700 nm - 1 mm.

1.1.1 Mid-Infrared

Infrared is traditionally split into three regions: near-, mid- and far-infrared. There is some discrepancy in the literature of the wavelength range covered by each region. This is especially true for the mid-IR where the near-mid boundary can be as low as 4 μm and the mid-far boundary as high as 40 μm. For the purpose of this thesis, when we refer to mid-IR we are describing a common definition of the spectral region, which ranges from 4.5 to 26 μm. The radiant excitance (otherwise known in astronomy as the energy flux Rybicki & Lightman 1986), is defined as the radiant flux emitted by a surface per unit area with units of Wm^{-2}. The radiant excitance of objects at terrestrial temperatures (i.e. $\sim 0 - 100\,^{\circ}\mathrm{C}$) peaks in this mid-IR spectral region. To fully understand this, we must first describe the radiation laws for a blackbody.

1.1.2 Blackbody Radiation

The concept of a blackbody was originally introduced in 1860 by Gustav Kirchhoff (Kirchhoff, 1860). Kirchhoff's law states that the ratio of emissivity to absorptivity for a body at a given wavelength depends only on its temperature (Glass, 1999). A blackbody is such that it absorbs all incident radiation, regardless of wavelength and direction, i.e. it has absorptivity equal to 1. From Kirchhoff's law, this also makes it a perfect emitter, with emissivity equal to 1. Experimentally, a blackbody is modelled by electromagnetic radiation at equilibrium within a cavity that has walls of a constant temperature.

1.1.2.1 Stefan-Boltzmann law

In 1879 Josef Stefan (Stefan, 1879) empirically deduced that the total energy radiated by a blackbody over all wavelengths (or over all frequencies) is proportional to the 4th power of temperature, i.e.:

$$-\left(\frac{\mathrm{dE}}{\mathrm{dt}}\right) = \text{total radiant energy per second } \propto T^4 \tag{1.1}$$

This was not widely accepted until proven by Ludwig Boltzmann (Boltzmann, 1884) through considerations of classical thermodynamics. Boltzmann derived the final form

of the Stefan-Boltzmann law by first considering a volume dV, consisting entirely of electromagnetic radiation that can be compressed or expanded. When applying heat dQ, to the system, the total internal energy increases by dU and the volume increases. Abiding by the first law of thermodynamics:

$$\mathrm{dQ} = \mathrm{dU} + \mathrm{pdV}, \tag{1.2}$$

where p is the radiation pressure of the electromagnetic radiation. The entropy of the system can be described by $\mathrm{dS} = \mathrm{dQ/T}$. By rearranging equation 1.2 to increase entropy for the system we achieve the following:

$$T\mathrm{dS} = \mathrm{dU} + \mathrm{pdV}. \tag{1.3}$$

To convert equation 1.3 into a partial differential equation, we divide by volume, dV at a constant temperature T:

$$T\Big(\frac{\partial S}{\partial V}\Big)_T = \Big(\frac{\partial U}{\partial V}\Big)_T + p. \tag{1.4}$$

Using the following of Maxwell's relations:

$$\Big(\frac{\partial p}{\partial T}\Big)_V = \Big(\frac{\partial S}{\partial V}\Big)_T, \tag{1.5}$$

we obtain the following:

$$T\Big(\frac{\partial p}{\partial T}\Big)_V = \Big(\frac{\partial U}{\partial V}\Big)_T + p. \tag{1.6}$$

From equation 1.6 we can derive the relation between the internal energy U and the temperature T from the relation between p, V and U, i.e. a known equation of state for the gas. From Maxwell's equations we know that $p = \frac{1}{3}u$ and $U = uV$, where u is the energy density of the radiation and only depends on the temperature as $\big(\frac{\partial U}{\partial V}\big)_T = u\big(\frac{\partial V}{\partial V}\big)_T = u$. From this we can re-write equation 1.6 as follows:

$$T\Big(\frac{\partial(\frac{1}{3}u)}{\partial T}\Big)_V = \Big(\frac{\partial(uV)}{\partial V}\Big)_T + \frac{1}{3}u, \text{and}$$

$$\frac{1}{3}T\Big(\frac{\partial u}{\partial T}\Big) = u + \frac{1}{3}u = \frac{4}{3}u. \tag{1.7}$$

From this we can solve a relation between energy density of the radiation and temperature:

$$\frac{\partial u}{u} = 4\frac{\partial T}{T},$$

$$\ln u = 4 \ln T, \text{ and hence}$$

$$u \propto T^4. \tag{1.8}$$

By including the Boltzmann constant $\sigma = 5.67 \times 10^{-8}$ $\mathrm{Wm^{-2}K^{-4}}$ we end up with the modern form of the Stefan-Boltzmann law for the radiant energy per unit area per second from the surface of a blackbody I:

$$I = \sigma T^4, \tag{1.9}$$

where the rate of emission of radiant energy is related to u by $u = \frac{4I}{c}$ (Longair, 2003) .

1.1.2.2 Wien's Displacement Law

Wilhelm Wien's displacement law was first derived in 1894 from consideration of the combination of electromagnetism and thermodynamics. He hypothesised and proved that the maximum amount of radiation emitted by a blackbody occured when the wavelength and temperature were equal to a constant:

$$\lambda_{max} T \approx 2.898 \times 10^{-3} \text{ mK} \tag{1.10}$$

Wien derived this law by considering gas undergoing adiabatic expansion, where $\mathrm{dQ} = 0$. From the first law of thermodynamics (equation 1.2) and Maxwell's relations of $U = uV$

and $p = \frac{1}{3}u$, the following expression for adiabatic expansion can be derived:

$$\mathrm{d}(uV) + \frac{1}{3}u\,\mathrm{d}\,V = 0,$$

$$V\mathrm{d}u + u\,\mathrm{d}\,V + \frac{1}{3}u\,\mathrm{d}\,V = 0, \text{ and}$$

$$\frac{\mathrm{d}u}{u} = -\frac{4}{3}\frac{\mathrm{d}\,V}{V}. \tag{1.11}$$

By integrating equation 1.11 we obtain $u = \text{constant} \times V^{-\frac{4}{3}}$. As derived in section 1.1.2.1, $u = \frac{\sigma T^4}{c}$ and hence:

$$TV^{\frac{1}{3}} = \text{constant}. \tag{1.12}$$

The volume V of a spherical object is proportional to the cube of the radius r, and so:

$$T \propto r^{-1}. \tag{1.13}$$

The relation between the peak wavelength λ of the radiation and the volume of the enclosure is:

$$\lambda \propto r, \tag{1.14}$$

i.e. the peak wavelength of radiation increases linearly with the spherical volume. Substituting equation 1.14 into equation 1.13 gives:

$$T \propto \lambda^{-1}. \tag{1.15}$$

Equation 1.15 is Wien's displacement law. It states that for the adiabatic expansion of radiation, the peak wavelength of the radiation scales inversely with temperature.

1.1.2.3 Planck's Theory of Blackbody Radiation

Prior to the derivation of Planck's theory, two other relations for the energy distribution of a black body spectrum M_λ, i.e. the power per unit area emitted by a blackbody at temperature T and at wavelength λ, were derived. Wien, after successfully deriving his displacement law (see section 1.1.2.2), published his attempt at modelling the blackbody function in 1897 (Wien, 1897). Commonly referred to as the Wien approximation,

this relation accurately models the short wavelength (high frequency) portion of the spectrum, where $\lambda T \lesssim 3100\,\mu$m (Stewart & Johnson, 2016), however it is invalid at high temperatures and long wavelengths (low frequencies).

In early 1900, Lord Rayleigh derived a relation in direct response to concerns about the behaviour of Wien's approximation at long wavelengths (Rayleigh, 1900). (To note, James Jeans later provided a correction to this theorem, and it is now known as the Rayleigh-Jeans law). Rayleigh derived his relationship from considerations of electromagnetic waves in a cube shaped cavity. From the equipartition theorem Rayleigh considered that for standing waves to exist inside the cavity, they must exist for only a discrete set of frequencies. However there is no upper limit to the frequency of a standing wave and consequently, the Rayleigh-Jeans law fails at high frequencies. The implications of this were that classical physics as applied in this instance would result in the electromagnetic radiation inside the cavity never reaching thermal equilibrium, and indefinitely absorbing energy to excite to higher and higher frequency standing waves.

Later in 1900, Max Planck derived what is now known as Planck's theory of blackbody radiation (Planck, 1900). When written with respect to wavelength, it takes the form:

$$M_\lambda = C_1 \lambda^{-5} (e^x - 1)^{-1}, \tag{1.16}$$

where C_1 is the first radiation constant given by $C_1 = 2c^2h$ and x is the dimensionless frequency, given by $x = \frac{hc}{\lambda k_B T}$. Here, c is the velocity of light in a vacuum, h is Planck's constant and k_B is Boltzmann's constant (Wolfe, 1996). The Planck function can also be expressed in terms of frequency ν, where:

$$M_\nu = \frac{2h\nu^3}{c^2}(e^{h\nu/k_B T} - 1). \tag{1.17}$$

Planck derived this function from the consideration of a blackbody as a collection of oscillators which can only absorb discrete, quantised energies of $E = nh\nu$, where ν is the frequency of the oscillator and n is some integer value. Planck understood that Wien's approximation was not valid at long wavelengths and at these wavelengths the entropy of the system had to satisfy the following relation:

$$\frac{\mathrm{d}^2\mathrm{S}}{\mathrm{dU}^2} = -\frac{(\mathrm{const})}{U^2}. \tag{1.18}$$

He integrated and combined equation 1.18 with the known relation for the energy in a resonator:

$$U_\nu = \frac{c^3}{8\pi\nu}\rho_\nu, \tag{1.19}$$

to derive equation 1.16 (Crepeau, 2009). We can demonstrate the validity of this theory by manipulating equation 1.16 to obtain both the Stefan-Boltzmann law and Wien's law.

Wien's displacement law, i.e. the relationship between peak radiant excitance and wavelength for a blackbody (derived in section 1.1.2.2) can be derived from the Planck function with respect to wavelength (equation 1.16) by taking the differential and finding where the gradient of M_λ is zero, i.e. $\frac{\mathrm{dM}_\lambda}{\mathrm{d}\lambda} = 0$:

$$\frac{\mathrm{d}}{\mathrm{d}\lambda}\left[C_1\lambda^{-5}\cdot(e^x-1)^{-1}\right] = 0,$$

$$\left[5\lambda^{-6}\Big(e^x-1\Big)^{-1} - \lambda^{-7}\Big(-\frac{hc}{k_BT}e^x\Big)\Big(e^x-1\Big)^{-2}\right] = 0,$$

$$\left[5 - \frac{1}{\lambda}\Big(e^x-1\Big)^{-1}e^x\Big(-\frac{hc}{k_BT}\Big)\right] = 0, \text{ and hence}$$

$$\lambda T = \frac{hc}{5k_B\big(1-e^{-x}\big)}. \tag{1.20}$$

The peak wavelength depends on the form of the blackbody function, with M_ν having a peak shifted with respect to M_λ. Hereafter, any values of peak wavelength quoted in the text will be calculated as the peak of the corresponding M_λ blackbody function.

The Stefan-Boltzmann law, i.e. the relation between the radiant excitance and temperature (derived in section 1.1.2.1) can be derived from the Planck function with respect to wavelength (equation 1.16) by considering a small blackbody surface radiating into a half-sphere. First, the Planck function must be multiplied by the solid angle, $\cos\theta\,\mathrm{d}\Omega$ over which it is radiating:

$$\frac{\mathrm{dM}_\lambda}{\mathrm{d}\lambda}\Big(\frac{1}{A}\Big) = \frac{2hc^2}{\lambda^5(e^{\frac{\lambda k_B T}{hc}}-1)}\cos\theta\,\mathrm{d}\Omega. \tag{1.21}$$

This is because blackbodies obey Lambert's Cosine Law (Lambert, 1892), i.e. the intensity observed will be the actual intensity multiplied by the cosine of the zenith angle ϕ, where $\mathrm{d}\Omega = \sin\theta\,\mathrm{d}\theta\,\mathrm{d}\phi$. Hence:

$$\frac{M_\lambda}{A} = 2hc^2 \int_0^\infty \frac{\mathrm{d}\lambda}{\lambda^5(e^{\frac{hc}{\lambda k_B T}} - 1)} \int_0^{2\pi} \mathrm{d}\phi \int_0^{\frac{\pi}{2}} \cos\theta\,\sin\theta\,\mathrm{d}\theta,$$

$$\frac{M_\lambda}{A} = 2\pi hc^2 \int_0^\infty \frac{\mathrm{d}\lambda}{\lambda^5(e^{\frac{hc}{\lambda k_B T}} - 1)}, \tag{1.22}$$

given the following substitutions: $x = \frac{hc}{\lambda k_B T}$ and $\mathrm{d}x = \frac{-\mathrm{hc}}{\lambda^2 \mathrm{k_B T}}$:

$$\frac{M_\lambda}{A} = \frac{2\pi(k_B T)^4}{h^3 c^2} \int_0^\infty \frac{x^3}{(e^x - 1)} \mathrm{d}x, \tag{1.23}$$

and using the standard integral:

$$\int_0^\infty \frac{x^3}{(e^x - 1)} \mathrm{d}x = \frac{\pi^4}{15}$$

$$\frac{M_\lambda}{A} = \frac{2\pi^5 k_B^4}{15h^3c^2} T^4$$

$$\frac{M_\lambda}{A} = \sigma T^4. \tag{1.24}$$

1.2 Microbolometers

There are three major types of infrared detector: photoconductive detectors such as arsenic-doped silicon (Si:As), photovoltaic detectors such as mercury cadmium zinc telluride (HgCdZnTe) and thermal detectors such as the bolometer (Low & Rieke, 1974). The bolometer is commonly used for detecting in the mid-IR and was invented by Samuel Pierpont Langley (1834 – 1906) in 1881. Langley was motivated by a desire to study solar radiation and introduced the premise of using narrow metal strips with low thermal capacity, to detect large changes in resistance for small amounts of absorbed radiant heat. This detector was sensitive to changes in temperature of 10^{-5} °C (Barr, 1963).

Each pixel in a microbolometer array acts as a single sensor element (Tempelhahn et al., 2016). These systems operate by using a camera lens to focus infrared radiation for absorption by each microbolometer element (or pixels) inside. There is no physical contact or thermal coupling between the pixels, as a result they are completely thermally isolated from one another. Each pixel consists of a 'bridge' suspended above a read out integrated circuit (ROIC). The bridge is a thin, infrared absorbing silicon nitride Si_3N_4, membrane with a layer of temperature sensitive resistor material at the centre. Polycrystalline vanadium oxide (VOx) is commonly used as this thermoresistive material. Vanadium readily forms a number of oxides (VO, V_2O_3, VO_2, V_2O_5) because of its half filled d-shell and several of these phases have a high temperature coefficient of resistance (TCR), i.e. exhibit a large rise in electrical resistance for a small rise in temperature making them ideal for use in uncooled microbolometers (Aryasomayajula & Reddy, 2008). The bridge and ROIC are connected by two long Si_3N_4 legs which provide the thermal isolation between the microbolometer and the read out substrate (Radford et al., 1999). A schematic of a microbolometer pixel can be seen in figure 1.1 courtesy of Moreno et al. (2012). As incident radiation heats the bridge material, the thermoresisitive element registers the temperature change of the bridge as a change in resistance. The ROIC directs current through the bridge in pulses (at the frame rate of the system) to detect these changes in resistance. This can be measured and processed to produce values quantifying the amount of radiation absorbed (Kohin & Butler, 2004).

The responsivity of each pixel can be characterised by the following expression:

$$R = \frac{\epsilon I R_d \alpha}{G_{th}(1+\omega^2\tau^2)^{0.5}}, \tag{1.25}$$

where ϵ is the detector absorptivity, I is the read-out current, R_d is the detector resistance, α is detector TCR, G_{th} is thermal conductance of the substrate, ω is the angular frequency and τ is the thermal time constant, determined from the conductance and heat capacity C of the detector (Wolfe et al., 1985), where:

$$\tau = \frac{C}{G_{th}}. \tag{1.26}$$

To maximise IR responsivity and to obtain a larger change in temperature for a given radiance, microbolometers are constructed from detector materials which have high R_d

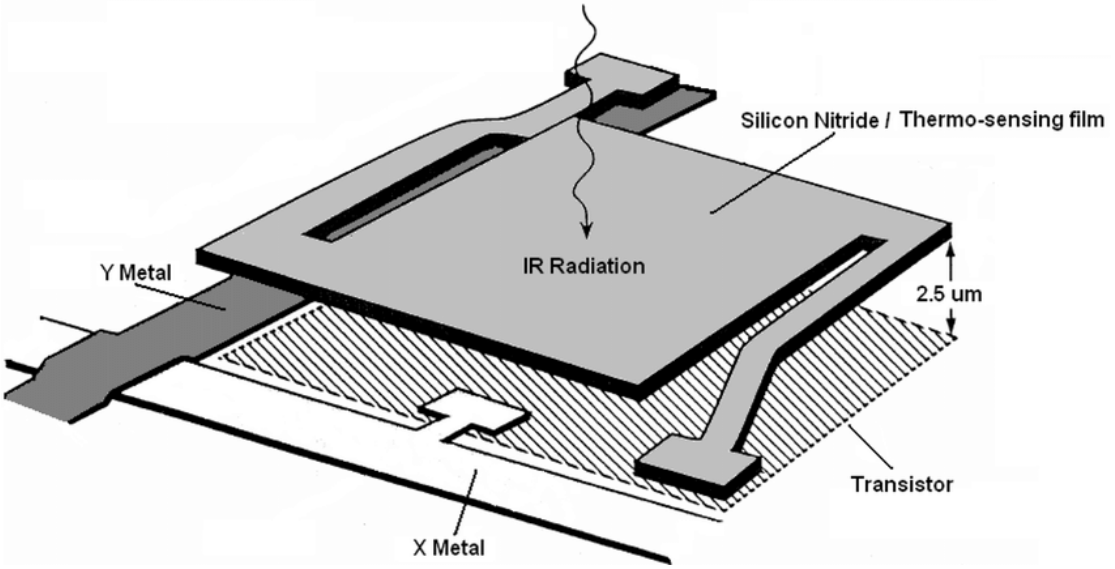

FIGURE 1.1: Schematic of a single microbolometer pixel from Moreno et al. 2012. The bridge, comprised of Si_3N_4 and the thermoresistive element, is suspended above the ROIC and connected by two long legs. As incident infrared radiation heats the bridge material, the thermoresisitive element registers this temperature change as a change in resistance. The ROIC detects this change in resistance by directing current through the legs to the bridge.

and α and designed to minimise G_{th} through the chosen length and cross-sectional area of the legs (Wood et al., 1992).

Since the late 1970's many advances have been made in the development of uncooled microbolometer arrays for detecting mid-IR radiation in defence, security and industrial applications. Microbolometer technology is commonly used for sensing in the 7 to 14μm band as it provides a high sensitivity at an affordable price, without the need for a cryogenic cooling system. They are available integrated into commercial camera systems for <10k GBP by manufacturers such as FLIR and can deliver noise-equivalent temperature differential (NEdT) measurements of <200mK (Benirschke & Howard, 2017) under factory conditions. NEdT is discussed further in section 2.4.1.

1.3 Application in Astronomy

Approximately half of the total energy density of radiation throughout the entirety of cosmic history is emitted at infrared wavelengths (e.g. Elbaz, 2002; Le Floc'h et al., 2005; Caputi, 2007). Ultraviolet and optical photons actively heat dust in regions of star and planet formation, evolved stars, and active galactic nuclei (AGN). This dust

absorbs the UV and optical photons and re-radiates at infrared wavelengths. As a result, the mid-IR spectral region covers a wide range of dust and molecular emission and absorption features, and recombination and fine structure lines. Mid-IR observations are particularly useful as the effect of dust extinction is much less prominent when compared to optical and near-infrared wavelengths (Mason et al., 2008).

Quantitative mid-IR astronomy began in the 1960's (e.g. Low, 1961) using heavily cooled single-element bolometric detectors on small telescopes. Since the 1970s, more complex and specialised mid-IR detectors have been successfully deployed on spaceborne and high-altitude facilities on telescopes such as Subaru (Spectro-Cam; Hayward et al. 1993, COMICS; Kataza et al. 2000), SOFIA (EXES; Richter et al. 2018, FORCAST; Herter et al. 2018), Kuiper Airborne Observatory (Cameron, 1976) and SPITZER (IRAC; Fazio et al. 1998).

High sensitivity, multi-pixel mid-IR detectors have been in operation at large ground based telescopes since the 1990's, such as the 3m IRTF (MIRSI; Deutsch et al. 2003), the 6.5m MMT (MIRAC; Hoffmann et al. 1993), the 8m Gemini (Michelle; Glasse et al. 1997, T-ReCS; Telesco et al. 1998, TEXES; Lacy et al. 2003) and VLT (VISIR; Lagage et al. 2000, MIDI; Leinert et al. 2003), and the 10m GTC (CanariCam; Packham et al. 2005).

Several high-profile, space-based and high-altitude surveys have also been conducted in the mid-IR, namely the Wide-field Infrared Survey Explorer (WISE) (Wright et al., 2010), Infrared Astronomical Satellite (IRAS) (Neugebauer et al., 1984), AKARI (Murakami et al., 2007), IRTS (Murakami et al., 1994), The European Large Area ISO Survey (Kessler et al., 1996), Midcourse Space Experiment (MSX) (Egan & Price, 1996) and the Revised Air Force Geophysical Laboratory (RAFGL) (Price & Murdock, 1983). With the imminent launch of the infrared-optimised JWST (MIRI; Rieke et al. 2015) we are entering a new era of mid-IR observations.

1.3.1 Atmospheric Transmission and Background Contribution

Mid-IR observations are very sensitive to observing conditions. With respect to the entire IR spectral region, only a small spectral window can be observed at ground based facilities. Figure 1.2 shows the estimated atmospheric transmission between 2

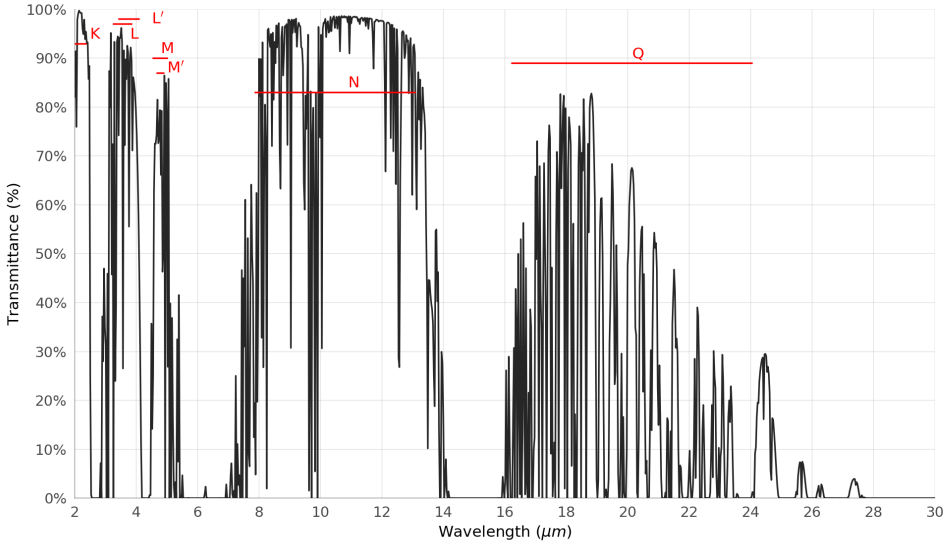

FIGURE 1.2: Synthetic spectrum of atmospheric transmission across the 2-30 μm wavelength range as observed at the Liverpool Telescope (altitude of $\sim$ 2363 m, latitude of 28 °) for observations with a zenith angle of 0 ° through 2 atmospheric layers. The spectrum was computed using ATRAN (Lord, S. D., 1992, NASA Technical Memorandum 103957). The spectrum has been interpolated with a spline of 1000 points. Common infrared filter bandpasses are shown as red horizontal lines. The central wavelengths of these filters are given in table 1.1.

Filter	λ (μm)	$\Delta\lambda$ (μm)	Vega (Jy)	Sirius (Jy)
K	2.179	0.41	655	2315.2
L	3.547	0.57	276	967.8
L′	3.761	0.65	248	868.4
M	4.769	0.45	160	557.5
M′	4.85	0.22	n/a	n/a
N	10.472	5.19	35.2	121.8
Q	20.130	7.8	9.70	n/a

TABLE 1.1: Flux of two standard sources Vega and Sirius in common infrared filter bandpasses as recorded by Cohen et al. (1992).

and 30 μm for the ground-based Liverpool telescope, which sits at an altitude of $\sim$ 2363m. Several standard filter bandpasses are described by red horizontal lines. The central wavelength λ and filter width $\Delta\lambda$ are recorded in table 1.1 alongside the flux of Vega and Sirius in each filter. Beyond 30 μm, infrared transmission drops to zero for ground based observations. As well as reducing the number of source photons that are transmitted to the ground, the atmosphere absorbs and isotropically re-radiates a fraction of the energy from space and the ground (Bertero et al., 2000). In particular, the telluric species H_2O, O_3, CO_2, N_2O and CH_4 contribute dominant emission lines and reduce atmospheric transparency in the mid-IR (Cox, 2000). High-altitude/space-based

observatories are favoured for mid-IR observations as they do not suffer from the effects of the atmosphere. Ground-based observing is much more challenging and has been traditionally viewed as impossible for simple, low cost instruments due to the very high thermal background and the requirement for specialist detector systems.

The mid-infrared background produced by the atmosphere can be several orders of magnitude brighter than most astronomical sources (Pietrow et al., 2019), with a surface brightness of -3 mag per square arcsecond at 11 μm (Mason et al., 2008). This overwhelming thermal background is combined with high spatial and temporal variability of sky emissions, which occur on subsecond timescales, and telescopic emissions, which occur on subminute timescales (Absil et al., 2004). Telescopic emissions arise from the opaque surfaces in the optical beam (i.e. the secondary mirror spiders, primary mirror cell and central borehole) which are near blackbody radiators, and greybody emitters such as the mirrors and warm optics (Bertero et al., 2000). As a result, observing at these wavelengths is very challenging, particularly for ground based facilities (Miyata et al., 1999).

Ground based telescopes must be optimised for infrared observations. Physical considerations to reduce photon noise include limiting baffling, having a thin primary, ensuring the emissivities of mirrors are low, making the primary borehole small and operating at stable mechanical temperatures. The frequent deployment of a chopping/nodding (see below) regime during observations is also required to reach the fundamental photon shot-noise limit of the thermal background (Bertero et al., 2000). These differential observations must occur at a rate faster than background fluctuations, with the frequency dependent on observing wavelength, weather conditions and telescope location. Chopping involves tilting either the secondary or a foreoptics mirror between on- and off-axis positions at a frequency of $\sim 10 - 50\,\mathrm{Hz}$ (Papoular, 1983). The difference between the images taken at these two positions improves background subtraction. However telescopic emission is not uniform and the on- and off-axis chop positions have different optical paths. This results in telescopic emission residuals in chop subtracted images. These residuals are removed by nodding, where the telescope is slewed to an off-axis position and the chop sequence repeated, at a frequency of $\sim 0.1\,\mathrm{Hz}$ (Papoular, 1983).

1.3.2 A Brief Overview of Mid-IR Astronomy

As mentioned above, the cosmic infrared background accounts for roughly half of the radiation emitted by stars throughout cosmic time. Mid-IR radiation in particular, is an effective tracer of star and planet forming regions, evolved stars, solar system objects and galaxies. In this section, we briefly introduce these areas of study. We describe the processes from which the mid-IR radiation arises and examples of observations with mid-IR photometry or spectroscopy.

1.3.2.1 Star Formation

The mechanics behind the formation of stars is still not well understood as they are born deep within giant molecular clouds where they are obscured by dust and gas at optical wavelengths (Richter et al., 2018). This circumstellar gas and dust is the only tracer of the physical processes of star formation happening inside. Photometric and spectroscopic observations in the infrared can be used to distinguish physical, chemical, and dynamical differences between high- and low-mass star-forming regions. They can also be used to investigate the circumstellar disks around young stars, i.e. the environment in which planets form, by helping to refine accretion and cooling models, and to study the kinematics, composition and evolution of disks around low-mass young stellar objects.

The embedded phase of young stars is a critical period during which several important physical processes occur: infall in the collapsing envelope, disk formation, material being shocked by outflows and the heating and disassociation of gas by UV photons. This is the critical period during which the final mass of the star is determined. The protostar heats the surrounding dust which creates a strong mid-IR continuum in the inner envelope or early disk. As the cloud begins to collapse into a star, it reaches the densities at which a variety of molecules form. Several of these molecules can be used as tracers of evolution in protostellar environments (Hatchell et al., 1998).

This phase is particularly exciting for the massive stars that dominate the energy budget of young galaxies and are effective tracers of star formation rates. At all stages of their lives, the feedback from massive stars drives the physical and chemical enrichment of the interstellar medium (ISM) in their host galaxies. At the start of their life, their powerful

jets and outflows can both destroy their surrounding natal molecular clouds halting further local star formation while triggering the next generation of star formation farther afield. At the end of their lives, the huge energy and momentum they release through their strong stellar winds and supernova explosions drives turbulence and supplies heavy elements to the interstellar medium (Tan et al., 2014).

Mid-IR photometry of protostars in active, luminous star-forming regions can be used to constrain their properties and determine the environmental dependence of star formation (Adams et al., 2012). Further information on the nature of the star-forming region can be determined from the many features present in mid-IR spectroscopic observations. The fundamental vibrational transitions of the gas-phase molecules H_2O, CH_4, C_2H_2, HCN, and CO_2 occur between 6 and 15 μm and can be used to probe physical conditions like the temperature and the density of gas (e.g. van Dishoeck, 1998), cooling (e.g. Helmich et al., 1996) and organic chemistry (e.g. Feuchtgruber et al., 2000). Various C-C and C-H bending and stretching modes of polycyclic aromatic hydrocarbons (PAHs) occur between 6.2 and 16.2 μm (Duley & Williams, 1981). These lines are indicators of the presence of complex carbonaceous material excited by UV radiation (Peeters et al., 2004b) and are a reliable tracer of large-scale star formation (Peeters et al., 2004a). H_2 rotational lines are present at 6 to 15 μm and can be used to probe properties like the mass and temperature of warm gas (e.g. Valentijn et al., 1996; Timmermann et al., 1996; Fuente et al., 1999; Wright et al., 2000), and differentiate between shock or photon heating (e.g. Black & van Dishoeck, 1987; Sternberg & Dalgarno, 1989; Larsson et al., 2002; Cabrit et al., 2004). Deep and broad vibrational bands of amorphous and crystalline silicates occur between 9.7 and 24.5 μm as a result of the Si-O stretch and O-Si-O bending modes (Gillett & Forrest, 1973). These can be used as diagnostics of processing/heating (van Dishoeck, 2004), mineralogy (e.g. Malfait et al., 1998; van den Ancker et al., 2000) and grain growth (Bouwman et al., 2001). Vibrational bands of sulfides, carbonates and ices occur between 4.67 and 23.5 μm. These can be used to probe the presence of volatile solids (e.g de Graauw et al., 1996; van Broekhuizen et al., 2004), organic chemistry (van Dishoeck, 2004), and thermal history (e.g Ehrenfreund et al., 1998; Keane et al., 2001).

1.3.2.2 Planet Formation

Some of the molecules that form during the cloud collapse stage of star formation end up in the rotating disks that surround young stars. The conservation of angular momentum when the circumstellar disk is gas-rich and the star is contracting towards the main sequence results in the formation of a protoplanetary disk (Natta & Testi, 2004). It is from the material left in this disk that planets are formed through dust processing, i.e. the coagulation of small ($\sim 0.1\,\mu$m) solid particles (Visser et al., 2009). The study of the chemical composition of this gaseous and solid-state material and how it is affected by the protostellar and protoplanetary environments is key to understanding the disk's ability to form planets.

Much of the knowledge about proto-planetary disks has been obtained from studying the infrared radiation emitted by warm dust particles located 1-10 AU from the star in the disk (Varga et al., 2020). Although dust makes up only a small fraction of the disk mass, the properties of the dust heavily influence the appearance and evolution of the disk. The main heating and cooling mechanism of the disk material is driven by the absorption and subsequent emission of radiation by dust. Consequently, the dust determines the temperature and spatial structure of the disk (van Boekel et al., 2005).

Mid-IR spectroscopy of protoplanetary disks and debris disks (i.e. features of older systems where star formation is complete or nearly complete but a large amount of short lived, second generation dust remains, e.g. the Kuiper Belt in our Solar system) can be used to determine the mineralogy of the dust and the physical conditions of the gas (e.g. Malfait et al., 1998; Fabian et al., 2001). Water ice condensation dominates the mass budget of newly formed planetestimals and determines the ability of the disk to form massive planets (Ciesla & Cuzzi, 2006). The strength of the water feature at 6 μm provides a direct measurement of water column density temperature (van Boekel, 2007) and grain growth (Meijerink et al., 2008). Evidence of crystallinity from emission lines in the 9-13 μm region can be used as a direct tracer of disk processing and evolution (Bouwman et al., 2008; van Boekel et al., 2005), and an indirect tracer of the formation of large planetary bodies (e.g. Bouwman et al., 2001), which are expected to form in the inner < 20 AU of protostellar disks (Boss, 2008). The shape of the 10 μm silicate feature can be used as an indicator of grain size and location in the disk. Small ($\sim 0.1\,\mu$m) primordial grains have a triangular-shaped silicate feature which peaks around 9.8 μm

and is seen in mid-IR spectra of the outer disk. Larger ($> 2\,\mu$m) grains have a silicate feature spectrum that plateaus between 10 and 11 μm and is seen in mid-IR spectra of the central region of the disk (van Boekel et al., 2005). Crystalline silicates also have smaller sharp features at 9.2, 10.5 and 11.3 μm. The temperature and mass, as a function of radius, of the warm molecular gas present in debris disks can be traced using the pure rotation lines of H_2 in the 6-15 μm region. These measurements can be used to constrain the age at which gas giants form (Thi et al., 2001). As temperatures in dense molecular clouds are low (< 50K) PAHs can freeze into grains and react with molecular ice grain mantles when exposed to ionising radiation (such as UV). This process produces biologically important molecules (e.g. alcohols, ketones, amino acids). Consequently, observations of PAH features in the 6.2 and 16.2 μm region of mid-IR spectra can be used to probe the creation of the hydrocarbon prebiotic material on small bodies that is a precursor to life (Bernstein et al., 1999).

1.3.2.3 Evolved Stars

Dust is formed in the ejecta of dying stars. The mid-IR region is dominated by spectral features that can be used to classify evolution stage, determine dust composition and (hence) mass loss rates from low mass ($< 8M\odot$) stars (e.g. AGB/post-AGB stars and novae) and high mass ($> 8M\odot$) stars (e.g. red supergiants (RSG), luminous blue variable stars, Wolf-Rayet stars and supernovae). The dusty environments around evolved stars can be divided into two categories of chemical composition; carbon (C) rich or oxygen (O) rich. This classification depends on the relative abundance of carbon and oxygen in the mass-losing star. This C/O ratio can be determined from mid-IR spectra. A star with more oxygen than carbon (i.e. C/O < 1) is identified by spectra dominated by absorption and emission features of amorphous and crystalline silicates between 9.7 and 24.5 μm (Sylvester, 1999). A star with more carbon than oxygen (i.e. C/O > 1) will have a spectrum dominated by carbonaceous dust species like silicon carbide (SiC), PAHs or amorphous carbon (Molster et al., 2002). Low mass-loss rates in these stars can be determined by the dominant presence of oxides (Cami & Yamamura, 2001). Features from heavy elements appear in the 4 -16 μm region of mid-IR spectra of novae and supernovae. There are a number of broad mid-IR atomic lines found in high velocity environments (widths $\sim$ 100-1000 km/s). For example, planetary nebulae show strong excitation lines of [Mg IV] at 4.49 μm, [Ar VI] at 4.53 μm, [Mg V] at 5.61 μm, [Ar II]

at 6.99 μm, [Ne VI] at 7.65 μm and [Ar III] at 8.99 μm in their spectra (Ennico et al., 2006).

Of particular interest is the evolution and eventual death of massive stars. Massive stars emit far-UV radiation that dominates the energetics and chemistry of their surrounding molecular clouds (Wolfire et al., 1990). The expansion, and subsequent cooling of stellar ejecta causes small dust grains to condense and absorb radiation from the star. These dust grains and PAHs reprocess most of this radiation into PAH infrared features and infrared continuum radiation. However, up to 1% of the absorbed radiation is converted to gas heating via photoelectric ejection of electrons from grains (Kaufman et al., 1999). The photoelectric heating efficiency increases with decreasing size of dust grains. PAH molecules are the smallest of dust grains, and play an important role in the heating of the gas by providing photo-electrons (e.g. Bakes & Tielens, 1994; Tielens & Hollenbach, 1985). PAHs are traced by several features in the mid-IR at 6.2, 7.7 and 11.2 μm. The relative strength and characteristics (e.g. shape, central wavelength) of the mid-IR features vary significantly with local physical conditions (e.g. Hony et al., 2001; Flagey et al., 2006; Smith et al., 2007; Vermeij et al., 2002; Galliano, 2006). These variations arise from modifications to the molecular structure of the PAHs, in different astrophysical environments.

Most massive stars with mass $\geq$ 9 M$\odot$ will become RSGs at some point in their lifetimes (Gordon et al., 2018). RSGs amongst the most common and luminous mid-IR populations of massive stars (Britavskiy et al., 2014). RSGs have some of the highest mass-loss rates observed in stars and shed a significant fraction of their initial mass. The duration and mass-loss rates in this stage influences the mechanism by which the star will die; as a supernova or in post-RSG evolution. However, the mechanism behind this mass loss is not well understood (Shenoy et al., 2016). Dust present in the circumstellar environment of RSGs can be an indication of recent or historical mass-loss episodes. This dust arises from stellar winds cooling to temperatures below the dust condensation temperature ($\sim$ 1000K). A higher mass-loss rate results in a high enough total mass of dust at the condensation radius for the dust emission to be detectable in the mid-IR. Emission spikes at $\sim$ 10 μm and $\sim$ 18 μm are caused by blended emission lines from this silicate dust. Mid-IR photometry can be used alongside spectral energy distribution (SED) models to provide estimates of the mass-loss rates, ejecta dust temperatures and mass-loss histories of these luminous supergiants (e.g. Gordon et al., 2018; Shenoy et al.,

2016; Yang et al., 2018). Spectral observations of RSGs can also be used to convert the intensity of the silicate emission into a mass-loss rate for the star (e.g. Beasor & Davies, 2016).

1.3.2.4 Solar System Objects and Exoplanets

The primitive bodies of our own solar system (i.e. comets and asteroids) consist of material that has not been significantly changed since the birth of the planets, and provide insight into the physical conditions and processes in the icy, cold regions of the protoplanetary disk from which our solar system was born (Wooden, 2008). The dust associated with comets has emission which peaks in the 7-20 μm region as a result of the prominent silicate mineral emission features (Kelley & Wooden, 2009). Mid-IR spectroscopy of comet dust can be used as a diagnostic of the origin of the constituents of the primitive solar system, and their subsequent evolution into planetesimals. The identification of features that can be attributed to various non-protoplanetary disk sources (e.g. supernovae, ISM clouds, etc.) in the mid-IR spectra of comets can provide constraints on solar system models (Wooden, 2008) and whether the population of planetesimals that comets were created from were heterogeneous in origin (Kelley et al., 2016). Mid-IR photometry is crucial for characterising the physical properties of distant objects which are otherwise too small to be resolved. When combined with measurements of reflected light, the mid-IR can be used to accurately determine the mass, diameter and albedo, and constrain the thermal properties (e.g. thermal inertia, surface emissivity, surface roughness) and spin axis orientation of the object (Müller et al., 2020). These properties can be used to gain insight into the processes that created the dynamical architecture of the outer Solar system (Milam et al., 2016).

Virtually all known exoplanets have been indirectly detected through observations of their transit or the effect they have on the radial velocity of their host star (Burrows et al., 1997). Direct imaging, through imaging and spectroscopy, is an important step for detecting and characterising exoplanets, particularly as planets at large radii from their central star are difficult to detect with in-direct methods (Brande et al., 2020). Characterising the climate and composition of exoplanet atmospheres, in particular their potential to develop and maintain atmospheres capable of supporting biology, is an important goal for exoplanet science. Mid-IR observations can be used to constrain

planetary atmospheric models and detect the presence of 'biosignatures', gases that make up the Earth's atmosphere (i.e. nitrogen/nitrous oxide, water, carbon dioxide, oxygen/ozone, and methane), which could indicate biological processes underway on the planet (Petit dit de la Roche et al., 2020). These 'biosignatures' can be detected in mid-IR spectra (e.g. Tremblay et al., 2019; Fauchez et al., 2020) with CO_2 features at 4.3 and 15 μm, H_2O features at 6.2 μm and beyond 17 μm, CH_4 features at 7.7 μm, N_2O features at 4.5, 7.8, 8.3 and 17 μm, O_3 features at 9.7 and 14.3 μm and CO features at 4.8μm (Leisawitz, 2020).

We can gain a further understanding of the formation and evolution of exoplanetary systems from mid-IR observations of planets in our own solar system. Solar system planets are divided into two major groups; the terrestrial planets (Mercury, Venus, Earth and Mars) which are characterised by their relative proximity to the Sun, small size, high density, small number of satellites, and atmospheres (if present) which are a negligible fraction of their total mass, and the giant planets (Jupiter, Saturn, Uranus and Neptune) which are characterised by their large volume, low density, large number of satellites, and atmospheres which are a large fraction of their total mass. These planets provide a reference for comparison to all other planetary systems.

Planetary spectra are comprised of two components; reflected sunlight ($< 4 - -5\,\mu$m) and intrinsic thermal emission ($> 4 - -5\,\mu$m) (Encrenaz, 2005). Mid-IR observations of the intrinsic thermal emission can probe fundamental properties such as the chemical composition and temperature/pressure structures at varying altitudes for planetary atmospheres, and the dimensions, surface thermophysical properties and reflectivities of bodies without atmospheres (e.g. Cruikshank, 1988; de Zotti et al., 1989). Spectra can also be used as a diagnostic of solid or liquid signatures by probing the presence of clouds and aerosols and their location (either suspended in the atmosphere or on the surface). For bodies without atmospheres (such as Mercury or the Moon), strong mid-IR emission results from the structural, chemical, and physical properties of silicate rocks and minerals. Thermophysical regolith properties can be determined from spectroscopy, including thermal inertia, particle size, temperature distribution with depth and the behaviour of volatiles on or under the surface. The silicate emission features at 7.6 and 9.6 μm are diagnostics of bulk rock types (Sprague, 2000). These features can be used to identify silica content and acidity level of the regolith (e.g. Murakami et al., 2007;

Salisbury et al., 1970). Measurements of thermal inertia can be used to constrain heat conduction models for the regolith (Lynch et al., 2007).

Observations of terrestrial planets can be used to probe localised temperatures and winds, cloud presence and coverage, aerosols, seasonal cycles and in the case of Mars, surface mineralogy. Terrestrial planets like Venus, which is comparable to Earth in size, location and composition but differs vastly in surface environment can be studied in the mid-IR to gain important insights that will aid in detecting and characterising Earth-like exoplanets (Norwood et al., 2016) . The mid-IR spectra of Venus and Mars are dominated by a strong CO_2 feature at 15 μm and O_3 (ozone) feature at 9.7 μm. For Venus the CO_2 absorption feature traces the atmosphere that lies above sulphuric H_2SO_4 clouds which obscure the surface. For Mars, the CO_2 feature can appear either in absorption or in emission, and varies as a function of latitude due to the temperature contrast between the atmosphere and the surface (e.g. Encrenaz et al., 2005). The shape of the CO_2 feature indicates any variation of atmospheric temperature with altitude (for the terrestrial planets this indicates a decreasing temperature for increasing altitude). Mars also has a H_2O_2 feature at 8 μm which has been proposed as a tracer of seasonal variations and/or regolith oxidisation (e.g. Encrenaz et al., 2004; Bullock et al., 1994).

The giant planets are further divided into the gaseous giants (Jupiter and Saturn) which are predominantly composed of primordial gas, and the icy giants (Uranus and Neptune) which have a significant fraction of mass ($\sim$ 50%) in their icy core. The stratosphere and troposphere of the giant planets are traced by emission and absorption features respectively. These spectra are dominated by hydrogen H_2 at 12 μm, hydrocarbons such as CH_4 at 7.7 μm and varying traces of other compounds like CO at 4.7 μm, CO_2 at 15 μm, H_2O at $5-6$ μm, GeH_4 at 5 μm, NH_3 at 5 and 10 μm, PH_3 at $8-9$ μm and AsH_3 at 5 μm (Encrenaz, 2008). The photodissociation of CH_4 at high pressures produces C_2H_6 absorption at 12.2 μm and C_2H_2 emission at 13.7 μm, and the abundance can probe atmospheric altitude, circulation and seasonal variations (e.g. Hammel et al., 2006, 2007; Burgdorf et al., 2006).

1.3.2.5 Galaxies

Mid-IR can provide a wealth of new insights into galaxies in the distant universe ($z \sim 2$) (Ohyama et al., 2018). Studies at mid-IR wavelengths can be used to constrain the

multi-wavelength global SED for galaxies. Of particular interest is the brightest galactic sources in the mid-IR such as starburst galaxies, luminous infrared galaxies (LIRGs) and ultra-luminous infrared galaxies (ULIRGs) (e.g. Spinoglio et al., 1995; Pearson, 2001; Lagache et al., 2004; Rowan-Robinson et al., 2004; Le Floc'h et al., 2005). The mid-IR spectra of galaxies are rich in emission lines with luminous galaxies dominated by prominent PAH emission features (e.g. Lutz et al., 1998; Xu et al., 1998). The mid-IR radiation of galaxies arises from many of the processes that have already been discussed, such as star and planet formation, and evolved stars. Observing galaxies in this spectral region provides an opportunity to probe how a large collection of these processes can affect their wider environment.

The ISM of galaxies is the reservoir from which stars are born and that they replenish as they age and die (Hollenbach & Tielens, 1999). Much of the infrared radiation emitted by the interstellar medium (ISM) has its origins in galactic photodissociation regions (PDRs). PDRs occur where far UV radiation dominates heating of the surrounding medium. As mentioned previously in section 1.3.2.3, far UV radiation can be reprocessed as PAH emission features in the mid-IR with physical characteristics which vary in different extragalactic environments (Markwick-Kemper et al., 2007; Armus et al., 2007; Spoon et al., 2006). These features can be used to probe the link between the composition and quantity of dust injected into the galactic ISM by evolved stars. For example, low-metallicity galaxies exhibit very weak or no PAH features (Madden et al., 2006). Mid-IR spectroscopy can be used to calibrate PAH features to obtain the ratio of C-C stretching to C-H stretching and bending modes of PAHs. By combining these observations with other multiwavelength observations, the local conditions (e.g. density, temperature, radiation field) can be determined (Galliano et al., 2008b).

A significant fraction of galaxies (over 40% of bright nearby galaxies and 50-75% of early-type galaxies) harbour an AGN (e.g. Ho, 1998, 2004, 2008). AGN are produced by accretion onto a nuclear supermassive black hole and are surrounded by a dust-torus which shrouds this process at optical and near infrared wavelengths, but strongly re-radiates and emits in the mid-IR. The observed diversity of AGN properties results from viewing different orientations relative to our line of sight. The centrally heated, optically thick torus surrounding an AGN shows silicate absorption between 9.7-18 μm (e.g Imanishi & Ueno, 2000) when viewed side on, and silicate emission between 9-13 μm (e.g Siebenmorgen et al., 2005; Sturm et al., 2005; Hao et al., 2005) when viewed face

on. PAH emission features are mostly absent in the intense radiation fields that lie close to AGN. However, the mid-IR still has a wealth of features to identify these regions. Excited fine structure lines like [Ne VI] at 7.65 μm, [Ne V] at 14.3 μm and 24.3 μm, and [O IV] at 25.9 μm arise from the hard UV radiation produced by black hole accretion (Sturm et al., 2000).

1.4 Application in Ecology

Global biodiversity and planet-wide conservation efforts have never been of more importance than right now. A loss of biodiversity is a threat to both valuable ecosystems and human well-being. Our current global society is destroying species at an accelerating rate, initialising a mass extinction episode so large it has been unparalleled for 65 million years and which will have ramifications that outlast humanity (Régnier et al., 2015). Monitoring the diversity and distribution of species provides insight into trends in biodiversity and ecosystem health to make informed decisions on resource use and protection which is key to slowing this rate down.

Historically, surveys to monitor biodiversity have been conducted either on the ground by foot or car, via manned aerial vehicles, or using space satellites (e.g. Buckland et al., 2001a; MacKenzie, 2006; Buckland et al., 2008; Franklin, 2010; Fretwell et al., 2012; McMahon et al., 2014). All of these methods have major limitations. Individual ground surveys are time intensive and only cover small areas. Although manned aerial surveys cover a great deal more area than ground surveys, they are cost prohibitive for conservation research. They are reliant on the availability of aircraft and are limited to safe flight paths with ample emergency landing opportunities (Sasse, 2003) which restricts the scope of the survey.

A further limitation is that data are often collected using cameras operating at optical wavelengths (Jones et al., 2006; RodrÃguez et al., 2012; Koh & Wich, 2012; Barasona et al., 2015; Linchant et al., 2015; Wich, 2015; Mulero-Pázmány et al., 2015; Van Andel et al., 2015; Canal et al., 2016). Optical cameras are limited to use during daylight hours so they are effectively blind 50% of the time, which greatly limits their use. Some of the major applications for which aerial surveys are needed in conservation occur predominantly at night, e.g. poaching, and many vulnerable species are part

or fully nocturnal. Furthermore optical light is just the reflection of sunlight, giving all objects within the footage, be they foreground or background, a similar brightness. This makes it difficult and computationally expensive to resolve objects of interest from the surrounding background in an automated way without some kind of manual intervention.

To mitigate these constraints researchers have started to combine mid-IR remote sensing with unmanned aerial vehicles (UAV), otherwise known as drones, to obtain survey data.

1.4.1 Mid-IR Emissions of Endothermic Homeotherms

Microbolometers can be used to detect sources that maintain temperatures within the endothermic range. Endothermic homeotherms are mammals and birds that use metabolic heat to maintain a stable internal temperature. Most placental mammals have internal body temperatures within the range 36 – 40 °C (approximately 309 – 313K) (Jessen, 2001) and bird species have internal body temperatures within the range of 38 – 48°C (approximately 311 – 321K) (Prinzinger et al., 1991). These values scale positively with body mass if phylogenetic effects are ignored (Clarke & Rothery, 2008) and are dependent on the means of temperature measurement, with auxiliary, oral and rectal temperatures varying by up to 3 °C in some circumstances (Sund-Levander et al., 2002). Figure 1.3 shows the radiant excitance as a function of wavelength of two temperatures; the approximate lower bound body temperature of mammals, 309 K, and the approximate boiling point of water at 1 atm, 373.15 K. The range at which the spectral energy distribution M_λ of endothermic homeotherms is expected to peak can be calculated as between 7.77 and 9.37 μm. This range is represented in figure 1.3 as the red filled line.

Thermoregulation in endothermic homeotherms is conducted by controlling the effective surface area involved in heat exchange. By controlling the blood flow to the periphery, endotherms regulate the flow of heat from the 'core' of the body to the skin, with changes in fur or fat layers, and posture, controlling the surface area this happens over (Phillips & Heath, 1995). Changes in vascular circulation can result in a measurable increase or decrease in tissue temperatures. This can be a measure of individual health with inflammatory responses generating and transferring heat to adjacent tissues via enhanced capillary blood flow (Knížková et al., 2007). Temperature variations less than 1 °C can be indicative of early or subclinical inflammation or infection and temperature variations greater than 1 °C are indicative of the later stages of inflammation development or

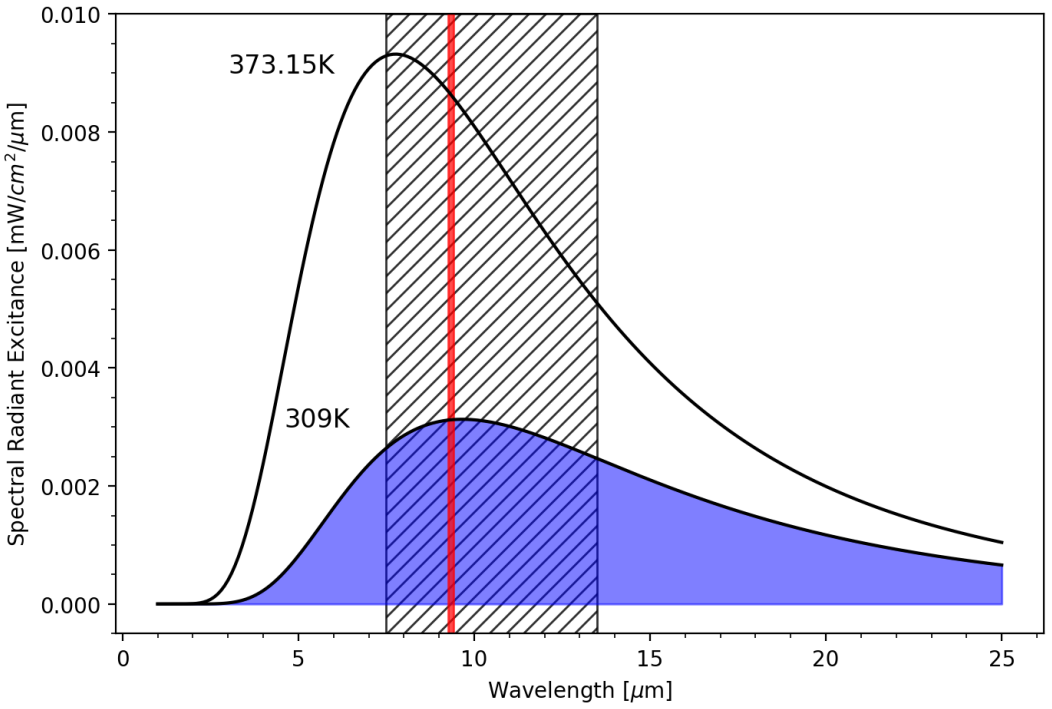

FIGURE 1.3: The radiant excitance (otherwise known as the emittance) of a blackbody in $W^{-3}cm^{-2}\mu m^{-2}$ as a function of wavelength for two temperatures; the approximate lower bound body temperature of mammals 309K which peaks at a wavelength of 9.37 μm, and the approximate temperature of boiling water 373.15K which peaks at a wavelength of 7.77 μm. The shifted peak between the two distributions is a consequence of Wien's law which describes the relationship between the temperature of a blackbody and the wavelength at which it has the greatest spectral radiant excitance. The red filled line represents wavelengths, λ_T, at which the blackbody profile of an endothermic homeotherm source, $309 \leqslant T \leqslant 321$ K, should theoretically peak. The blue shaded area represents the total power per unit area emitted by the blackbody, $\frac{M_\lambda}{A}$. The black hatched area represents the wavelength range mid-IR cameras are sensitive to, 7-15 μm.

clinical infection (Schaefer et al., 2004). Hormonal fluctuations have also been observed to produce changes in body temperature in cows, with periods in the oestrous cycle causing a deviation of temperature between 0.5 and 1 °C (Hellebrand et al., 2003). In humans, temperature variations in bilateral symmetry greater than 0.7 °C are considered abnormal and could potentially be an indication of physiological or anatomical variance (Szentkuti et al., 2011).

1.4.2 Coupling Mid-IR and UAV to Survey Species

Using mid-IR instead of optical imaging greatly increases the likelihood of successful detections of endothermic homeotherms as there can be a large contrast between them and the background environment. This contrast is maximised in cold, dry environments

and diminishes as the temperature and humidity increase (Mulero-Pázmány et al., 2014). The recent decrease in the price of mid-IR cameras has made them affordable for use in small scale research projects and their major advantages in detection have been tested in single and multi-species surveys, detecting; American bison, fallow deer, grey wolves and elks (Chrétien et al., 2015), grey seal (Wich & Koh, 2018), koala (Gonzalez et al., 2016), roe deer (Israel, 2011), hippos (Lhoest et al., 2015) and rhinos (Mulero-Pázmány et al., 2014). The latter study comprehensively compared the efficacy of aerial footage at thermal and RGB wavelengths for target species surveillance and people detection, with a focus on anti-poaching operations. Thus the use of mid-IR cameras has been investigated and proven as an effective means of detecting animals.

A major benefit of using UAV technology coupled with a mid-IR regime for imaging is the increase in the volume of data obtained for a fraction of the price and time compared to the methods mentioned above. However, as the volume of data from such studies increases, so does the need for data analysis tools that can maximise the scientific output in as short a time possible. In the field of conservation biology, these analysis tools are fairly well developed for visible wavelengths. While they can be adapted for thermal imaging, they would need to be used in conjunction with manual detection/identification in order to be effective. This introduces a layer of human bias and also makes the entire process very time-inefficient, and almost impossible to adapt into a live or almost real-time pipeline. To counteract this, the detection and identification stages of survey data analysis can be automated with the use of algorithms. Several different groups have already attempted to develop such analysis tools (e.g. Lhoest et al., 2015; Chrétien et al., 2015; Gonzalez et al., 2016).

1.5 Motivation

From the concepts discussed in sections 1.3 and 1.4, there is potential for low-cost, mid-IR observing to be beneficial in both astronomy and conservation ecology. As established in this chapter, microbolometers are affordable, uncooled, commercial 'off the shelf' (COTS), detectors that cover a small spectral range of the mid-IR. For the purposes of this thesis, we focus our interests on successful application of microbolometers in these two very different fields. We therefore explore three major questions:

1. How can mid-IR imaging and astronomical data analysis and reduction techniques be applied practically in ecology?

2. How can we develop inexpensive ground-based astronomical instruments for mid-IR observations?

3. What techniques can we use to improve the performance of these instruments?

Part I (Chapter 2) is focused on introducing and understanding the microbolometer system used throughout this thesis. We attempt to address the question of what detector systematics limit read-out accuracy by accessing and understanding the detector response using standard astronomical techniques to potentially overcome these limitations.

Part II (Chapter 3) of this thesis is dedicated to a unique and novel application of microbolometers in a cross discipline field. We study the feasibility of coupling mid-IR imaging technology and instrumentation techniques commonly found in astronomy with Unmanned Aerial Vehicles for use in the field of conservation biology.

Part III (Chapter 4 - 5) of this thesis is dedicated to the development and testing of a mid-IR instrument for use on ground-based telescopes, using a microbolometer as the detector. We explore whether widely-available mid-IR technology can provide the opportunity to expand, at low cost, the availability of mid-IR observing.

We conclude our findings in Chapter 6, which immediately precedes an appendix of supplementary material.

Chapter 2

Part I Laboratory Characterisation of an Uncooled Microbolometer Array

2.1 Overview of Contents

This chapter provides an introduction to the mid-IR camera that is used as the detector throughout the thesis. Various standard astronomical instrumentation techniques are investigated for the purpose of characterising systematics and statistical errors that limit read-out accuracy and precision. A series of lab-based experiments are presented, and the performance of the real detector is measured against an ideal theoretical detector. Random noise and spatial systematics are introduced, and the effect these have on the sensitivity of the system is discussed. In an attempt to determine whether standard microbolometer technology can achieve the scientific goals of the project, a feasible minimum detectable change in temperature given the measured SNR and observed systematics is theoretically determined. The Chapter concludes with a discussion on what limits this imposes on the scientific goals of using COTS mid-IR imaging in ecology and in astronomy.

The works described in this chapter were conducted by myself under the guidance of Prof. I. Steele (LT Telescope Director).

2.2 Detector/Camera Specifications

There are several companies manufacturing detectors for the COTS 'thermal-imaging' market (e.g. FLIR, Raytheon, Micro-Epsilon). The works presented in this thesis are conducted with, and built from, a pre-assembled FLIR Systems Inc. Tau 2 LWIR Thermal Imaging Camera core which is comprised of a vanadium oxide microbolometer (640 x 512 pixels, each of dimension 17 x 17 μm), and a 13mm focal length lens of unspecified prescription. This system reads out data at a frequency up to 8.3Hz. The full detector specification can be seen in table 2.1 courtesy of the FLIR product page[1].

FLIR (2015) describe the conversion of the signal count produced by mid-IR radiation incident on a microbolometer array (see section 1.2) into a temperature output by the system. Initially, the signal count is converted into digital counts using an analogue-to-digital (A/D) converter. For this system, the A/D converter has a 14-bit range, i.e. the digital output has count values in the range $0-16383$. Digital counts are converted into a radiance ($\mathrm{W}\cdot\mathrm{sr}^{-1}\cdot\mathrm{m}^{-2}$) and compared to a calibration curve to determine an effective blackbody temperature. These calibration curves are created by the manufacturer through a series of measurements of blackbody sources at known temperatures, radiance levels, emissivities, and distances. For the camera system described here this conversion occurs when the camera is operated in 'high resolution, T-Linear enabled' mode. The read-out values $(x,y)_T$ in this mode are temperatures T which can be converted to Kelvins with the following linear relationship:

$$T = (x,y)_T \times 0.04 \tag{2.1}$$

As a result, each pixel is assigned a value corresponding to the mid-IR temperature of the scene.

During operation, the FLIR system self calibrates by introducing an opaque shutter between the 13mm lens and the detector. This flat field calibration (FFC) acts to correct any non-uniform changes in response across the detector focal plane array (FPA) after this has changed unevenly with time. The shutter deploys at a pre-defined intervals of $\sim$ 2.5 minutes, but can also be triggered by any significant changes in environment or detector temperature. By applying this correction, the offset correction factors of

[1] `www.flir.com/products/tau-2/`

Lens specification	13mm - f/1.25
Resolution	640 x 512
Field of View (FOV)	45°(H)x37°(V)
Instantaneous FOV	1.308 mrad
Pixel Pitch	17 μm
Spectral Band	7.5 - 13.5 μm
Exportable frame rates	7.5 Hz NTSC; 8.3 Hz PAL
NEdT	<50 mK at f/1.0
Scene Range	-25°C to +135°C
Time to image	<5.0 sec
Size (without lens)	1.75" x 1.75" x 1.18"
Weight	72g
Primary electrical connector	50-pin Hirose
Input supply voltage	4.0 - 6.0 VDC
Power dissipation (Steady state)	<1.2 W
Flat-Field Correction (FFC) Duration	<0.5 sec
Operating temperature range	-40°C to +80°C
Non-operating temperature range	-55°C to +95°C
Temperature shock	°/min
Operational altitude	+40,000 feet
Humidity	5% - 95% non-condensing
Vibration	4.3g three axis, 8 hr each

TABLE 2.1: An overview of the camera specification as provided by FLIR at `www.flir.com/products/tau-2/`

the microbolometer elements are reset to factory standard to reduce thermal drift (see section 3.3.2), which is due to the changing of the sensor temperature with time and causes counts to increase steadily until the camera self calibrates. As the shutter is operational, observations are disturbed. As a result many off the shelf systems record at a higher frame rate than they read out. FLIR offers the functionality to change the period in between calibrations, and this can have a significant effect on the accuracy of values recorded. This period has been left unadjusted and set to factory standards.

2.3 The Importance of Characterising System Response

This thesis aims to present the application of the same mid-IR imaging technology in two very different fields; astronomy and ecology. For all uncooled COTS mid-IR systems, the presence of systematics and lens aberrations have a severe impact on the sensitivity of the detector and read-out temperature values. Successful application requires thorough detector calibration to account for the systematics that limit read-out accuracy. In both

fields, remote temperature sensing relies on the ability to accurately compensate for target surface, atmospheric emission, and the imaging system itself.

2.4 Modelling the Noise present in Uncooled Microbolometer Systems

The intensity, $I_{x,y}$, measured by a detector can be reproduced using a standard noise model:

$$I_{x,y} = S_{x,y} f_{x,y} + D_{x,y} d_{x,y} + \sigma_{x,y} + B_{x,y} \,, \tag{2.2}$$

where $S_{x,y}$ is the source image (the 'true intensity'), $f_{x,y}$ is the flat field response, $D_{x,y}$ is the time-dependent element of the dark current, $d_{x,y}$ is the relative dark current intensity between different pixels, $\sigma_{x,y}$ is the contribution of random noise and $B_{x,y}$ is the bias. Our aim is to recover the true intensity from the measured intensity:

$$S_{x,y} = \frac{I_{x,y} - D_{x,y} d_{x,y} - \sigma_{x,y} - B_{x,y}}{f_{x,y}} \,. \tag{2.3}$$

Usually it is assumed that $D_{x,y} = D$ (and often that $D = 0$ for cryogenically cooled detectors), $\sigma_{x,y} = \sigma$ (the 'read noise'), and $B_{x,y} = B$ (the bias level). This results in:

$$I_{x,y} = S_{x,y} f_{x,y} + \sigma + B \,. \tag{2.4}$$

Generally we measure B by setting $S_{x,y} = 0$ and taking the mean of many frames, N:

$$B = \frac{(I_{x,y})_n + \sigma_n \sqrt{N}}{N} \,. \tag{2.5}$$

As N tends towards infinity the effect of the read noise on the measurement is therefore minimised. We obtain a measure of $f_{x,y}$ by setting $S_{x,y}$ equal to a constant, i.e. by observing a flat field.

For microbolometers we are unable to set $S_{x,y}$ to zero and obtain direct measurements of the dark current or bias level of the system because the shutter can not be controlled externally and there are limits to observable scene temperatures. As a result we have chosen to initially model our system simply as the sum of the signal from the source, $S_{x,y}$, the additive effect of D, and the read noise. This model relies on the assumption

that $S_{x,y}$ and D are uniform, and that the flat field and dark response of $f_{x,y}$ is the same:

$$I_{x,y} = S_{x,y} f_{x,y} + \sigma + D f_{x,y} \,. \tag{2.6}$$

In IR detectors both σ and $f_{x,y}$ are potentially variable with time and pixel location. Spatially variable noise is particularly severe in uncooled models as any temperature variations in the measure environment or internal camera elements result in a phenomenon known as thermal drift which can exacerbate the negative effect of the observed noise.

2.4.1 Random Noise

Random noise, otherwise known as shot noise, changes from frame to frame and limits the precision of any measurement made from data. Shot noise is the random fluctuations that can be attributed to the stochastic nature of how photons are emitted, it follows a Poisson distribution. In astronomical observations, shot noise arises from several sources; the target object, the sky background, the dark current and the read noise. Dark Current arises from thermally generated charge carriers within the FPA. The dark current adds an offset to the signal for every exposure which can be removed by subtracting dark frames. However to reduce the dark current, and not just remove the offset, detectors are cooled and exposures are stacked. Read noise arises due to losses or gains in the camera's read out electronics. Read noise is independent of exposure time and has the greatest effect on low signals (faint sources). To ensure read noise doesn't overwhelm the signal from faint sources, exposure time must be long enough that the signal from the source is sufficient to make an observation.

The random noise is generally referred to as the detector sensitivity by COTS system manufacturers. This sensitivity value, one often quoted as the measure of precision, refers to the noise equivalent temperature difference (NEdT) and is often normalised to f/1.0. NEdT is defined as the temperature difference between a test target and the background that produces a signal equal to the temporal noise, and provides a measure of the smallest temperature difference that can be detected with a thermal imager. If we assume σ can be approximated as a Gaussian distribution, it can be isolated using equation 2.6 with two consecutive measurements of $I_{(x,y)}$. In consecutive measurements all three terms of equation 2.6 can be assumed constant; the source image remains at a constant temperature, σ is approximately constant and a short timescale between

measurements ($\sim 1/7$ of a second) means the the fixed pattern can also be assumed constant:

$$\sigma_{(x,y)} = \frac{I_{(x,y)_1} - I_{(x,y)_2}}{\sqrt{2}} \tag{2.7}$$

2.4.2 Spatial Noise

Spatial noise is generally static over short timescales and otherwise referred to as fixed pattern noise (FPN). FPN arises from imperfections in detectors and variations in how different elements in a detector array can show significant differences in sensitivity, gain and dark-current. Commonly known as non-uniformity (NU) noise this effect imposes a pattern over the true data (Wolf et al., 2016) as each microbolometer in the matrix responds differently to the same infrared excitation, producing a spatially heterogeneous response of the IR camera to uniform incoming radiation. The spatially heterogenous sensitivity of a detector can be corrected by dividing a flat-field, and the dark-current and gain non uniformity can be corrected with dark and bias calibration frames. Equation 2.6 introduces this spatially heterogeneous response as the multiplicative corrections $f_{x,y}$. Isolating the fixed pattern noise in our model, as described in equation 2.6, is slightly more complex than isolating the random noise as our simple model assumes $f_{x,y}$ affects $S_{x,y}$ and D in the same way. So we require an approximate measure of the multiplicative effect of D from the mean value of 2 images with different dark currents in the case where $S_{x,y}$ is constant:

$$f_{x,y} = \frac{I_{(x,y)_1} - I_{(x,y)_2}}{(D_1 - D_2)}\,. \tag{2.8}$$

2.5 Characterising the Noise present in Uncooled Microbolometer Systems

The reduction of data in astronomy is a well defined process. Exposures taken with CCD cameras are known to contain a number of unwanted signals and therefore calibration and correction must occur to produce an image that accurately portrays the desired signal incident on the detector array. For CCD detectors, the result of these systematics is two additive effects and one multiplicative effect on the signal. These are removed using bias frames, dark frames and flat fields, respectively. To understand how transferable

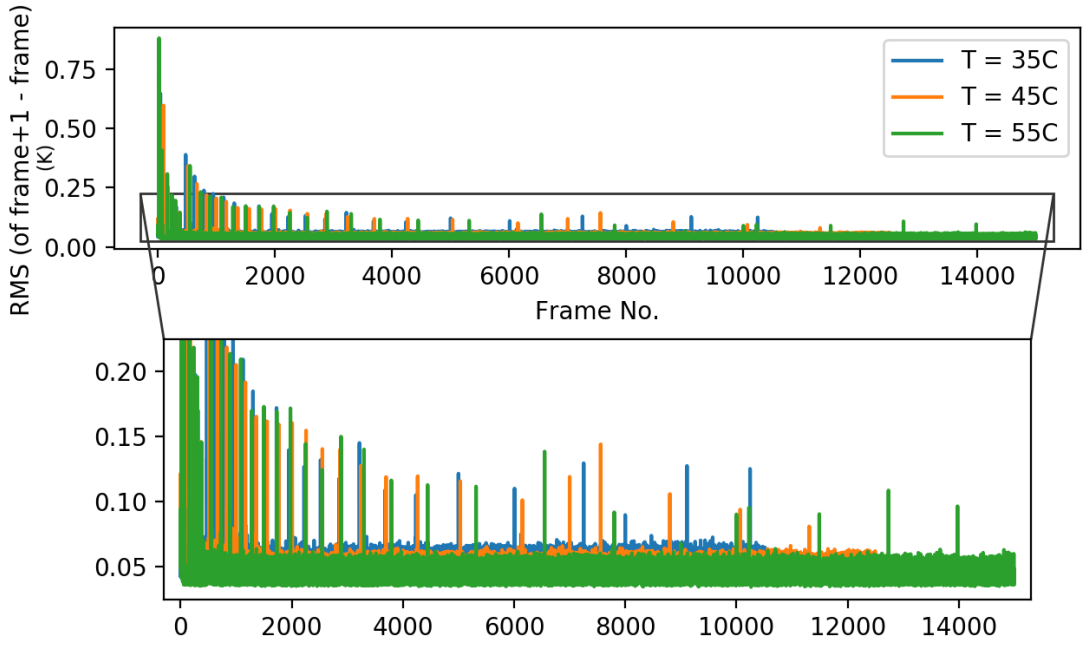

FIGURE 2.1: The RMS of three sets of exposures at varying temperatures; 35°C (blue), 45°C (orange) and 55°C (green). Values were obtained by calculating the RMS of the image resulting from the subtraction of consecutive exposures using equation 2.9.

these data reduction techniques are to COTS microbolometer systems, we must first characterise how the systematics that are present in the detector affect the recorded signal. Not all of the techniques applied to characterise CCD cameras are applicable to microbolometers. Taking dark frames is difficult with mid-IR detectors, even more so with COTS systems that have a limited range of viewable scene temperature (see table 2.1) and therefore are unable to be calibrated using exposures of super cooled surfaces. Sections 2.5.1, 2.5.2 and 2.5.3 discuss our application of three techniques commonly used in astronomy to characterise the sensitivity of a detector; flat fielding, median stacking and binning exposures. These three techniques have been chosen as a means of determining the temporal and spatial variation in the pixel-to-pixel response of the detector.

2.5.1 Flat Fields

To characterise the sensitivity of each element in the microbolometer array we require 'flat field' observations of a source capable of maintaining a constant and known temperature. For this we use a Voltcraft IRS-350 blackbody which has a thermal source

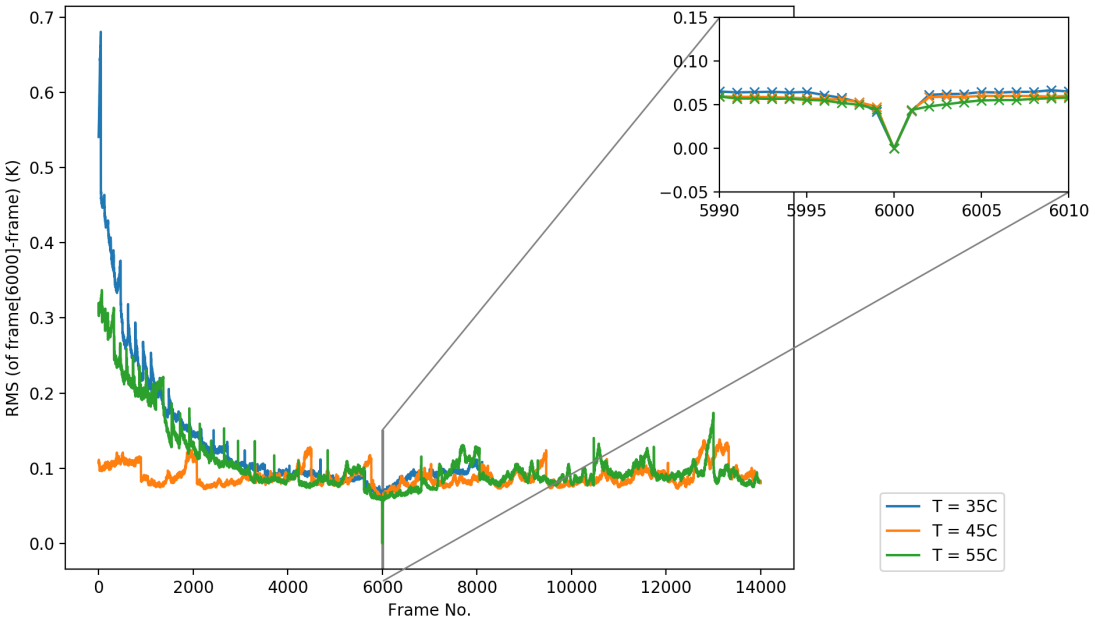

FIGURE 2.2: The time dependency of the fixed noise pattern of three sets of exposures of a blackbody at varying temperatures; 35°C (blue), 45°C (orange) and 55°C (green), as modelled by equation 5. Values were obtained by calculating the RMS of the image resulting from the subtraction of each exposure from one specific exposure, exposure 6000, using equation 2.9.

of diameter 58 mm with a fixed emissivity of 95%. A simple experimental set up was fabricated wherein the thermal source filled the entire FOV and 1/9 second exposures were taken at three temperatures; 35, 45 and 55°C. The root mean square (RMS) has been used as a measure of detector response uniformity, and is calculated as follows:

$$RMS = \sqrt{\frac{\sum_{i=1}^{N} \left(\bar{x} - x_i\right)^2}{N}}, \tag{2.9}$$

where x_i is each pixel in the exposure, $\bar{x}$ is the mean value of the entire exposure and N is the total number of pixels.

Figure 2.1 is the result of applying equation (2.7) to the flat-field exposures, with values determined by subtracting consecutive exposures and calculating the RMS, this removes the effect of the fixed pattern noise and reveals the effect of the calibrations applied by the camera as periodic spikes in the RMS. From this plot we can see that the random noise ranges between $\sim$ 30mK and 60mK.

FPN is fixed for a given sensor but varies from sensor to sensor. On short timescales FPN is stable and dominates over random noise. However over longer timescales, the FPN varies with time. To accurately model the intensity, $I_{x,y}$, measured by a detector we must include this temporal dependency. Figure 2.2 is the RMS as calculated by subtracting each exposure from one standard exposure for a set of $\sim$ 14000 exposures, i.e. not during or close to a shutter re-calibration; for the standard exposure we chose exposure number 6000. Figure 2.2 demonstrates how the FPN of the camera changes temporally. The zoomed portion of the plot shows the RMS of exposures 5990 to 6010 with the expected dip to zero at exposure 6000. On this short timescale of $\sim$ 3 seconds, if the FPN changed significantly we would expect to see no other points in the curve of the dip except the measurement of exposure 6000. As figure 2.2 shows, $\sim$ 3 exposures either side of exposure 6000 lie at points on this curve and so we can conclude that individual pixels have short timescale variability ($\sim$ 0.5 seconds) in the FPN.

2.5.2 Stacking

To determine the temporal stability of spatial noise we can use median images. In astronomy, to obtain a satisfactory signal-to-noise value a master flat field is created from median stacking a large number of de-biased, dark subtracted and normalised (where mean $\bar{x}, = 1$) exposures. Median stacks are created by assigning to each pixel of the resultant image the value in the stack that has an equal number of values greater and smaller than itself. Taking the median intensity of 50 or more exposures will result in flat fields that only contain noise that remains fairly stable, with any noise that changes temporally smoothed.

Figure 2.3 compares the performance of three methods of stacking exposures; median stacks of regular exposures, median stacks of $f_{x,y}$ images created using equation (2.8) and mean stacks of regular exposures. For each stack, 1000 exposures were selected at random from a sample of $\sim$ 14000 consecutive flat field images. These sets of exposures were normalised prior to stacking using one of two methods; (i) by setting $\bar{x}, = 1$ and (ii) by setting all values between 0 and 1, otherwise known as min-max scaling. To determine if the FPN present in these stacks has temporal stability, the images along the bottom row of figure 2.3 which are the result of dividing the above pairs of independently created stacks, should produce a flat field with most of the noise removed and therefore a lower

RMS. The RMS of each image is provided, however for stacks normalised using method (i), to make values comparable to those obtained using min-max scaling, the normalised RMS (NRMS) was used instead:

$$NRMS = \frac{RMS}{x_{max} - x_{min}}. \tag{2.10}$$

It is not clear from figure 2.3 as to whether median stacks or mean stacks contain less short timescale spatial scale noise. However, we can see that normalising exposures by (i) produces more temporal variation in median stacks than when exposures are normalised by min-max scaling. It is likely that for normalising exposures prior to stacking, min-max scaling is the most suitable method for flat-field exposures that have not been through any noise reduction.

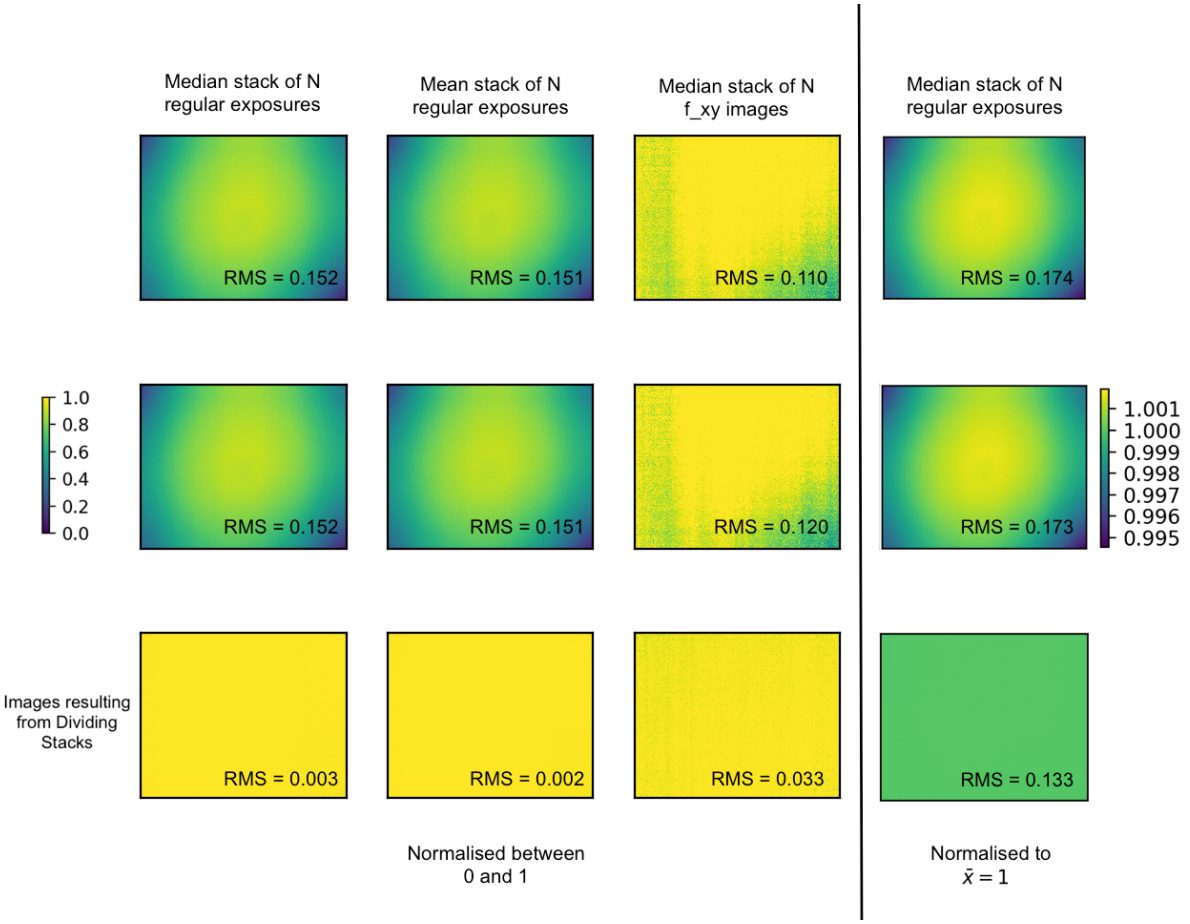

FIGURE 2.3: Comparing three methods of stacking exposures; from left to right median stacks of regular exposures, mean stacks of regular exposures and median stacks of $f_{x,y}$ images created using equation (2.8). Two methods of normalising exposures prior to stacking have also been compared; from right to left of vertical line (i) by setting $\bar{x}, = 1$ and (ii) by min-max scaling i.e. setting all values between 0 and 1. For each method described, two stacks of 1000 exposures were independently created by selecting flat-field exposures at random, as shown in the top and middle rows. Images along the bottom row are the result of dividing the images in the two rows above.

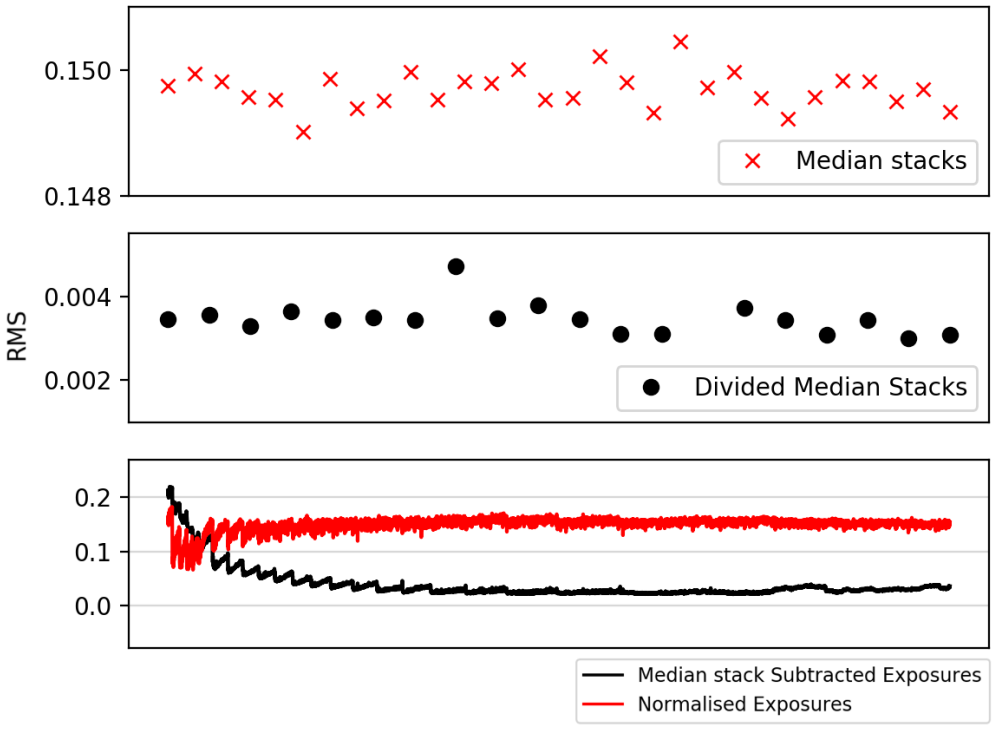

FIGURE 2.4: Top: The RMS of 30 median stacks created from 1000 randomly selected exposures normalised by min-max scaling. Middle: The RMS of the images resulting from dividing randomly selected pairs of the above stacks. Bottom: The RMS of 8100 consecutive exposures normalised by min-max scaling in red is compared to the RMS of those same exposures after subtracting a median stack created from 1000 randomly selected, normalised exposures.

To ascertain further if the FPN present in the median stacks normalised by min-max scaling have temporal stability, pairs of 1000 exposure stacks were randomly selected from a sample of 30 stacks. These pairs were then divided and the RMS of the resultant image was recorded. Figure 2.4 shows how the RMS of median stacks compares with the RMS of their divided counterparts, (top and middle plots). The reduction in RMS suggests that by dividing median stacks we can remove a large portion of fixed noise to produce a flat field with less scatter. The bottom plot in figure 2.4 shows the result of subtracting a 1000-frame median stack from each normalised exposure. This implies that the detector response is dominated by large scale structure and by subtracting a median stack we reduce the FPN present in flat fields.

2.5.3 Binning

Spatial noise occurs on two scales; the small-scale structure of consecutive pixel-to-pixel variation and the larger patterns of structure across the entire frame. To confirm the findings in Sec. 2.5.2, that large-scale spatial noise dominates in our system, we can 'bin' exposures as shown on the left in figure 2.5. This is done by grouping x by y pixels and taking their mean value to determine the overall reading given to that bin. By lowering the spatial resolution of the images we can get a visual measure of how the FPN varies across the detector array. This can be quantified by determining the change in RMS of the image as the bin size is increased. The left-hand figure in figure 2.5 shows a flat-field exposure binned into 4×4, 8×8, 16×16, 32×32 and 64×64 pixels to demonstrate how this method decreases the spatial resolution but increases signal to noise ratio. From this visual representation we can see that the overall structure of the flat field does not change with increasing bin size. The two plots on the right of figure 2.5 show the mean RMS $\pm$ one standard deviation for $\sim$ 12000 median-stack subtracted (top) and $\sim$ 12000 regular (bottom) flat fields taken at three blackbody temperatures; 35, 45 and 55 °C. To quantify how binning affects the noise structure, we would expect the RMS of binned exposures to decrease as $1/\sqrt{binsize}$ (plotted in red) if spatial noise occurs predominantly on small pixel scales. From these plots we can verify that our system is dominated by spatial noise with a large structure. Subtracting median stacks from exposures corrects for this large-scale FPN and as a result leaves only small-scale, pixel-to-pixel variations which scale with binning.

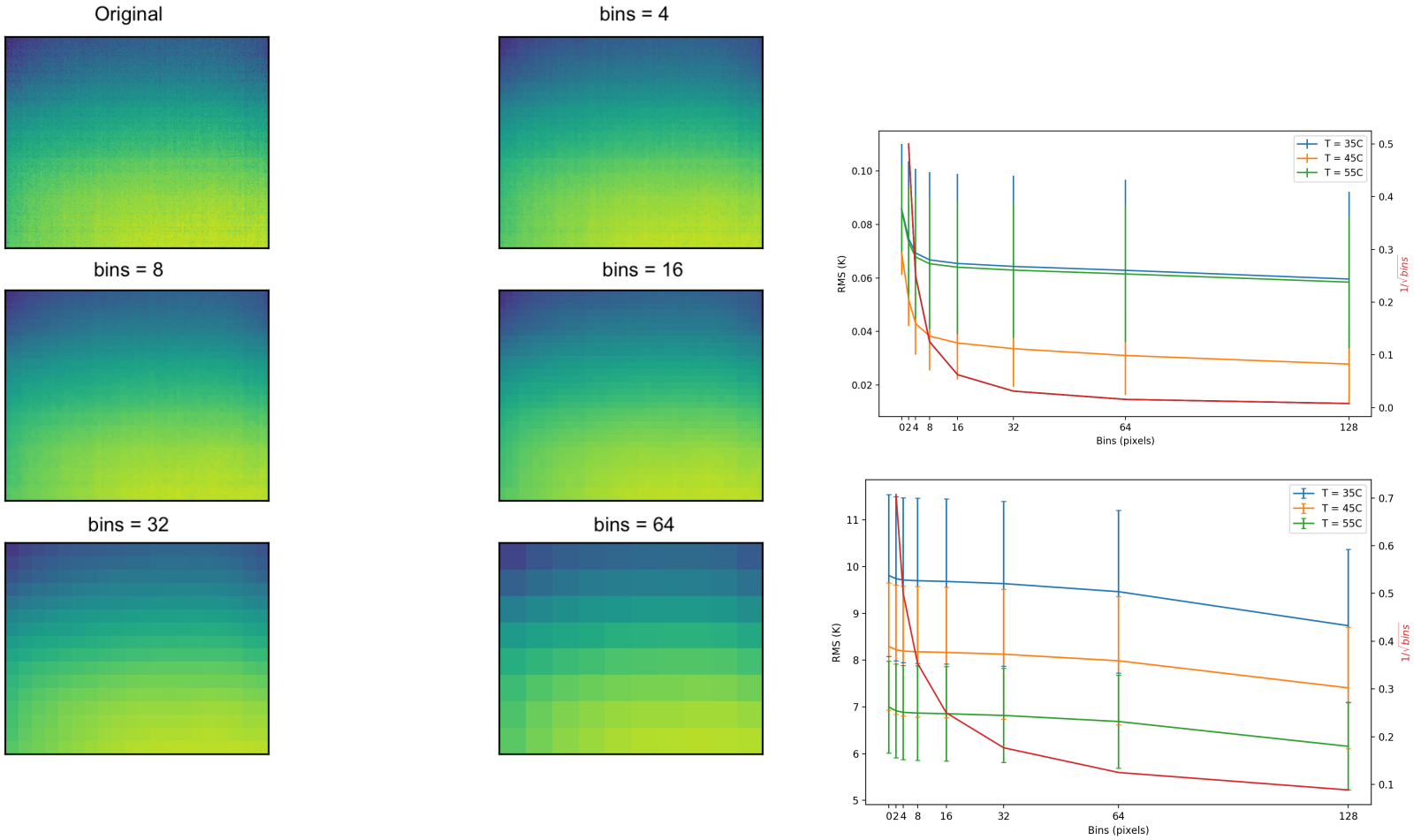

FIGURE 2.5: (Left) Images showing the result of binning exposures into 4×4, 8×8, 16×16, 32×32 and 64×64 pixel bins. (Right) The RMS after binning three sets of exposures of a blackbody at temperature; 35°C (blue), 45°C (orange) and 55°C (green), into 2×2, 4×4, 8×8, 16×16, 32×32, 64×64 and 128×128 pixel bins. This was repeated for median-subtracted exposures (top) and regular exposures (bottom). Also shown is the $1/\sqrt{\text{bin size}}$ relation (red curve) we would see if the noise were on a pixel-to-pixel spatial scale. Each line represents the mean and one standard deviation of the RMS of binned exposures across every frame.

2.5.4 NEdT

For a detection in the mid-infrared, the signal-to-noise ratio (defined as the ratio of incident flux on a detector from the source being observed to random noise fluctuations from other sources) can be calculated as the ratio of the change in temperature, ΔT, to be detected and camera sensitivity, otherwise known as the NEdT:

$$SNR = \frac{\Delta T}{NEdT} \tag{2.11}$$

Theoretically, a large number of independent measurements will tend towards a normal probability distribution. In a normal distribution the standard deviation is related to the width of the curve, with the distribution having equal mean, median and mode values. The further a measurement lies from the mean, the less likely it is to be a result of random noise. A three-sigma detection, 3σ, is a measure of the percentage of measurements that lie within three standard deviations from the mean of a normal distribution. A 3σ detection means that 99.7% of measurements lie within this range and a detection has 0.3% probability of occurring by chance. From equation 2.11, we can estimate that a $\sim 0.2\,\mathrm{K}$ change in temperature would correspond to a 3σ detection with this COTS microbolometer system:

$$\Delta T = 3\sigma \cdot 0.06 = 0.18^{\circ}C \tag{2.12}$$

2.6 Summary of Chapter

In this Chapter a naïve attempt to characterise the systematics present in COTS microbolometer systems has been presented. For this purpose have three techniques that are commonly employed to characterise and correct for the systematics present in astronomical imaging instruments, are applied. Flat fielding of a high emissivity thermal source at known and fixed temperature was employed to obtain exposures for each technique. From un-reduced flat fields the low-level random noise at $<$ 60mk designated the NeDT is isolated in section 2.5.1. A number of methods of stacking flat fields were explored and it was found that median stacking normalised images gave the best results in terms of the temporal stability of spatial noise. Determining the optimal method of median stacking came down to the method of normalisation. In general the method

of normalisation used in astronomy, to set the mean value equal to 1, resulted in an increased pixel-to-pixel RMS in resultant stacks and this is likely to be due to astronomical images being noise reduced prior to stacking. Min-max scaling was used going forwards to demonstrate that median stacks can be used to remove FPN structure from flat field exposures and this was further confirmed by binning images. Median stacks of flat field exposures were successfully used to correct for large-scale FPN, with only small scale FPN remaining. From these observations it was predicted that temperature changes as low as $\pm\,0.2\,\mathrm{K}$ can be resolved in lab conditions.

Chapter 3

Part II Terrestrial applications in Ecology

3.1 Overview of Contents

This Chapter introduces the field of Astro-Ecology. This field aims to provide a novel application of infrared detectors in a cross-discipline field, coupling infrared imaging technology and astronomy instrumentation techniques with Unmanned Aerial Vehicles (UAVs) applied to the field of conservation biology. Several field studies with varying success are presented; Riverine rabbits, Orangutans, Humans. The challenges the performance of a real detector that were faced when trying to determine analogous techniques between the two fields of astronomy and Ecology are described, and used to determine whether the basic assumptions that bring these two fields together hold.

All the 'laboratory' and pipeline works described in this chapter were conducted by me. I was present for the field applications discussed in sections 3.5.2 and 3.5.3. Unless stated otherwise, while on-site for field applications, camera operation and data analysis was conducted by myself with input from Dr C. Burke. All UAV flights were conducted by a licensed UAV pilot under the guidance of myself, Dr C. Burke, Prof. S. Longmore and Prof. S. Wich.

3.2 Astro-Ecology

The spectral energy distribution of warm-blooded vertebrates peaks within the mid-IR range (see figure 1.3 in chapter 1.4.1). This makes COTS mid-IR systems potentially ideal to use for the detection and monitoring of vulnerable species with regular surveys, especially as this technology is becoming more cost effective. Ecologists are beginning to couple mid-IR technology with UAVs to yield high volumes of data of various species (e.g. Chrétien et al., 2015; Gonzalez et al., 2016; Israel, 2011; Lhoest et al., 2015; Mulero-Pázmány et al., 2014). However, animal populations are often estimated from imaging data by human observers. This reduces accuracy and precision and invites human bias into the process, with recent studies indicating that humans do not detect the vast majority of animal sources in data (Eikelboom et al., 2019; Lamprey et al., 2019). This need for human intervention when processing large volumes of data creates a reduction and analysis bottleneck that contributes to the low efficacy and efficiency of surveys for conservation.

The field of Astro-Ecology was first introduced by Longmore et al. (2017), who demonstrated that the use of astronomical source detection software coupled with a machine-learning-led identification component could provide the framework for an efficient data-analysis pipeline that could make use of microbolometers terrestrially in conservation surveys. The developed pipeline was able to process large volumes of data to detect objects of interest using their peak in mid-infrared emittance. From these potential detections, they deployed an open-source, support vector, histogram of oriented gradients (HOG) algorithm, to detect 2D features in data and identify the number of detections that were genuine. Although this study was data-limited, they detected $70 \pm 10\%$ of the target sources at an ascertained optimum UAV height. This provided a preliminary proof of concept that astronomical object detection techniques, and physical understanding, at mid-IR wavelengths could be applied in ecology.

Overall, the concept behind Astro-Ecology was to adapt the well developed processes and experience in IR observing that astronomy has, to make an impact in ecology. The intention was to improve the efficacy of survey techniques, while reducing time and financial cost, and removing the effect of human bias. The original idea was born from several generalisations about the similarities of observing astronomical sources and animal sources in mid-IR. These similarities are summarised in table 3.1.

Astronomy	Ecology
In optical observations, astronomical sources appear brighter than their surroundings, with background brightness much lower than source brightness.	In mid-IR observations animals appear like bright objects on dark backgrounds (i.e. 'background' temperatures are lower than sources to be observed).
Astronomical sources are mostly static point sources with a standard or fixed shape.	Above a certain height animals are point sources of standard or of fixed shape.
The observing platform is stable and sources traverse a predictable path in the sky.	Animals can be tracked by comparing consecutive images.

TABLE 3.1: The similarities between astronomical observing and mid-IR ecology survey data identified by Longmore et al. (2017). These simple comparisons were the motivation behind the origin of the field of Astro-Ecology.

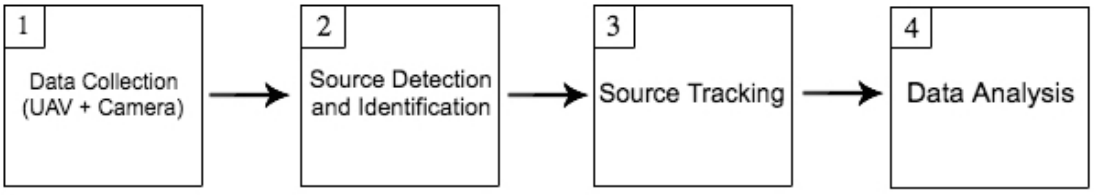

FIGURE 3.1: Flow chart of the pipeline proposed by Longmore et al. (2017), split into the four major components: Data collection, source detection and identification, source tracking and data analysis.

3.2.1 Framework

The overarching aim of Astro-Ecology is to reduce the time and manpower needed to handle the data from UAV biodiversity surveys by producing an end-to-end data reduction and analysis pipeline designed to automate the process of detecting, identifying and tracking a specified target species. There were three major goals associated with the design of this pipeline, with fulfilment of each identified as an indicator of successful implementation:

1. The deployment of a COTS mid-IR detector, mounted on a UAV, as an optimised system for collecting survey data of a variety of species in a range of environments.

2. The application of automated astronomy source detection techniques to mid-IR animal data.

3. The automatic identification of animal species using mid-IR data.

To reach these goals, Longmore et al. (2017) proposed the development of a pipeline for the automation of ecology surveys. Figure 3.1 describes the four major components of this pipeline. This chapter details the very early development of Astro-Ecology. At the time this work was conducted, each component was considered of equal importance and Astro-Ecology was operating as a very small team. As such, the work presented here is a preliminary investigation into all areas of the pipeline and are described under sections relating to the 4 different components listed in figure 3.1.

3.3 Data Collection

For all applications in ecology, data were to be collected using the mid-IR camera mounted on a multi-rotor UAV using custom-built mounts to reduce camera movement during flights. To maximise scientific output, we aimed to produce effective flight plans in advance. This section details the work done to optimise data collection, through the characterisation of the camera system (as introduced in chapter 2) for use in Astro-Ecology.

3.3.1 Temperature Stabilisation

It is assumed that when non-operational, the camera itself remains in thermal equilibrium with the local environment. Any changes in environmental temperature would, over time, be reflected in a change in camera temperature. When operational however, the camera gains enough heat that it feels hot to the touch. The most likely predominant cause of this is power dissipating as heat in the electronics. In Astro-Ecology, power is supplied to the system via a 16750mAh external battery with a USB connection. As described in chapter 2.2, when the system registers a change in environmental temperature, it will trigger a FFC event. We hypothesised that the sudden change in camera temperature as a result of supplying power would be registered in the same way.

We confirmed this initially, by observing that the frequency of FFC events, which are identified by an audible sound, increased over a short period at the beginning of operation. Eventually, providing the camera was not exposed to any sudden environmental changes, FFC events settled to the periodic intervals expected of the system. From

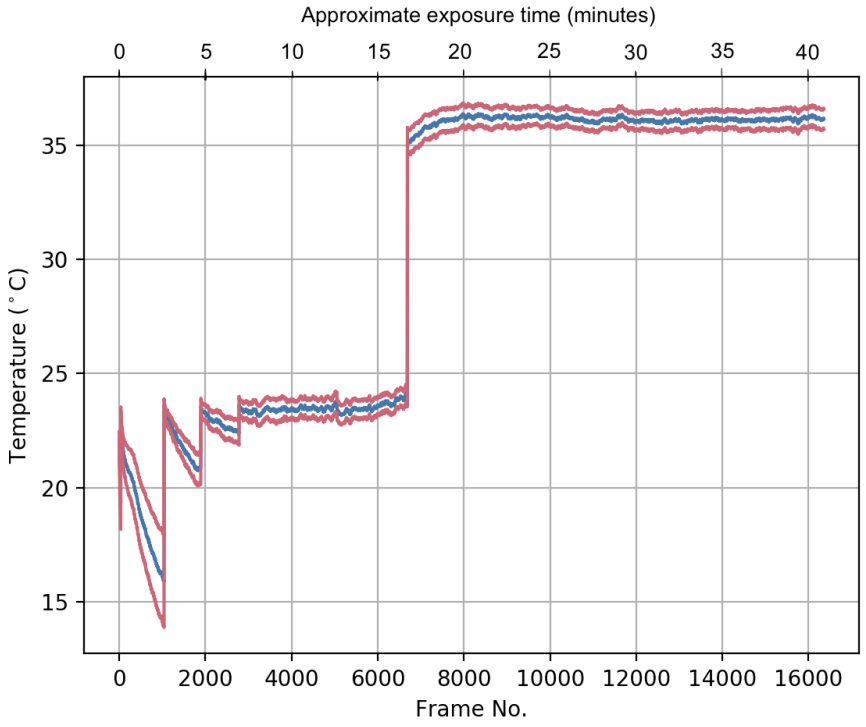

FIGURE 3.2: Observations of a thermal source at 35°C after a stabilisation period of 15 minutes viewing a room temperature scene. Blue lines represent the average temperature measurement of the thermal source and red lines are ± 1 standard deviation.

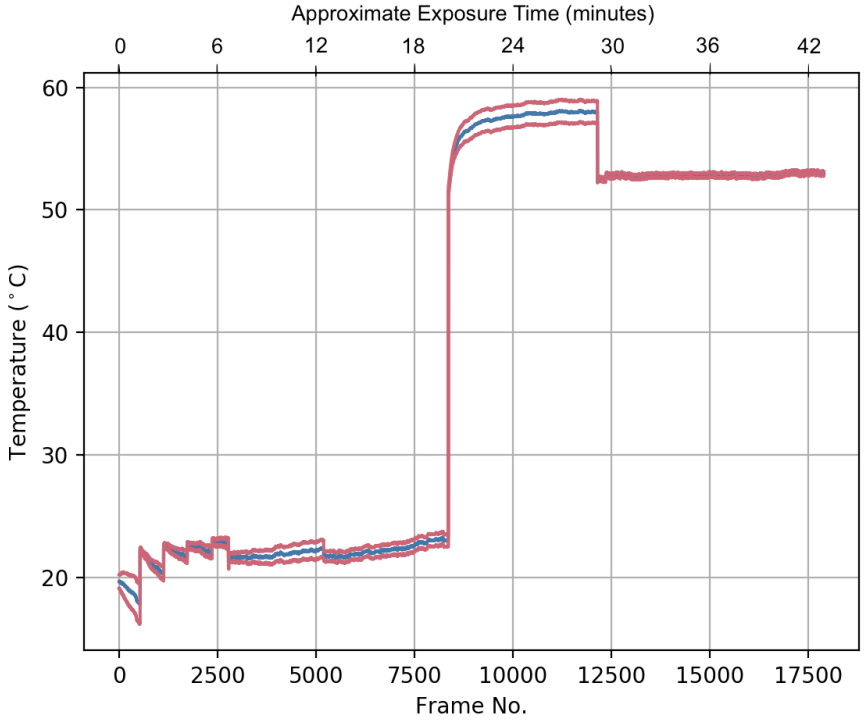

FIGURE 3.3: Observations of a thermal source at 50°C after a stabilisation period of 15 minutes viewing a room temperature scene. Blue lines represent the average temperature measurement of the thermal source and red lines are ± 1 standard deviation.

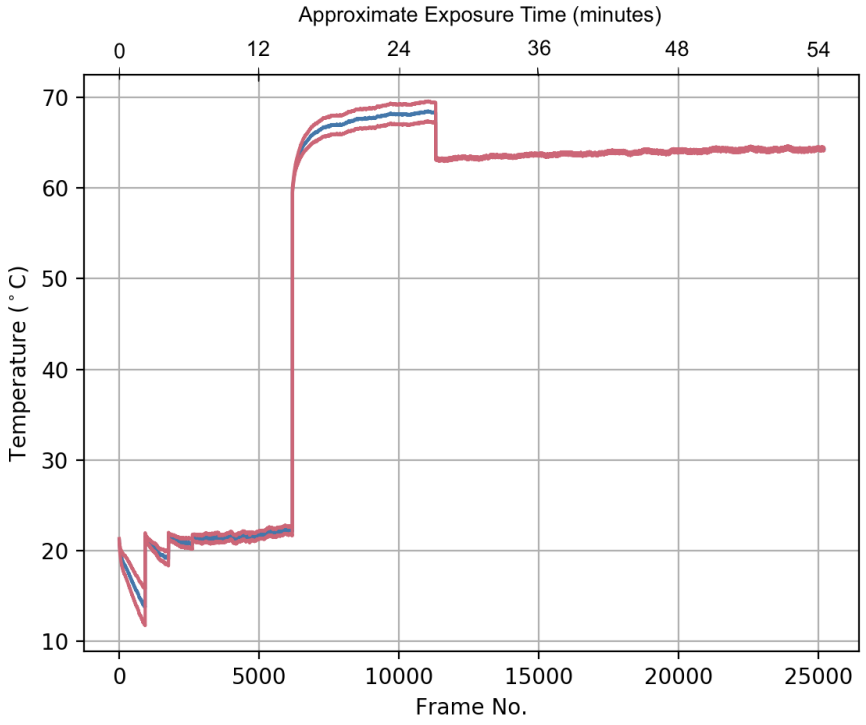

FIGURE 3.4: Observations of a thermal source at 60°C after a stabilisation period of 15 minutes viewing a room temperature scene. Blue lines represent the average temperature measurement of the thermal source and red lines are ± 1 standard deviation.

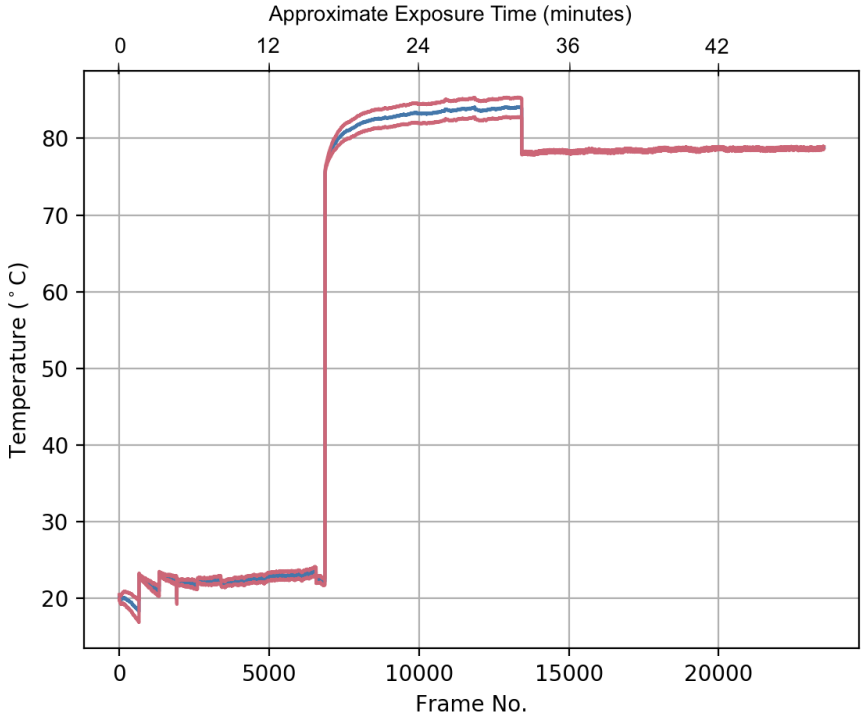

FIGURE 3.5: Observations of a thermal source at 75°C after a stabilisation period of 15 minutes viewing a room temperature scene. Blue lines represent the average temperature measurement of the thermal source and red lines are ± 1 standard deviation.

these observations we made the following assumptions about camera temperature stability; there is a period after power supply where the camera operates at a steadily increasing temperature, causing frequent, out-of-sequence FFC events until the camera reaches a stable operational temperature.

To observe this, and determine the time between power supply and the temperature stabilisation of the camera housing and electronics, a simple experiment was conducted. To reduce the possibility of any external environmental changes influencing the results, the system was placed in a temperature controlled room, with an ambient temperature of 20°C, and left for several hours. Once it could be assumed the camera was at thermal equilibrium with the room, it was mounted in front of a window in the lab for $\sim$ 15 minutes. The window was chosen because the glass material is opaque to mid-IR radiation and there was no access to a more controlled material. It was assumed that over short time periods the temperature of the window would not change significantly, and care was taken to ensure any room reflections remained unchanged. Once $\sim$ 15 minutes of window data had been obtained, the system was placed in front of a thermal source (as described in section 2.5.1), which had been stabilised at a known temperature, such that it filled the entire FOV of the camera. This was repeated for source temperatures of 35, 50, 60 and 75°C. The average scene temperatures, i.e. the average value calculated from all 640x512 pixels, over the duration of the experiment were plotted, as shown in figures 3.2, 3.3, 3.4 and 3.5.

We observe from these plots that there is a short period after power is applied where several FFC events occur in response to apparent temperature variations of up to 10°C which lasts for approximately $\sim$ 10 minutes. From this we can assume that recorded temperature values in the first ten minutes of operation have a much lower accuracy than expected, with the recorded temperatures after stabilisation falling within the quoted precision specifications of the camera ($\pm$5°C or 5%). Although the dissipation of power inside the camera housing is out of our control, we can take measures to alleviate this effect by recommending that data acquisition occurs once the camera has reached a stable operating temperature, with power supplied to the system for a minimum of 10 minutes in advance.

From figures 3.3, 3.4 and 3.5 we can also see that a sudden change in scene temperature of $>$ 30°C will also result in an overestimate of scene temperature for a further $\sim$ 10

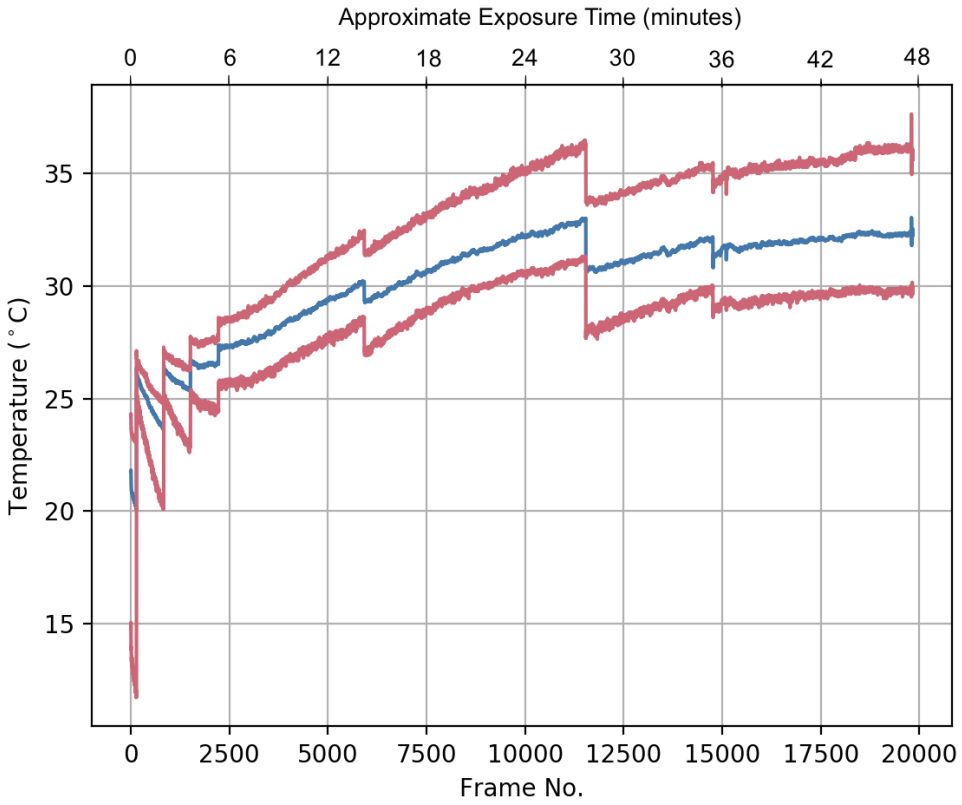

FIGURE 3.6: Camera observing a thermal source at 30°C for a time period of $\sim$ 48 minutes. With the blue line representing the average temperature measurement of the thermal source and the red lines representing $\pm$ 1 standard deviation. After $\sim$ 5000 exposures, the initial period required for the camera to stabilise in operational temperature, the variation in temperature, seen as a gradual rise and sharp fall are a result of thermal drift and the periodic corrections applied.

minutes.

3.3.2 Thermal Drift

The uncooled nature of the camera, however stable in operational temperature, gives rise to an unavoidable consequence of external, environmental temperature variations, known as thermal drift. The signal voltage $V_{i,j}$ of a pixel (ij) is linearly related to the exchanged (incident minus emitted) radiant flux of the pixel $\Phi_{i,j}$, as follows:

$$V_{i,j} = \Phi_{i,j} R_{i,j} + V_0 \tag{3.1}$$

where $R_{i,j}$ and V_0 are the responsivity and offset voltage of the pixel respectively (Tempelhahn et al., 2015). These two terms may not be consistent across all pixels as a result of slight variations during the microfabrication of the microbolometer array. But it is

their changing unevenly with time, in response to any drift in the sensor temperature, that results in the appearance of false temperature gradients in read-out data. This is a phenomenon that effects temperature measurements by as much as 1°C per minute (Olbrycht & Więcek, 2015).

Figure 3.6, shows the effect of thermal drift and the periodic introduction of a FFC on read-out data. Data were obtained from observations of the thermal source at a constant 30°C for $\sim$ 48 minutes. The gradual increase in the observed temperature is attributed to thermal drift, with sharp falls being the result of FFC events. As discussed in chapter 2.2, FFCs are introduced periodically to reduce the effect of thermal drift. This period is pre-defined but adjustable. A reduction in the time between FFC events would decrease the gradient imposed by thermal drift but would also increase the total time over which the shutter is deployed and data acquisition interrupted. For Astro-Ecology, data is predominantly collected using a UAV platform. where flight time is limited and UAV speed is a trade off between the area to be covered and the battery lifetime. There is potential to decrease the period between FFC events but this would limit the volume of data obtained, and potentially make data more vulnerable to the effect of motion blur.

3.3.3 Illumination/Vignetting

There can be substantial 'vignetting' (otherwise known as 'roll off') at the corners of the field of view. Vignetting in this case refers to areas that appear significantly cooler than the overall scene. Radiation incident on a curved lens, particularly a wide angle lens, doesn't illuminate uniformly across the entire lens and depending on the positioning, the corners receive the least illumination. These apparent cold spots are a function of viewing angle and are a direct result of lens curvature. This results in the areas towards the edge of the frame and at the corners being perceived as colder than the overall scene. From private communication with FLIR, we know the 'roll-off' effect is substantial with their wide FOV lenses and high resolution camera models. While factory corrections have been applied by FLIR to correct for this, their residual effects still remain in our data.

To determine the areas most affected by vignetting, the camera was temperature stabilised and mounted such that the blackbody source filled the entire FOV. Figure 3.7 shows the location of the coldest pixel over a 75 minute duration. Each data point, with

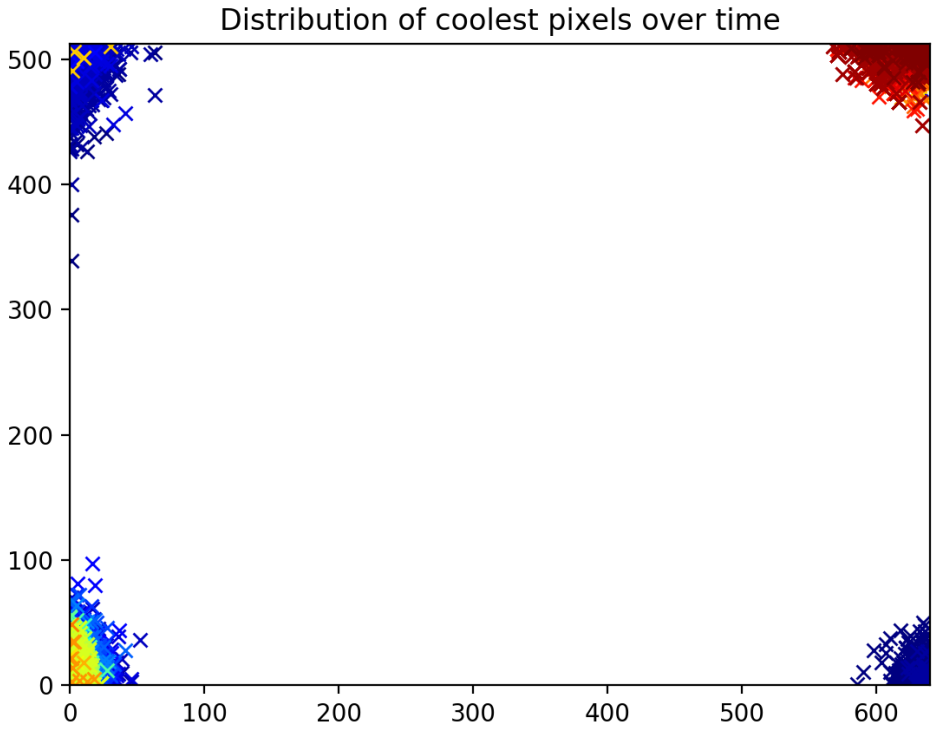

FIGURE 3.7: The location of the coldest pixels over time when viewing a uniform scene of constant temperature. Bluer colours represent early observations and redder colours represent later observations.

there being over 36000 points in total, have been scaled to a colour spectrum which reflects the time at which they were recorded. The earliest exposures are marked in blue and the latest in red.

This is a clear representation of the vignetting effect at work. After repeating these exposures three more times, with our thermal source operating at different temperatures, we have been able to quantify that, given a thermally stabilised camera, this vignetting produces a detector read-out $\sim (5 \pm 2)$ % °C lower than the overall average temperature of the scene. This has the potential to decrease the contrast between a source and the environment when imaged by this area on the detector, reducing detectability when paired with a thresholding algorithm. We can take appropriate measures to compensate for this effect. A simple means of doing this would be to not record temperature values for objects when they are imaged by the outer 50 pixels of the frame. To correct values recorded in this region would require full characterisation of the spatial and temporal variability of this effect. If the variability were found to be predictable and repeatable, then a correction factor could be applied to remove the effect.

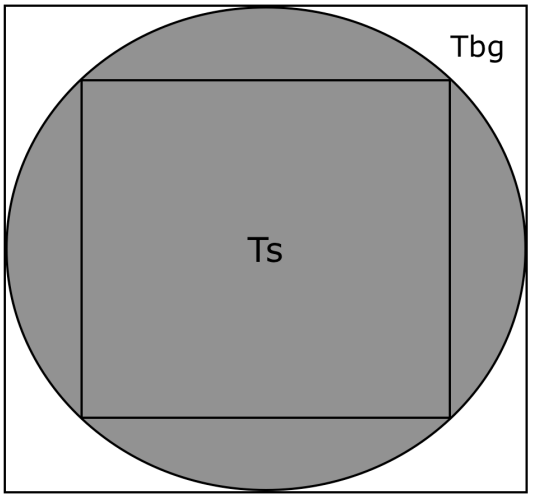

FIGURE 3.8: A representation of an idealised scenario where the source to be detected is a circular source of temperature T_s. Due to the detector pixels being square, the measured temperature of the source will include a contribution of the background temperature T_{bg}.

3.3.4 Resolving Sources

The resolution of an imaging system can be characterised by the point spread function (PSF) and the diffraction limit which denotes the minimum angular separation θ between two sources that can be resolved:

$$\theta = 1.22\frac{\lambda}{D}\,, \tag{3.2}$$

where λ is the wavelength and D is the diameter of the lens' aperture. The instantaneous field of view (iFOV), i.e. the an angular projection of just one of the detector's pixels, for the camera lens is listed as 1.308 mrad (see table 2.1) or $\sim 270''$. The diffraction limit at 10 μm, calculated using equation 3.2, for the camera is $\sim 0.24''$, this indicates that the PSF is unlikely to limit the resolution of the system given the large angular size of the pixels. Animals imaged from a UAV in ecology are more likely to be unresolved due to 'undersampling', where the pixels are too large with respect to the source, which results in a mixture of source and background in a pixel. However, when mounted on a telescope for use in astronomy (see Chapters 4 and 5), point sources are broadened by the PSF of the telescope, lens and mirror aberrations and atmospheric turbulence. 'Undersampling' is avoided by designing the instrument optics to have an appropriate pixel scale with 2–3 pixels sampling the predicted PSF.

Because of 'undersampling', it is necessary to consider target size relative to pixel scale when determining the flying height (i.e. the distance between target and camera). All

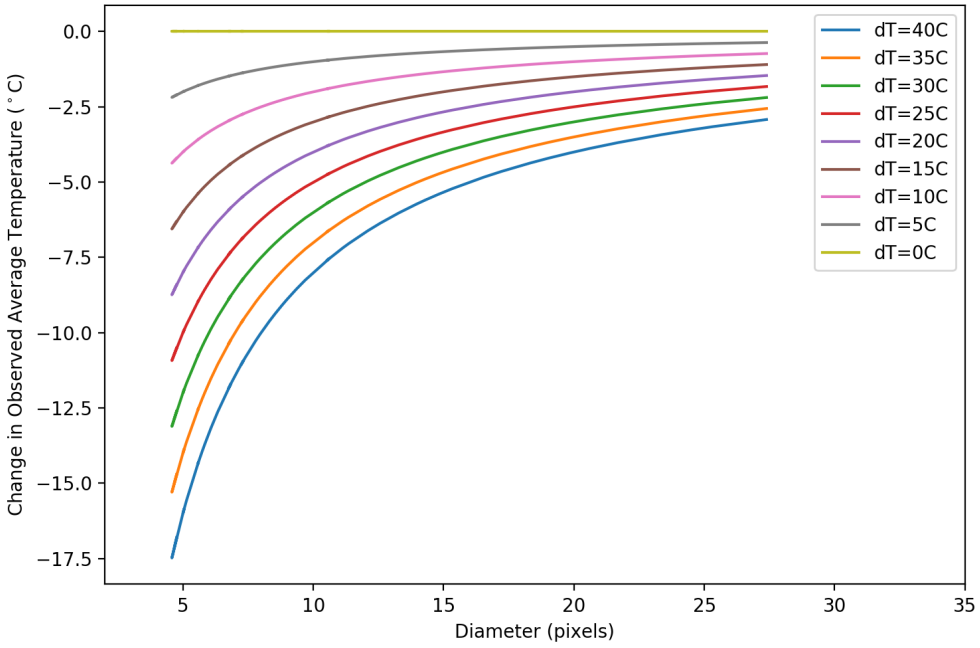

FIGURE 3.9: Theoretical models of the spot-size effect for a circular source with known radius r. Source temperature remains fixed at 45°C and models have been produced for a range of background values, where dT is the difference between source and background temperatures.

data are vulnerable to the 'spot-size' effect when the projected target size approaches the angular scale of individual pixels. The spot-size effect in this instance is the degradation of temperature measurement accuracy due to the way the sensor processes the image. The smaller the desired target appears in data, the fewer pixels sensing it, the more the background and nearby surfaces will be present in measurements. This skews averages either warmer or colder than the actual surface temperature of the target. The effect of background blending on the observed temperature of a pixel, T_{pix}, can be described by the sum of the source, T_s, and background, T_{bg}, contributions with respect to the fraction of pixel area they cover, x and y respectively:

$$T_{pix} = xT_s + yT_{bg}, \tag{3.3}$$

where $x + y = 1$. When determining the average temperature of a source, taking the average temperature of all source pixels, this relation can be extended to calculate the observed temperature of the source as a whole, T_{obs}. This takes into account the total

area of blended pixels, A_{bg}, and the total area of pure source pixels, A_{tot}− A_{bg}:

$$T_{obs} = \frac{T_s(A_{tot} - A_{bg}) + (x_{tot}T_s A_{bg}) + (y_{tot}T_{bg}A_{bg})}{A_{tot}} \tag{3.4}$$

where x_{tot} is the fraction of A_{bg} that the source contributes to and y_{tot} is the fraction of A_{bg} that the background contributes to, i.e. x_{tot}, $y_{tot} = \sum_{i=1}^{A_{bg}} \frac{x_i, y_i}{A_{bg}}$.

Consider an idealised scenario of a circular source with known radius r and area πr^2. Due to the shape of the detector pixels, the source temperature will be detected over a square area of pixels (see figure 3.8). We can model the pixels containing pure source contribution to observed temperature as a square circumscribed by the circle with area $2r^2$. The area over which the source contributes to the blended pixels can be modelled as the area between the inner square and circle $r^2(\pi - 2)$. The area over which the background contributes to the blended pixels can be modelled as the area between the circle and the outer square $r^2(4 - \pi)$. As a result, the recorded temperature can be modelled as follows:

$$T_{obs} = \frac{(T_s \times 2r^2) + (T_s \times r^2(\pi - 2)) + (T_{bg} \times r^2(4 - \pi))}{4r^2} \tag{3.5}$$

Figure 3.9 shows theoretical models for a circular source with fixed temperature, T_s = 45°C, and varied background temperatures,T_{bg}, such that dT = T_s - T_{bg}. From this we can estimate the spot-size effect for different source-background temperature gradients. This effect is exacerbated as diameter decreases and temperature gradient increases.

Realistically, when observing, we don't have control over the temperature difference between the source to be observed and the background environment. However, to limit the spot-size effect we can determine the minimum pixel diameter needed for measurements of the source to not be impacted. To do this we need to have an understanding of how the camera resolves the same object over a range of distances.

Observations of the thermal source at a constant 45°C were taken, with distance varied in increments of 25cm. The apparent diameter, in pixels, and the average temperature of the thermal source at each distance was determined from each series of observations. Figure 3.10 shows how the average temperature varies depending on the pixel diameter of the thermal source. Above 15 pixels, the average temperature measurements are mostly consistent. Below 15 pixels, the average temperature values begin to drop, with anything

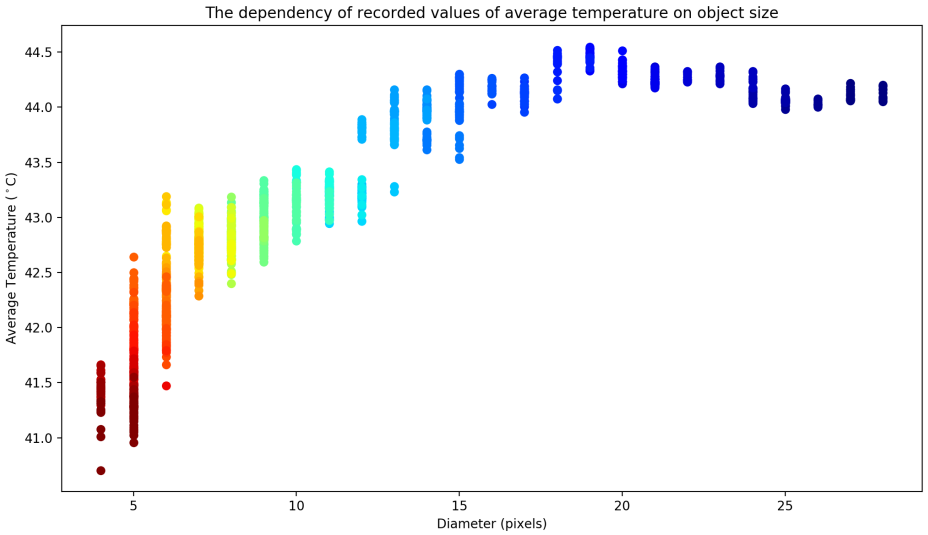

FIGURE 3.10: Change in average recorded temperature with pixel size of a thermal source at 45°C. Pixel size is varied as a function of distance, with vertical height of each bar representing the spread of average temperature recorded at that size. The colouring of each bar visually represents the temperature spread of each data set, going from red to blue, cooler to warmer.

less than $\sim$ 13 pixels being too convolved with the background for accurate radiometric readings. For Astro-Ecology, to consider recorded temperatures representative of source surface temperature, a source must therefore be resolved with a diameter of no less than 13 pixels.

We can use this minimum size limitation to inform optimum UAV flying heights for various species using the following equation:

$$height = \frac{0.5a}{tan(\frac{\theta}{2})} \tag{3.6}$$

where a is the diameter in metres of the target object and the angle subtended by the target object θ to be considered resolved is:

$$\theta = \frac{\text{Angular field of view } (^\circ)}{\text{No.of pixels}} \tag{3.7}$$

The maximum flying height can be determined by setting the number of pixels to our calculated minimum pixel diameter. This will vary depending on the size of the target object.

3.4 Source Detection and Identification

As outlined previously, Longmore et al. (2017) made use of analysis software designed to detect point-like (i.e stellar) sources. Two routines from *PHOTUTILS*, a package affiliated with *ASTROPY*, were tested; *DAOStarFinder* and *find_peaks*. *DAOStarFinder* is an implementation of the DAOFIND crowded-field algorithm (Stetson, 1987). It finds local density maxima with peak amplitude greater than a specified threshold and a size and shape that is comparable to a specified 2D elliptical Gaussian kernel. It fits 1D Gaussian functions to find objects and to obtain their x and y centroids. In comparison, *find_peaks* locates any objects above a specified threshold value in a local region, that are separated by a specified minimum number of pixels. It returns integer values for peak pixel position, with no centroiding performed. Having tested the suitability of these routines for the extraction of point sources within their data, Longmore et al. (2017) concluded that the most functional and time-efficient routine was *find_peaks*. The output values of peak pixel position were sufficient, given the data set, to detect the potential location of animal sources and feed into a machine-learning component to determine which detections were real.

We chose to re-test the suitability of these routines for use on animal data before moving forward. These are robust methods for detecting point sources in images prior to performing photometry. However, as determined in section 3.3.4, animal sources must subtend at least 13 pixels for a reliable detection. Further to this, there is a dependence of mid-IR intensity on source orientation and a varying distribution of intensity across the animal body. This limits how effective *DAOStarFinder*, *find_peaks* and other pre-packaged point-source detection software will be. Instead, we chose to adopt the same basic principles used by both routines and work with *OPENCV* to develop our own source detection algorithm. This algorithm operates much like its astronomical counterparts while taking into account the extended and irregular nature of the sources that need to be detected, tracked and potentially identified to achieve the goals of Astro-Ecology.

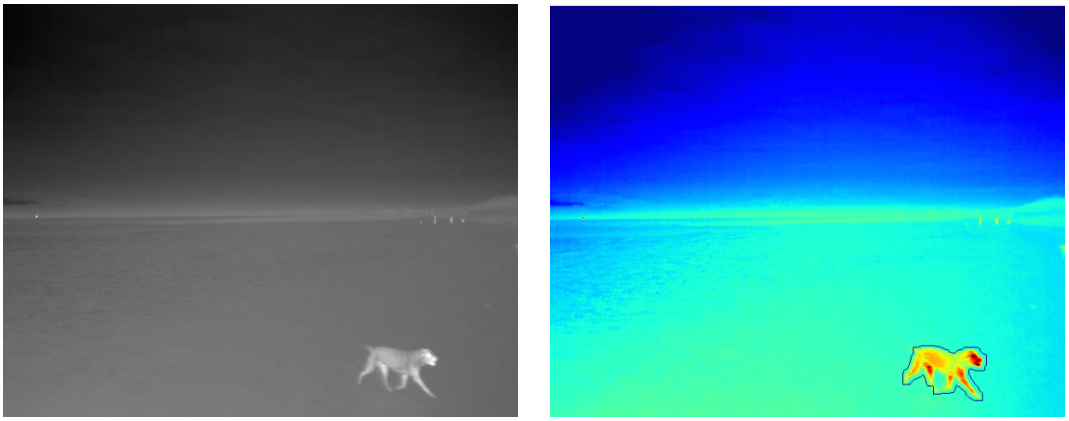

(a) (b)

FIGURE 3.11: The transformation of an original frame (a) to a frame that has been run through our pipeline, and had the target detected (b).

3.4.1 Detection

Given the nature of the type of data we are working with, namely the varying range of topography and vegetation coverage a biodiversity monitoring survey could have, we felt the most suitable means of detecting sources of interest was to first isolate them from their surroundings. One of the basic assumptions of Astro-Ecology is that endothermic homeotherms are generally warmer than their environments. So, borrowing from astronomical source detection software, we begin by applying a threshold to each frame. Changes in lighting, terrain and weather conditions at the time of data collection can result in an overall variation of scene temperature range from frame to frame. Thermal drift, as discussed in section 3.3.2, causes positive temperature gradients in data, skewing values higher and higher until corrected by a FFC event. As a result, specifying a single, value of signal to threshold the data is not applicable. To counter this, we have opted to threshold data based on an upper percentile limit of the overall scene to allow for any changes in scene range between frames without affecting source detection. To do this we use *numpy.percentile* and create a duplicate frame containing RGB masks of all the pixels that have values above the threshold. RGB masks are required to parse to *OPENCV* functions. In these simplified frames, any pixels above the given threshold are coloured white, any pixels below the given threshold are coloured black. Once these masks are created, there are several fine-tunable parameters to determine if there are any erroneous sources present.

Depending on the conditions at the time of data collection, false detections of clusters of pixels usually considerably smaller than any potential objects of interest can arise. This is often the case in particularly wet or warm conditions. The variation of these sources from frame to frame can cause complications with source detection and tracking, so to reduce and in some cases eliminate any of these erroneous sources we adopt a technique widely used in astronomical source detection and choose to ignore all potential detections that do not have more than a specified number of connected pixels that are all greater than the threshold value. The required number of connected pixels is determined from the average size of the target species and the UAV flying height, and a tolerance is applied for variation in overall size due to viewing angle, and source obscuration caused by environmental features.

The variation of mid-IR emissions across the body is dependent on species and orientation or viewing angle. This variation results in areas of the body being considerably warmer than others and being recorded as having a much higher signal than the rest of the body. This can result in several detections for a particular individual and reduces the likelihood of an object of interest being detected consistently as one source in all data frames. To minimise this effect, all potential detections present in the mask are dilated. Sometimes used in astronomical source detection, dilation acts to smooth the image of a point source and maximises the detectability of sources with shapes similar to a specified 2D kernel, usually a Gaussian. The same fundamental process applied to potential detections in our data acts as a means to smooth the intensity over the entire source and reduce any large contrast between warmer and cooler parts of the body.

Once any false positives are identified they can be ignored. After this, the *OPENCV findcontour* function is employed on each frame to detect the pixel positions of the edges of each mask. We then implement the *drawcontour* function on the original frame, transcribing the pixel positions of contours around masks in the thresholded image with pixel positions in the original frame, to apply visible, fluid boundaries around each source. This is done on every frame to detect each source in the data. An example of the source detection can be seen in figure 3.11. Here the pipeline successfully detected and highlighted the animal in the frame. An example of this code can be seen in appendix A.

3.4.2 Source Tracking

We had success in deploying the pipeline to detect single sources in an open environment free from any potential sources of confusion, through data that were taken with a stationary camera. However, we encountered several issues when trying to use the *OPENCV contour* detection functions for tracking multiple sources, in crowded environments or when sources are not present in the FOV for the full duration of the observation. *OPENCV* does not offer the functionality to apply a unique ID to each contour, rather it orders contours dependent on their position within the frame. This makes it very difficult to track the same contour in different frames. Over the course of pipeline development, we also encountered an issue entirely unique to studying organic and living sources, when they occasionally produced waste that emitted a similar mid-IR signal for a period of time.

An early attempt at finding a solution to these issues was to order contours by their size. This however assumes that all sources remain consistent in size within a certain tolerance. Depending on species and viewing angle, minor changes to source orientation can cause large changes in the overall size of the detection. The high likelihood of contour area changing multiple times in the duration of a single set of data makes this an unreliable means of tracking. A more robust method of tracking sources from frame to frame is to use change in position relative to consecutive frames. Given the short time ($\sim 1/9\,\mathrm{s}$) between consecutive frames, we assumed that sources will only display a small change in x and y position between the two frames. By identifying sources in each frame this way we hoped to build a robust tracking component into the pipeline. To maximise the potential of this method we also compared pixel positions in consecutive frames to determine if there was any overlap. Overlapping pixels in consecutive frames are, in most cases, likely to correspond to the same source. In practice, these methods require planning UAV flights for data collection to maximise camera stability and reduce any change in source position that isn't dependent on their individual movements. This method is unable to handle scenarios in which multiple sources appear to merge or are not present throughout the entire data set. This method is also not applicable to imaging moving targets with a moving camera. In fact tracking objects in these kinds of scenes is an ongoing area of research in the field of computer vision with potential solutions

requiring complicated particle filters that predict the most likely paths of targets and produce maps of the area covered.

3.4.3 Identification

When the detection code is successfully deployed, the temperatures of detected sources and any variation across the body can be measured. It has been proposed that differences in the spatial distribution of mid-IR emission across the body profile (the 'thermal-profile') can be used to identify different species. In order to determine the feasibility of this, we took data of a variety of different species. Data were taken from the ground, and as close to individual animals as possible, to resolve sufficient detail. The majority of data were collected at Chester Zoo in the UK, as well as during the field experiments described in section 3.5. Figures 3.13 to 3.19 are a small but representative sample of the types of species and resolution recorded.

Over the course of this study, we have observed that there is a complication in using 'thermal-profiles' as a means of identification. Variations in 'thermal-profile' are not necessarily limited to inter-species. Juveniles can have significantly different mid-IR emissions to their adult counterparts, e.g. figures 3.12 and 3.13 are observations of new-born lambs and adult sheep. The young lambs peak in the mid-IR almost uniformly across the torso, with the ears, legs and tail recorded as much cooler. Adult sheep can have a variable 'thermal-profile' depending on their wool which is an effective insulator and obscures any mid-IR emission from the torso. When un-sheared, like those present in figure 3.13, the predominant area for heat loss in an adult sheep is the surface of the head and legs. Without the wool to insulate their torso, the distribution of mid-IR emissions across the body of an adult sheep will differ. This poses problems for identifying species without knowing the age distribution or grooming status of the individuals to be surveyed.

The health of individuals can also cause intra-species variation. Figure 3.14 and 3.15 show Black rhinos in two different environments. While these animals are of the same species, the adult rhino observed in figure 3.14 has patchy emission across the body. This is a result of a diagnosed skin condition. As described in chapter 1.4.1, a deviation from bilateral symmetry in the mid-IR can occur as a result of inflammation, infection or hormonal fluctuations. While this makes mid-IR observations a potential tool for

non-invasive health diagnostics, it can also pose an issue for automated identification. It is impossible to understand and model all of the potential variations to the general 'thermal-profile' that could be caused by poor health.

Resolution can also play a large part in the presentation of characteristic mid-IR emission. Figures 3.16 and 3.17 are of a giraffe, in two different environments and viewed from different distances. In the former image, where the camera-animal distance is smallest, the characteristic spot patterns on the neck of the giraffe can be seen. These spots are visible in the mid-IR because they are surrounded by large blood vessels, which act as a means of thermoregulation. However, when resolved by fewer pixels in figure 3.17 because of a larger camera-animal distance, the spots appear far less distinct. As described in section 3.3.4, for sources to be detected reliably they must be resolved by > 13 pixels. However, to utilise the distinct features in the 'thermal-profiles' of various animal species as a means of identification, the individual features must also be resolved by > 13 pixels. This limits the animal-camera distance for data that is to be used for identification purposes.

The final complexity lies in the angle at which the animal is viewed and the position the animal is in. Figure 3.18 is an observation of four wild Elands in South Africa. Each Eland is pictured with a different posture. Figure 3.19 is an observation of thirteen fruit bats. The observed 'thermal-profile' of the bat in flight is significantly different to those that are roosting. These figures are two simple examples of how viewing angle and animal position can significantly alter the appearance of an individual in mid-IR data.

While not a problem for human-led identification, automatic identification that does not acknowledge differences in the spatial distribution of mid-IR emittance caused by age, health, resolution and viewing angle could significantly misrepresent the true population density.

FIGURE 3.12: False colour mid-IR image of several newborn lambs. The temperature range of the scene is described by the colour bar, with units of degrees Celcius.

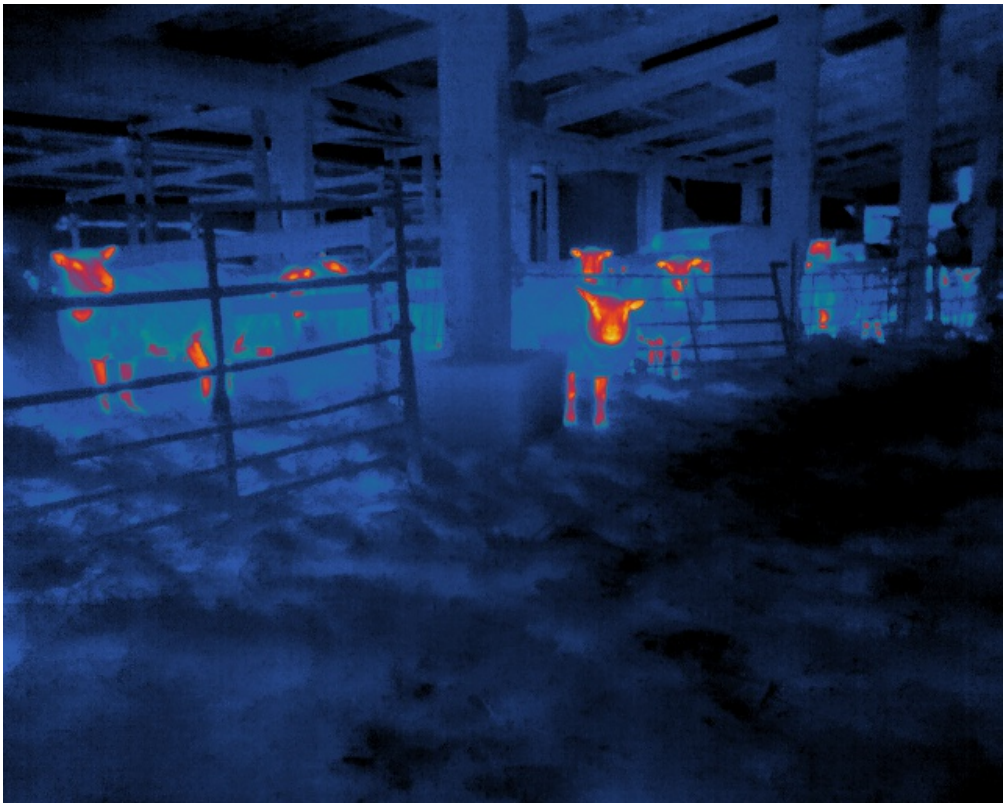

FIGURE 3.13: False colour mid-IR image of several sheep. Temperature scales cold to warm, blue to red.

FIGURE 3.14: False colour mid-IR image of a two black rhinos, an adult and a juvenile, taken inside an enclosure at Chester Zoo. Temperature scales cold to warm, blue to red.

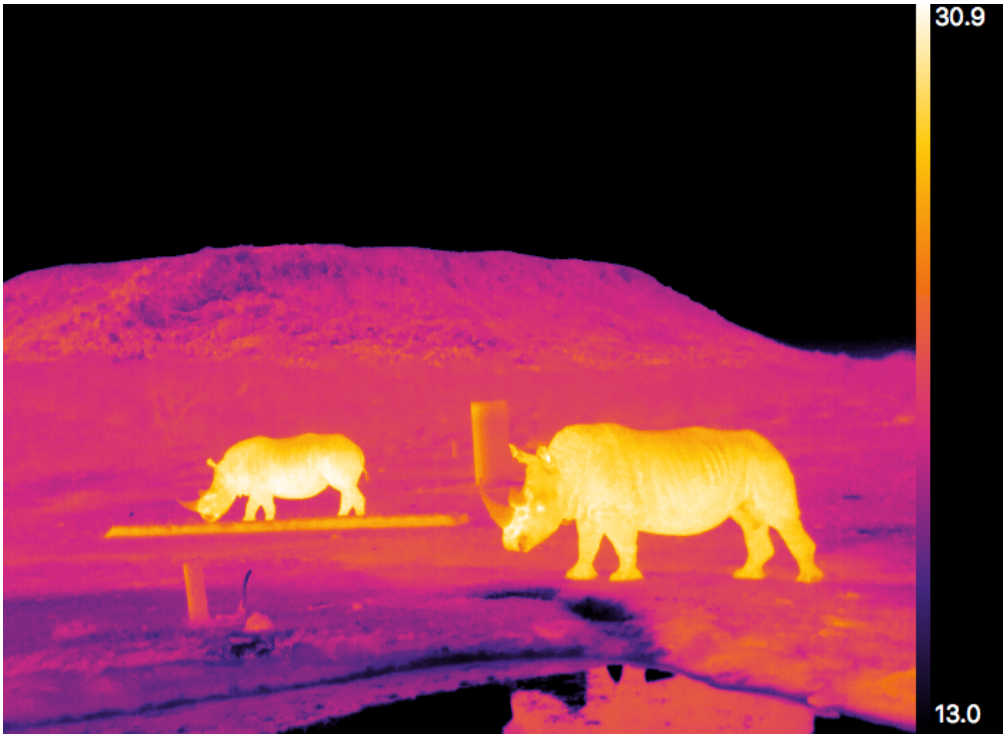

FIGURE 3.15: False colour mid-IR image of two wild rhinos in South Africa. The temperature range of the scene is described by the colour bar, with units of degrees Celcius.

FIGURE 3.16: False colour mid-IR image of a giraffe in an enclosure at Chester Zoo. Temperature scales cold to warm, blue to red.

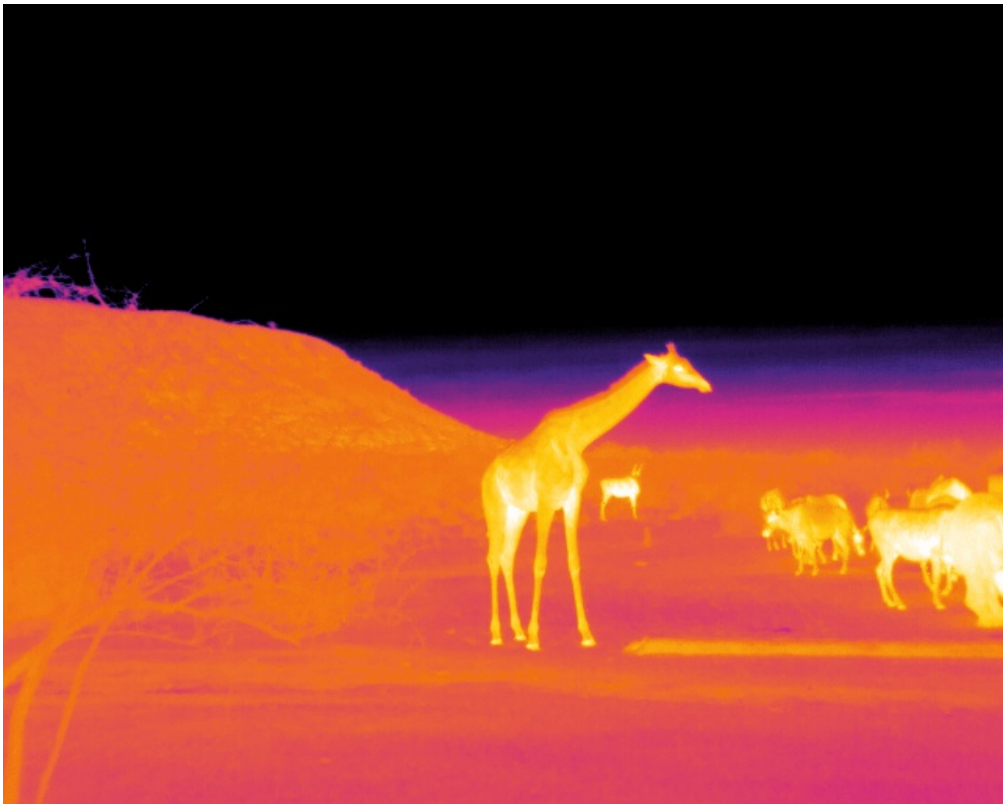

FIGURE 3.17: False colour mid-IR image of a wild giraffe in South Africa. Temperature scales cold to warm, blue to red.

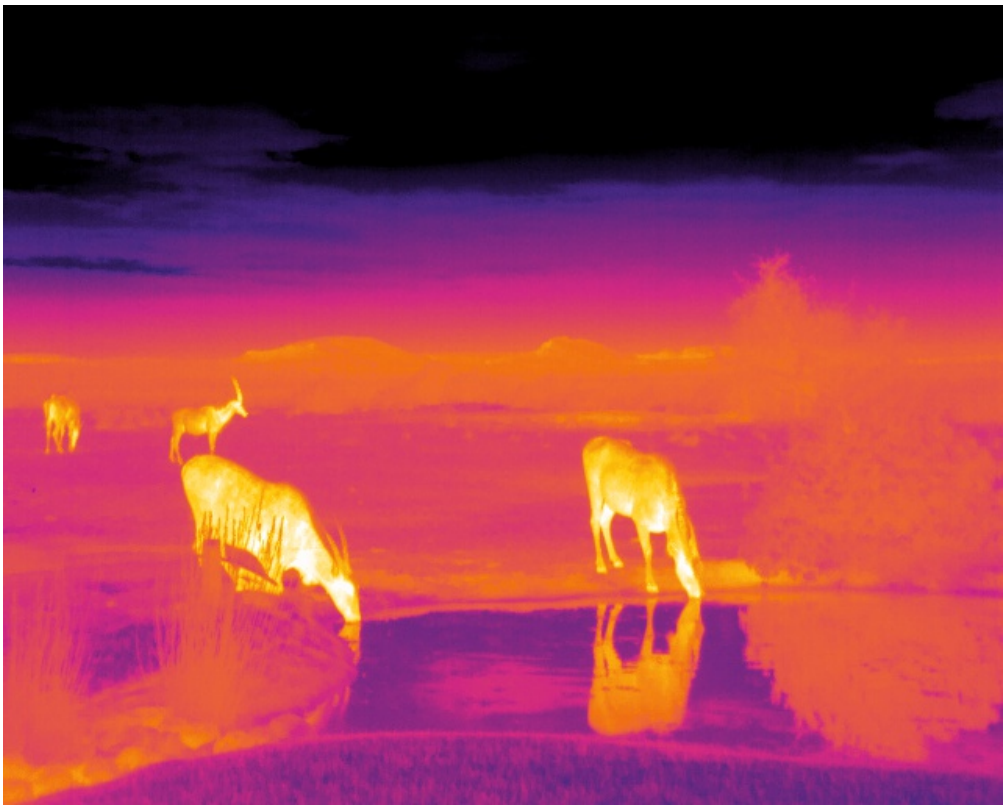

FIGURE 3.18: False colour mid-IR image of Eland in South Africa. Temperature scales cold to warm, blue to red.

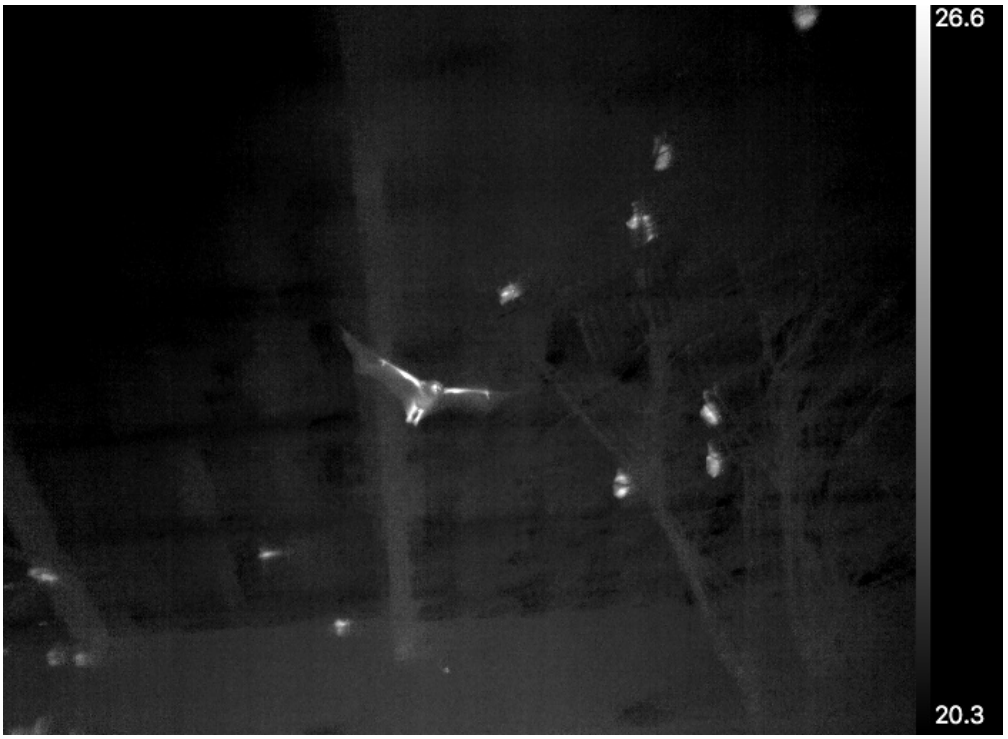

FIGURE 3.19: Mid-IR image of Fruit Bats in an enclosure at Chester Zoo. The temperature range of the scene is described by the greyscale bar, with units of degrees Celcius.

3.5 Applications

3.5.1 Human Detection for Poaching

3.5.1.1 Motivation

One of the major issues facing conservationists is how to detect and intervene in situations where endangered species are harmed or killed by humans for personal gain. Poaching is a major cause of population decline in some of the world's most vulnerable species. Illegal trade in animal products is very lucrative and has a major impact on animal diversity and ecosystems across the world. Building up a 'thermal-profile' of humans in environments where poachers operate was identified as an important first step for Astro-Ecology, to fufill the goal of creating a rapid response system to raise the alarm when potential suspects are seen in areas known to be vulnerable to poaching.

For this purpose, several sets of data were obtained, courtesy of of Prof. Serge Wich, in Tonge West Joint District-Village Forest Reserve, Tanzania in March 2017. Tanzania was identified as a region with high poaching activity and declining populations of vulnerable mega fauna. The data were collected to make an early comparison as to whether the use of mid-IR imaging, instead of regular optical imaging, was more beneficial for the detection and prevention of poaching activity. The mid-IR data were analysed and reduced by the Astro-Ecology team, with the optical data analysed by an external ecology team.

The data were used to determine how poachers are likely to appear in the mid-IR and whether they could be detected with the pipeline described in section 3.4.1. The secondary goal of this field application was to take the first steps towards identifying individuals without the need for human intervention from their average measured temperatures or 'thermal-profiles'. This application was the first field study of Astro-Ecology and had a lasting impact on the development of the pipeline.

3.5.1.2 Instrumentation

All data obtained from this trip were collected using the FLIR Tau 2 core (see chapter 2.2), custom mounted to a DJI F550 hexacopter. The mount was built for the camera

Flight No.	Date	Take-off	Landing
13	20/03/17	16:06	16:12
14	20/03/17	18:46	18:51
20	21/03/17	19:02	19:08
21	21/03/17	07:32	07:38
27	22/03/17	19:12	19:19
28	23/03/17	07:23	07:29
37	23/03/17	19:12	19:18
38	24/03/17	N/A	N/A

TABLE 3.2: Information about flights taken to collect mid-IR data in Tanzania. All flight data were provided to us with a flight number, date and take-off and landing times except flight 38. Times are quoted in local Tanzania time.

to be in a nadir position (i.e. looking straight down). After reviewing the data we discovered that the dampening features of the mount were not sufficient, resulting in a degradation of data quality due to the presence of a significant motion blur in many frames.

3.5.1.3 Data Collection

Eight flights were conducted to collect mid-IR data. Each flight was performed at two heights; 70 and 100 metres, over an area that contained between 6 and 23 humans. These individuals simulated a potential poaching scenario by hiding under and around varying levels of tree canopy and foliage. Table 3.2 collates the information recorded for these flights. The Astro-Ecology team had no input with regards to flight plans or data collection. Subsequently, the information relayed was incomplete, with no record of ground temperatures, ambient temperatures or humidity provided. In general, this information is important for data analysis to understand the effect of the local environment on observations, in particular on recorded temperature values.

3.5.1.4 Experience & Method Development

At the time of data analysis, the pipeline operated on the assumption that sources were irregularly shaped, as most animals tend to be. It also only contained rudimentary functionality to begin separating out genuine detections from erroneous ones using previously defined parameters such as size, average temperature, shape, etc. These Tanzania data

FIGURE 3.20: Three individual sources, detected by the pipeline in Flight 28. These sources were visually confirmed as human and have positions denoted by red circles.

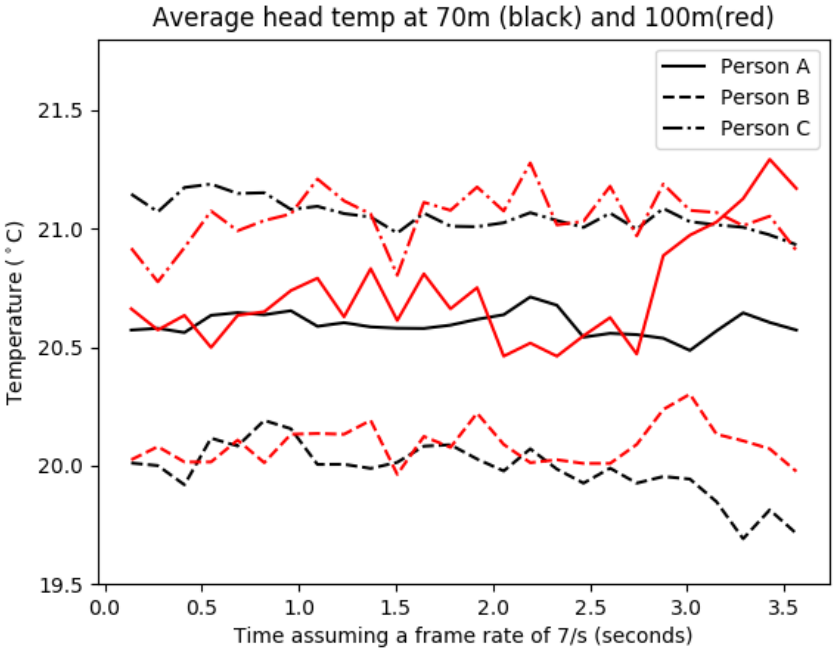

FIGURE 3.21: The Average Temperature of three individual sources, as shown in figure 3.20. Each source, labeled A, B and C, was manually tracked for $\sim$ 3.5 seconds. The black lines indicate the values recorded at 70m and the red lines indicate the values recorded at 100m.

focused on detecting humans from a height of up to 100m above ground level, predominantly viewing their heads and small parts of their shoulders. These data presented an opportunity to begin working on optimising the detection parameters for humans, with the added simplification of the target sources appearing to be fairly circular and

uniform.

All data were run through the pipeline with thresholding at 99.98%. As there was no operational, multi-source tracking component to the pipeline in place, we manually identified three individuals recorded in the 70m and the 100m data for flight 28, as seen in figure 3.20. Flight 28 was chosen because of particularly good contrast between ground and sources. The identified individuals were stationary and remained in the FOV for a total of $\sim$ 3.5 seconds. Properties such as the semi-major and semi-minor axes were obtained from RGB masks of detections. The non-centroided pixel coordinates in the masks were compared with the original mid-IR data and average temperature values were recorded. These properties (e.g. size, shape, temperature), enabled unique species identifiers for humans to be determined. Figure 3.21 shows the average temperature recorded for the three individuals. The black lines represent values recorded at 70 metres and the red lines represent those at 100 metres. The results show that individuals remain fairly stable in average temperature and the effects that could cause signal attenuation between 70 and 100 metres are minimised for this data set.

In figure 3.21 the large deviation around 3 s at 100 metres for person A is largely due to obscuration of the entire source leading to a smaller recorded size and in this instance an increase in average temperature. Sources obscuration is a result of parallax and environmental features, and its effect in the data is an indication of how pre-defined parameters for species based on size and temperature will make any results vulnerable to environmental features.

This effect can be seen clearly in figure 3.22, which shows the histogram of recorded size, with red indicating values recorded at 70 metres and black indicating values recorded at 100 metres. Size estimates here have been calculated using the recorded semi-major axis values and equations 3.6 and 3.7. These size estimates range from 0.1 to 0.4 metres at a height of 70 metres and $\sim$ 0.15 to 0.6 at 100 metres. The extreme values on either side of this range are caused by environmental features either obscuring large parts of the source or, given a warmer environment and the lower resolution of flights at greater heights, environmental obscuration causing genuine sources to have poorly defined edges and be recorded as larger than they really are.

In accordance with the scientific goals of Astro-Ecology, i.e. to determine the feasibility of using mid-IR data and 'thermal-profiles' of a species to identify individuals, we then

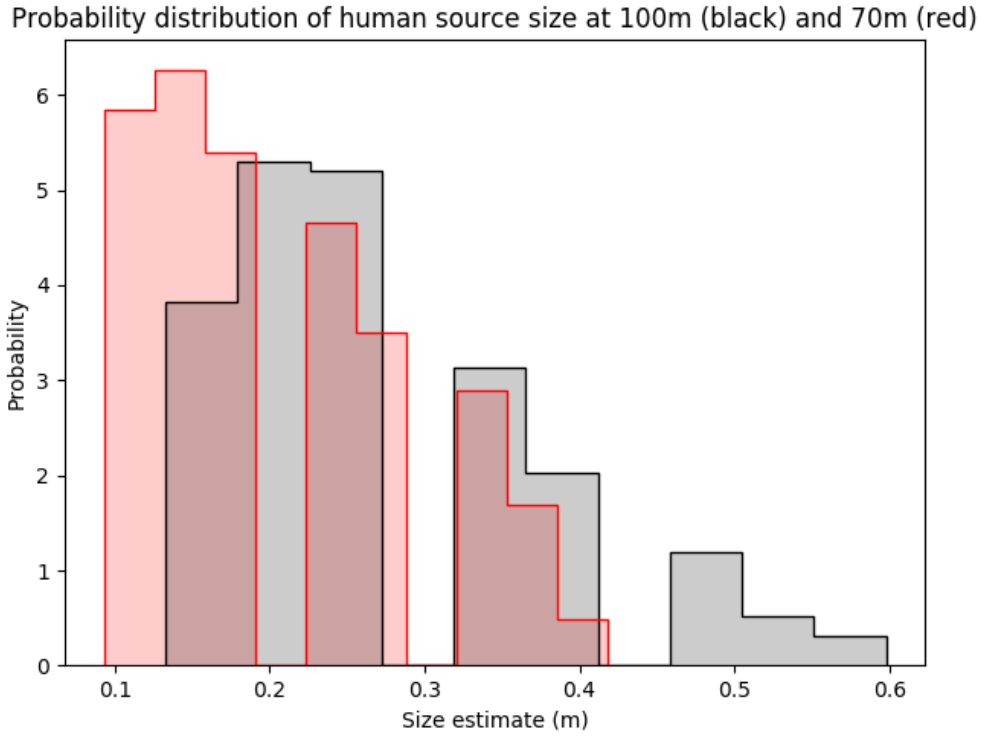

FIGURE 3.22: Histogram of size estimates of all the human sources detected in every flight calculated from their semi-major axis values. Red columns represent values recorded at 70m and black columns represent values recorded at 100m.

investigated the range of temperatures recorded for the human sources. Of the $\sim$ 1000 frames obtained from the 8 flights, the pipeline detected 2073 sources in data at 70m and 1474 sources in data at 100m. Detections were confirmed as human providing the semi-major axes fell in the size range defined above. We then obtained the average temperature of each detection. Figure 3.23 plots the overall frequency distribution of average human temperature at both heights. Overall the human sources detected in the flights fall within a tolerance of 10°C.

3.5.1.5 Limitations & Conclusions

While almost all of the flights produced reasonable results for isolating potential human sources by thresholding and applying size constraints, flight 13 produced non-human detections. When investigating the data, we discovered that ground and environmental feature temperatures were so high that every threshold applied to this data fell way above our 'human-range' presented in figure 3.23, with the lowest thresholds applied

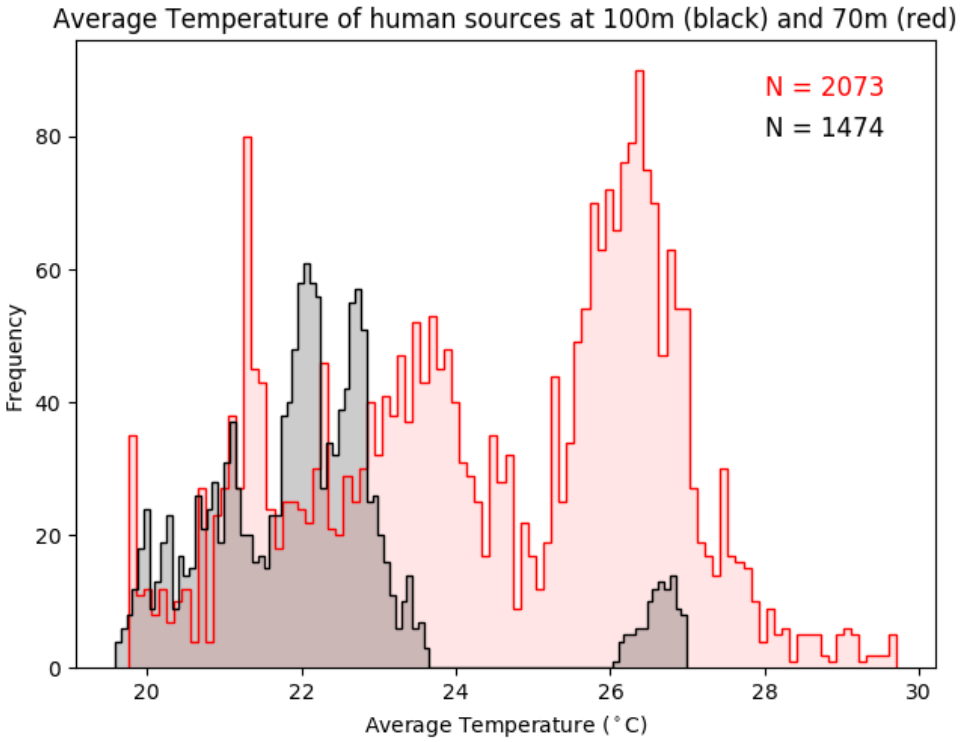

FIGURE 3.23: The frequency distribution of the average temperature values calculated for all of the human sources detected in every flight. Red columns represent values recorded at 70m and black columns represent values recorded at 100m.

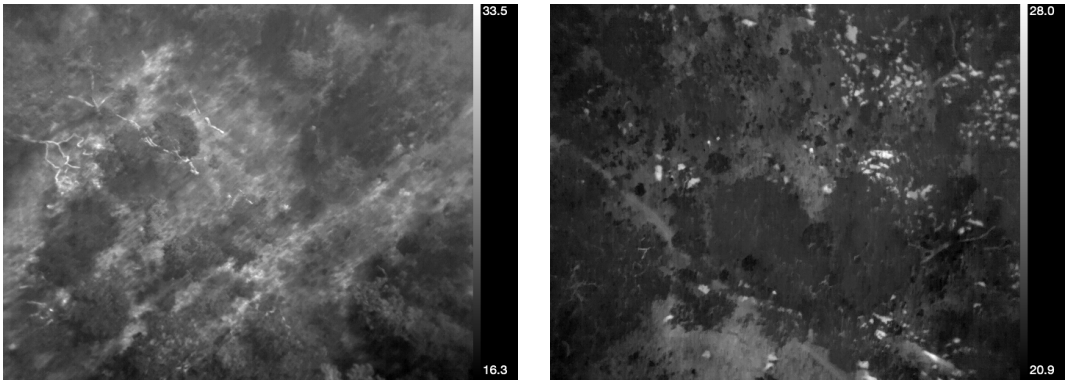

(a) branches (b) rocks

FIGURE 3.24: Most spurious detections arose because of warm environmental features such as tree branches (a) and rocks (b) which can be comparable to humans in size, shape and temperature

being $\sim 30°C$ and the highest $\sim 39°C$. The thresholding pipeline detected sources by isolating pixels with the top 0.02% values. This approach assumes that for living beings to stand out in mid-IR data, they have to be some of the brightest objects in the field of view. While in the other flights we have seen this was the case, flight 13 proves that this

is not always the case. Given the information in table 3.2 we can see that flight 13 was conducted between 16:06 and 16:12 local time, making this the only flight conducted in the afternoon, at a time when the ground is at its warmest. Without recordings of the ambient and ground temperature for each flight we care unable to quantify the effect ground temperature has on this data set.

Although the other flights did not suffer from the same high thresholding problem, they did produce their fair share of spurious detections. Most of these arose because of warm environmental features such as tree branches and rocks, seen in figure 3.24 (a) and (b) respectively. Given a warm enough environment these features can heat up to temperatures comparable to those of humans. These features also do not emit uniformly and can be detected as warm clusters of pixels instead of as large-scale structures, producing detections comparable to humans in shape and size. For the purpose of obtaining human temperatures, these spurious features were manually identified and removed from the data set. However, it was clear that this effect was exacerbated by the time of day at which flights were conducted, with morning flights, 21 and 28 as seen in table 3.2 and figure 3.24, producing far fewer false detections, and with a visibly greater contrast between human sources and environmental features. This confirms the need for robust flight plans, which takes seasonal and diurnal changes to ambient air and ground temperatures into account.

3.5.2 Endangered Species in a Desert Environment

3.5.2.1 Motivation

The Riverine rabbit (*Bunolagus monticularis*) is classified as a critically endangered mammal. Studies have estimated species numbers of only a few hundred (Collins & du Toit, 2016) with their chosen habitat unlikely to support more than 1500 individuals (Duthie et al., 1989). Endemic to the central Karoo region of the western and northern cape provinces of South Africa (Hughes et al., 2008), Riverine rabbits are a small, nocturnal species which spend daylight hours in 'scrapes' beneath riparian shrubs (Skinner & Chimimba, 2005). Accurate population densities are hard to determine because of this.

This field work was conducted in collaboration with the Loxton-based subsection of the Endangered Wildlife Trust (EWT) Riverine Rabbit conservation group, who have implemented strategies to monitor population densities in their surrounding area and to discover more about the behaviour of the species. The EWT use dogs and camera traps to advance the collective knowledge about Riverine Rabbits. Of particular interest is determining the areas they occupy, their hours of activity, and their reactions to potential predators. These are time and labour intensive strategies, making them costly to deploy in the long term. With no pre-existing efficient means of monitoring the Riverine rabbit population thus far, this was selected as a field study for Astro-Ecology.

3.5.2.2 Instrumentation

All flights were conducted with a Matrice 600 with two sets of batteries. Given the size of the Matrice and the vibration-dampening structures on our mount, the footage remained fairly stable in even the windiest conditions. Using an estimate of the Riverine rabbits average size, around 30cm, prior to flying we determined an optimum flying height, from equation 3.6, in the range of 15-20m. The apps Pix4DCapture and DJI Go were used on an Ipad Mini for observations. These applications were used to design flight paths using GPS mapping which were executed by the drone, and to obtain estimates of flight duration and length prior to observations. Each flight was designed using these apps, as a grid, with a specified overlap between each path. To maximise on the flying time, the furthest point in the grid was designated as the start, allowing a shorter distance for safe abortion of a flight if battery percentage dropped too low or there were complications with the software. Overall, the flight paths were executed by the GPS software successfully for most flights, however on a few occasions flights were aborted due to drone errors.

3.5.2.3 Data Collection

As the Karoo is an unfamiliar environment, we conducted an on-foot survey, prior to any data collection, through an area with confirmed sightings to get an idea of the terrain and best flight location. From this survey, and with guidance from the EWT, two flying locations were selected: Silveryhome and Sakrivierspoort. As mentioned above, during the daytime Riverine rabbits sit underneath specific vegetation endemic to the region.

To better understand how Riverine rabbits may appear in mid-IR data when display this behaviour, we chose to perform supplementary experiments at a controlled location where these endemic riparian shrubs were cultivated, hereafter referred to as the Nursery.

Table 3.3 contains information on each flight conducted. Total flight times ranged from 18 mins to 29 mins and covered a distance of up to a few hundred metres depending on the weather conditions and flight path.

Date	Location	Launch Time	Flight Duration (minutes)	Air Temp (°C)	Ground Temp (°C)	Camera Angle (° from nadir)
21.09.17	Silveryhome	07:37	20	22	20	0
22.09.17	Silveryhome	06:34	25	19.7	19.5	0
22.09.17	Silveryhome	07:13	23	20	19.5	0
22.09.17	Nursery	18:27	18	18	22	0
23.09.17	Silverhome	06:49	23	5	5	0
23.09.17	Silveryhome	08:35	24	9.4	12.4	30
23.09.17	Nursery	18:08	17	21.5	20	30
24.09.17	Silveryhome	06:33	18	7.7	9	30
24.09.17	Silveryhome	07:05	29	10	10	30
25.09.17	Sakrivierspoort	06:17	23	9	8	30
25.09.17	Sakrivierspoort	06:57	23	11	10	30
26.09.17	Sakrivierspoort	08:09	21	8	8	30
26.09.17	Sakrivierspoort	09:27	20	8.5	15	30

TABLE 3.3: Flight logs of flights taken to collect mid-IR data in South Africa. Times quoted are local time.

3.5.2.4 Experience & Method development

Data were taken at the Nursery location in the evenings just before sundown. As discussed in section 3.5.2.5, the early morning was determined to be the best time to survey the natural habitat of Riverine rabbits due to the low ambient air and ground temperatures. To not impede on these morning flights (which were already limited by the short duration of the trip), and as a result of long battery charging times, the evenings were the only feasible time to conduct these supplementary experiments. Consequently, ambient air and ground temperatures were not comparable to those we were hoping to observe in flights conducted in the morning. To better understand the appearance in mid-IR data of the Riverine rabbit when occupying their 'scrapes', domestic animals of a comparable size were imaged at a range of flying heights and with a variety of vegetation cover. These flights confirmed the optimum height range of 15-20 m, and that resolving individuals was possible even though the experiments were performed late in the day with the ground still warm from the Sun. We determined that riparian shrubs are capable of fully obscuring the mid-IR emissions of small animals. Therefore we would be unable to resolve Riverine rabbits lying in scrapes under vegetation.

To account for this, we adjusted the flying strategies of morning flights to reduce height and position the camera at an angle of 30 degrees from the nadir, for a better view of the ground underneath the vegetation. We also adjusted flight paths going forward to have a greater overlap for each individual patch of vegetation to allow it to be viewed from two angles during flight, with the side that would be illuminated by the rising sun captured in the footage one way and the side still in the shade captured the other way. With the uncertainty around which side of the bush we would expect to find Riverine rabbits at any given time of day, this gave us the best possibility of detecting them in the field.

In response to the vegetation experiments carried out at the Nursery, survey methods were developed to flush individual Riverine rabbits out, alongside collecting mid-IR data with the UAV. This was successful several times and from the footage it was clear that Riverine rabbits appear much smaller and cooler in the mid-IR than initially anticipated. Figure 3.25 shows the clearest observation of a Riverine rabbit that we obtained. When reviewing the footage leading up to the rabbit flushing, there is no indication of its

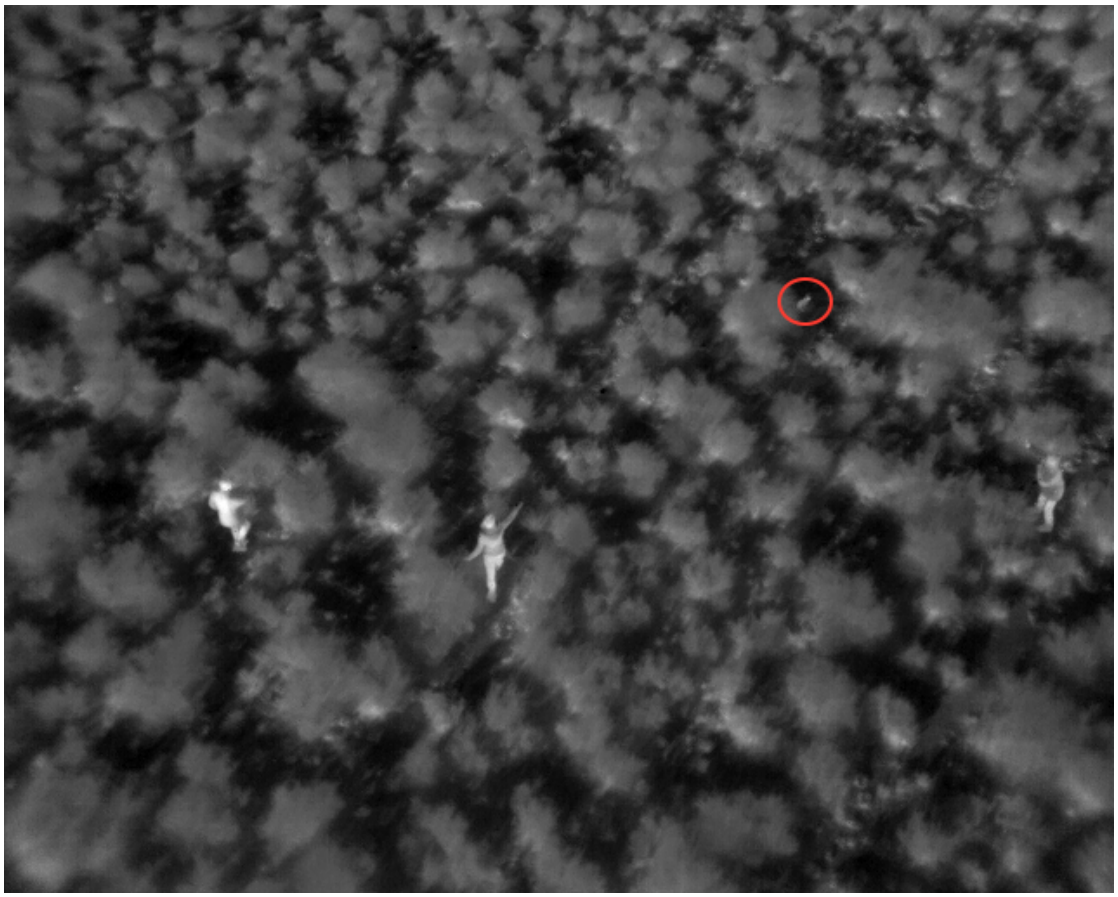

FIGURE 3.25: Successful flushing of a Riverine rabbit, position marked with red circle, as imaged by our camera mounted to a drone flying 20m above. It is clear from this footage that the mid-IR emissions of Riverine rabbits struggle to compete with the emissions of the surrounding vegetation.

resting position under the vegetation, confirming that the vegetation obscures all mid-IR emissions from the animal.

3.5.2.5 Limitations & Conclusions

Flights were limited by the battery life of the drone, and the long recharge time required. Because of this we were only able to conduct two flights per morning, with the potential for one further flight in the evening provided both sets of batteries were charged over the day. The season in which flights were operated limited our ability to conduct flights early in the morning, however the timing of the trip was out of my control. We encountered an unexpected issue in that the Matrice batteries produced flight errors when operating at temperatures below 5 °C. The capacity of drone batteries is known to decrease at colder temperatures (see Kim et al. 2018 and references therein) and these errors we experienced

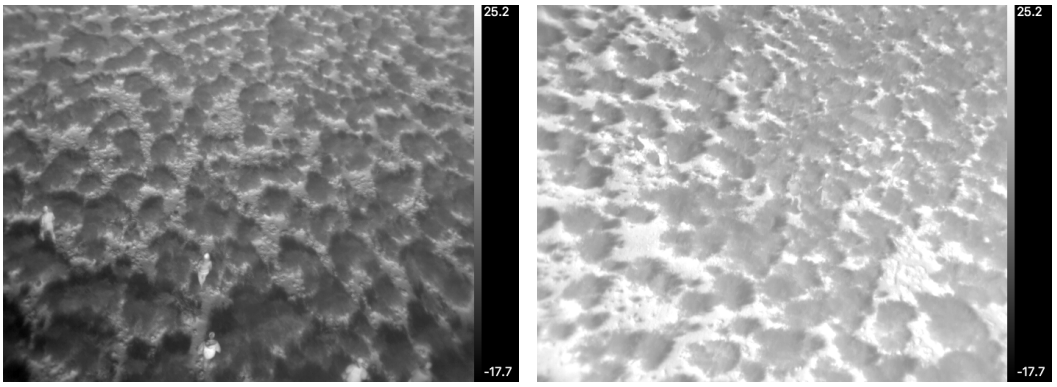

(a) (b)

FIGURE 3.26: Frames from data taken on the same day (26/09/2017) but at different times. Data from flight (a) were taken between 08:09 and 08:30 with recorded ground temperature of $<\sim 8°C$ and air temperature of 8°C. In this image the people are clearly visible and comprise the warmest values in the data. Data from flight (b) were taken between 09:27 and 09:47 with recorded ground temperature of $>\sim 15°C$ and air temperature of 8.5°C. The people in this footage are barely visible and ground temperatures make up the warmest values in the data.

were likely to be a result of a fail-safe mechanism programmed into the drone operating software. Ideally the timing of data collection would be decided by selecting dates where annual land surface climatology displayed average diurnal temperatures that were not too hot for mid-IR observations, nor too cold for UAV battery technology.

As expected from the climate and ground temperature models produced prior to data collection, just before and during sunrise was the best time to observe in the mid-IR. As observed in section 3.5.1, when ambient air and environmental temperatures are high, it becomes increasingly difficult to distinguish the mid-IR emission of mammals from the surrounding environment. Ground temperatures increase rapidly after sunrise and produce poor observing conditions. Figure 3.26 shows the variation in contrast only an hour can cause. Flight (a) occured shortly after sunrise between 08:09 and 08:30, with an air temperature of 8°C and a ground temperature of $<\sim 8\,°C$. Flight (b), was conducted after sunrise, commencing at 09:27. In this time, air temperatures had only risen by 0.5 °C but ground temperatures more than doubled to $>\sim 15\,°C$ in the space of an hour. Because of this, collecting mid-IR data more than ~ 2 hours after sunrise yields data in which it is very hard to distinguish animal species from their local environment.

Again, as discussed in section 3.5.1, even when collecting data at low ground temperatures, there are environmental features emitting significantly in the images. These environmental features retain high temperatures overnight, and contrast against their

cooler surroundings in the morning. The two recurring environmental features that emit strongly in the mid-IR and produce erroneous detections were identified as bush rats' nests and animal burrows. Bush rats' nests, which visually look like large piles of sticks, may contain tens of rats all providing a heat source. In mid-IR data they appear as large, warm, amorphous structures.

Animal burrows appear different to bush rats' nests as they are more circular in shape and have a clearly defined edge. They are deep holes in the ground and account for a large percentage of all false detections. Overnight, deep ground maintains a higher temperature than the surface. However, after sunrise surface temperatures rise and surpass deep ground temperatures. Consequently, during the daytime animal burrows appear as some of the coolest features in the environment.

3.5.3 Endangered Species in Rainforest Environment

3.5.3.1 Motivation

The Bornean Orangutan (Pongo Pygmaeus) was classified as an endangered species after a population decline of $\sim>$ 50% in the 20th century (Payne & Andau, 1997). Breeding populations of Bornean orangutans are endemic to low-lying (below sea-level), tropical forest areas. The severe decline in population is widely attributed to legal and illegal de-forestation for logging and agricultural purposes (Swarna Nantha & Tisdell, 2008). This work was carried out in partnership with WWF-UK and WWF-Malaysia to aid in optimising survey strategies for the Bornean Orangutan in order to accurately estimate population densities in their remaining habitat.

Wildlife surveys in tropical forests frequently consist of ground or aerial transects along which animals are counted. In the absence of individual animals, signs of their recent presence are counted (Laing et al., 2003; Wich & Koh, 1995; Marshall et al., 2008; Buckland et al., 2010; Ancrenaz et al., 2005). For example, elephants in forests are mostly surveyed using dung (Laing et al., 2003), and many ape populations are determined by the presence of their nests (Ancrenaz et al., 2004). These indirect counts are imprecise population estimators leading to wide confidence intervals (Wich et al., 2016; Voigt et al., 2018), but are often more practical than counting individual animals. In the case of orangutans such large confidence intervals are partially due to extrapolating nest

density to orangutan density. This involves parameters such as nest decay, proportion of nest builders, and daily nest building rate, to be estimated (Marshall & Meijaard, 2009). For elephants, the uncertainties lie in assuming rates of dung decay and amount of dung produced daily (Laing et al., 2003). Such large confidence intervals make detection of population changes more difficult, and can lead to population declines not being detected in time to adapt conservation strategies accordingly.

3.5.3.2 Instrumentation

Flights were conducted using a Tarot X4 drone equipped with a custom gimbal and a multi-wavelength camera. Instead of the system introduced in chapter 2, a Thermal Capture Fusion Zoom was used as the primary detector. The Fusion Zoom consists of a 640x512 pixel FLIR Tau 2 640 core equipped with a 19mm focal length lens and housed alongside a 1920x1080 pixel 1080p TAMRON RGB camera. The fields of view of the optical and thermal cameras are centred at approximately the same point, with the FOV of the optical camera ∼2x larger. Images from both components can be aligned in post processing. We used a custom built gimbal to decouple the motion of the camera from that of the drone in order to provide a stable platform for data collection. High frequency oscillations are dampened by isolating the entire gimbal mechanism from the airframe by means of a tuned rubber mount. Low frequency motions are compensated in both the roll and pitch axis by the presence of a closed-loop brushless stabilisation mechanism which maintains the camera at a constant attitude, independent of the motion of the airframe. Ancillary data were also collected at ground level using the system introduced in chapter 2.

3.5.3.3 Data Collection

We recorded 28 flights over six days, between the 10th and 15th of May 2018. Flights were performed at two sites: Sepilok Orangutan Rehabilitation Centre (A) and the Kinabatangan Orangutan Conservation Project (KOCP) study site (E 118° 17' 00" to 118° 18' 40" - N 5° 32' 20" to 5° 33' 30") (B). Table 3.4 contains the flight log information for data collection.

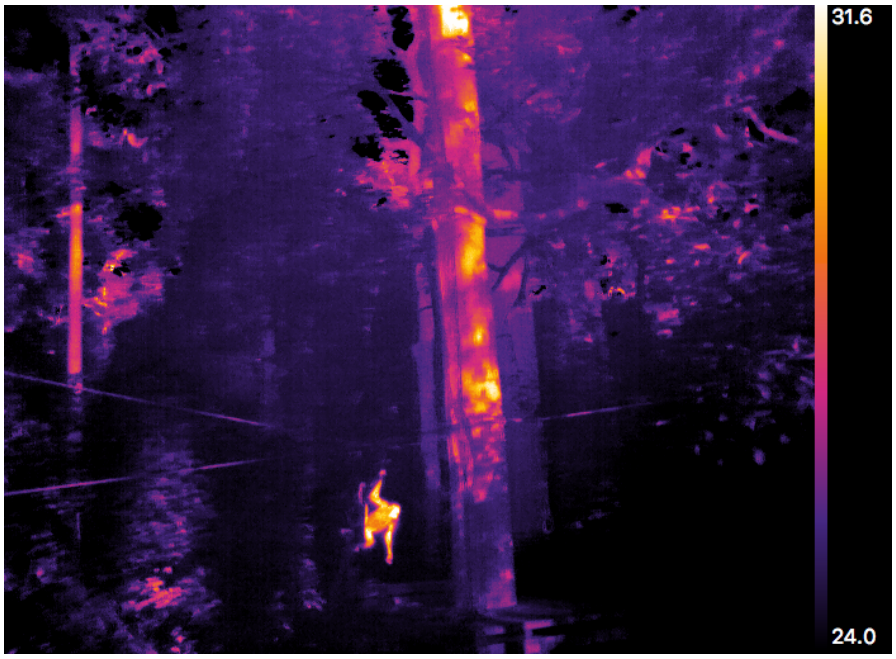

FIGURE 3.27: An example of data taken from the Tau 2 camera while hand held on the ground to confirm the surface or skin temperatures of orangutans in order to plan flights. The scale bar on the right side displays the temperature range of the scene in °C. The surface temperature of orangutans can be seen to be between $27 - 30$°C.

The diurnal range for the land surface temperature in Sabah, Malaysia, is between 22 and 33 degrees Celsius during the month of May. From initial observations on the ground using the Tau 2 thermal infrared camera (as described in chapter 2) we found that the recorded surface temperature of orangutans was in the range $27 - 30$°C (see figure 3.27). Flights were performed as close to sunrise (∼06:00) and sunset (∼18:00) local time, as possible. Having some amount of sunlight also meant the RGB camera wasn't entirely redundant.

Prior to flying, we calculated a maximum flying height of no greater than ∼ 90m above an orangutan (assuming adult Bornean orangutans are approximately 1.1m in length Mittermeier et al. 2013) for it to be > 13 pixels as discussed in section 3.3.4. In reality, for the region surveyed, other environmental factors influenced our decision on maximum flying height. Flights were performed at heights above ground level (AGL) between $30 - 120$m depending on the conditions discussed below. For most flights the camera was in the nadir position, however for some flights the camera angle was changed between 45 degrees and the nadir during the flight to examine how camera angle affected detectability of animals.

Two main strategies were employed to confirm orangutan detections from the drone.

Date (dd.mm.yy)	Launch site	Flying height (m)	Flying speed (m/s)	Camera angle (°)	Launch time	Flight duration (mins)
10.05.18	A	80	-	90	06:13	9
10.05.18	A	120	-	90	06:22	7
10.05.18	A	120	7	90	07:17	9
10.05.18	A	20*	-	45/90	18:24	11
10.05.18	A	120	-	90	19:03	13
11.05.18	A	70*	-	45/90	05:21	16
11.05.18	A	120	-	90	05:28	5
11.05.18	A	100	5	90	05:35	8
11.05.18	A	30*	-	45/90	17:44	4
11.05.18	A	30*	-	45/90	17:50	3
11.05.18	A	100	1	90	18:04	4
11.05.18	A	100	5	90	18:30	10
12.05.18	A	100	-	45/90	05:21	10
12.05.18	A	100	-	45	05:41	10
12.05.18	A	100	1	90	06:17	4
12.05.18	A	100	-	90	18:04	12
12.05.18	A	76	-	90	18:40	9
13.05.18	B	80	-	90	18:28	10
13.05.18	B	80	5	90	18:59	11
14.05.18	B	80	5	90	05:43	12
14.05.18	B	80	5	45	06:12	12
14.05.18	B	120	6	90	18:30	12
14.05.18	-	150*	-	45/90	20:20	14
15.05.18	B	120	6	90	05:12	12
15.05.18	B	120	6	90	05:39	4
15.05.18	B	100	6	90	05:43	2
15.05.18	B	80	6	90	05:45	3
15.05.18	B	60	6	90	05:48	5

TABLE 3.4: The details of each flight conducted. Column 3 provides the maximum height above ground level recorded for each flight with a standard error of ± 1 metres. If flying height was varied, values have been recorded with an asterisk (*). Column 4 contains the minimum flying speed. The estimated uncertainty on this is ±0.1 m/s. Column 5 describes the angle of the camera during flight in degrees, with an angle of 90° denoting a nadir position. A forwards slash (/) between two values refers to a change in angle during the flight.

In the first strategy, before evening flights, a field team was deployed to observe the orangutans and to follow individuals until they nested. In area A this was done by

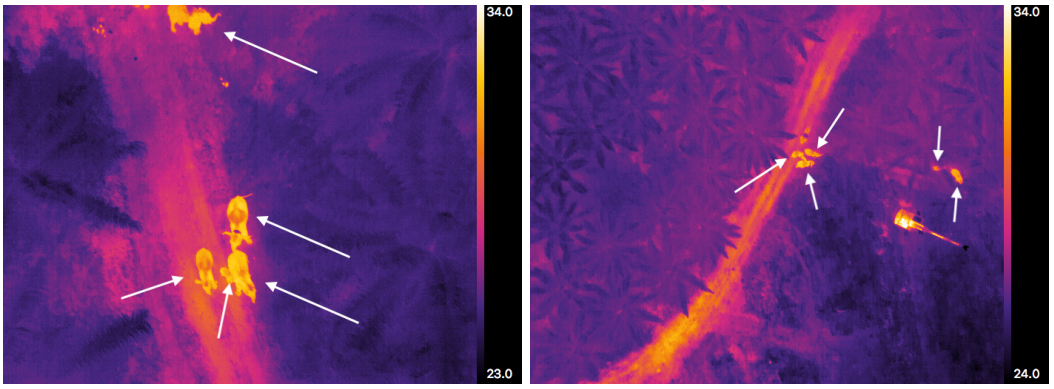

FIGURE 3.28: Bornean elephants observed with the thermal camera at 60m (left) and 150m (right). Data were taken just after sunset making the elephants impossible to see in the RGB footage recorded (not shown). In the left image some elephant dung can also be seen, and in the right a piece of farming equipment is visible.

observing individuals as they left the feeding platform in the rehabilitation centre. In area B, the ongoing research conducted by the Hutan Orangutan field team located known individuals and followed them until they nested. The GPS location of the nesting site was then recorded and the drone flown to that location. The flight pattern selected depended on the distance and visibility of the location from the take-off site. In general, if the pilot had a line of sight view of the GPS position, they flew manually. At larger distances and/or with no line of sight, an automated flight pattern was used. The same nesting sites were also surveyed the following morning with the same flight pattern as the previous night.

The second observing strategy was to conduct a blind survey of a larger area using a grid pattern, in which the distance between the transects was sufficient to ensure the field of view of the thermal camera overlapped approximately 30% between transects. The thermal data were then inspected after landing, and the GPS location of any potential detections was recorded. Potential detections were then confirmed from the ground by the observation of either an orangutan and/or a fresh nest (with green leaves) at that location.

3.5.3.4 Experience & Method Development

All footage was reviewed by eye for potential orangutan detections, and any detections were cross referenced with known GPS locations of nests or orangutans found on the ground. In total there were 41 potential detections and 41 confirmed detections of

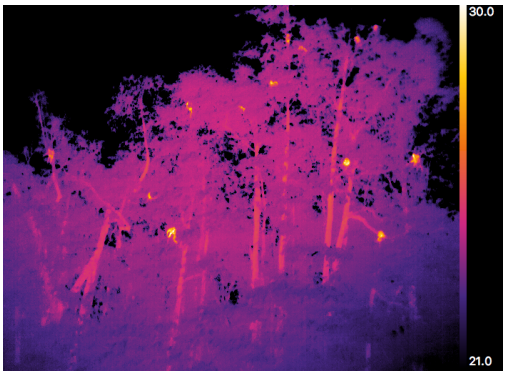

FIGURE 3.29: Proboscis monkeys viewed from ground level with the Tau 2 camera.

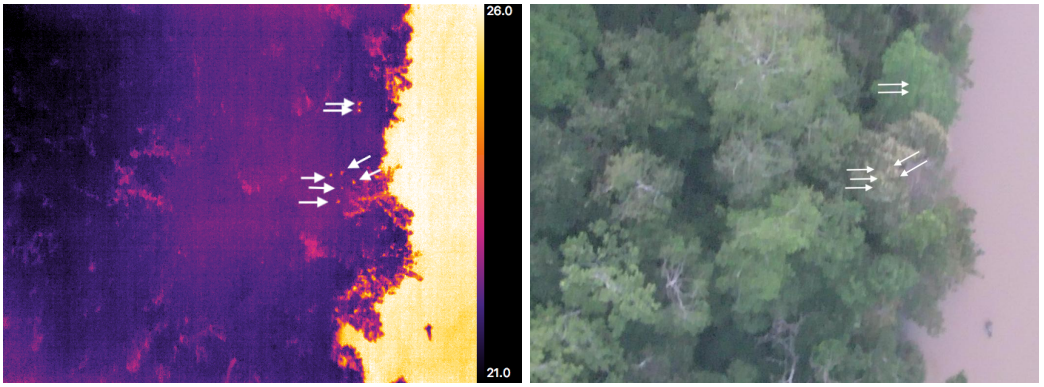

FIGURE 3.30: Proboscis monkeys from a drone at a height of 100m with thermal camera (left) and RGB camera (right).

orangutans in mid-IR data. 13 detections were found using the grid survey method. The true positive rate for flights was 100% with all identified potential detections corresponding to the confirmed location of orangutans and/or nests. Confirmed detections comprised of 31 orangutans and 10 recently vacated nests. These nests ranged from 8 to 20+ m in height. In 8 flights, 10 nests and nesting orangutans were detected but canopy cover was not estimated by the ground team. There were no false positives identified. Although the true completion rate, and the false negatives cannot be estimated from these low number statistics (the relatively small number of observations performed), this is a promising start.

During our observations at site B, we found that there were other animals in the area which we were also able to observe from the drone, namely proboscis monkeys (*Nasalis larvatus*) and Bornean elephants (*Elephas maximus borneensis*). We performed 2 flights at heights of 60m and 150m on 20/05/2018 to gather thermal data for Bornean elephants (see figure 3.28). As elephants are larger than orangutans, we recalculated the maximum distance between drone and target to resolve the elephants at a minimum of 10 pixels.

Assuming elephants are approximately 2m in length the maximum distance is 230m. Flights were performed with the elephants within line of sight on the ground. These observations were performed around 20:20 local time.

We also carried out 4 flights over a troop of proboscis monkeys, which were observed simultaneously from ground level. Examples from ground and drone are shown in figures 3.29 and 3.30. The numbers of monkeys detected in the mid-IR was confirmed from the ground.

3.5.3.5 Limitations & Conclusions

One challenge we faced when adapting the mid-IR and UAV technology to survey for orangutans was determining the 'in-practice' flying height for the UAV given the constraints of the environment. We calculated a maximum height for detections of orangutan-sized animals of 90m. But, when trying to detect arboreal species, this calculation becomes more complicated and it is important to know the height of the canopy in the area of study. The height of the canopy was in the range $30-50$m and $10-30$m for sites A and B, respectively. Emergent trees with heights up to 65m at site A and 35m at site B were common. In an ideal situation we would fly lower than our calculated height to produce the best resolution data for reliable detections. However, for many of these flights we had to fly at heights that were verified as safe for the UAV in order to avoid emergent trees. Where distances were large the drone was flown at a larger height above the launch site to account for changes in terrain height and to give a wider field of view for the camera. Because of this, flying height was in the range $80-120$m. In cases where the drone was flown higher than 100m, it became noticeably more difficult to detect orangutans.

This limitation will prove challenging for large-scale surveys over canopies of large or unknown height and without knowledge of orangutan behaviours. Since orangutans nest and travel through the canopy at varying heights from the ground we believe that the orangutans were closer to the drone than the minimum distance of 90m for most of our flights. However, we only have a direct estimate of the actual distance between drone and orangutan in the cases where the nest height was recorded. If necessary, flights can be conducted higher above the canopy level but this will require a longer focal length lens, leading to a smaller field of view. The reduction in area covered by the field of

view with a longer lens will also require either a higher frame rate or a slower drone speed, which can in turn limit the size of the area covered. A potential method for determining the flying height for long-term studies of forest environments would be to conduct a canopy cover survey to locate and measure any emergent trees in the area. This would provide a minimum flying height which when coupled with our maximum height calculations will provide the most feasible range of flying heights for a given area and allow decisions on the optimal lens prior to flying. In this case it might also be possible to develop drone flying strategies to avoid emergent trees allowing lower flying heights.

As described in section 3.5.2, studies prior to this field work found local vegetation to be mostly impenetrable to mid-IR and posed a major issue by obscuring detectable sources. As a result, the density of rainforest canopy has the potential to be the largest limiting factor for the use of mid-IR systems to survey arboreal species such as orangutans. We found that it was easier to identify orangutans in the data from flights conducted with the mid-IR camera at the nadir than those conducted with the camera at 45°. This is because of the difference in physical properties between canopy leaves and tree stems and branches, which absorb and reflect light differently. The 'directional gap fraction' is a measure of how much light is absorbed and scattered by the canopy biomass as a function of height, basal area and sun zenith angle (Hadi et al., 2017). For areas with a substantial gap fraction, as the camera angle deviates from 90° more of the biomass below the crown will be imaged. This can pose an issue as this view underneath the crown can present many transient bright sources arising from tree branches and stems that are exposed to direct light. These sources may appear as false positives to those less familiar with mid-IR data or to an automated system without a component to remove such artifacts. Flying with a camera in the nadir position is preferable as this provides a scene of canopy leaves with a more uniform albedo. At this angle, any gaps in foliage cover will appear much cooler and less likely to produce erroneous detections.

To be an effective technique for surveying orangutan and other tropical forest species, mid-IR sensors must be capable of detecting species where canopy cover is high. Because female orangutans with young select nesting locations with more tree stem and canopy cover (Rayadin & Saitoh, 2009), an indication of the potential for mid-IR imagery is provided by the four flights where mother and infant pairs were successfully detected despite estimated canopy coverage of 75-100%. From the 11 detections recorded with

50% + canopy cover, we found that the canopy cover did not pose a significant limiting factor in the detections we confirmed. However with false negatives and true negatives undetermined it is uncertain whether additional data would help determine whether or not we missed any orangutans. Therefore, we cannot conclude whether canopy cover is, or is not a limiting factor.

This study highlights the benefits of using mid-IR over visible imagery for surveying wildlife under a range of environmental conditions. Because mid-IR sensors record emitted radiation rather than reflected sunlight, data can be collected during low light conditions when optical imagery would be impractical: 58% of the detections presented here occurred in conditions where the optical data were unusable. There were two causes of this; time of day and environmental (weather) conditions. Aerial surveys to detect orangutans, particularly those conducted with drones, are most effective when individuals are nesting as they are stationary for longer periods of time and wild individuals most commonly make their nests off the ground. To verify this, all but one of our mid-IR detections came from imaging orangutans in their nests. But the times at which orangutans nest are unsuitable for collecting optical data, as they tend to occupy their nests shortly before sunset and vacate them just after sunrise. Mid-IR observations had the added advantage of being able to detect an individual nesting in the evening and re-verify the detection the next morning before the nest was vacated.

Mid-IR data is also unaffected by some weather conditions that negatively affect optical data and are common in rainforest areas. Several flights were conducted in misty conditions where optical visibility was significantly reduced and estimated by eye from the ground to be only 20m. However there were no problems with the identification of orangutans in mid-IR data in these conditions. This makes the mid-IR the optimum regime for collecting data in areas prone to high humidity and fog.

3.6 Concluding remarks on Astro-Ecology

In section 3.2.1 we describe three milestones for successful deployment of the Astro-Ecology framework. In this section I will summarise the findings presented in this chapter with respect to how they relate to these goals.

3.6.1 The deployment of a COTS mid-IR detector, mounted on a UAV, as an optimised system for collecting survey data of a variety of species in a range of environments.

Mid-IR data of animals have successfully been collected in several different environments using a UAV as the observing platform. The animals surveyed have spanned a wide variety of species, sizes and occupied many different habitats. However, there were several limiting factors highlighted. In short; UAVs are becoming heavily regulated, require batteries that discharge very rapidly, present an environmental disturbance and require a clear flight path.

UAV battery technology is an ongoing area of commercial development but until battery technology advances to give much longer flight times, UAVs are only suitable for surveying species that occur at higher densities or range over smaller areas. The range of hover times, i.e. the time for which the UAV can hover with no extra payload, for the three UAVs used in the field-applications described in section 3.5, was between 35 and 50 minutes. In reality, even with the small payload of the mid-IR camera, these systems were unable to fly safely for more than 30 minutes. These short flight times could be negated somewhat by using fixed-wing UAVs that can fly for longer durations than multirotor systems, but the gain in flight time is not significant enough to cover very large areas. The use of UAVs that can fly for longer generally means an increase in the size of the system and hence constrains portability, take-off and landing options, and costs. A third possible strategy is to fly faster, which can increase the area covered, albeit by a limited amount. This would require a high-frame-rate mid-IR camera, which increases costs. A camera with a higher resolution or larger field of view would allow flying altitude to be increased.

Conservation ecologists have the most to gain from using mid-IR cameras at night. However, UAV flights are often regulated such that flying without visual confirmation of the system at all times is prohibited. This limits data collection to daylight hours, which as seen in the field applications, poses its own issues for mid-IR systems. Observing in the mid-IR, in environments with high daytime temperatures can be achieved by carefully planning observing times using predictions of the diurnal and annual land-surface climatology. However, in many environments, data collection can only occur in short periods post-sunrise and pre-sunset.

In section 3.3.4 we determine that sources must be larger than 13 pixels in size in order to provide reliable temperature values. However, environmental constraints take precedence and determining the height at which to fly a UAV is not a simple task for non ground-dwelling species. This was particularly problematic when deployed to survey Bornean Orangutans as described in section 3.5.3. Drone altitude, and hence the resolution of individuals was heavily limited by the height of emergent trees and the possibility for orangutans to sit at any height of forest. The noise and presence of UAVs can also be a great disturbance. In many environments, flying heights were increased to avoid the risk of startling or distressing animals. When coupled with environmental hazards, these two factors meant the optimum height of the UAV was rarely achieved.

3.6.2 The application of automated astronomy source detection techniques to mid-IR animal data.

Astro-Ecology was motivated by three similarities between the field of astronomy and conservation ecology. These similarities are detailed in table 3.1. Animals that use metabolic heat to maintain a stable internal temperature are assumed to appear as bright objects on a mostly dark background. This, coupled with the decades of experience astronomers have using IR systems and autonomous pipelines was the driving factor behind such an unusual cross-discipline approach. However, the work presented in this chapter has highlighted many differences between 'normal' IR astronomical observing and using mid-IR cameras to observe animals that make astronomical source detection techniques unsuited to conservation ecology.

In section 3.5 we describe three applications of Astro-Ecology in the field. Ground and environmental temperatures were found to be significantly warmer (with temperatures which could surpass 35°C) than the background in astronomical images ($\sim$ -20°C). Detecting animals in mid-IR is therefore not as simple as locating the brightest sources in the data. There are several sources of error that are unique to mid-IR observing in ecology and not replicated in astronomy. Ground temperatures have comparable or higher temperatures than animals, even when air temperatures are low. Environmental features have the potential to emit or reflect significantly enough to overwhelm animal sources. All three field applications highlighted the need to understand and account for the effects of climate and environment with land surface temperature models, such as

those described in Burke et al. (2018a). Data collection can only occur at times when the source-environment contrast is large, otherwise the primary advantage of mid-IR is lost.

Animals rarely appear like point sources. In section 3.4.3 we present several examples of how the orientation, resolution and viewing angle of an individual can drastically alter the observed mid-IR emission and the shape of the animal. This is in contrast to astronomical images where sources are mostly static and point like or of fixed shape. When studying humans in the field, we discovered an individual source can span a large range of apparent sizes, as seen in figure 3.22. The foreground environment plays a large role in the observed size of an object, as many features can obscure mid-IR emissions from target sources.

We couple mid-IR observing with UAV technology to increase the efficacy of surveying species. However, by doing this we introduce a 'moving observer' effect that isn't replicated in ground-based astronomy where telescopes are stationary and stable. Scientifically significant analysis is limited without a robust tracking component, to not just identify target sources across several frames of the same observation, but also to aid in identifying environmental features as spurious sources. Tracking moving objects with a moving observing platform is a non-trivial task.

3.6.3 The automatic identification of animal species using mid-IR data.

It is a common misconception that homeothermic endotherms have a standard core body temperature that is unique to species or individuals (McCafferty et al., 2015). Thermoregulation is a complex and dynamic process. The temperature of any part of the body is a mixture of heat conducted to the surface by blood flow and heat transported from the surface by the environment. Surface temperatures are highly dependent on the surroundings of an individual and cannot be given absolute values (Taylor et al., 2014).

This was verified by an early attempt to determine if recorded temperatures could be used to identify individuals. Figure 3.21 shows the frequency distribution of the observed temperature of human sources as recorded in several flights. The large variation in recorded temperatures for human sources is likely to be a result of the scaling of surface temperatures with ambient temperatures. While the lack of climate information for

our data means this cannot be independently verified, it is safe to assume that surface temperatures of endothermic homeotherms cannot be modelled in any absolute way, and the use of mid-IR observations for identification purposes is entirely limited to the 'thermal-profile'.

We present examples of the complex nature of the spatial distribution of mid-IR emissions across the bodies of a range of species in section 3.4.3. From observing a wide variety of species in the mid-IR, we can verify that many species have very distinct emissions as a result of their unique thermo-regulatory systems. These 'thermal-profiles' could in theory be used as an identifier. However, to accurately model different species, the mid-IR distribution must be well understood at all orientations, taking into account the full range of movement of the animal, the difference in emissions with age, the degradation of spatial information with lower resolution, and the potential for injury to alter the 'thermal-profile'. This is an excellent case for machine learning. However, the study is data limited and algorithms would need to be bespoke and complex.

3.6.4 Summary of Chapter

In this Chapter the field of Astro-Ecology is introduced. A pipeline developed with the aim of facilitating an improvement to the efficacy and efficiency of surveys for wildlife conservation and poaching prevention is presented. This pipeline works by coupling mid-IR cameras and UAV systems to collect data, and by employing standard astronomical source detection techniques. The development of the pipeline and 3 applications in the field are described.

Of the three initial goals of the field, one was fulfilled with the successful deployment of mid-IR and UAV technology to collect data. However, for all of the reasons mentioned above, an algorithm that operates on the same principles as those in astronomy to detect, track and identify sources is not a feasible option for use in ecology. This was an issue that led to a reliance on visual confirmation of detections by human observers, in direct contradiction to the goals of Astro-Ecology. This work highlights that the issues that Astro-Ecology aims to tackle are far more complex in nature than originally considered. As a burgeoning field, the work presented in this Chapter and the investigation into the validity of the initial assumptions, has been an important step in the continued

development of the pipeline. These studies have provided the baseline from which Astro-Ecology will grow to ensure the developed pipeline is as effective as possible.

Future work in this area will now concentrate on two areas highlighted in this Chapter. Firstly data collection must be optimised for different environments. The issues raised by the field applications, such as the environmentally-constrained flying heights, the need for ground confirmation, the time limits placed on data collection as a result of ambient and ground temperatures, etc, need to be carefully considered and accounted for prior to data collection. This will be no trivial task as each species and each environment poses new challenges to address. Secondly, an alternative to an astronomy-led detection and identification code, one without reliance on sources being brighter than their surroundings, stationary and sampled as point sources in data needs to be built. This alternative exists as a machine learning algorithm. With ample data, for expected species, sampled in a range of different conditions (i.e. environmental features, ambient temperatures, ground temperatures) a machine learning algorithm can be used to train a probabilistic model to output a species classification or a FOV coordinate. McWhirter et al. (2019) describes the development of such an algorithm.

Chapter 4

Part III Astronomical Application in Ground-Based Observing: Initial Prototype

4.1 Overview of Contents

This Chapter describes the design and commissioning of a simple, prototype low-cost mid-IR instrument, built using commercially available components and the uncooled microbolometer array as a detector. The prototype N-band ($\sim 10\mu$m) instrument is presented alongside the results of a week-long programme of observations on the Liverpool Telescope (LT). These observations were conducted to test the system sensitivity and stability, and determine the feasibility of using this technology in 'facility' class instruments for small (1-2m) telescopes. Finally, as an example science case observations of the cooling of lunar surface features during the 2019 January lunar eclipse are presented.

This work was conducted using funds from the Royal Astronomical Society (RAS) Patricia Tomkins Instrumentation award. The grant application was written by myself ($\sim$ 1 week) and submitted with Prof. I. Steele as the PI (RAS member required as PI). The optical design ($\sim$ 5 weeks), mechanical construction ($\sim$ 2 weeks), software design and construction ($\sim$ 5 weeks), data collection ($\sim$ 1 week) and data analysis ($\sim$ 8 weeks) was all done by myself. The mechanical design was translated into CAD by

Mr S. Bates (engineering manager for the LT) from the optical design and under my guidance of the desired optical and mechanical components ($\sim$ 2 days). Commissioning and de-commissioning on the telescope ($\sim$ 2 days) was done by myself with the help of Mr D. Copley (NRT Systems Engineer). All works were conducted under the guidance of Prof. I. Steele (Telescope Director).

4.2 The Liverpool Telescope

The instrument was initially designed for use on the Liverpool Telescope (LT) (Steele et al., 2004). The LT is owned and maintained by the Astrophysics Research Institute at Liverpool John Moores University, and is situated at the Observatorio del Roque de Los Muchachos (ORM) in La Palma. It is currently the world's largest, fully robotic telescope with a full suite of instruments. The telescope has been scheduling, conducting and reducing observations in a fully automated manner since 2004.

The LT is an f/10 telescope with a Ritchey-Chrétien design. It is comprised of a 2.0 m concave primary mirror and a 0.65 m convex secondary mirror which directs rays into an acquisition and guidance (A&G) box at the Cassegrain focus. The A&G box is the mounting point for the LT instruments and contains a 0.2 m science fold mirror at a 45 ° angle to direct light towards the instruments. The LT has a 10 μm diffraction limit of 1.23 arcsec.

4.3 Feasibility Study

To determine the feasibility of observing in the mid-IR range with a non-infrared optimised telescope such as the LT, we began by characterising the mid-IR sensitivity of the LT optical system by considering the contribution of the LT mirrors to the flux incident on a single pixel and comparing this estimate to the magnitude equivalent flux of a zero-magnitude star incident on a single pixel. We then make a 'best-case' approximation of the flux required to register a temperature increase equal to one NEdT of the system, by considering all the flux from a star falling on only a single pixel. From this we determine the N-band magnitude of such a star.

Measurements were taken on site by S.Bates in June 2018 with a handheld FLIR InfraCAM SD 25 °. The temperature of the science fold mirror $T_{mirror} = 293\,\mathrm{K}$ and sky temperature as reflected off the science fold mirror $T_{measured} = 253\,\mathrm{K}$ were recorded. The actual sky temperature was recorded as $T_{sky} \sim 250\,\mathrm{K}$. FLIR record the accuracy of this system as the larger of either 2 K or 2%.

The total energy E_{tot} recorded off the science fold mirror is the sum of emitted $E_{emitted}$, and reflected $E_{reflected}$ energy:

$$E_{tot} = E_{emitted} + E_{reflected}. \tag{4.1}$$

The emissivity of a material ϵ, is the ratio of the energy radiated and the maximum energy radiated by a blackbody at the same temperature. Where the blackbody would have $\epsilon = 1$. Assuming the LT mirrors have zero transmittance, reflectivity R, and emissivity are related as:

$$\epsilon = 1 - R. \tag{4.2}$$

To estimate the emissivity of the LT mirrors, we used a modified form of the Stefan-Boltzmann law (as defined in equation 1.24 in chapter 1.1) for a non-blackbody surface:

$$F = \epsilon\sigma T^4, \tag{4.3}$$

and combined equations 4.3 and 4.1:

$$\sigma T^4_{measured} = \epsilon\sigma T^4_{mirror} + (1-\epsilon)\sigma T^4_{sky}, \tag{4.4}$$

$$\epsilon = \frac{T^4_{measured} - T^4_{sky}}{T^4_{mirror} - T^4_{sky}}. \tag{4.5}$$

From this we obtained an estimate of $\epsilon = 0.058 \pm 0.131$ for the LT as measured from the science fold mirror. Comparatively, reflectivity measurements of the science fold mirror, taken on site, yield an IR ($0.8\,\mu$m) emissivity value of $\sim 50\%$ before cleaning and $\sim 20\%$ after cleaning. Our calculated value is therefore only a very rough estimate particularly as the error makes it consistent with both an emissivity of zero and with the post-cleaning value measured on site. Realistically, the LT primary mirror is not a perfect reflector and will not have an emissivity of zero, and due to dust and other

contaminants collecting on the surface of the mirror, the true emissivity will cover a range of values over time. Using our calculated estimate of emissivity, and equations 4.1 and 4.4 we calculated a total radiant flux of $E = 232.9\text{Wm}^{-2}$.

The radiant intensity is defined as the radiant flux divided by the solid angle subtended by the source as viewed from the detector, Ω:

$$I = \frac{dE}{d\Omega}. \tag{4.6}$$

The solid angle subtended by the science fold mirror at a detector positioned at the focal plane of the telescope is $\Omega \sim 0.161$ ster. From this and equation 4.6 we calculated a radiant intensity of 1455.6 $\text{Wm}^{-2}\text{sr}^{-1}$ incident on the detector. As described in chapter 2 each pixel of the detector has dimensions of 17 x 17 μm with an area of $2.89\text{x}10^{-10}\text{m}^2$. Therefore, the contribution of the telescope structure to the mid-IR flux incident on a single pixel can be estimated as follows:

$$1455.6 \cdot 2.89\text{x}10^{-10} \cdot 0.161 \text{ Wm}^{-2}\text{sr}^{-1}\text{m}^2\text{sr} = 6.77\text{x}10^{-8} \text{ W/pixel} \tag{4.7}$$

In comparison, Cohen et al. (1999) define the zero magnitude flux density of standard stars in the N-band as 35.21 Jy (35.21 x 10^{-26} $\text{Wm}^{-2}\text{Hz}^{-1}$). The frequency range covered by the detector is 2.29 x 10^{13} Hz and the area of the primary mirror is 3.14 m^2. So the mid-IR flux equivalent to that from a zero-magnitude star, incident on a single pixel of the detector is estimated as follows:

$$35.21 \text{ x}10^{-26} \cdot 3.14 \cdot 2.29 \text{ x } 10^{13} \,\text{Wm}^{-2}\,\text{Hz}^{-1}\text{m}^2\text{Hz} = 2.53 \text{ x } 10^{-11} \text{ W/pixel} \tag{4.8}$$

The NEdT of the system was measured to be $< 60\,\text{mK}$ in chapter 2. An additional flux needed per pixel ΔF, to give a measurable temperature increase of 60 mK was calculated as follows:

$$E_{telescope} + \Delta E = k(T_{mirror} + \Delta T)^4 \tag{4.9}$$

Where k is a constant determined from a modified form of equation 4.3, where $E_{telescope} = kT^4_{mirror}$ and ΔT is equal to the NEdT of the system. From this we obtained an estimate of $\Delta E = 0.191$ Wm^{-2}, corresponding to $\Delta F = 5.52 \times 10^{-11}$ W incident on a single

pixel. This value is approximately 2 times larger than the flux received from the zero magnitude standard star, corresponding to flux from $\sim$ -1 mag star.

4.4 Optical Design

The prototype N-band instrument was built around the FLIR camera, with full specs provided in chapter 2. This system is supplied with a 13mm focal length lens of unknown specification. There is no obvious way to remove this lens without damaging the system, and potentially breaking the vacuum seal around the detector. As such it was necessary to design foreoptics to rescale the image to an appropriate plate scale for use on the LT. From the Nyquist sampling theorem we know that we require 2 pixels across the diffraction limit of the telescope to sample the image optimally. As the diffraction limit of the LT at 10μm is 1.23 arcsec, the optics were designed to get as close to a 0.6 arcsec per pixel plate scale as possible.

To do this, the 13mm focal-length lens and detector were modelled as a paraxial system and a ray tracing analysis for on- and off- axis light was conducted. The full optical design of the LT and proposed instrument can be seen in figure 4.1. A close up of the additional foreoptics and the FLIR system can be seen in Fig. 4.2. The optical prescription of the LT and prototype is given in Table 4.1. The reimaging optics were designed to be adjustable, to allow the instrument to be adapted to other 1-2m class telescopes with a similar focal ratio.

This optical prescription was then translated into a low-cost, COTS re-imager comprised of an Edmund Optics 50mm diameter, 100mm focal length, 8-12 μm, AR coated, germanium plano-convex field lens and a Thorlabs 25mm diameter, 75mm focal length, 7-12 μm, AR coated, germanium plano-convex collimator lens. Both lenses act to collimate the light collected with the LT onto the FLIR imaging system. Both lenses have an anti-reflection coating which reduces reflection losses to $< 3\%$ in the 8-12μm wavelength range. When mounted to the LT, the prototype has a plate scale of 0.75$''$ per pixel, with approximately two pixels sampling the 10 micron diffraction limit of the LT. In practice we found that, as there was uncertainty in the location of the pupil and the presence of an aperture stop within the FLIR system, the imaging field of view (FOV) reduced to a circular aperture of 500 pixel diameter. This results in a $\sim 6.25'$ diameter FOV at LT.

Spot diagrams for on-axis and $\pm$ 2.7′ off-axis rays are shown in Fig. 4.3. The spot diagram describes how an infinitely small point source (i.e. a 2d delta function) of light would appear when viewed through the entire optical system of the telescope and foreoptics and imaged on the detector. Spot diagrams provide a visual indication of the image quality. These figures highlight the off-axis aberration that is inherent in the optical design. The prototype has an 80% geometric encircled energy (GEE) diameter of <1.1 arcsec for on-axis rays and <3.1 arcsec for off-axis rays, as seen in figure 4.4. Assuming a 2D Gaussian profile, this corresponds to a spatial full width half maximum (FWHM) of < 0.7 and < 2.0 arcsec for on- and off-axis rays respectively. Two pixels was therefore predicted to sample the diffraction limit for on-axis rays, with slightly worse performance off-axis.

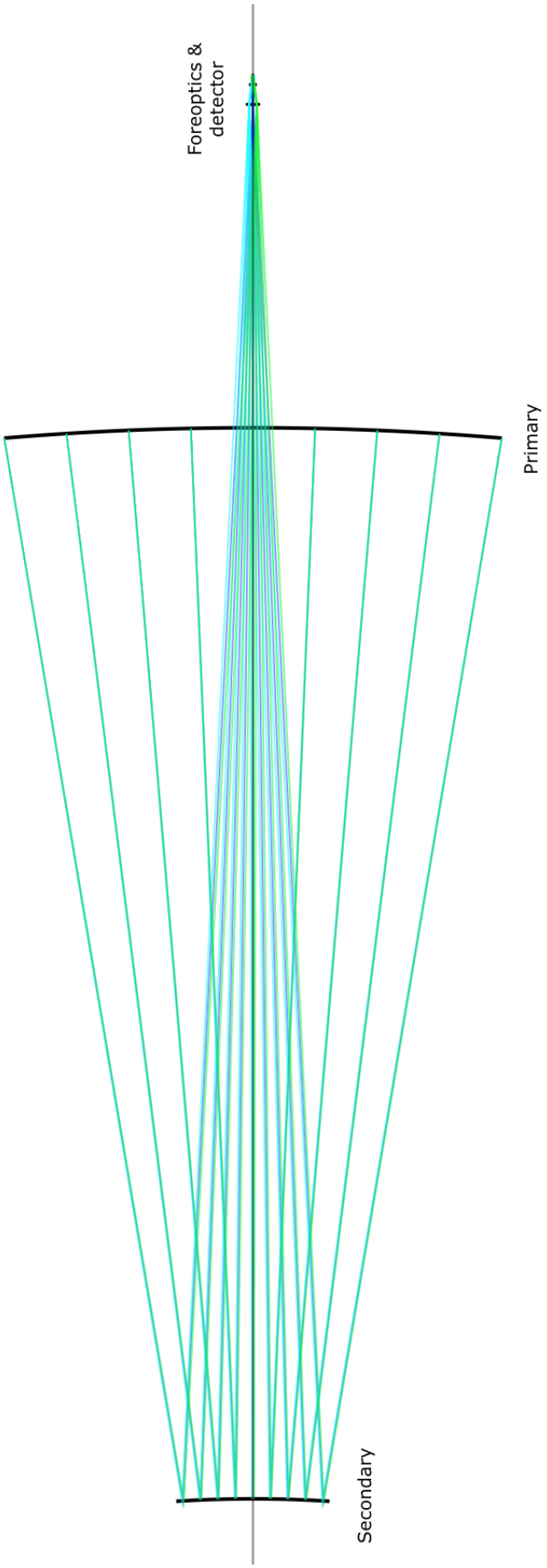

FIGURE 4.1: Ray trace of the LT and instrument optical design for on- and off-axis beams of 2.7 arcmin.

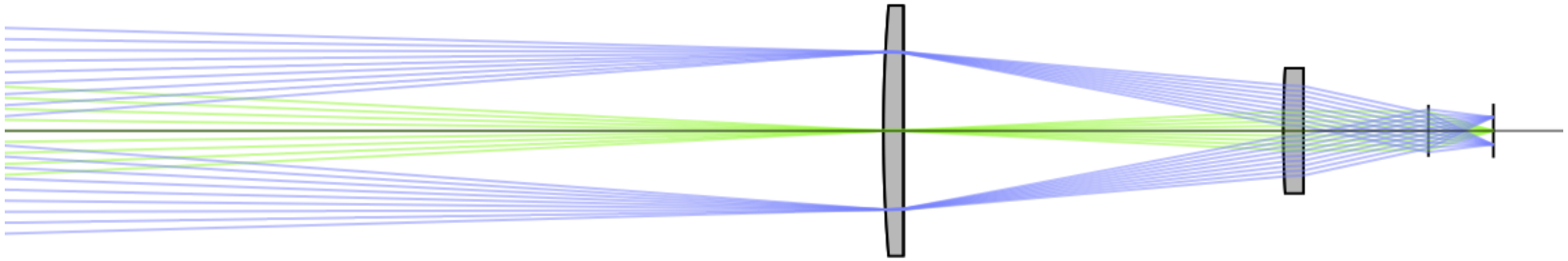

FIGURE 4.2: Ray trace for on- and off-axis beams of 2.7 arcmin. The 50mm diameter field and 25mm diameter collimator lenses bend the rays incident off the secondary mirror onto the camera system.

Comment	Type	Radius of Curvature	Thickness	Glass	Semidiameter
Source	Standard	inf	inf		0.000
Primary	Asphere	-12000.0000	0.0000	MIRROR	1000.0000
	Standard	inf	-4315.385		1000.0000
Secondary	Asphere	-4813.0000	0.0000	MIRROR	308.0000
	Standard	inf	5615.889		308.0000
Field Lens 50mm	Standard	300.3900	4.000	GERMANIUM	25.000
	Standard	inf	76.000		25.000
Collimator 25mm	Standard	225.0000	4.000	GERMANIUM	12.500
	Standard	inf	25.000		12.500
Lens	Paraxial	inf	13.000		5.200
Detector	Standard	inf	0.000		5.400

TABLE 4.1: Combined optical prescription of the LT and prototype camera system. All dimensions are in mm. The thickness quoted in column 4 refers to the separation between each component.

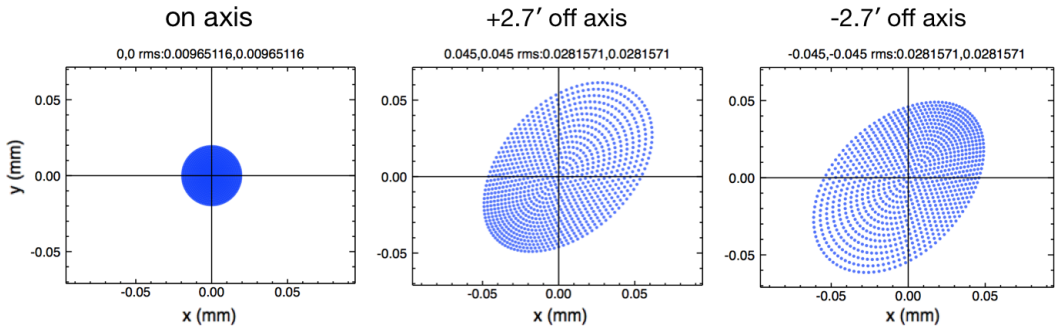

FIGURE 4.3: Spot diagrams generated assuming a 10μm wavelength point source, with no atmospheric seeing, on-axis and $\pm 2.7'$ off axis. The x- and y-axes are mm in the focal plane, where 0.11mm $\sim$ 4.4 arcsec.

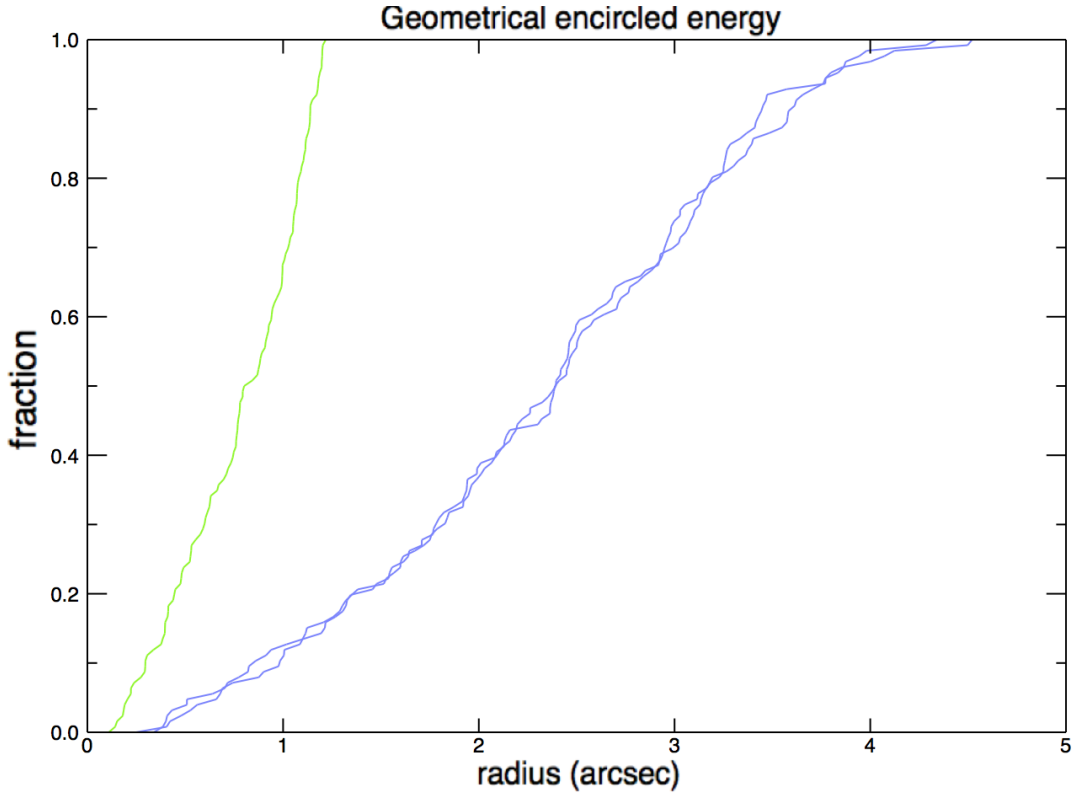

FIGURE 4.4: The geometrical encircled energy for, from left to right, on-axis and $\pm 2.7'$ off-axis rays for a wavelength of 10μm.

4.5 Mechanical Design

The overall aim of this project was to build a low cost mid-IR camera that could be constructed from commercially available components. As a result of this, we opted to translate the optical design into a lens system using tubing purchased from Thorlabs. The field lens and collimator were housed in a black anodised aluminium tube of length 114mm and diameter 50mm. The field lens was secured at the front of the lens system. The collimator was secured 76mm behind the field lens inside the tubing, using a 25mm to 50mm adjustable adaptor to allow small changes to the focus of the lens. Two custom pieces milled from low-grade aluminium were commissioned. These pieces acted to secure placement of the FLIR 13mm lens, $\sim$ 25mm from the collimator and to attach the entire prototype $\sim$ 75mm from the telescope mounting flange, roughly at the telescope focal point. When constructed, the prototype has dimensions of $\sim$ 171mm x 60mm and a weight of 0.33$\pm$0.05 kg. This makes the prototype a very compact system and suitable for mounting on 1-2m class telescopes provided there is a sufficient counter-balance. The assembly can be seen as modelled in figure 4.5. Individual components are identified and their respective manufacturer and part numbers are listed. A photograph of the instrument assembly can be seen in figure 4.6.

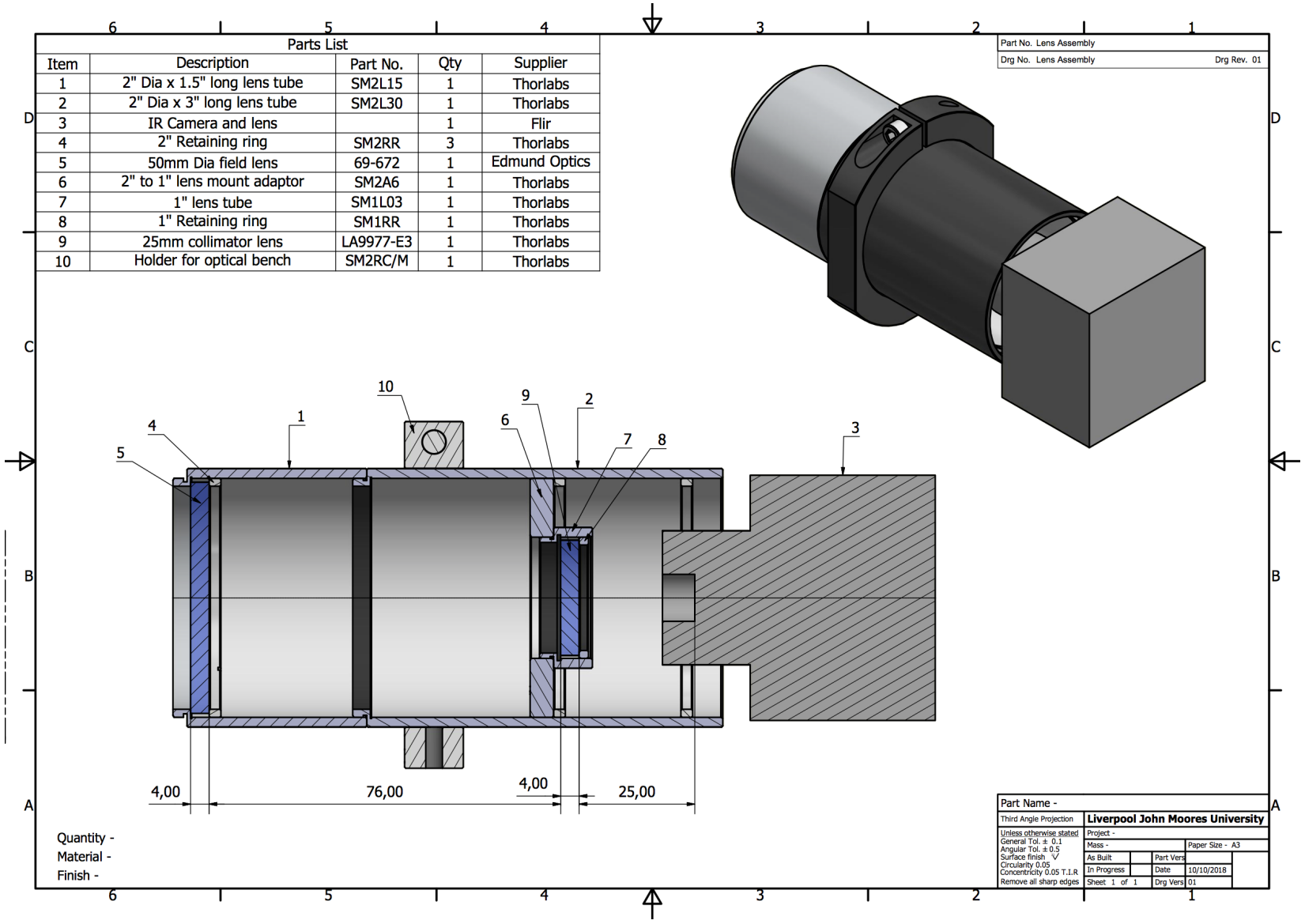

FIGURE 4.5: CAD model of the instrument assembly, with all parts identified and listed against their respective supplier and part number. All measurements are in mm. Image acknowledgement: S.Bates, Engineering Manager for the LT.

FIGURE 4.6: Photograph of the assembled prototype camera.

As the LT is a fully robotic system, remote access to the instrument was essential. The FLIR Tau 2 is an OEM camera core with only low-level serial or parallel data outputs via a high-density connector. In this configuration there is no internal command set for the system. To obtain data from the camera using a PC, an adapter board is required that can translate this low-level connection into a more convenient interface like USB. For this purpose, a Teax ThermalCapture Grabber USB module was installed on the back of the FLIR system which provides a USB2.0 connection to the camera. When paired with a Beelink J45 Mini PC running Xubuntu these components allowed for remote control of the instrument when accessed through the LT local access network.

Teax provide a C++ API with functions to establish a connection to the camera, initialise image acquisition and adjust basic parameters. These commands were used to design software to collect data by downloading images and saving them to FITS files with headers populated with basic timestamps (see code B.2 in appendix A). This software is wrapped in a bash script (see code B.1 in appendix A) to run simultaneously alongside a Python script which reads and displays a live feed (delayed by $\sim$ 1 second) of observations (see code B.3 in appendix A). This was beneficial when deploying the prototype to be able to determine parameters such as the optimum focus of the secondary mirror and telescope pointing during operation. A live feed also allowed for manual nodding of the telescope which was important for centring calibration sources and mapping non-sidereal, non-point sources (e.g.. the moon).

4.6 Calibration

To approximate read-out values $(x, y)_T$, as un-scaled counts we have assumed the following relation, based on the Stefan-Boltzmann equation:

$$\text{counts} = (x, y)_T^4. \tag{4.10}$$

The prescription of the optical system (see table 4.1) records an image space f/ratio of $\sim$ f/1.7. To correct for the difference between this and the raw imaging system using the supplied camera lens (with f/1.25), a scaling factor of 1.85 is introduced, where:

$$\left(\frac{f_1}{f_2}\right)^2 = 1.85 \tag{4.11}$$

For the purpose of testing the prototype, and due to the LT not being optimised for IR observations, we were unable to deploy chopping/nodding techniques to remove sky contributions. Sky background frames were taken prior to observations of point sources. However, for extended sources (i.e. the moon), background reduction occurred post-observation, during the data reduction stage.

Gaussian maps were used to 'flat field' observations. This is a simple correction for the large-scale variations across the detector (e.g. arising from vignetting or spatially-heterogeneous variation in sensitivity) but does not correct for the effects of FPN. For each exposure $S_{x,y}$, a Gaussian map was created by smoothing with a 2D Gaussian function with $\sigma = (15, 15)$ pixels. The resulting Gaussian map, $g_{x,y}$, was applied to the data as follows:

$$I_{x,y} = \frac{S_{x,y}}{g_{x,y}} \cdot \bar{S}_{i,j} \tag{4.12}$$

where $I_{x,y}$ is the corrected exposure and $\bar{S}_{i,j}$ is the mean value inside the imaging aperture. The mean of the entire frame $\bar{S}_{x,y}$ is not used to re-scale values as the outer aperture contains no sky signal and is likely to skew values towards telescopic background. Figure 4.7 illustrates this process; (a) is a raw observation of the eclipsing moon. There is considerable large scale structure present in the FOV that can be seen as large light and dark regions. This type of structure is characteristic of that found in all our un-reduced data. (b) is the unique Gaussian map created from (a). (c) is exposure (a) after it has been fully reduced by applying equation 4.12.

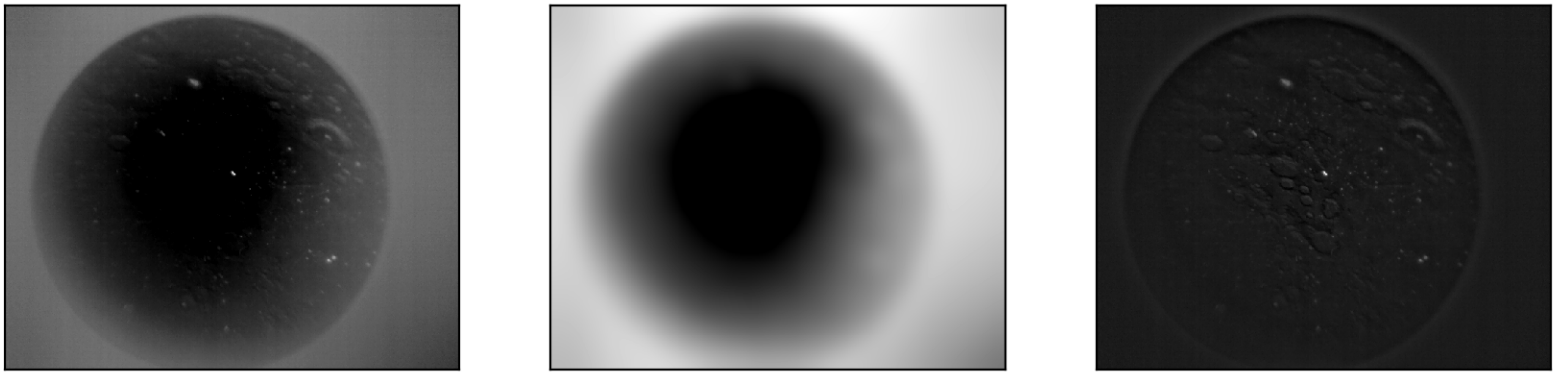

FIGURE 4.7: Observations were calibrated using Gaussian Maps to remove the large-scale structure present in the image. (a) is a raw observation of the moon during lunar eclipse, (b) is the Gaussian map produced from this exposure with $\sigma = (15, 15)$ pixels, and (c) is the result of applying equation 4.12 to the image.

4.7 Commissioning and On Sky Testing

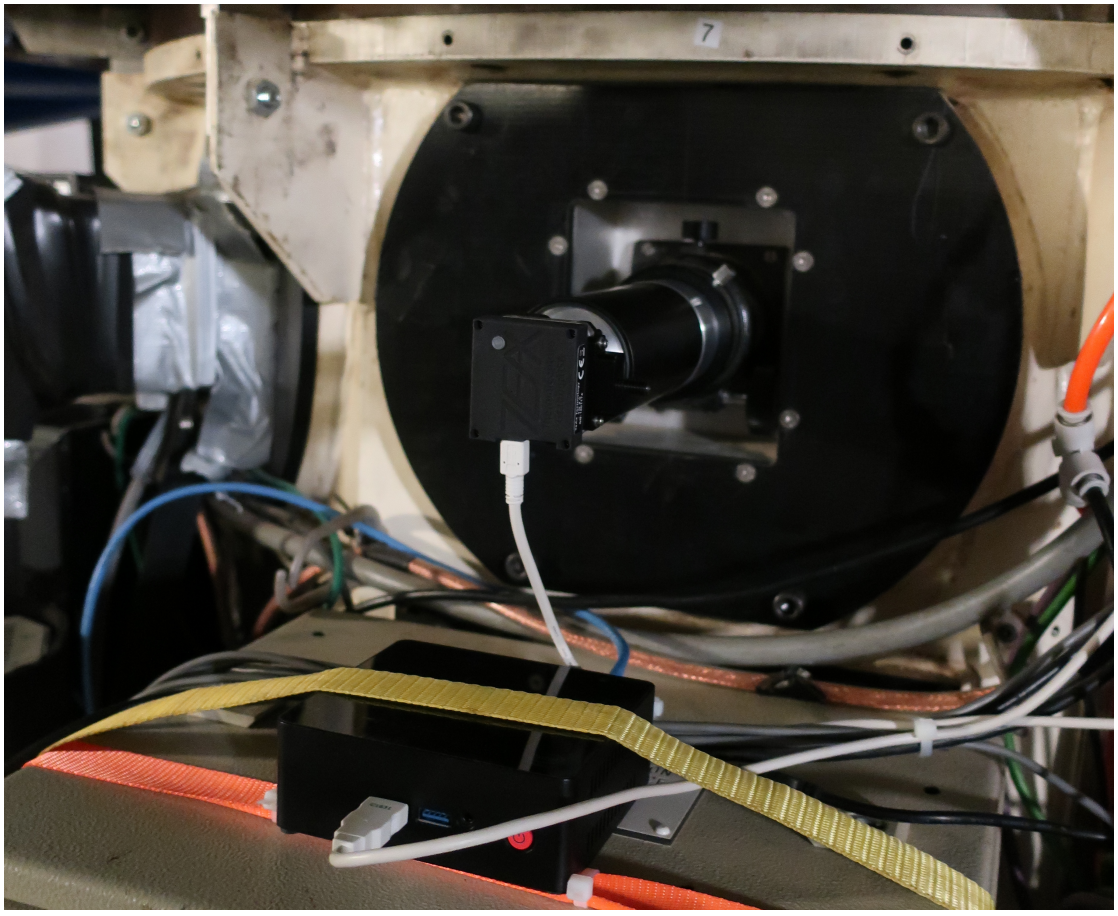

FIGURE 4.8: The prototype mid-IR camera installed on the LT.

The prototype was installed on the LT on 2019 Jan 19. It was installed at port 7 on the A&G box, replacing the now retired LOTUS instrument. Figure 4.8 shows a view of the instrument as mounted on the A&G box of the instrument. The instrument was used on-sky on three nights, on Jan 19, Jan 20 and Jan 22, with several additional nights lost to poor weather conditions.

To determine the performance of the system, observations were taken of two bright mid-IR sources; Mars and IRC+10216 (Neugebauer & Leighton, 1969). These two sources can be seen in the flat-fielded observations shown in figure 4.9.

4.7.1 Focusing the instrument

To focus the instrument, the secondary mirror was adjusted between positions -1.0 to 0.5 mm, in steps of 0.1 mm, for successive observations of Mars. Figure 4.10 shows the

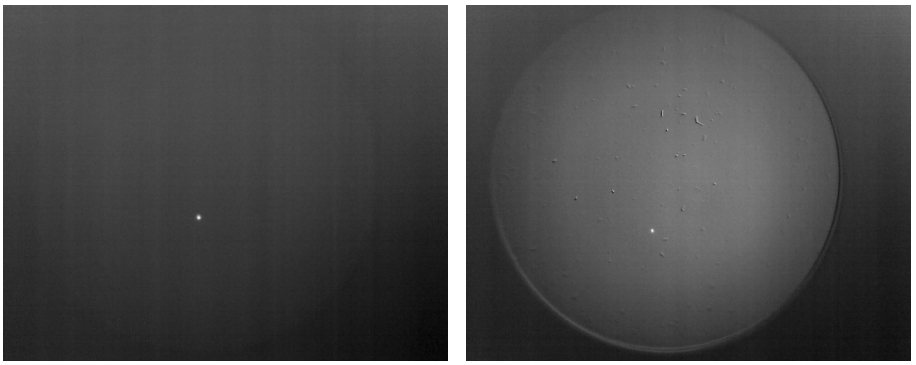

(a) Mars (b) IRC+10216

FIGURE 4.9: Observations of (a) Mars and (b) IRC+10216 taken on 2019 Jan 22. Both (a) and (b) are median stacks created from 1000 non-Gaussian corrected, sky background subtracted observations.

result of focusing the secondary on the observed full-width-half-maximum (FWHM) of Mars. The optimum position of the secondary was determined by fitting a quadratic function to the data (seen in red in figure 4.10) and obtaining the minimum of the parabola at a focus position of $\sim -0.2\,\mathrm{mm}$.

4.7.2 Photometric Accuracy and stability

Offsetting the telescope pointing during our observations of Mars confirmed a pixel scale of $0.75''$ per pixel for the system. IRC+10216 was observed at a FWHM of ~ 2 pixels, confirming that the optical design allows diffraction-limited imaging. Figure 4.11 shows the variation in FWHM and counts of IRC+10216 over 348 seconds, taken shortly after a flat field correction to reduce the effect of thermal drift (see section 3.3.2). The $\sim 10\%$ variability in these observations can be attributed to the sky variations during observing and represents a crude estimate of the photometric stability.

The photometric accuracy was tested by comparing known and observed values of the 12 micron flux for Mars and IRC+10216. A 12 micron flux of $4.75\times10^4\,\mathrm{Jy}$ was obtained for IRC+10216 from the IRAS catalogue of point sources (Beichman et al., 1988). IRC+10216 is a known variable source. However, for this purpose we approximated the 12 micron flux as constant. The apparent brightness of Mars depends on the sub-Earth longitude of the illuminated disk (Mallama, 2007) and therefore varies seasonally and as a function of viewing angle. To determine an approximate value of 12 micron flux

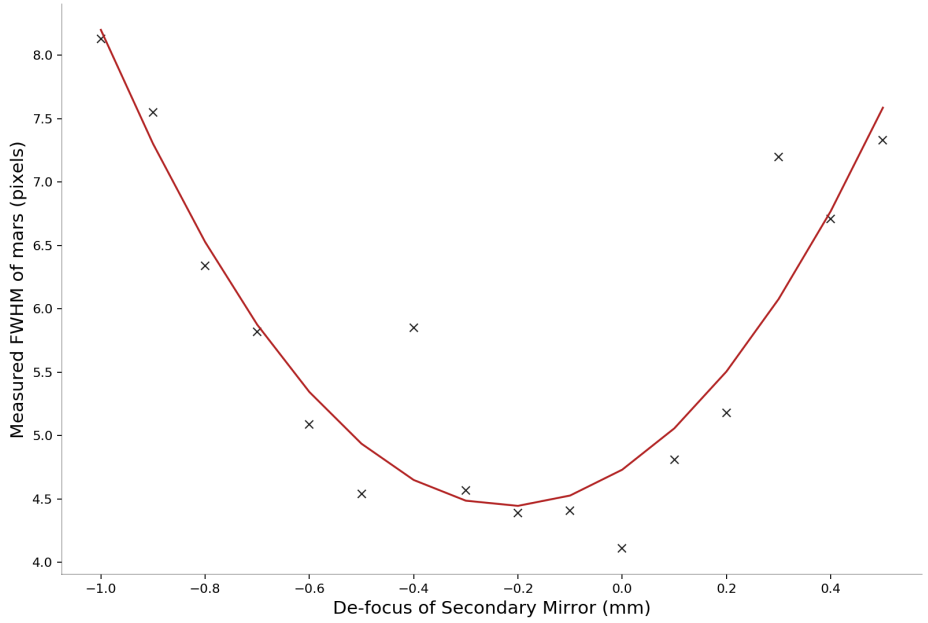

FIGURE 4.10: The observed FWHM of Mars with different positioning (i.e. focus) of the secondary mirror. Observed values are recorded in black. The red line represents a quadratic fit to the data with the following parameters a = 6.11817224, b = 2.64982141, c = 4.73183299. The optimum focus position of the secondary is represented by the minimum of the parabola.

on our observing date for Mars, we obtained brightness temperatures at 12 and 450 microns from models derived by Wright (1976), and implemented in the FLUXES routine developed for JCMT (Dempsey et al., 2013). These brightness temperatures were then used to calculate a 12 micron flux of 76147.5 Jy using the following equation:

$$S_\nu = \frac{2h\nu^3}{c^2} \frac{\Omega_p}{exp(\frac{h\nu}{kT_\nu}) - 1}, \tag{4.13}$$

where ν is the observing frequency in GHz, S_ν is the integrated flux density of Mars, Ω_p is the solid angle subtended by Mars from Earth, T_ν is the brightness temperature and h, k and c are the Planck constant, Boltzmann constant and speed of light respectively. The flux ratio of IRC+10216/Mars for catalogue and observed values were calculated as 0.62 and 0.72 respectively. These values are consistent with a 15% uncertainty on photometric accuracy with the caveat that both sources are known to be variable and without a measure of the extent of their variability, we cannot comment on whether a 15% uncertainty is acceptable.

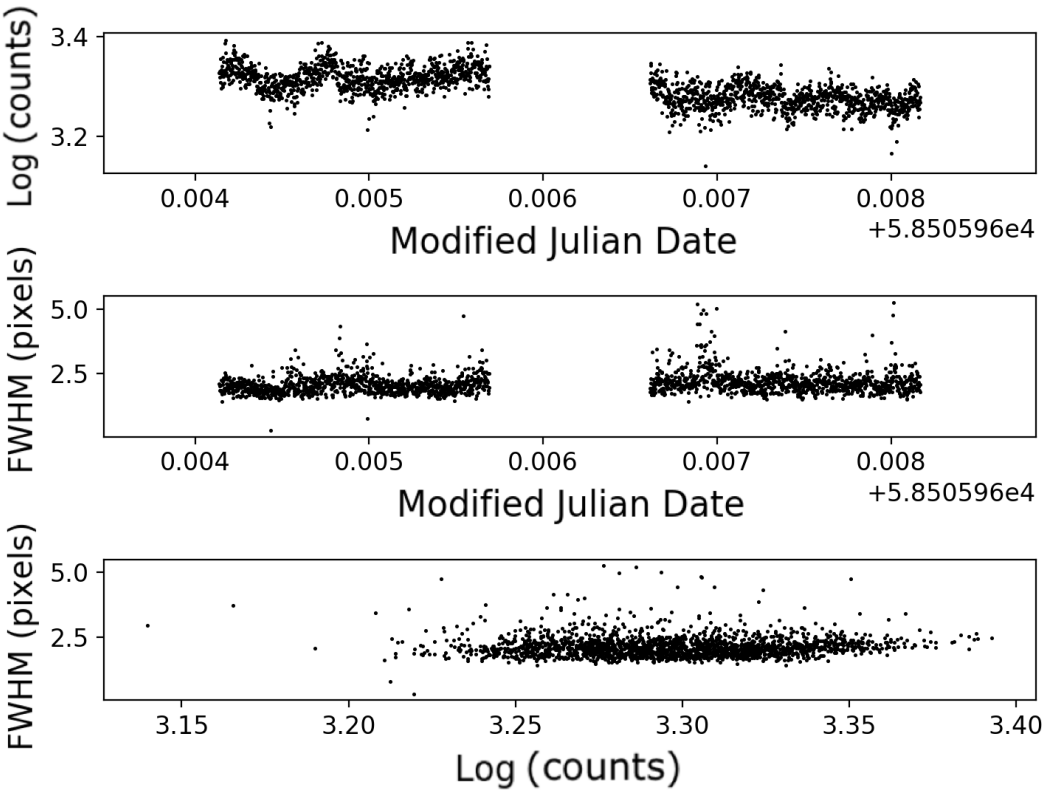

FIGURE 4.11: The variation in background-subtracted counts and FWHM for observations of IRC+10216 taken on 2019 Jan 22. Observations appear reasonably stable, with $\sim 10\%$ variability (determined from the RMS of the light curve) attributed to the highly variable seeing conditions on this date, although there is no formal correlation between FWHM and counts (with a Spearman rank coefficient value of -0.03).

4.7.3 Sensitivity

Our observations of IRC+10216 were used to determine the sensitivity of the system. Measurements of the object were obtained using apertures with a 1.5 pixel radius and sky background counts were estimated for subtraction using an annulus of 1.5-2 pixel radius. These apertures were selected using a curve of growth technique to maximise SNR. Over a short duration ($\sim$ 10 seconds) of exposures, which appear to be unaffected by sky variation, IRC+10216 has SNR=21. Assuming our observations are sky noise dominated, then SNR will be proportional to source flux. For a single exposure (with exposure time t $\sim$ 1/9 seconds), a 3σ detection would correspond to a background-subtracted flux 7 times fainter than those observed in figure 4.11, i.e. $\sim 7 \times 10^3$ Jy. In theory, the sensitivity can be improved by stacking exposures, with a 60 second exposure stack having a predicted 3σ detection for a source 163 times fainter than IRC+10216, i.e. $\sim 3 \times 10^2$ Jy.

Using the IRAS point source catalogue v2.1 (Beichman et al., 1988) we can see that reaching this sensitivity limit would make a further ~ 163 extra-solar sources observable with the current instrument setup. Given the IRAS point spread function at $12\mu m$ corresponds to a FWHM of $< 16''$ some of these sources may be extended and therefore our calculation is an estimate of the upper limit of the number of observable mid-IR sources. In practice, without a nodding/chopping system, this limit is unlikely to be reached with the current setup, and for observations of bright asteroids, such as Ceres, it would have to be improved by a factor of two (Müller & Lagerros, 2002).

4.7.4 Lunar Eclipse Observation

Observations of the Jan 21, 2019 lunar eclipse and full moon ($\pm$ 2 days) were taken to obtain measurements of surface temperature and its variability during a lunar eclipse. The eclipsed lunar disk has been well studied since the first observations of thermal anomalies in 1960 (Shorthill et al. 1960; Saari & Shorthill 1963; Shorthill & Saari 1965; Saari et al. 1966; Fudali 1966; Hunt et al. 1968; Shorthill & Saari 1972; Winter 1972; Fountain et al. 1976; Price et al. 2003; Lawson et al. 2003).

The general thermophysical properties of the lunar surface have been well mapped in the mid-IR (see Paige et al. 2010; Vasavada et al. 2012 and references therein). The low thermal conductivity of the fine-grained regolith that makes up the upper ~ 0.02m surface layer, results in extreme diurnal temperature variations. During lunar daytime, illuminated surfaces are close to radiative equilibrium and high surface temperatures (approaching 400K) are a result of incident solar flux. Comparatively, during a lunar eclipse or during lunar nighttime, with no incident solar radiation and no atmosphere to trap heat, surface temperatures drop by $\sim$ 300K. The Moon also shows significant topographic heterogeneity. This results in high spatial variation in the thermophysical properties of lunar surface features.

A simple temperature model for the lunar surface (equation 4.14), derived by Shaw et al. (2015), can be used to estimate the expected temperature of the lunar surface, T_m, at any given time where E_m is the spectrally averaged solar irradiance at the surface (adjusted for seasonal variations in Earth-Sun distance). The subsolar point, where lunar latitude angle $\varphi = 0$, can be used to approximate the maximum temperature of the lunar surface, T_{max}. Latitudinal and diurnal variation in T_m across increasing lunar radius is mostly

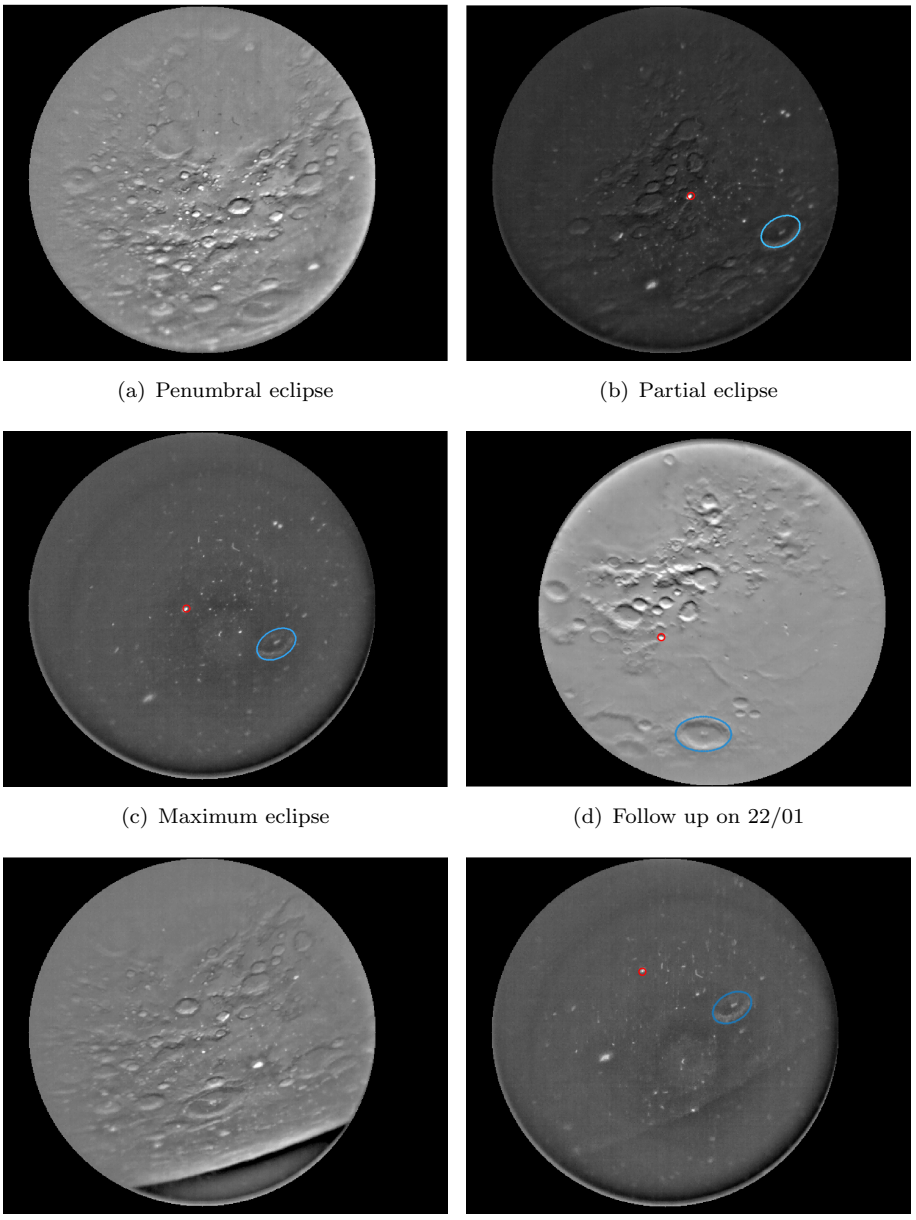

(a) Penumbral eclipse (b) Partial eclipse

(c) Maximum eclipse (d) Follow up on 22/01

(e) Edge of lunar limb during penumbral eclipse (f) Edge of lunar limb at Maximum eclipse

FIGURE 4.12: Observations of the moon during the lunar eclipse on 2019 Jan 21 and follow-up of the full Moon on 2019 Jan 22. Lunar limb observations highlight the change in temperature between early and maximum eclipse. Where possible, the locations of two craters; Bellot (red) and Langrenus (blue), have been indicated. The presence of dust on the field lens can masquerade as bright features on the lunar surface, this can be seen very clearly in image (f) where bright features lie beyond the limb. As these dust contaminants remain fixed in position in the FOV, genuine bright features have been confirmed through their movement with the lunar surface due to poor non-sidereal tracking of the telescope. For scale, one pixel $\sim$ 4 km on the lunar surface.

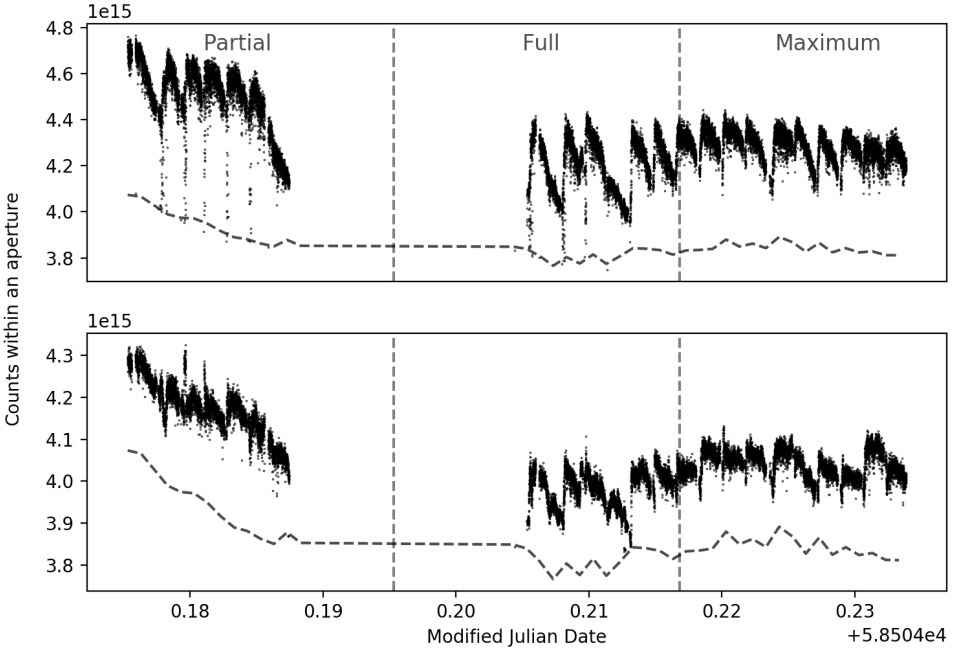

FIGURE 4.13: Observations of Bellot (top) and Langrenus (bottom) during the lunar eclipse on 2019 Jan 21. Count values are maximum values within an aperture. The background counts are plotted as the dashed lines. A large period between partial and full eclipse went unobserved due to a sudden spike in humidity that halted observation. The periodic fluctuating pattern present in all curves is thermal drift. This is described in more detail in chapter 3.

controlled by angular distance to the subsolar point.

$$T_m(\varphi) = \left(\frac{E_m \ \cos(\varphi)}{\sigma}\right)^{1/4} = T_{max} \ \cos^{1/4}(\varphi). \tag{4.14}$$

Using equation 4.14, we can calculate that the expected maximum temperature of the lunar surface on the 19th and 22nd of January 2019, two days either side of the full moon, is 396.8K. The radiation incident on the Liverpool telescope can be modelled as:

$$I(\phi_z, \lambda) \ = \ I_0 \ e^{-AM(\phi_z)\cdot\tau_N(\lambda)} \tag{4.15}$$

where $AM(\phi_z)$ is the airmass for a given zenith angle and $\tau_N(\lambda)$ is the normal optical thickness. $\tau_N(\lambda)$ is dependent on the atmospheric transmission for a given wavelength. For mid-IR wavelengths, the theoretical atmospheric transmission at normal incidence ranges from 0.70 to 0.75 (Vollmer & Möllmann, 2012). From equation 4.15, equation 4.10 and the Stefan-Boltzmann relation (see equation 1.9) we obtain an expected value of observed lunar surface temperature of 362.9K. Our observations on these dates recorded

an average temperature of 350 ± 6 K. This slightly lower value is likely to be due to losses in the telescope and instrument optics.

Observations of partial, full and maximum phases of the lunar eclipse were taken (see figure 4.12). Significant heat loss occurs prior to this, during the penumbral phase (Vollmer & Möllmann, 2012). Unfortunately, we were unable to obtain enough sequential observations of the same region due to poor weather conditions to include these exposures in our analysis.

Visually, the change in lunar surface from partial eclipse onwards is quite significant. As the eclipse reaches totality, the different thermophysical properties of features of the lunar surface become very apparent. During this time, many features become unobservable. However, the hundreds of thermal anomalies that were first seen by Shorthill et al. (1960) appear as very bright 'hot spots' during partial eclipse and remained bright throughout totality. During our observations, we focused on several lunar features in the mare Fecunditatis region (7.8°S, 51.3°E). Analysis was conducted for two craters; Bellot (12.49°S, 48.2°E) and Langrenus (9°S, 62°E). Langrenus is an early Copernican crater with a faint ray pattern, a high albedo, a central peak of brecciated bedrock and a moderate thermal anomaly (Shorthill & Saari, 1972). Bellot is a smooth, dark, haloed crater with a high albedo, likely to be a result of freshly exposed, brecciated rock (Elston & Holt, 1967), resulting in a significant thermal anomaly.

To conduct data analysis for $\sim$ 30000 eclipse exposures we employed a semi-automated feature tracker to determine the approximate centre of the brightest source, Bellot. The coordinates of Bellot were then used to anchor the movement of other features in the field of view. Each exposure was reduced, and raw values approximated as counts, as described in section 4.6. Counts for each feature were obtained by taking the maximum value from apertures containing each feature. A circular aperture with 5 pixel diameter was used for Bellot and an elliptical aperture with 30 pixel semi-major axis, and $\pi/3$ rotation for Langrenus.

Analysis of observations during partial eclipse showed approximate temperature loss rates of 0.98K per minute for Bellot and 0.50K per minute for Langrenus. Comparatively the average heat loss in regions with no 'hot spots' or crater features occurred at a rate of 0.26K per minute. Figure 4.13 are count measurements of Bellot (top) and Langrenus (bottom) during the eclipse. The dashed line in both plots represents the background

counts recorded from an aperture with 10 pixel diameter in a region of mare with no crater features. The apparent plateau in all three curves is likely to be a result of telescope and system emissions limiting the range of temperatures that can be recorded.

The low conductivity of the upper lunar regolith results in little exchange of energy between warmer subsurface and surface layers. As a result, the lunar surface cannot maintain surface temperatures without incident radiation from the Sun. Coupling this fact with the high emissivity of the lunar surface around full moon ($\epsilon \sim 0.97$, Shaw et al. 2015), we can approximate that the energy required ΔE, to maintain the lunar daytime temperature, T, is equal to the energy release over time $\mathrm{d}t$, during eclipse:

$$\Delta E = \frac{mc\Delta T}{\mathrm{d}t} = \epsilon\sigma T^4 \tag{4.16}$$

where m is mass, c is the specific heat capacity and σ is the Stefan-Boltzmann constant. We can derive the following differential equations from equation 4.16 for a temperature change of T_1-T_2 in time t_1 to t_2:

$$\int_{T_1}^{T_2} \frac{1}{T^4}\,\mathrm{d}T = \int_{t_1}^{t_2} \frac{\epsilon\sigma}{mc}\,\mathrm{d}t \tag{4.17}$$

The bulk density of the lunar regolith sharply increases at a depth of $\sim 0.02\,\mathrm{m}$. So, solving equation 4.17 for a $1\,\mathrm{m}^2$ area, we can calculate a naive estimate of specific heat capacity, c, for different regions in our observations. For Bellot and Langrenus, we calculate a specific heat capacity of 2.3 and $4.1 \pm 0.02\,\mathrm{kJ/kg/K}$, respectively. There is a discrepancy between our naive estimates and the specific heat capacity of the lunar regolith quoted in the literature. Analysis of the Apollo 14, 15 and 16 samples recorded specific heat capacities of between 0.21 and 0.8 kJ/kg/K (Hemingway et al., 1973). More recent studies of sintered Australian Lunar Regolith Simulant (ALRS-1) have found values of up to 1.63 kJ/kg/K (Bonanno et al., 2015). The disgreement between these values and our own could be largely in part due to the Apollo samples being collected from regions different to ours. This would be applicable to the values obtained from ALRS-1 as it is created to have a chemical composition comparable to the Apollo 12 samples and not the Apollo 14, 15 and 16 samples. We also make several assumptions in our calculations that may not be applicable to our crater regions. The quoted emissivity and depth values are approximated across the entire lunar surface, but these are known

to vary with region age and regolith material. It is also possible that the shape of both craters contributes to the storage of heat during eclipse.

4.8 Summary of Chapter

In this Chapter a prototype instrument which adapts mid-IR uncooled microbolometer technology for use on ground-based telescopes is presented. For this purpose, additional optics were designed to rescale the image onto the detector to optimally sample the diffraction limit. The instrument was designed and built from commercially available units, at a low cost. The instrument was tested on the LT over 3 days in 2019 Jan. A small programme of observations of solar system and stellar objects was conducted. From these observations a plate scale of $0.75''$ per pixel was confirmed and the photometric stability was measured to be $\sim 10\%$. A 3σ limiting flux of $\sim 7 \times 10^3$ Jy for a single exposure was recorded, this corresponds to a sensitivity limit of $\sim 3 \times 10^2$ Jy for an integration time of 60 seconds.

Observations of the Moon during a lunar eclipse are presented. In general, the overwhelming sky and telescopic emission limited observations to very bright mid-IR sources and made data reduction difficult. The germanium foreoptics have significant transmission into the wings of the N-band. As a result, there is likely excess sky noise limiting our observations which could be improved with the inclusion of a narrow bandpass filter. In Chapter 5 the prototype is further developed to include a chopping/nodding technique and to test whether the stability and sensitivity of the system can be improved to increase the number of observable sources.

Chapter 5

Part III Astronomical application in ground-based observing: Experimenting with Chopping and Nodding for Background Reduction

5.1 Overview of Contents

This Chapter describes an upgrade to the prototype instrument presented in Chapter 4 to include a chopping mirror in the foreoptics. The results from a week-long programme of observations on the Carlos Sanchez Telescope (TCS) operated on the island of Tenerife by the Instituto de Astrofísica de Canarias (IAC) (Jones, 1978) at Observatorio del Teide are presented. These observations were conducted to test the chopping mirror, implement nodding, and determine if the improvements increase the sensitivity of the instrument.

Time on the TCS was awarded to an observing proposal written by myself ($\sim$ 1 week), and submitted with Prof. J. Knapen as the PI (IAS staff required as PI). The optical

design ($\sim$ 2 weeks), mechanical construction ($\sim$ 4 weeks), software design and construction ($\sim$ 4 weeks), data collection ($\sim$ 1 week) and data analysis ($\sim$ 8 weeks) was all done by myself. The mechanical design was translated into CAD by Mr S. Bates (engineering manager for the LT) from the optical design and under my guidance of the desired optical and mechanical components ($\sim$ 2 days). Commissioning and de-commissioning on the telescope ($\sim$ 2 days) was done by the TCS telescope engineers however, all in situ changes to the mechanics of the instrument were done by myself. Telescope operation was conducted by the on-site support astronomer and telescope operator for the first 2 nights of observation, and by myself for the remaining time. All works were conducted under the guidance of Prof. I. Steele (Telescope Director).

5.2 Optical Design

The basic instrument is described in detail in chapter 4. Building on this work, our goal was to improve instrument sensitivity, with the integration of a chopping mirror to the existing foreoptics, comprised of a 50mm diameter field lens and 25mm diameter collimator lens with 76mm separation. In addition to this, any further testing was to be carried out on the TCS which is optimised for infrared imaging. The TCS is an f/13.8 telescope with a Dall-Kirkham design. The TCS is comprised of a thin 1.52m concave ellipsoid primary mirror and an undersized 0.37m convex spherical secondary mirror, with minimal baffling. These features act to lower the thermal background compared to a conventional optical telescope such as the LT. The TCS has a 10 μm diffraction limit of 1.66 arcsec. To include a chopping mirror in the foreoptics and determine the plate scale and image-quality for use on the TCS, we conducted a ray tracing analysis for on- and off-axis light. The updated design can be seen in Fig. 5.1.

Spot diagrams for on-axis and $\pm\,2.7'$ off-axis rays show no deviation from previous spot diagrams (see explanation and figure 4.3 in chapter 4), with off-axis aberration still present. With the chopping mirror at 45°, the system has an 80% geometric encircled energy (GEE) diameter of <1.61 arcsec for on-axis rays and <3.55 arcsec for $\pm$ 2.7′ off-axis rays. Assuming a 2D Gaussian profile, this corresponds to a spatial FWHM of $<$ 1.1 and $<$ 2.3 arcsec for on- and off-axis rays respectively. From this, we predicted that 2 pixels would sample the diffraction limit, with a plate scale of 0.96″, for on-axis rays, with slightly worse performance off-axis. The imaging field of view (FOV) is still

a circular aperture of 500 pixel diameter. As discussed in chapter 4 we had no access to the optical prescription of the 13mm focal length lens and the reduction in FOV is due to the uncertainty of an aperture stop within the camera system.

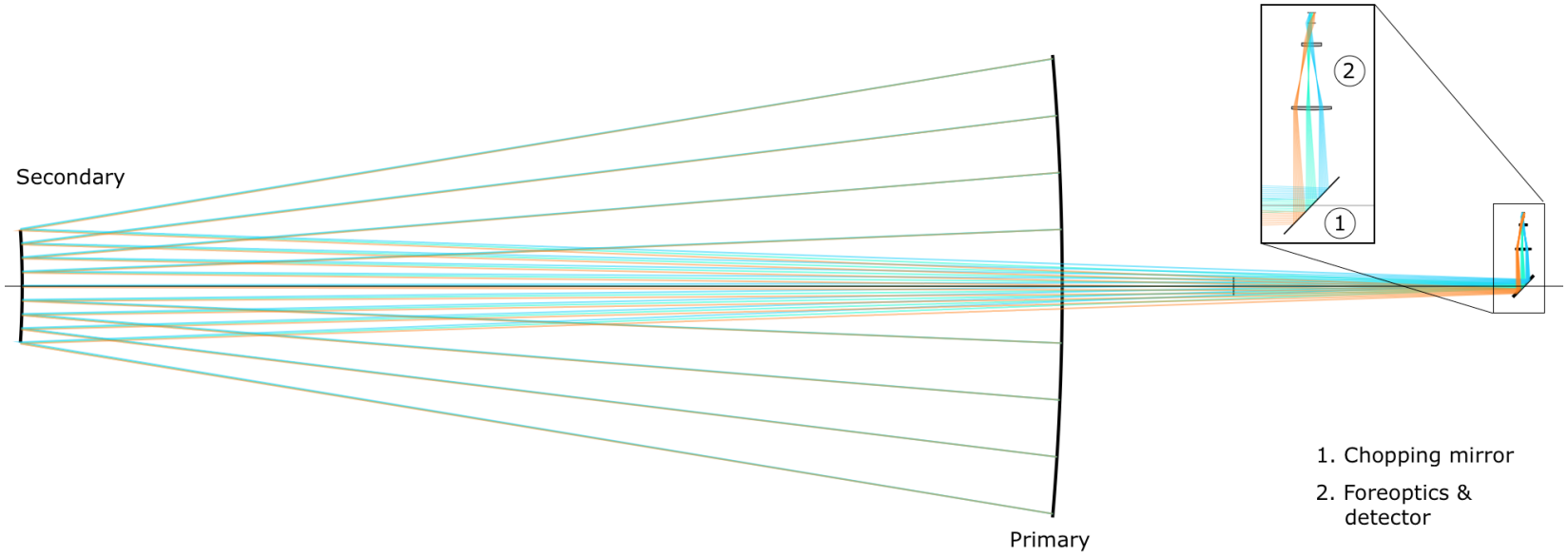

FIGURE 5.1: Ray trace of the TCS with the instrument mounted for on- and off-axis beams of 2.7 arcmin. The zoomed in portion shows how the chopping mirror acts to direct the rays perpendicular to the telescope optical axis and onto the 50mm diameter field that sits at the front of the existing foreoptics (see chapter 4).

Comment	Type	Radius of Curvature	Thickness	Glass	Semidiameter
Source	Standard	inf	inf		0.000
Primary	Asphere	-9134.3900	0.0000	MIRROR	762.000
	Standard	inf	-3429.000		762.000
Secondary	Asphere	-2925.0000	0.0000	MIRROR	185.500
	Standard	inf	3429.000		101.600
	Standard	inf	565.150		49.995
	Standard	inf	1021.650		29.993
	Break	inf	0.000		30.764
	Asphere	inf	0.000	MIRROR	50.000
	Break	inf	0.000		23.626
	Standard	inf	-120.000		23.626
Field Lens 50mm	Standard	-300.3900	-4.000	GERMANIUM	25.000
	Standard	inf	-76.000		25.000
Collimator 25mm	Standard	-225.0000	-4.000	GERMANIUM	12.500
	Standard	inf	-25.000		12.500
Lens	Paraxial	inf	-13.000		5.200
Detector	Standard	inf	0.000		5.400

TABLE 5.1: Combined optical prescription of the TCS and prototype FLIR camera and chopping mirror
. All dimensions are in mm. The thickness quoted in column 4 refers to the separation between each component.

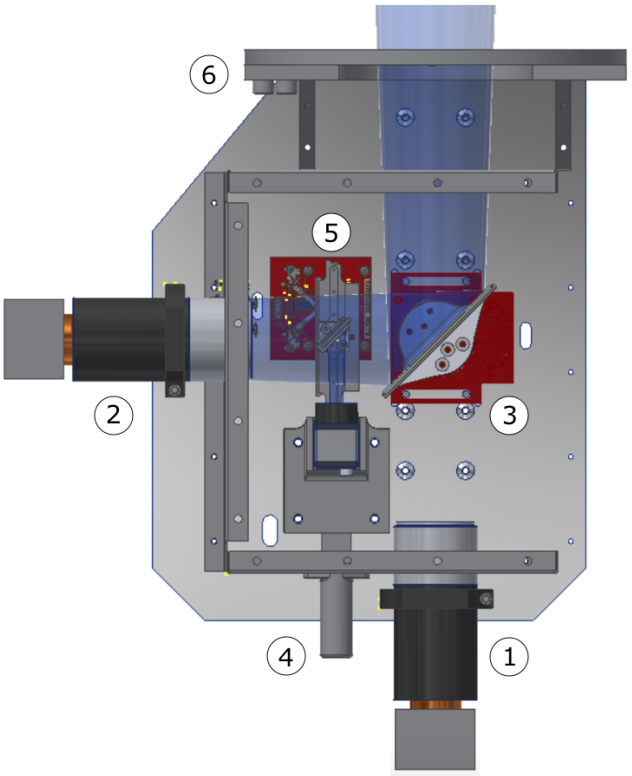

FIGURE 5.2: The mechanical design of the instrument. The main components are numbered: (1) first mount position for camera and foreoptics, (2) second mount position for camera and foreoptics, (3) chopping mirror on rotational platform, (4) Optical camera on adjustable mount for focusing, (5) deployable silver-coated mirror on sliding platform, (6) mounting plate.

5.3 Mechanical Design

We constructed the instrument as modelled in figure 5.2. The full construction can be seen with the faceplate in figure 5.3 and without the faceplate in figure 5.4. The field and collimator lenses were housed in an anodised aluminium tube of length 114mm and diameter 50mm. The camera was mounted to this tube via a custom adaptor milled from low-grade aluminium. Rather than integrate these parts into the main body of the instrument, they were left self-contained and the instrument body was designed to have two options for mounting; (1) at the straight through position, used only when the chopping mirror is removed, to aid in initial setup of the instrument, (2) perpendicular to the direction of rays entering the instrument. The Edmund Optics 75 x 100mm gold coated, 4-6λ surface flatness (reflectance R_{avg}, at 45°: $R_{avg} > 96\%$ for 3-8μm and 10-14μm, dropping to $R_{avg} > 75\%$ for 8-10μm) chopping mirror (3) sits atop a Thorlabs

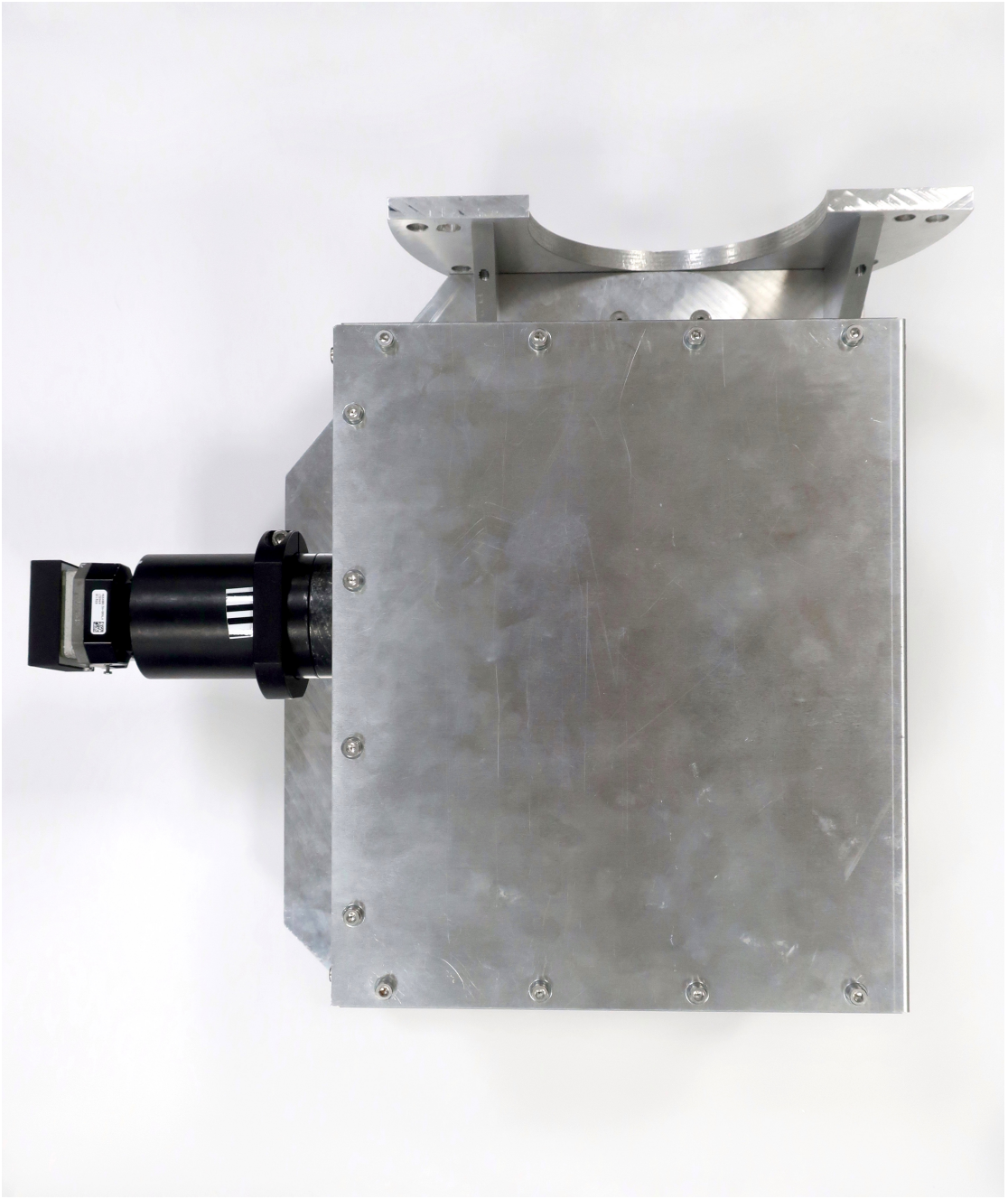

FIGURE 5.3: Photograph of the instrument, with the faceplate. The detector and foreoptics as described in chapter 4 can be seen protruding from the instrument on the left. The mounting plate that was custom milled for attachment to the TCS is visible at the top of the instrument.

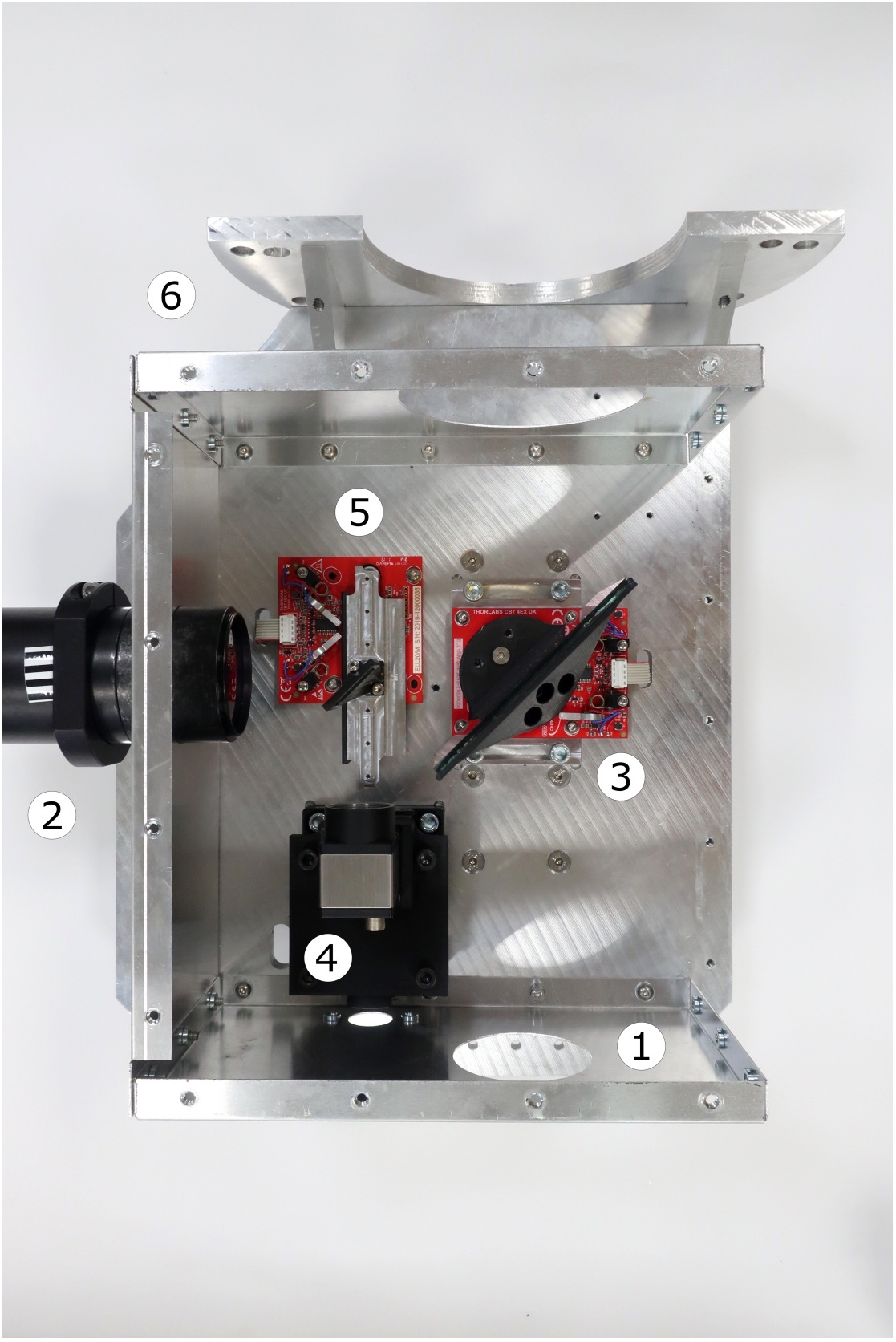

FIGURE 5.4: Photograph of the interior of the instrument, with the face plate removed. The main components are numbered: (1) first mount position for camera and foreoptics, (2) second mount position for camera and foreoptics, (3) chopping mirror on rotational platform, (4) Optical camera on adjustable mount for focusing, (5) deployable silver-coated mirror on sliding platform, (6) mounting plate.

ELL18K 50.0mm piezoelectric rotation stage which operates with a home angle of 45 ° and directs the light in the perpendicular direction onto the field lens. The rotation stage has a communication speed of 9600 baud for 8-bit data, a maximum velocity of 430 $°s^{-1}$, a homing repeatability of 0.25 ° and a bi-directional positional repeatability of 0.05 °. A 1 ° angular tilt of the chopping mirror results in a relative chop size of $\sim$ 44 pixels on the detector and hence 22 arcseconds on sky. A Thorlabs DCC3240M optical CMOS camera (4) was included to provide the possibility of dual wavelength data acquisition or to act as a guide camera. This can be deployed with a 25.0 mm x 23.5 mm x 1.0 mm polished germanium optical window acting as a dichroic on a Thorlabs 60 mm Piezo Elliptical Linear Stage (5). We used low cost, rapid prototyping techniques including 3D printing to create mounts for the optomechanical components. All parts were installed on a 1cm thick aluminium baseplate with a folded aluminium cover. The instrument was installed at $\sim$ 0.84 m from the TCS mounting flange using the mounting plate (see (6) in figure 5.4). When constructed, the prototype has dimensions of $\sim$ 35x40x20 cm and a weight of 6 $\pm$ 0.05 kg.

When paired with a Beelink J45 Mini PC running Xubuntu, all parts of the instrument could be controlled remotely. Software was written to trigger data acquisition with each exposing period lasting for $\sim$ 2 minutes, with images downloading at a frequency of $\sim$ 9Hz. The Python Pyserial module was employed to communicate with the mechanical platforms. A python code was written to control the rotational platform for chopping (Appendix B.4). Upon establishing a connection to the platform, the code sends a homing command. Once successfully homed, the code initialises a sequence of moving the platform forwards and backwards by 0.5 ° with a 1 s separation. The time at the beginning and end of every chop throw is recorded in a .csv file. This code and chop timestamp file were integrated into the exposing routine for smooth operation of the instrument and to aid in identifying mirror position for each exposure. A complementary python pipeline (Appendix B.5) was designed to reduce the raw data. This pipeline sorts input observations into chopped and unchopped subsets using the timestamp file. Any observations taken while the chopping mirror is in motion are identified and removed. The *nth* observation in a subset of chopped exposures is subtracted from the *nth* exposure in the previous unchopped subset. The resulting chop subtracted observations are then mean stacked to output one master observation for each exposing period.

5.4 Commissioning and On Sky Testing

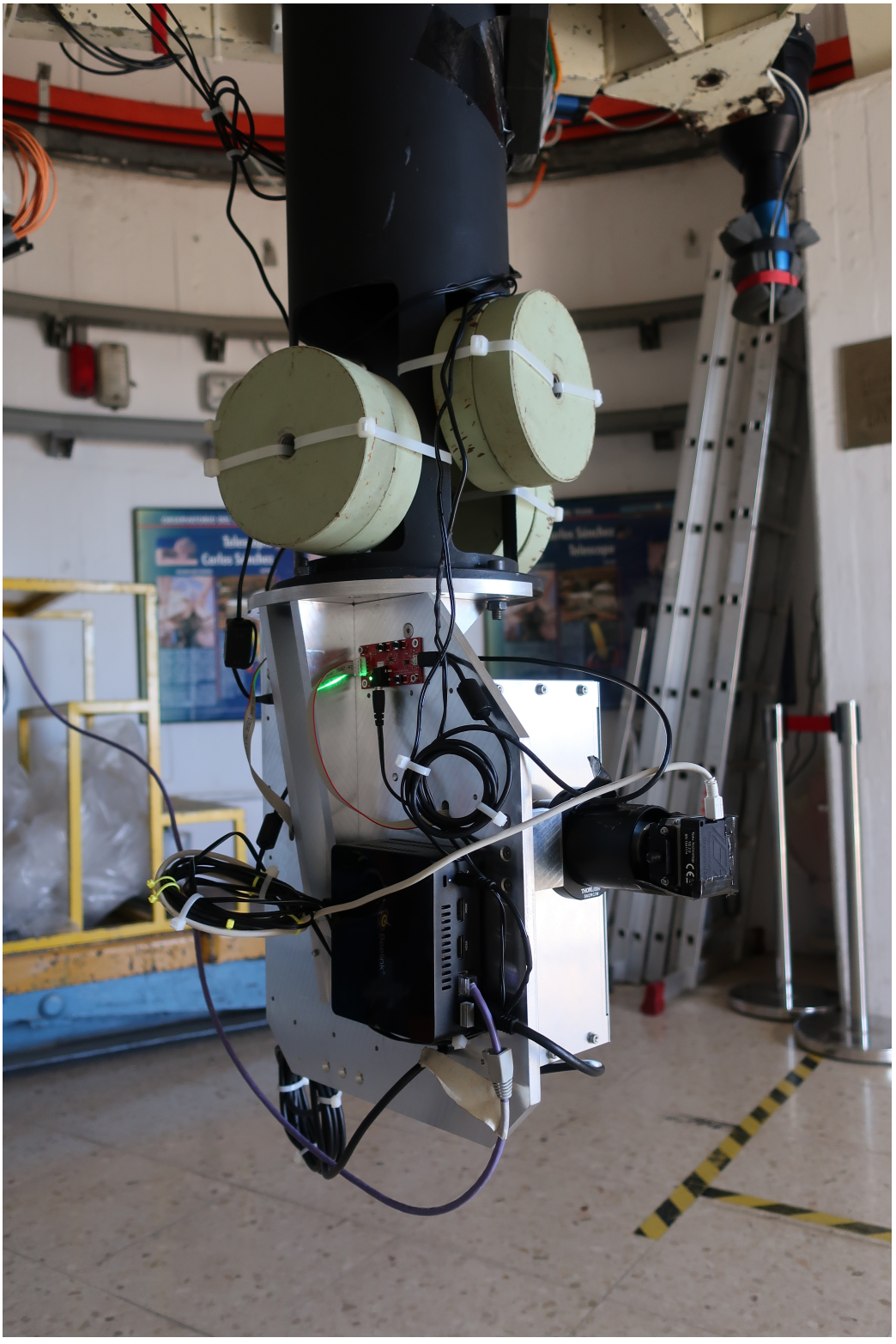

FIGURE 5.5: The instrument as installed on the TCS in September 2019. In view is the backside of the instrument, where the Beelink CPU and interface boards are mounted. The detector and foreoptics described in chapter 4 can be see protruding on the right side of the instrument.

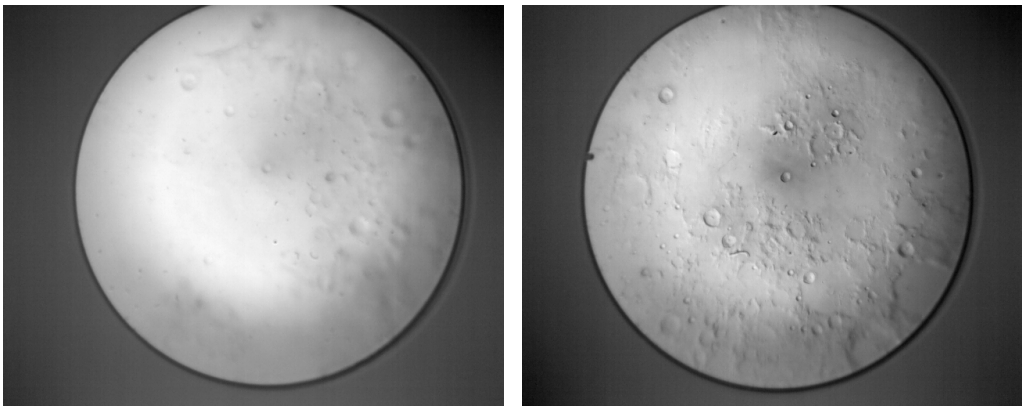

(a) 40900μm (b) 40500μm

FIGURE 5.6: First light observations of the lunar surface. These observations were used to focus the instrument. The focus was determined by making small adjustments to the focus of the secondary mirror. Figure (a) is the first observation, with the focus set at 40900μm. Figure (b) is a focused observation, with the focus set at 40500μm.

The instrument was installed on the TCS on 2019 September 10. It was deployed and tested over eight nights, with three nights (September 15, 16 and 17) lost to inclement weather conditions. Un-chopped observations of the Moon were taken with the detector mounted at the straight-through port (labelled as point 1 in figures 5.2 and 5.4). For first light, observations of the lunar surface were taken to check the alignment of the foreoptics and achieve focus. Figure 5.6(a) and Figure 5.6(b) demonstrate the improvement to the alignment and focus of the instrument by adjusting the secondary mirror from 40900 to 40500μm.

5.4.1 Background reduction

All observations were taken with a chop throw of $\sim 11''$, at a frequency of 1Hz. The chop frequency was limited by the speed and positional accuracy of the rotational platform. The communication time for the rotation platform was such that when the period between chop throw and return was set too short, the platform would not have sufficient time to return to the un-chopped position. A frequency of 1Hz was observed to have a zero fail rate and selected as the shortest possible time between chop throws. When homing, the platform deploys coarse and fine tuning successively to reach position. This causes blurring of sources if homing is used to return the platform after a chop throw. Instead, directing the platform to absolute positions and not homing negated this effect.

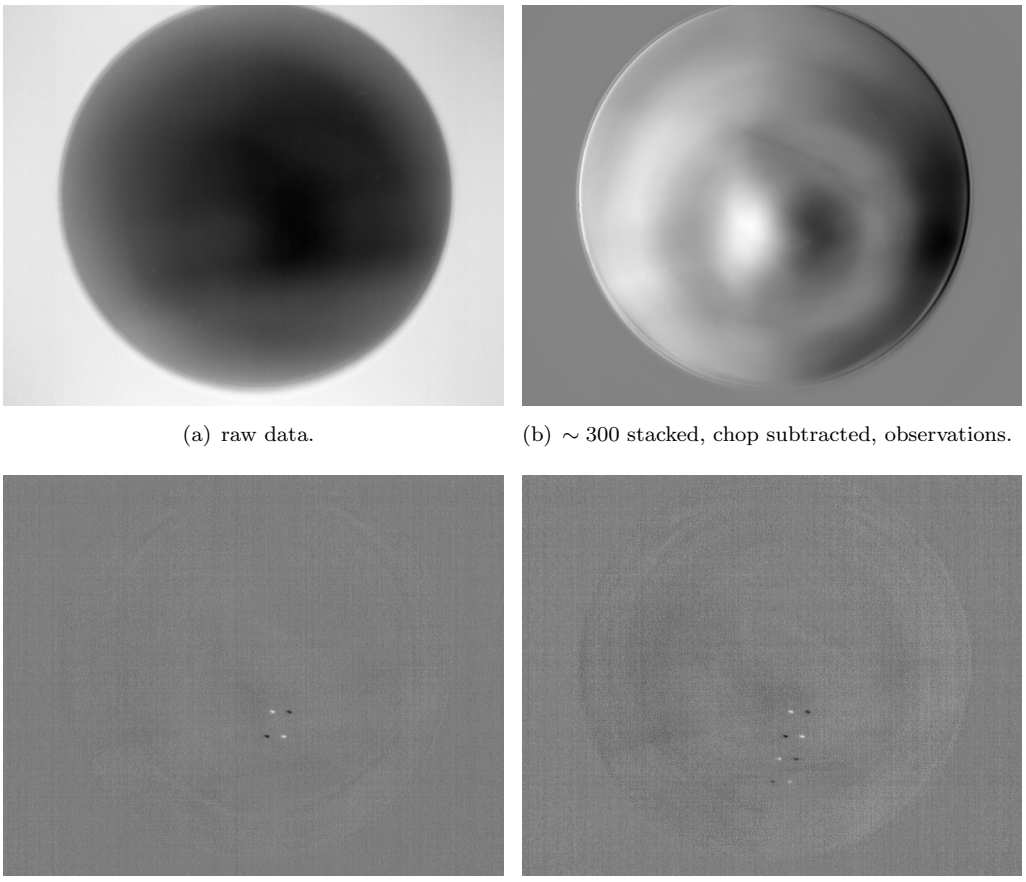

(a) raw data.

(b) ~ 300 stacked, chop subtracted, observations.

(c) Subtraction of stacks from nod positions A and B.

(d) Full ABCD chop/nod reduction.

FIGURE 5.7: An example of background subtraction after upgrading the instrument to include a chopping mirror and taking observations with an ABCD nod regime. This observation of the red supergiant NML Cygni was taken with the TCS on 2019 September 14. Note: the imaging field of view is limited by the pupil stop to the circular area in the centre.

An example of full background reduction can be seen in figure 5.7. The observation seen in figure 5.7(a) is characteristic of a single (1/9 s) raw observation taken in an exposing period with the instrument. The FOV is limited to the circular aperture in the centre. Emission from the telescope is visible as the spider-like structure. Fig 5.7(b) is the output from the chop data-reduction pipeline which stacked ~ 300 chop-subtracted observations. Fig. 5.7(c) and 5.7(d) show the subtraction of nod positions (see section 5.4.1.1) for this exposure. This is an example of where background reduction worked particularly well. However, as described below, the quality of chop/nod reduced observations was variable.

5.4.1.1 Nod Pattern

The instrument was initially intended for use with a standard ABBA nod pattern. Where chop sequences occur at nod positions A and B, with the final observation produced from the subtraction pattern (A−B)−(B−A). When all the sources are properly aligned, this produces an image with four images of the object; two negative and two positive. However, the offset positional accuracy of the TCS used to implement nodding was poor. Figure 5.8 and 5.9 are of fully reduced observations taken with an ABBA nod pattern. Six object images are present as a result of the lack of alignment between positive and negative sources in subtracted chop images. To find the dominant cause of this, we took observations with an ABBC nod pattern. For an ABBC pattern, chop sequences occur at nod positions A and B and C, with two successive observations at position 'B'. The final observation is produced from the subtraction of (A−B)−(B−C). An example of this reduction can be seen in figure 5.10. The duplication of the sources in the 'B' position indicate the telescope tracking is also somewhat responsible for the poor positional accuracy. To negate the effect of poor telescope offsetting and tracking on observations, we adopted an ABCD nod pattern. For an ABCD, the telescope is nodded perpendicular to the chop direction through 4 different positions in 15″ increments. Chop sequences occur at all positions and the final observation is produced from an (A−B)−(C−D) subtraction pattern. This can be seen in practice in figure 5.11. There is an increased number of positive and negative images of the source in the observation but the need for accurate positioning and tracking is removed. We opted to nod through 4 positions with the ABCD instead of just 2 with an AB to increase the SNR in the resulting image.

Overall, we found that nodding produced variable results when it came to removing telescopic emissions. The nod period ($>$ 2 minutes) was determined by the offset speed of the telescope and the exposing period of the instrument. This is much higher than nod periods deployed at other facilities as the timescale over which telescopic emissions are expected to vary is $<$ 1 minute. It is likely that the variable success of background correction would be improved by reducing the nod period. Regrettably, due to weather constraints, we were unable to test the effect of reduced nod periods and whether this would improve the quality of the background correction in our target observations.

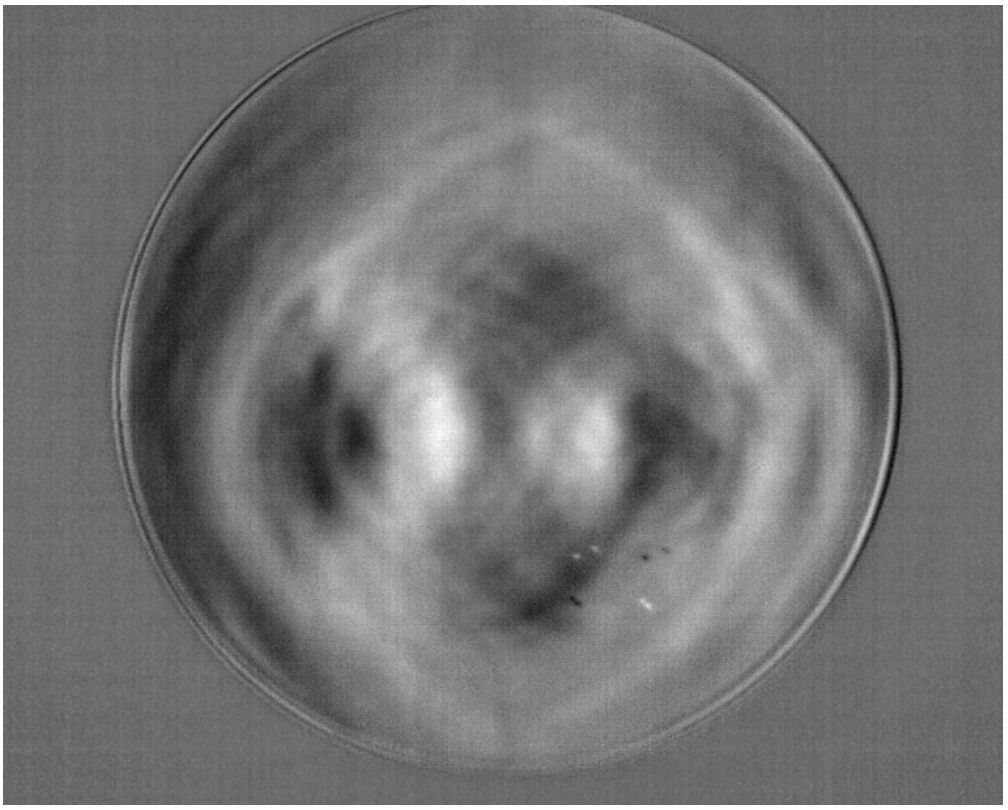

FIGURE 5.8: An observation post chop/nod reduction where a standard ABBA nod pattern was deployed. The duplication of all four sources indicates that the telescope positioning and tracking are not accurate for repeating positions in a nod pattern.

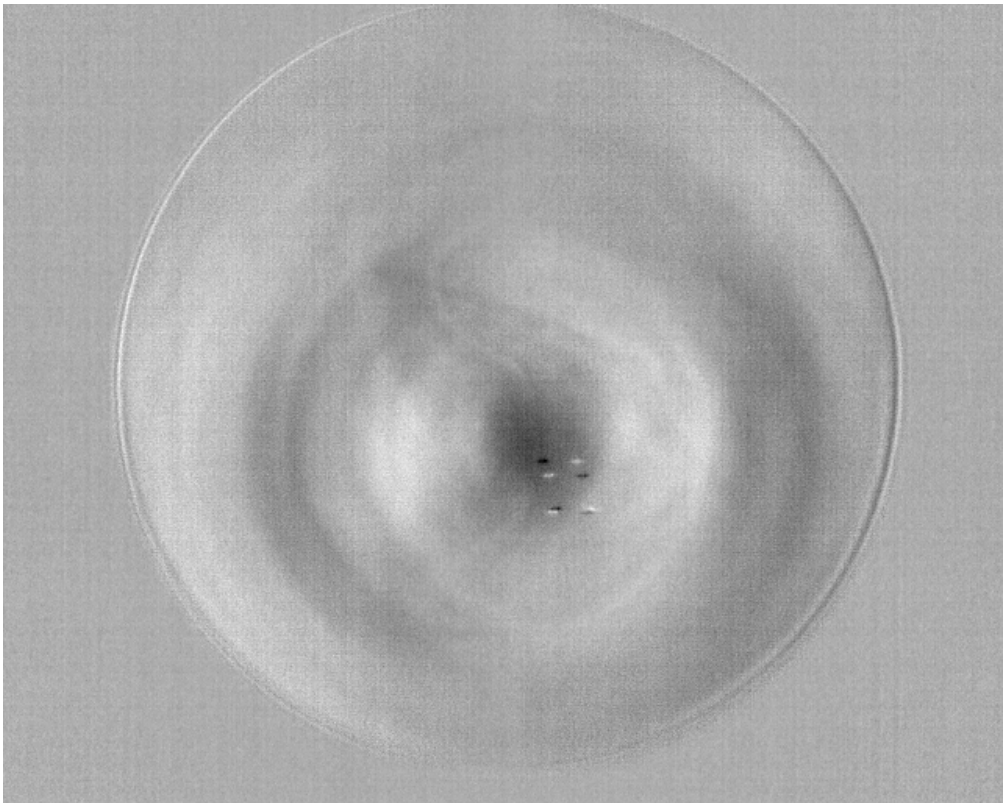

FIGURE 5.9: An observation post chop/nod reduction where a standard ABBA nod pattern was deployed. The duplication of all four sources indicates that the telescope positioning and tracking are not accurate for repeating positions in a nod pattern.

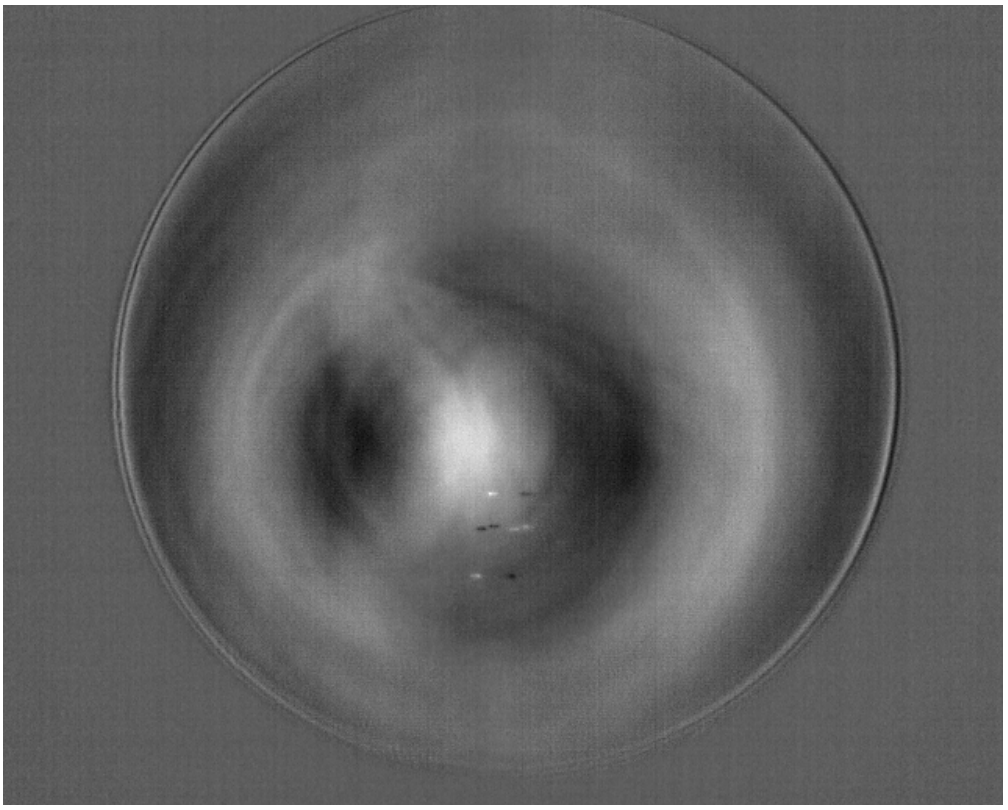

FIGURE 5.10: An observation post chop/nod reduction where an ABBC nod pattern was deployed. The duplication of sources in the central 'B' position indicate that the tracking of the telescope was not sufficient to repeat positions within a nod pattern.

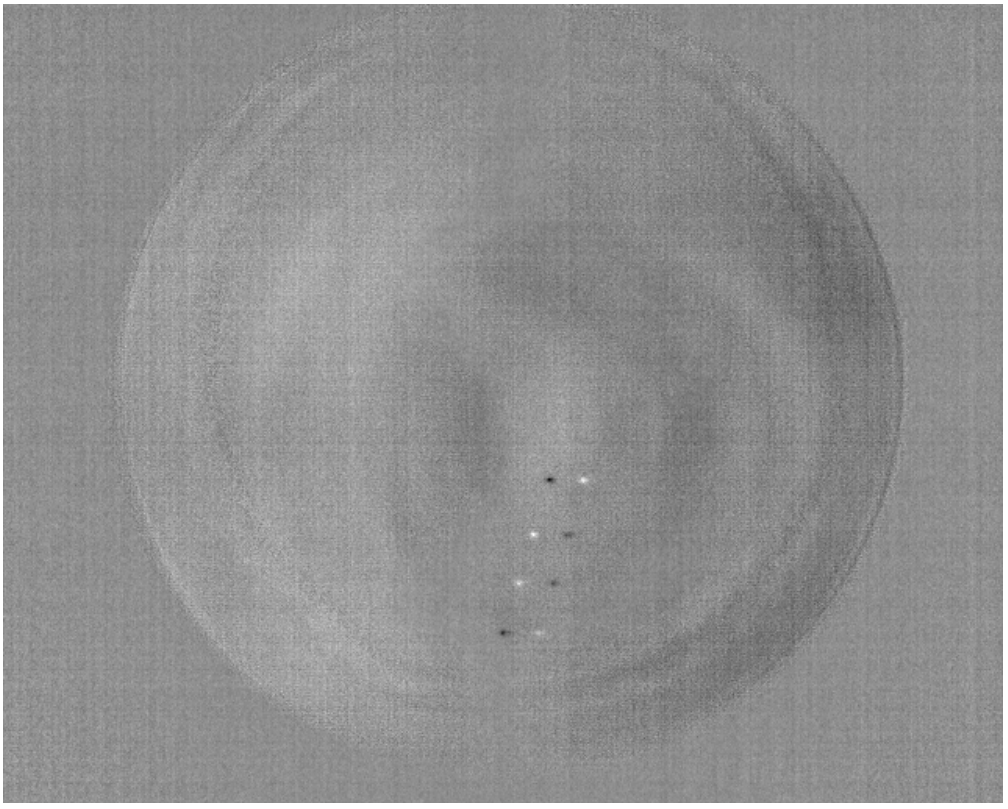

FIGURE 5.11: An observation post chop/nod reduction where an ABCD nod pattern was deployed. Removing the need to align sources in any position results in 4 positive and 4 negative sources in reduced observations.

5.4.2 Source Selection

We selected thirteen bright $11\mu m$ sources from the Revised Air Force Geophysical Laboratory (RAFGL) catalogue (Price & Murdock, 1983). Table 5.2 lists these sources by their common identifier. Each object was cross referenced across three other mid-infrared catalogues; the Wide-field Infrared Survey Explorer (WISE) All-Sky source catalogue (Wright et al., 2010), the Infrared Astronomical Satellite (IRAS) point source catalogue v2.1 (Beichman et al., 1988) and the Midcourse Space Experiment (MSX) catalogue (Egan & Price, 1996). The object types as listed in the SIMBAD astronomical database (Wenger et al., 2000) are also listed in table 5.2, with all sources likely to show at least some variability.

To compare catalogue values to get a measure of the variability of the selected sources, RAFGL magnitudes were converted to flux using the zero point flux $f_0 = 8.3 \times 10^{-17}$ $\mathrm{Wcm^{-2}\mu m^{-1}}$ (Price et al., 1976).

First f_0 was converted to $f(\nu)_0$ as follows:

$$f(\lambda)_0 = \frac{f_0 \times 10^7}{10^4} \text{ erg s}^{-1} \text{ cm}^{-2} \text{ A}^{-1}, \tag{5.1}$$

$$f(\nu)_0 = \frac{f(\lambda)_0 \cdot \lambda^2}{3 \times 10^{13}} \times 10^{-26} \text{ Jy}. \tag{5.2}$$

Then the apparent magnitude formulae was used to convert RAFGL magnitudes to flux values in Jy:

$$m = -2.5\log_{10}\left(\frac{f}{f(\nu)_0}\right). \tag{5.3}$$

Figure 5.12 compares the flux values obtained from IRAS and converted from RAFGL magnitudes for all sources, excluding α Herculis which was not included in the IRAS survey.

Identifier	11 μm mag (RAFGL)	11.6 μm mag (WISE)	12 μm Flux Jy (IRAS)	12.13 μm Flux Jy (MSX)	Type
NML Cyg	- 5.7	- 2.920	2.812e+03		Red supergiant
R Cas	- 4.2	- 2.725	1.34e+03		Variable Star (Mira Cet)
IRC+10420	- 4.2	- 2.664 $\pm$ 0.131	1.35e+03	1.2925e+03	Post-AGB Star (proto-PN)
α Hereculis	- 4.0	- 2.818			Double or multiple
χ Cyg	- 3.9	- 2.810	1.69e+03	1.7482e+03	S Star
IRC -10529*	- 3.7	- 2.468 $\pm$ 0.264	1.26e+03		OH/IR star
W Aql	- 3.7	- 2.582	1.58e+03		S Star
IRC +10365	- 3.5	- 2.464	7.20e+02		Variable Star (Mira Cet)
V Cyg	- 3.5	- 2.572	6.65e+02	8.9260e+02	Carbon Star
IRC +20370	- 3.5	- 2.474 $\pm$ 0.254	5.34e+02		Carbon Star
e Aql*	- 3.2	+ 0.166	2.79e+01		Variable
GY Aql	- 3.1	- 2.458	4.61e+02		Variable Star (Mira Cet)
X Oph*	- 3.1	- 2.378	4.09e+02		Variable Star (Mira Cet)

TABLE 5.2: The 13 bright 11μm sources selected for observation from the RAFGL catalogue. All objects are listed by their common identifier with those marked by an asterisk (*) confirmed as not detected in the data. All objects have been cross referenced against four catalogues (RAFGL, WISE, IRAS and MSX) and flux/magnitude values quoted. Sources are either identified as known variables or likely to display some variability.

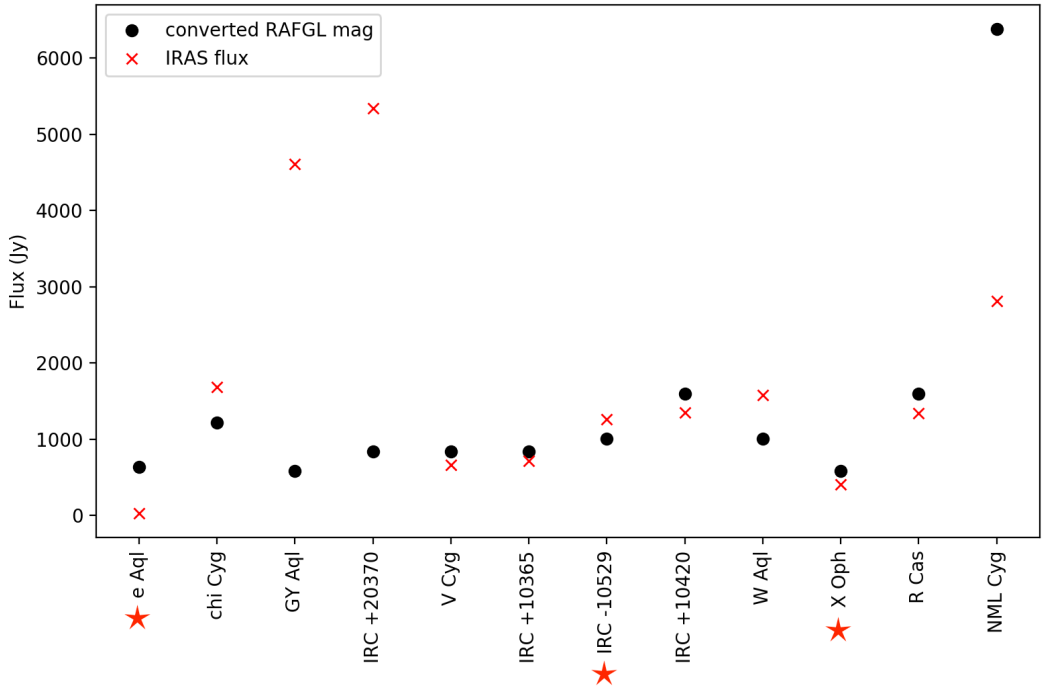

FIGURE 5.12: The catalogue fluxes of twelve selected sources. Values found in IRAS are marked by red crosses. Values found in RAFGL are marked as black dots. RAFGL magnitudes were converted to flux using the zero point flux given by Price et al. (1976). Red stars indicate sources that were not observed with our camera.

5.4.3 Observations

Observations of selected sources were taken on September 14 2020. Of the 13 sources observed, 10 were detectable by eye in the chop/nod reduced data. The objects marked by an asterisk in table 5.2 were not confirmed in the data. Examples of the chop-reduced and ABCD nod-reduced data of each detected source can be seen in figures 5.13 to 5.32.

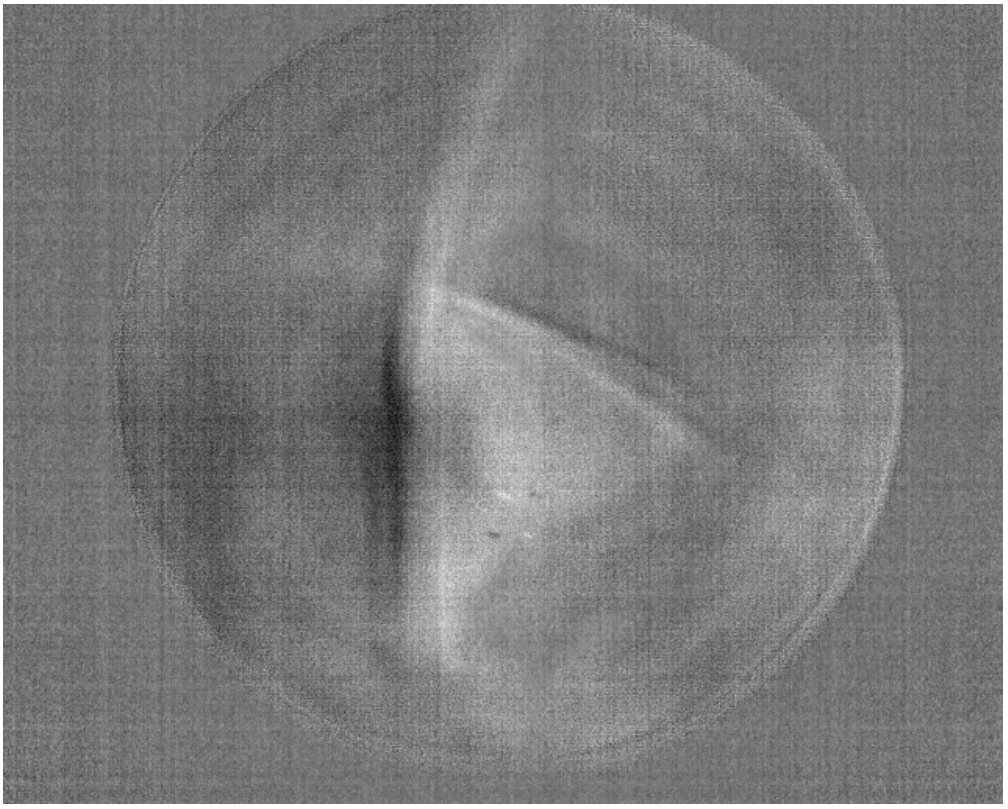

FIGURE 5.13: Chop-reduced observation of the double or multiple star α Herculis.

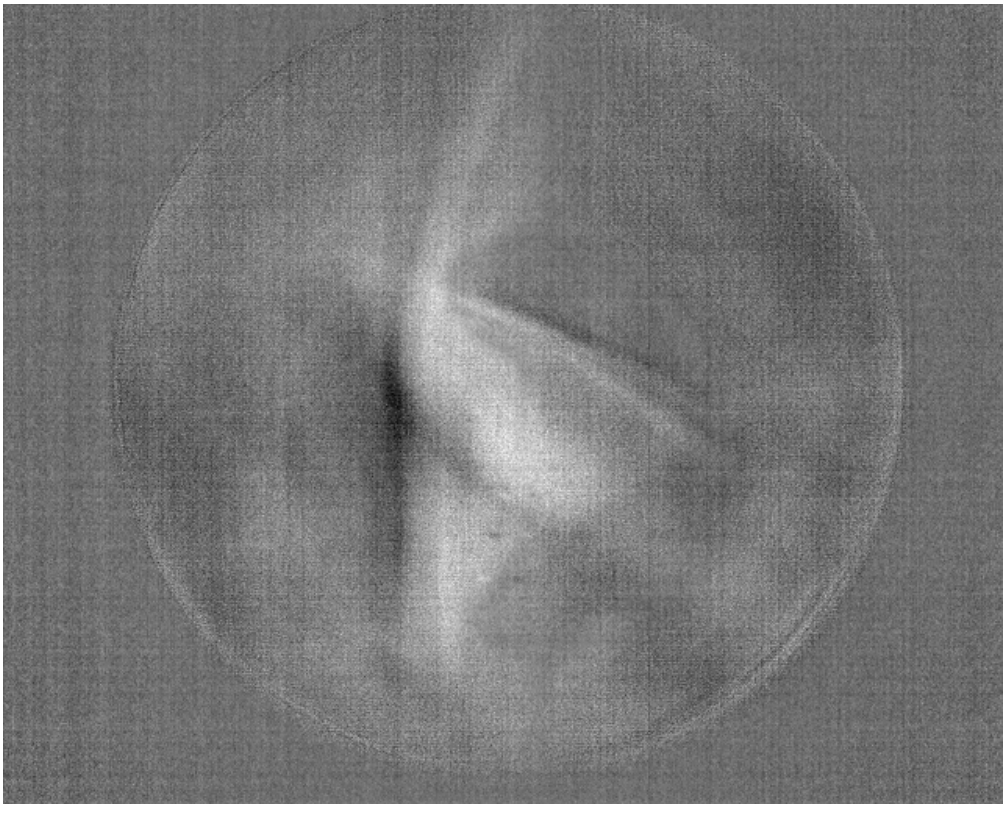

FIGURE 5.14: Fully nod-reduced observation of the double or multiple star α Herculis.

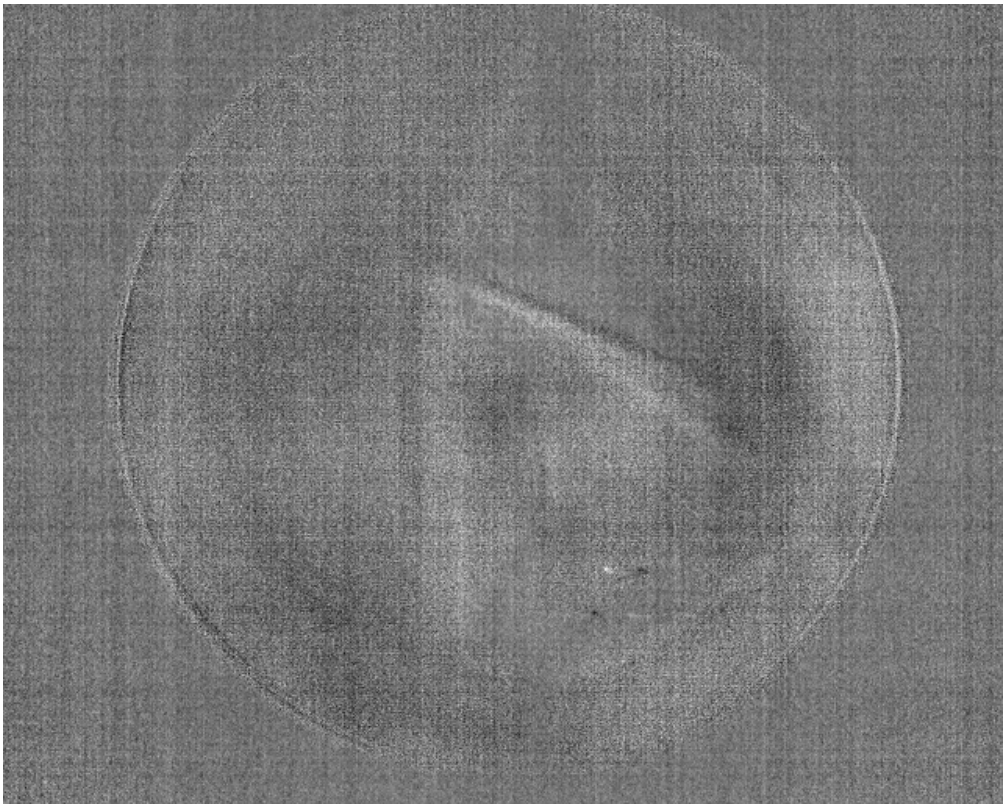

FIGURE 5.15: Chop-reduced observation of the S star χ Cygni

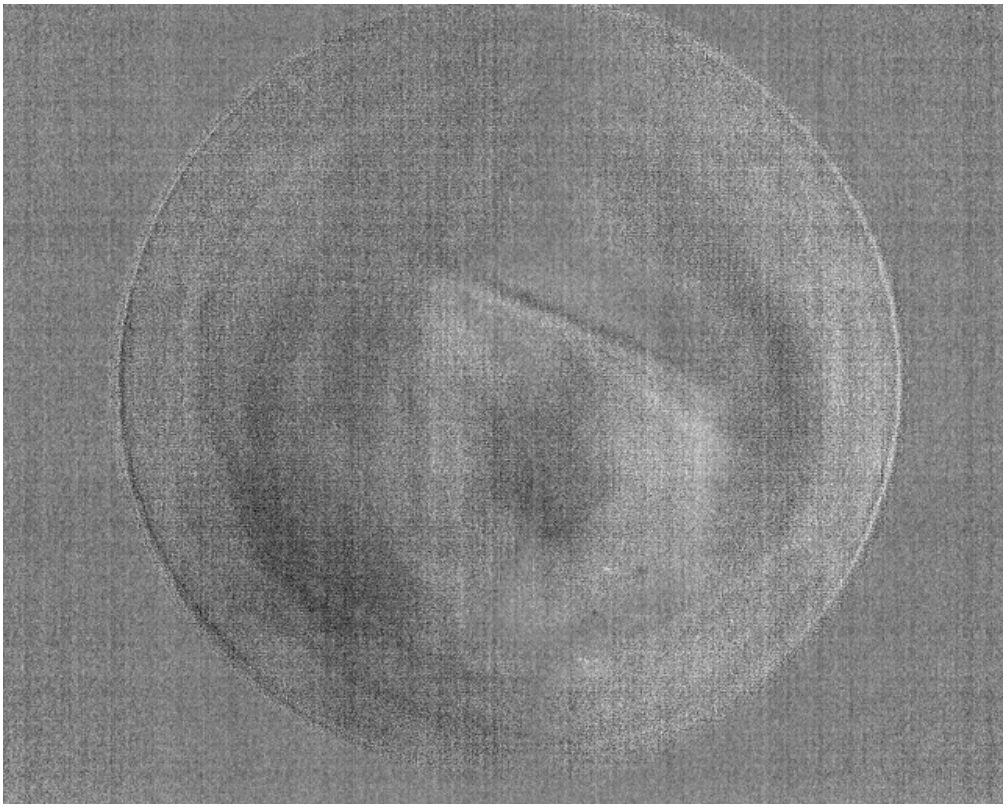

FIGURE 5.16: Fully nod-reduced observation of the S star χ Cygni

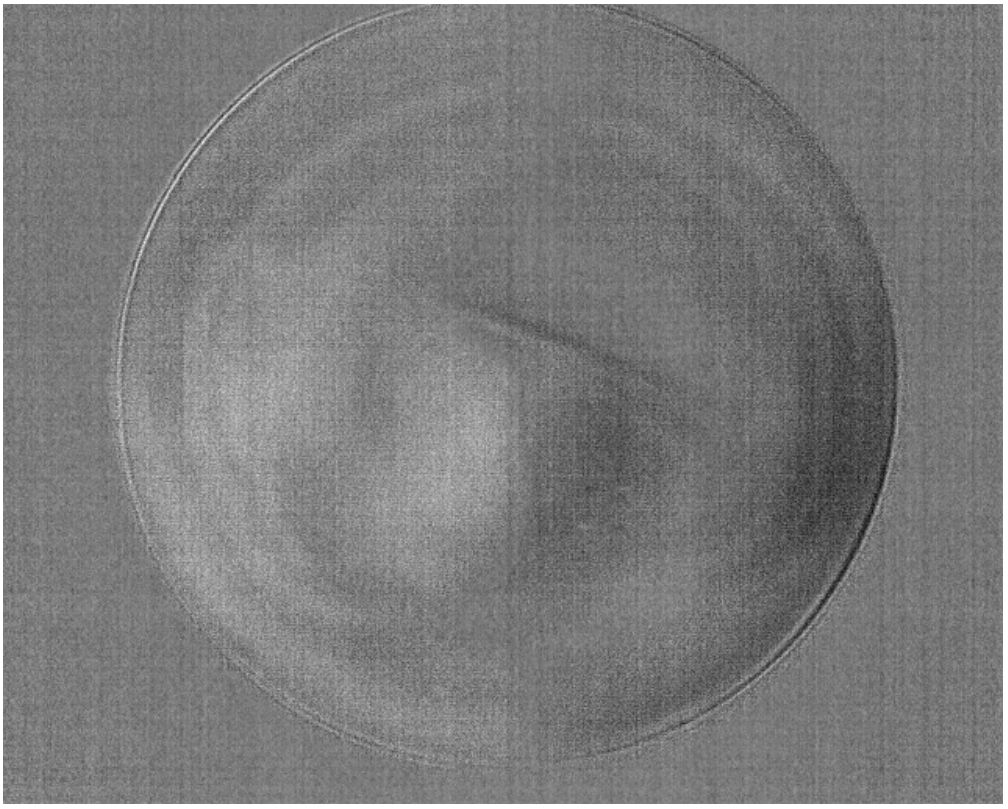

FIGURE 5.17: Chop-reduced observation of the variable star GY Aql

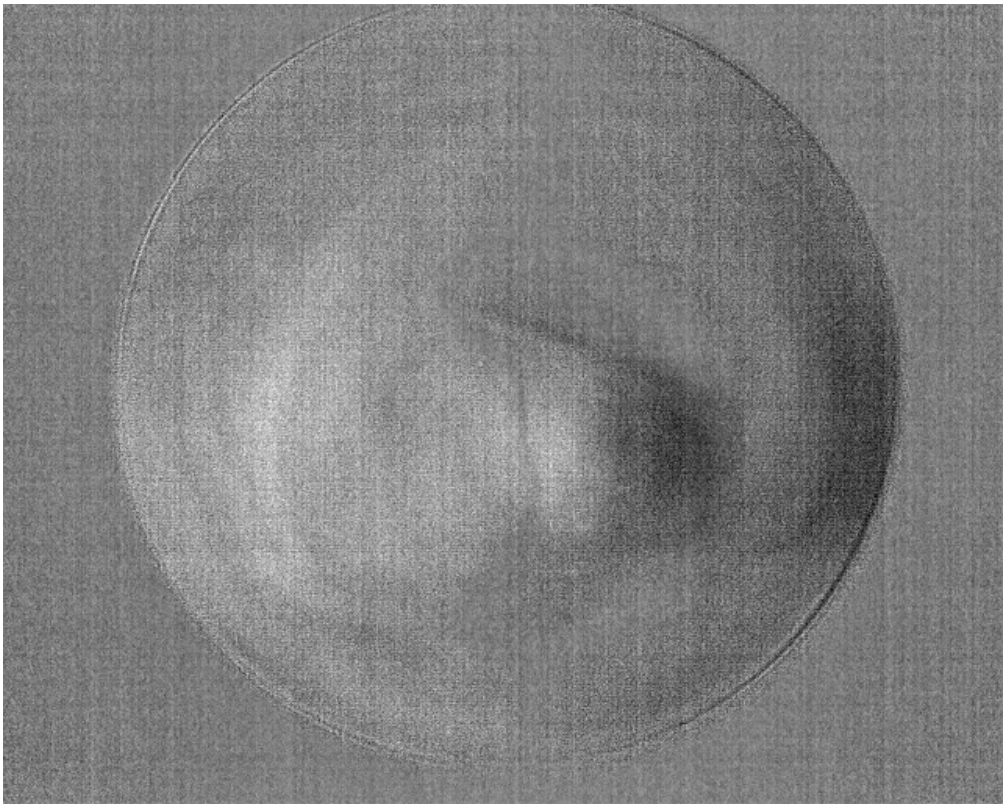

FIGURE 5.18: Fully nod-reduced observation of the variable star GY Aql

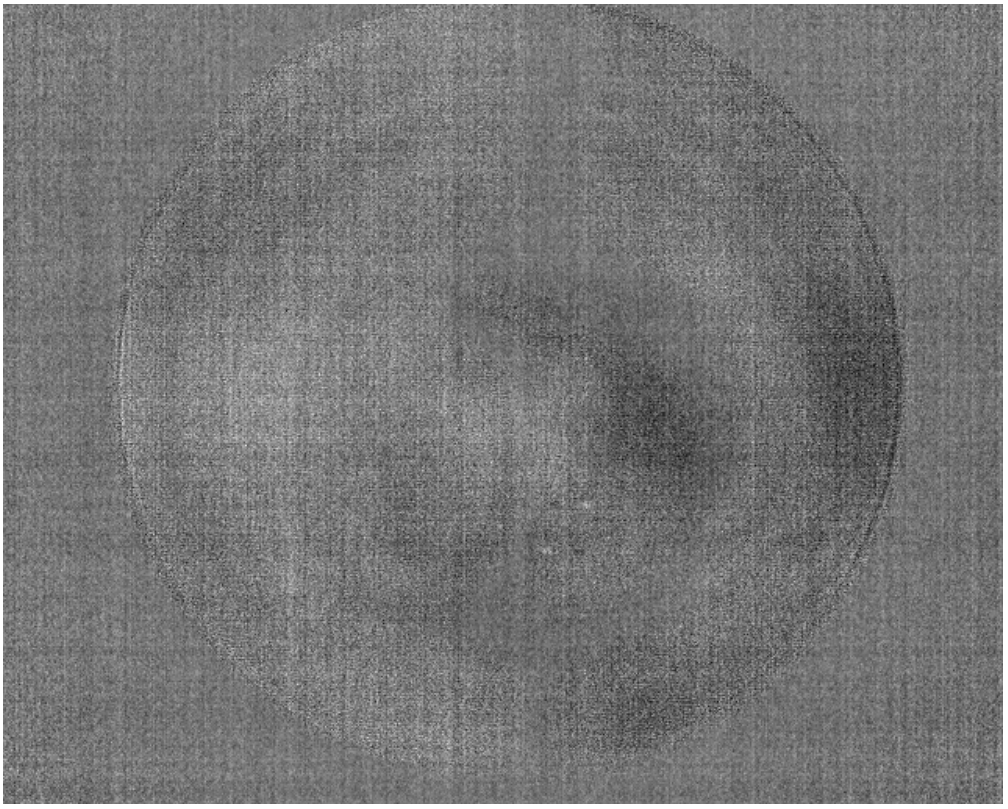

FIGURE 5.19: Chop-reduced observation of the carbon star IRC +20370

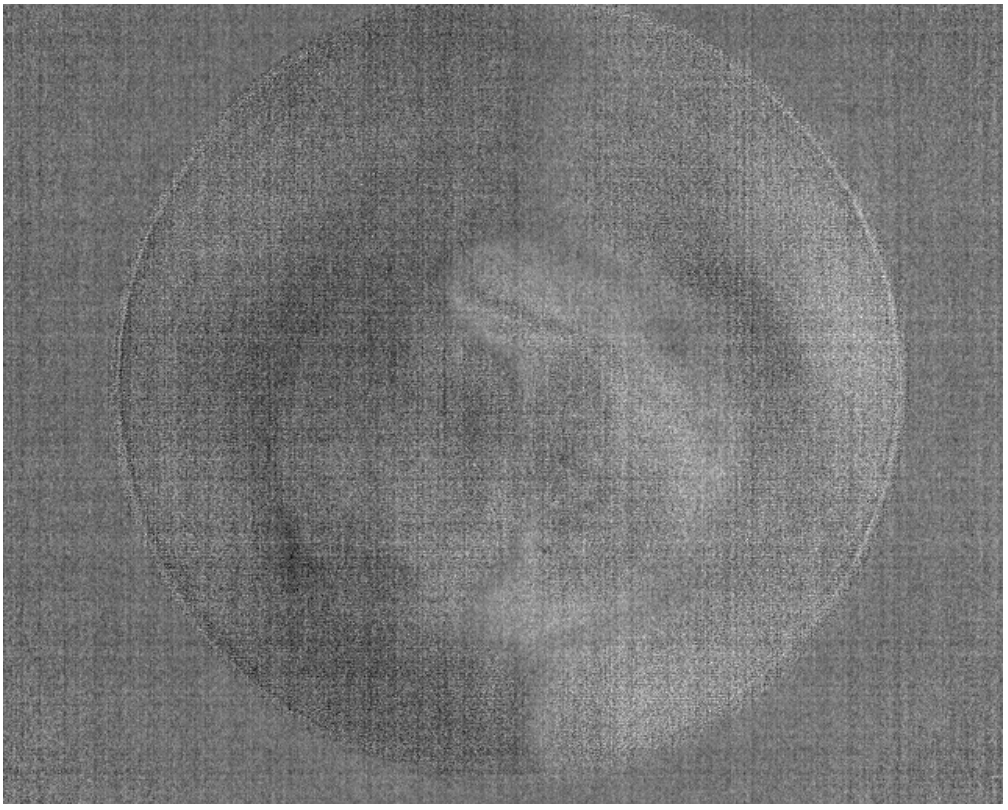

FIGURE 5.20: Fully nod-reduced observation of the carbon star IRC +20370

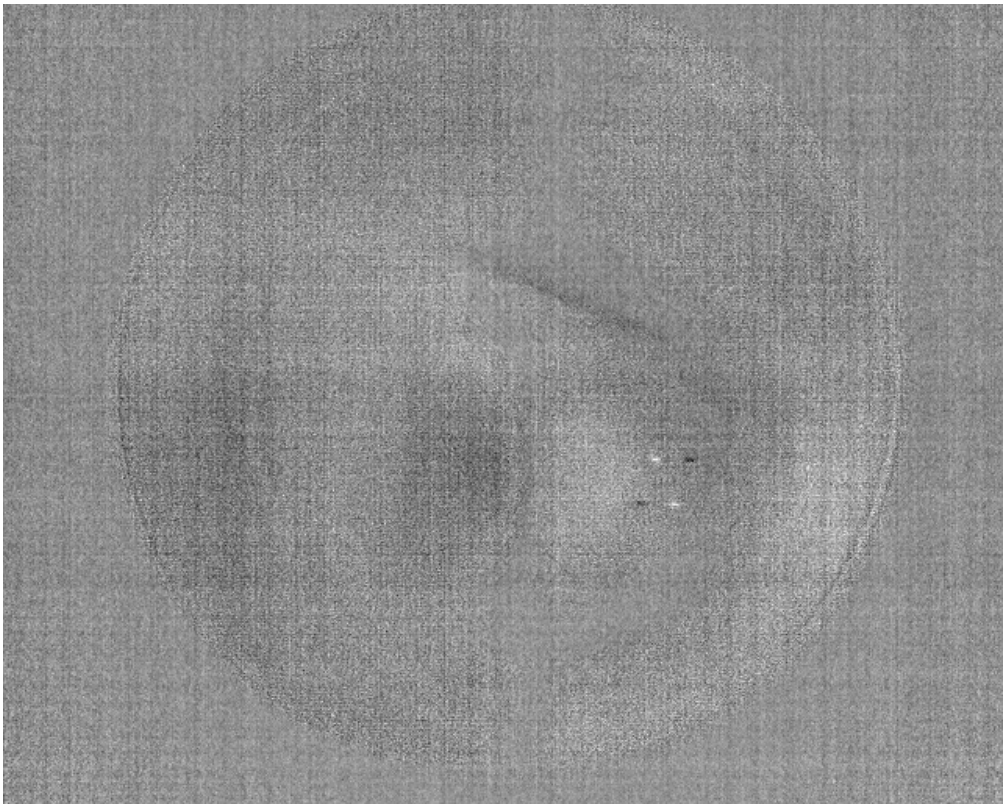

FIGURE 5.21: Chop-reduced observation of the carbon star V Cygni

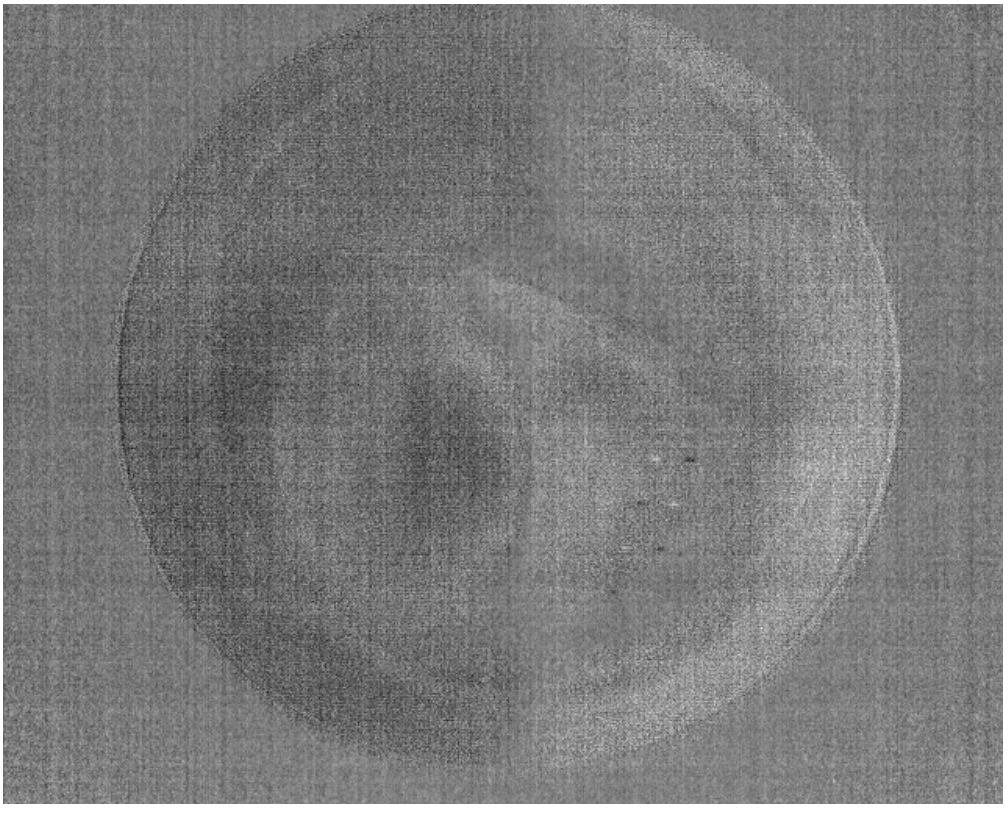

FIGURE 5.22: Fully nod-reduced observation of the carbon star V Cygni

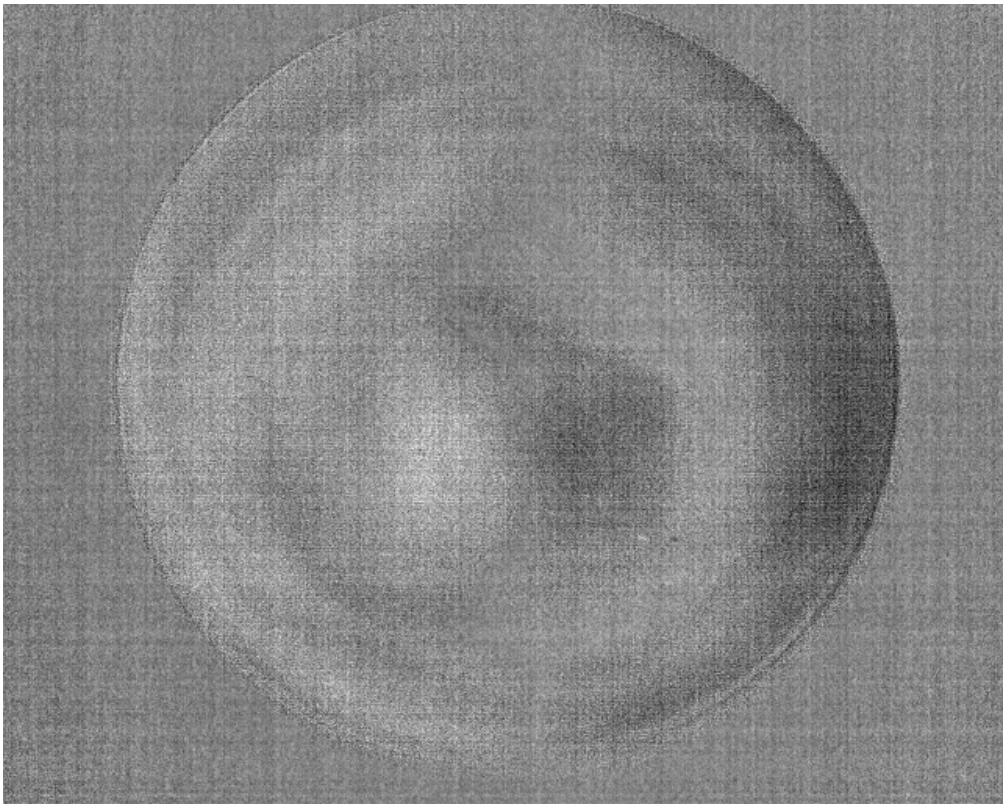

FIGURE 5.23: Chop-reduced observation of the variable star IRC +10365

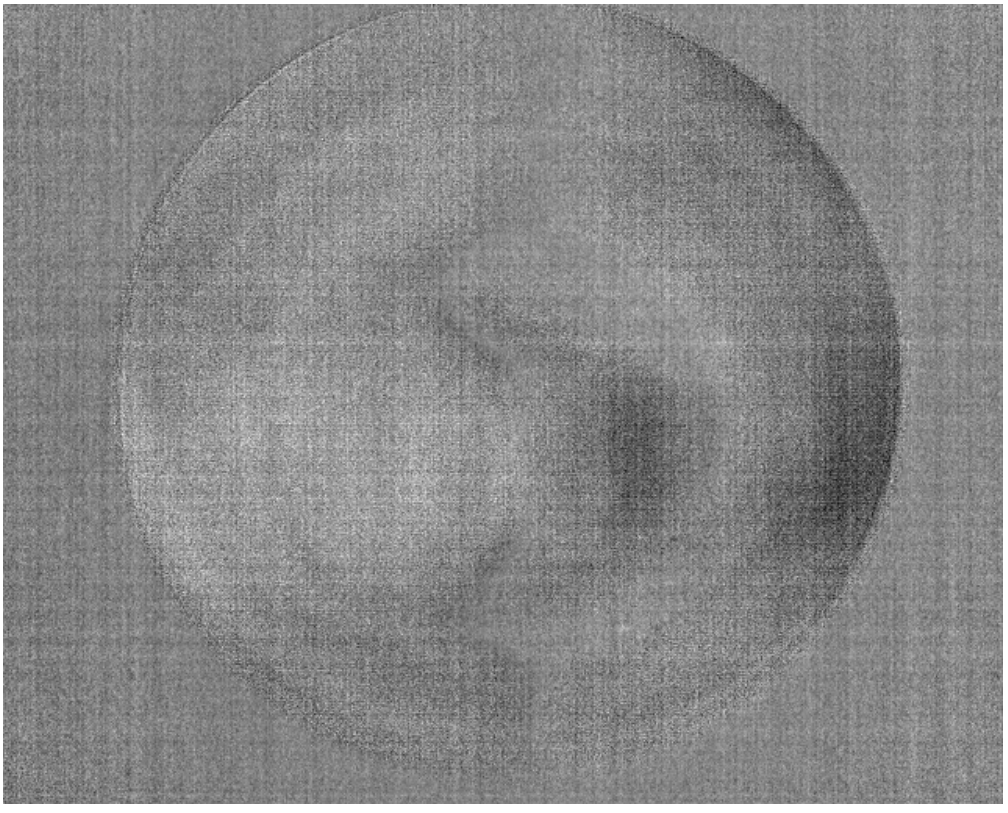

FIGURE 5.24: Fully nod-reduced observation of the variable star IRC +10365

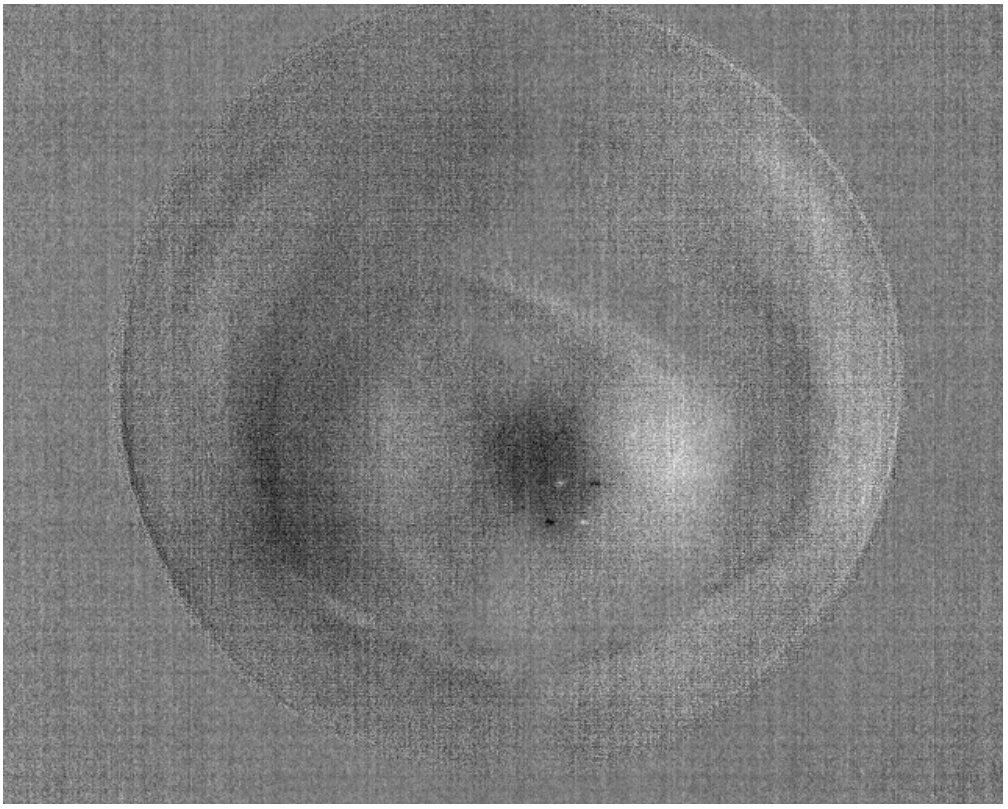

FIGURE 5.25: Chop-reduced observation of the post-AGB star IRC+10420

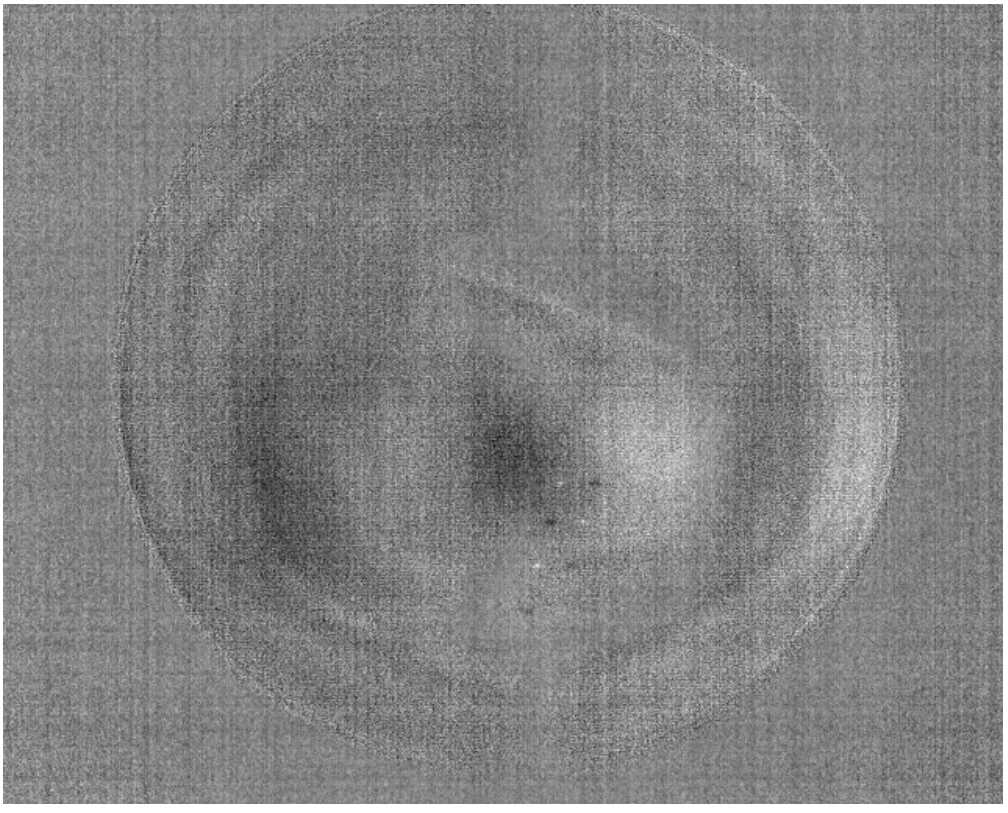

FIGURE 5.26: Fully nod-reduced observation of the post-AGB star IRC+10420

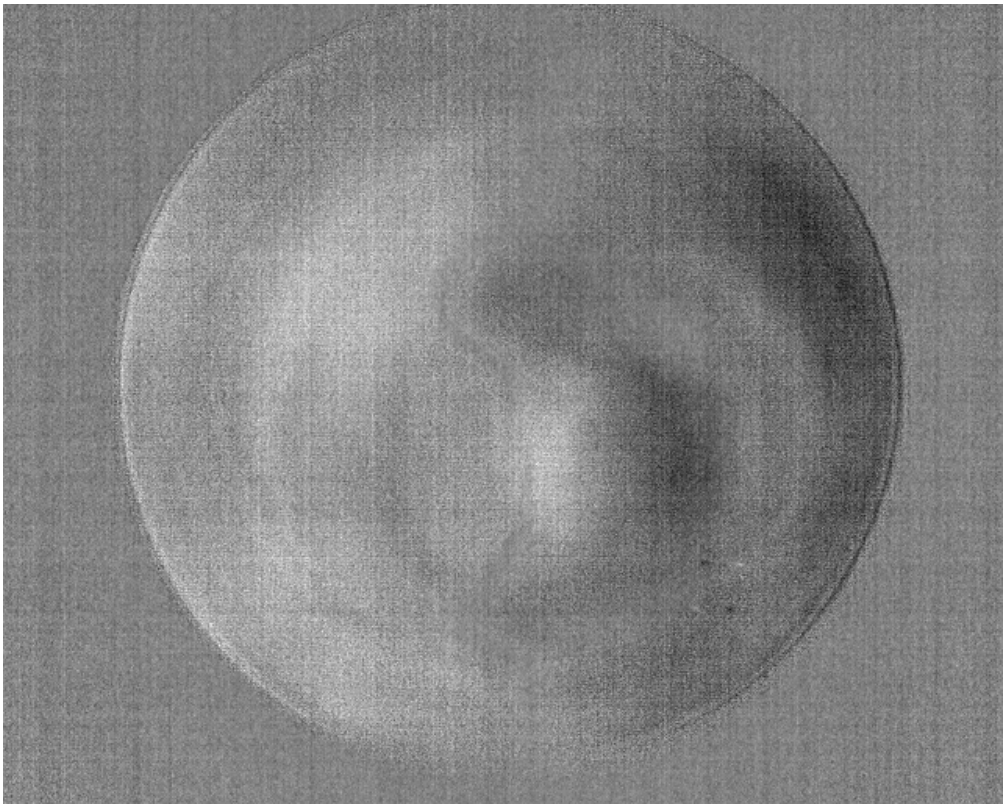

FIGURE 5.27: Chop-reduced observation of the S star W Aql

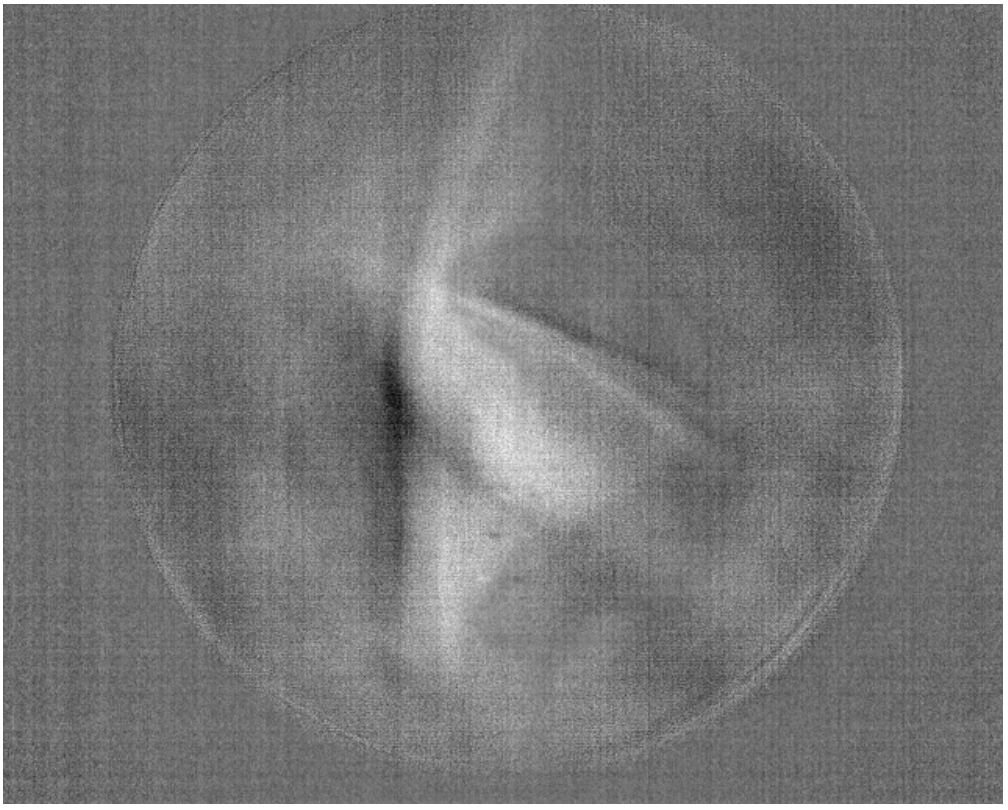

FIGURE 5.28: Fully nod-reduced observation of the S star W Aql

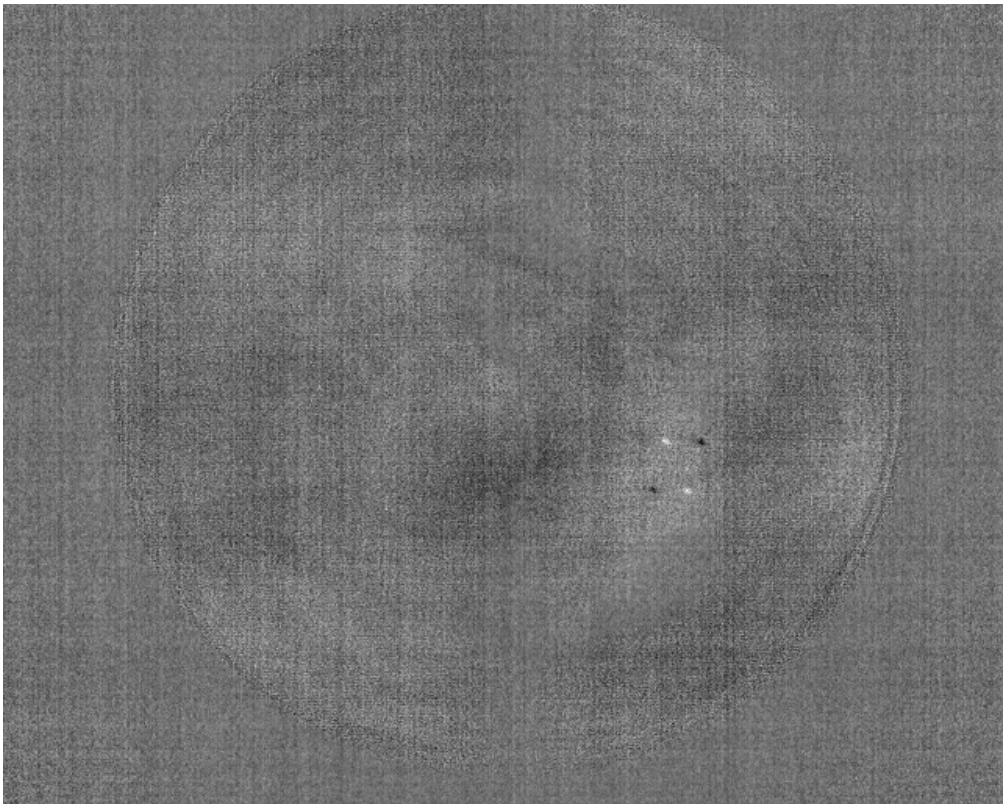

FIGURE 5.29: Chop-reduced observation of the variable star R Cas

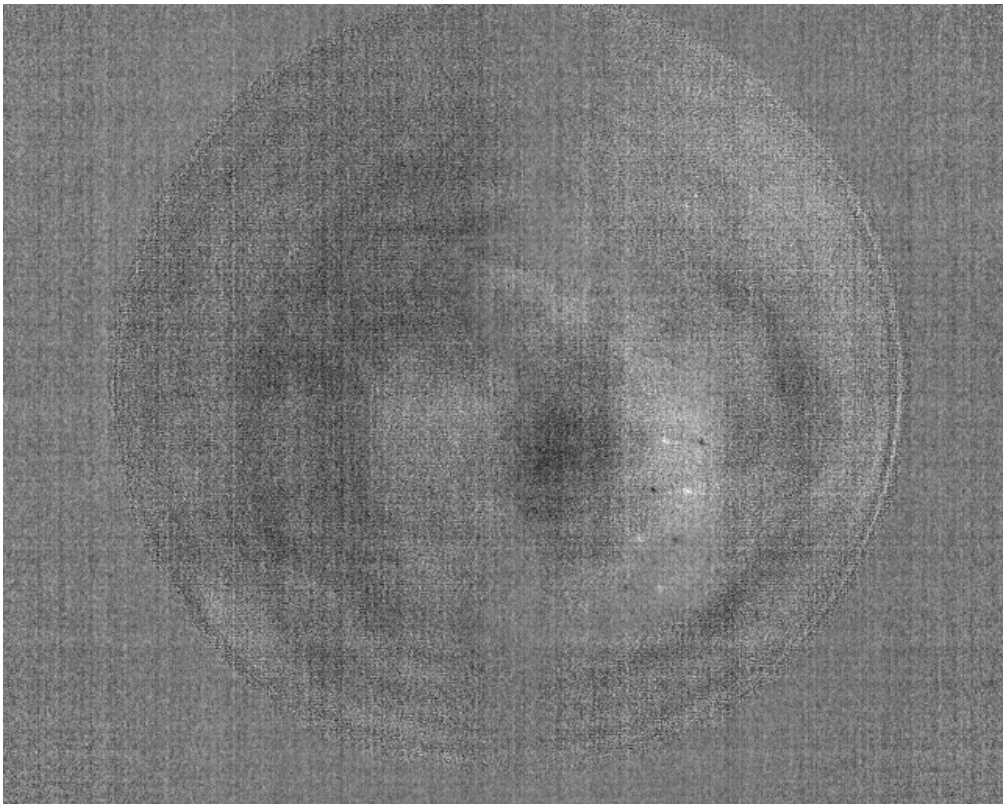

FIGURE 5.30: Fully nod-reduced observation of the variable star R Cas

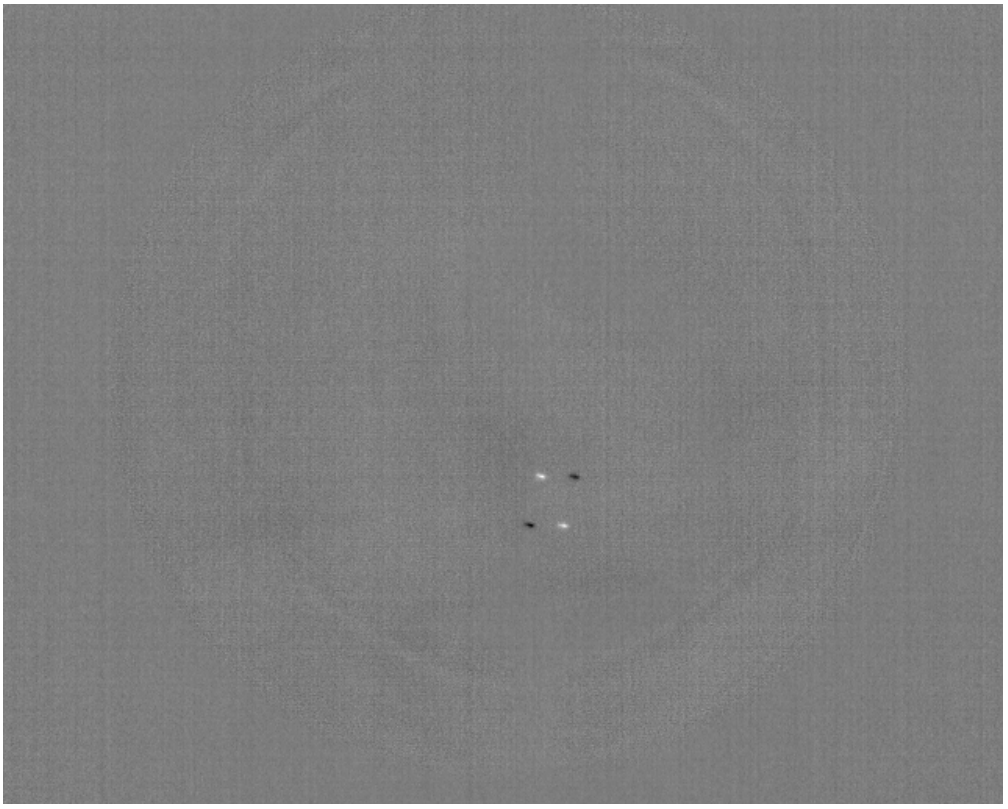

FIGURE 5.31: Chop-reduced observation of the red supergiant NML Cyg

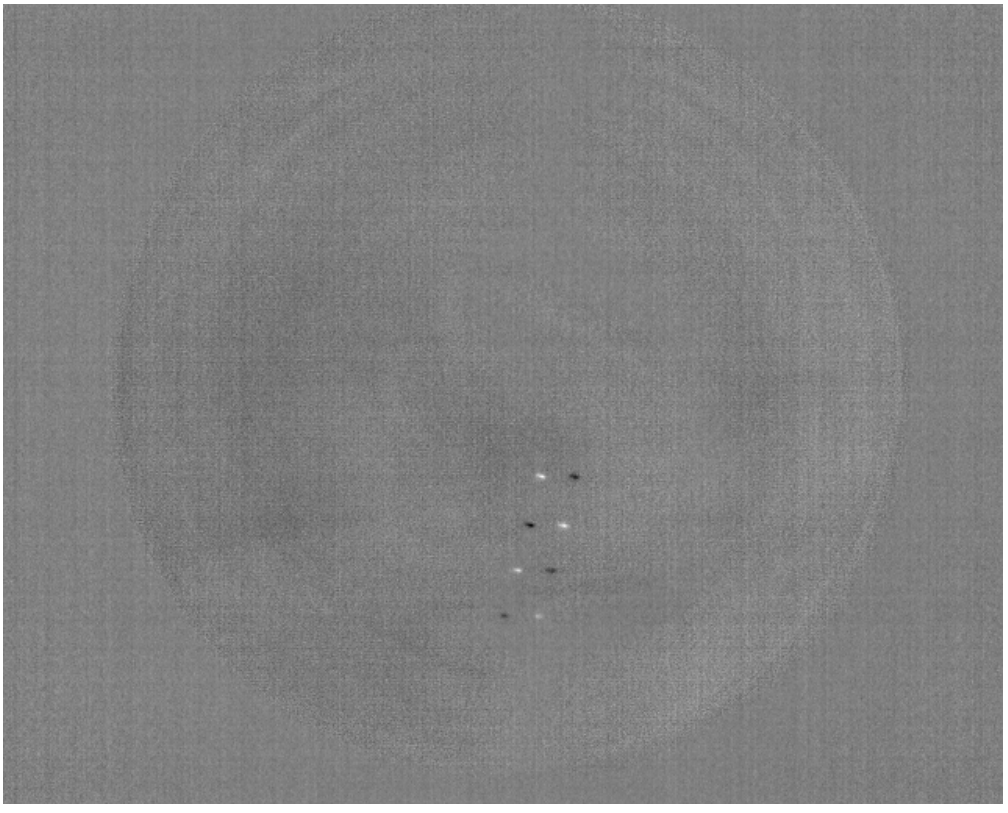

FIGURE 5.32: Fully nod-reduced observation of the red supergiant NML Cyg

5.4.3.1 Combined Source Images

The positive and negative sources present in ABCD nod-reduced observations were combined. The sources were selected using a bounding box centred on the centroid of the source. Negative sources were multiplied by minus one. The sources were then added. The spatial profile of the combined sources was measured by taking a 'cut' across the centroid of the source in the x- and y-axes. This profile was fitted with a Gaussian (where possible), to determine the FWHM of the source. These combined source images and their respective plots can be seen in figures 5.33 to 5.52. As mentioned in Section 5.2 the optical design has an 80% geometric encircled energy (GEE) diameter that corresponds to a spatial FWHM of < 1.1 and < 2.3 arcsec for on- and off-axis rays respectively. The FWHM of the fitted Gaussian profiles range from $0.5 - 4.5$ arcsec. However, some of the combined sources do not display a Gaussian like profile in both axes, e.g. α Herculis (Figures 5.33 and 5.34), GY Aql (Figures 5.37 and 5.38), which results in a larger FWHM. Many of these sources were faint, and did not have the full 8 positive/negative sources visible in the nod reduced observation. The two brightest sources observed, R Cas (Figures 5.49 and 5.50) and NML Cyg (Figures 5.51 and 5.52) are fitted with Gaussian profiles that have a FWHM in the range of $1.0 - 2.0$ arcsec which is consistent with the spatial FWHM obtained from the optical design. Many of the combined source images appear to be extended and irregular in shape, this could be a result of the optics and the off-axis aberration that is inherent in the design. However, there are several other processes that occured in obtaining the chop/nod reduced observations that could have contributed to the apparent spreading of sources. The telescope tracking was poor and over the course of a chop cycle, may have drifted sufficiently that the sources in early and late, chopped and unchopped, observations were no longer aligned or likewise the positional accuracy of the rotational platform on which the chopping mirror was mounted could have been insufficient.

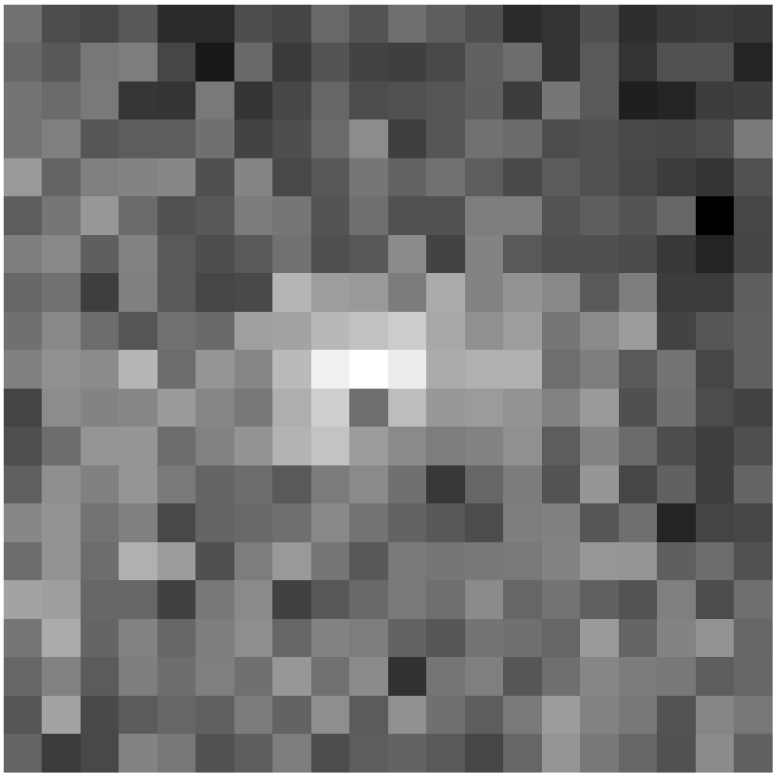

FIGURE 5.33: Combined source image of α Herculis.

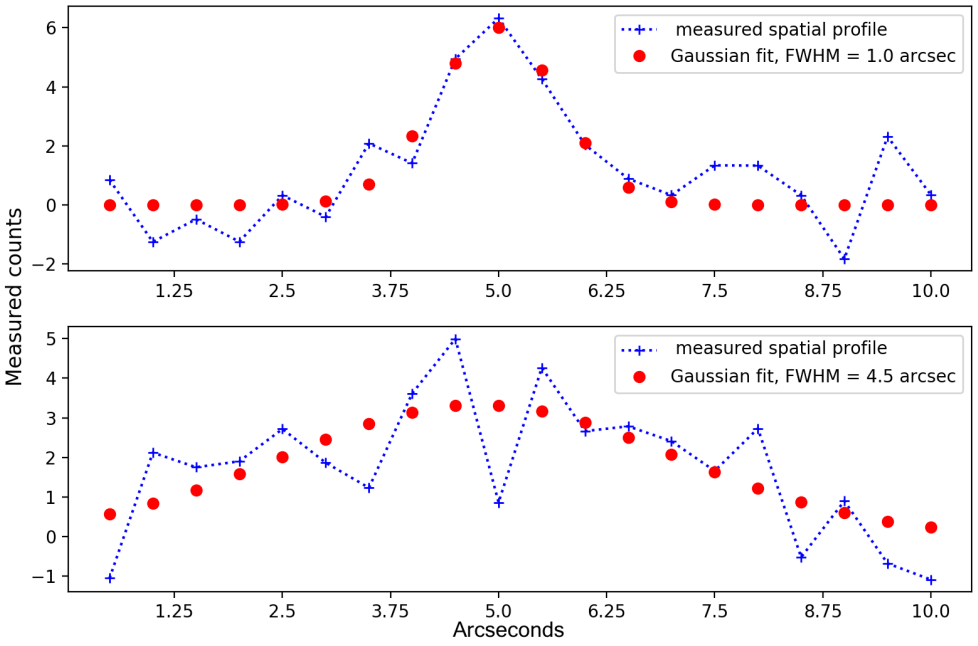

FIGURE 5.34: The spatial profile of the combined source image of α Herculis as measured across the centroid in the x-axis (top) and y-axis (bottom).

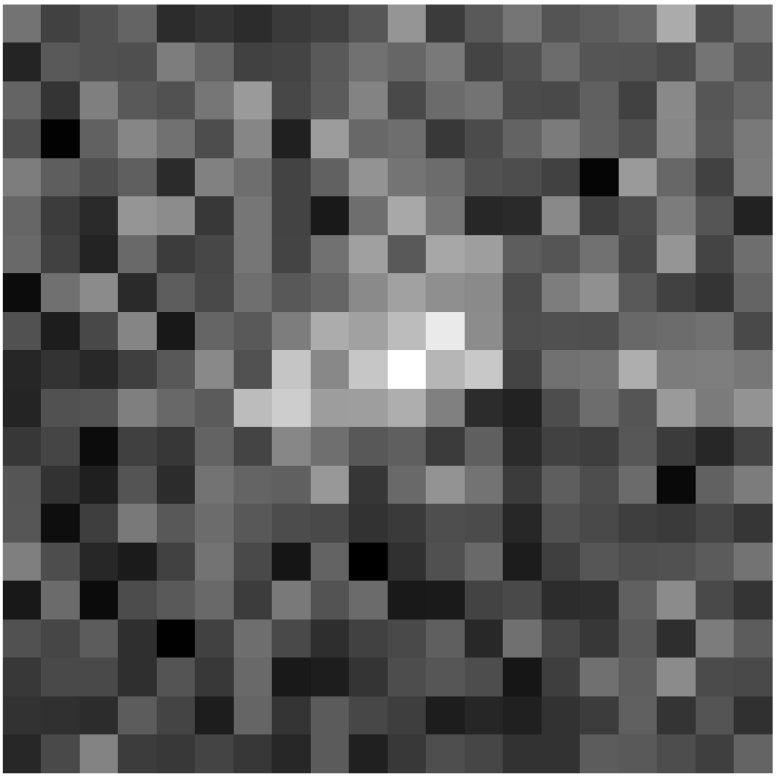

FIGURE 5.35: Combined source image of χ Cygni.

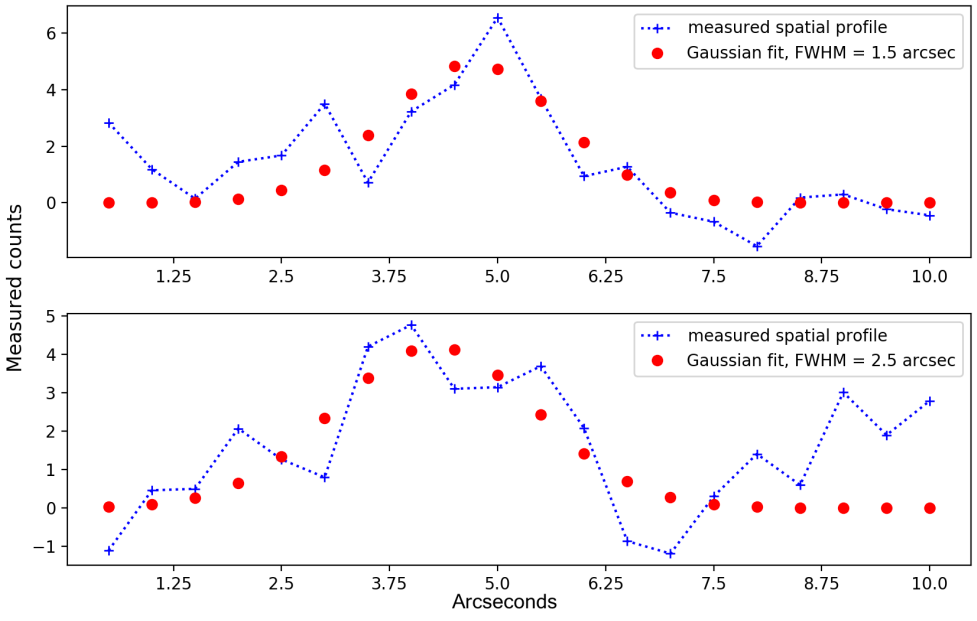

FIGURE 5.36: The spatial profile of the combined source image of χ Cygni as measured across the centroid in the x-axis (top) and y-axis (bottom).

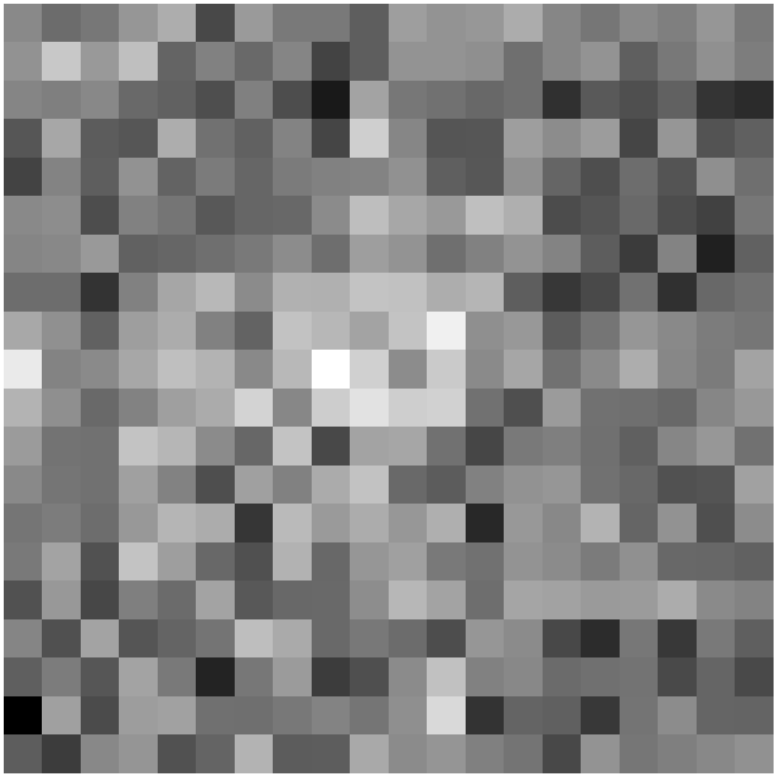

FIGURE 5.37: Combined source image of GY Aql.

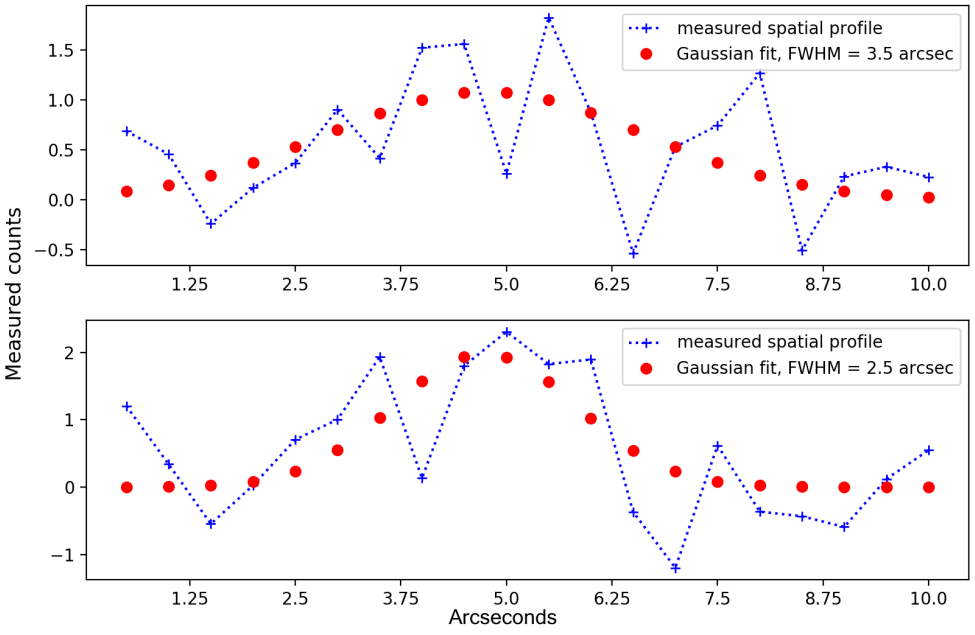

FIGURE 5.38: The spatial profile of the combined source image of GY Aql as measured across the centroid in the x-axis (top) and y-axis (bottom).

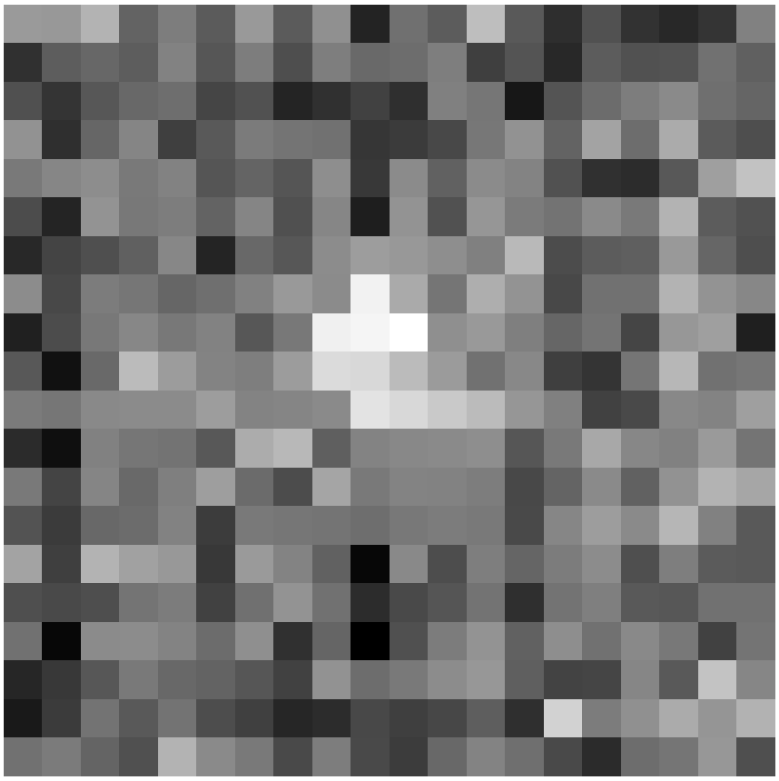

FIGURE 5.39: Combined source image of IRC +20370.

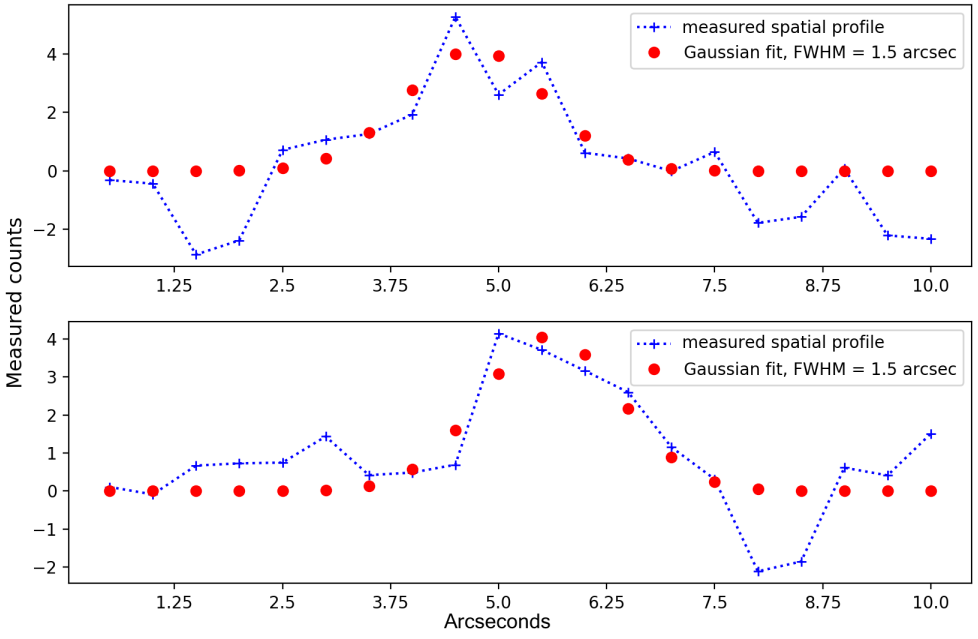

FIGURE 5.40: The spatial profile of the combined source image of IRC +20370 as measured across the centroid in the x-axis (top) and y-axis (bottom).

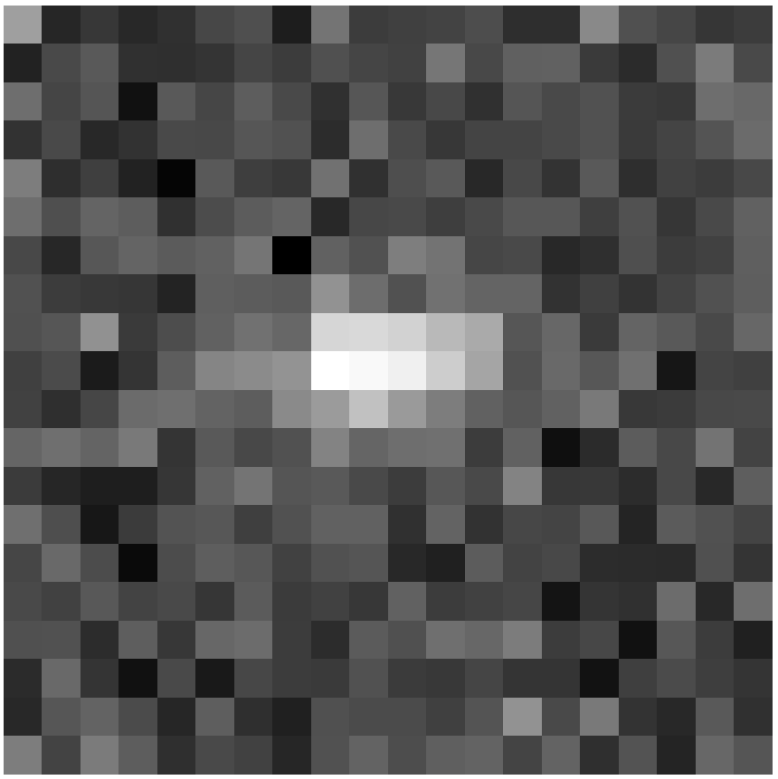

FIGURE 5.41: Combined source image of V Cygni.

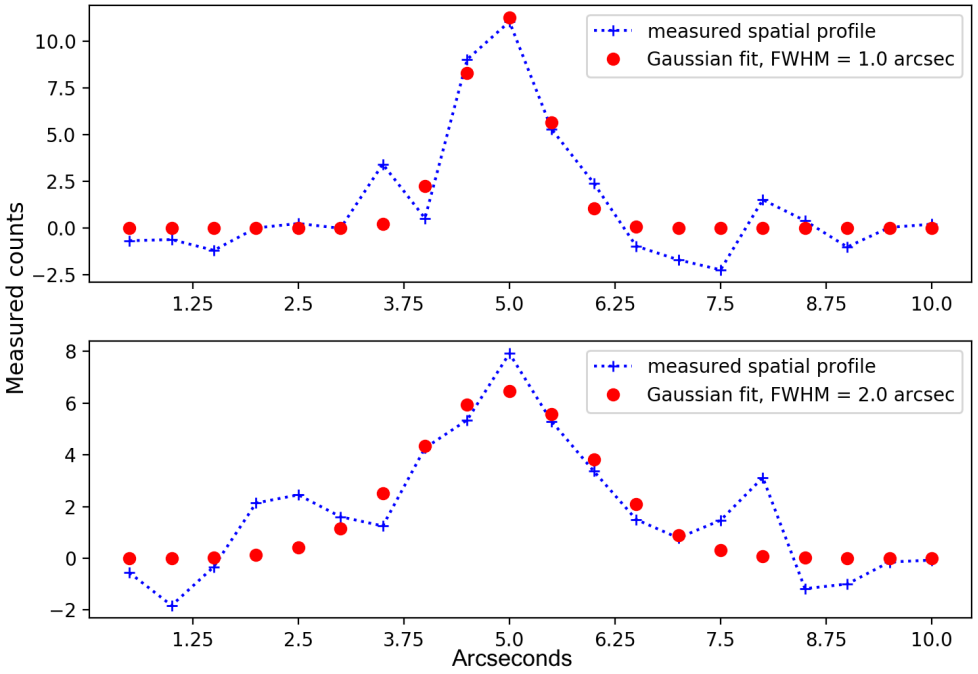

FIGURE 5.42: The spatial profile of the combined source image of V Cygni as measured across the centroid in the x-axis (top) and y-axis (bottom).

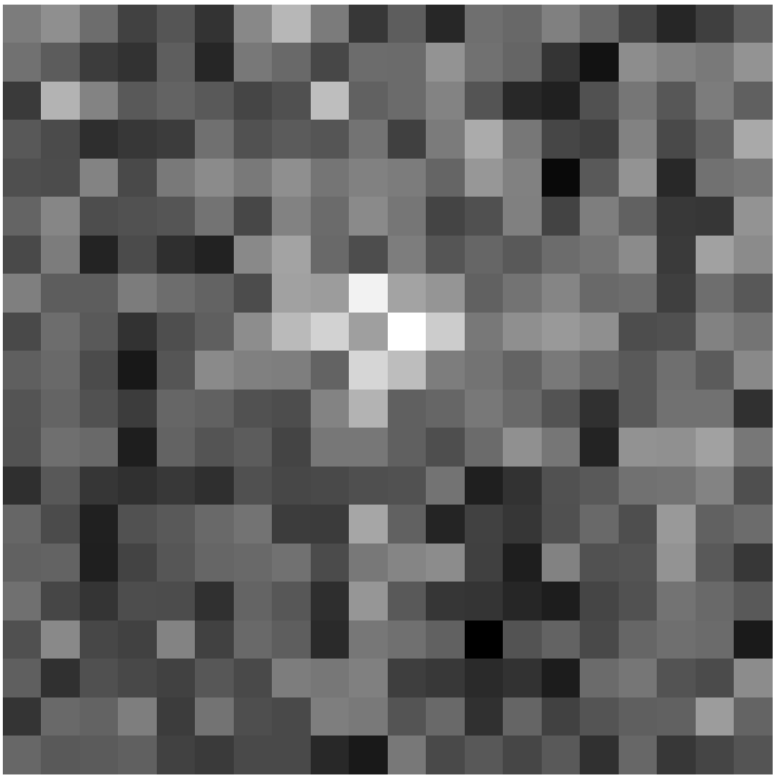

FIGURE 5.43: Combined source image of IRC +10365.

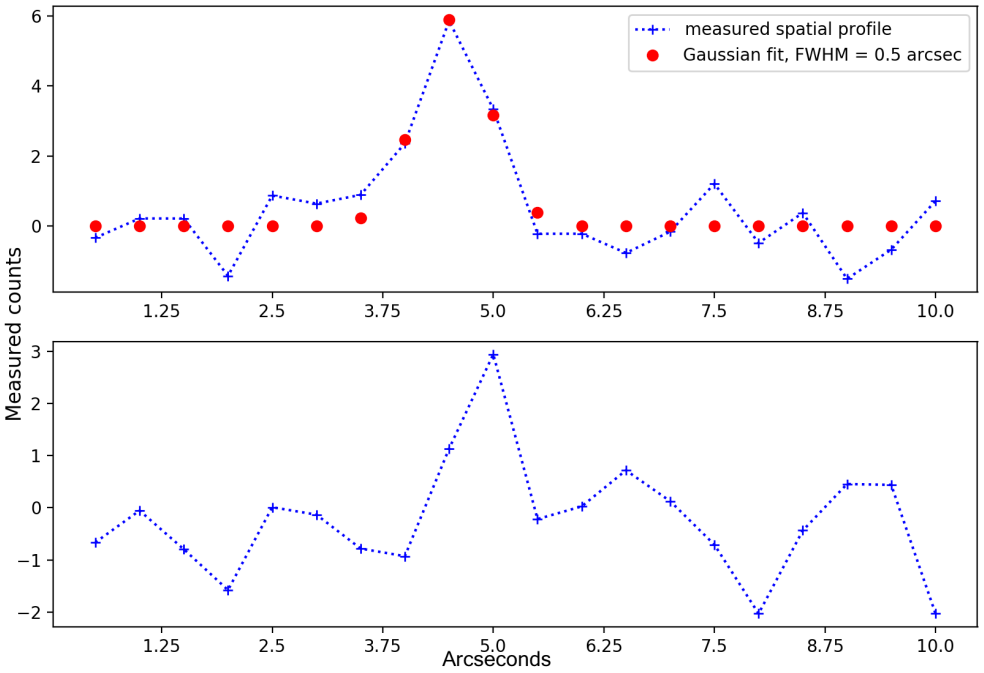

FIGURE 5.44: The spatial profile of the combined source image of IRC +10365 as measured across the centroid in the x-axis (top) and y-axis (bottom). The y-axis spatial profile was unable to be fit with a Gaussian model.

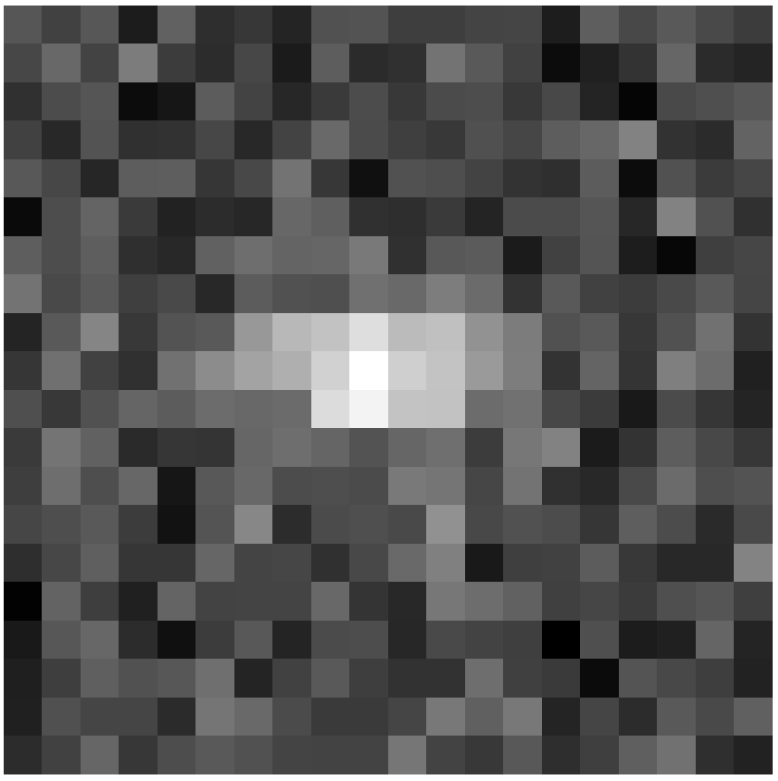

FIGURE 5.45: Combined source image of IRC +10420.

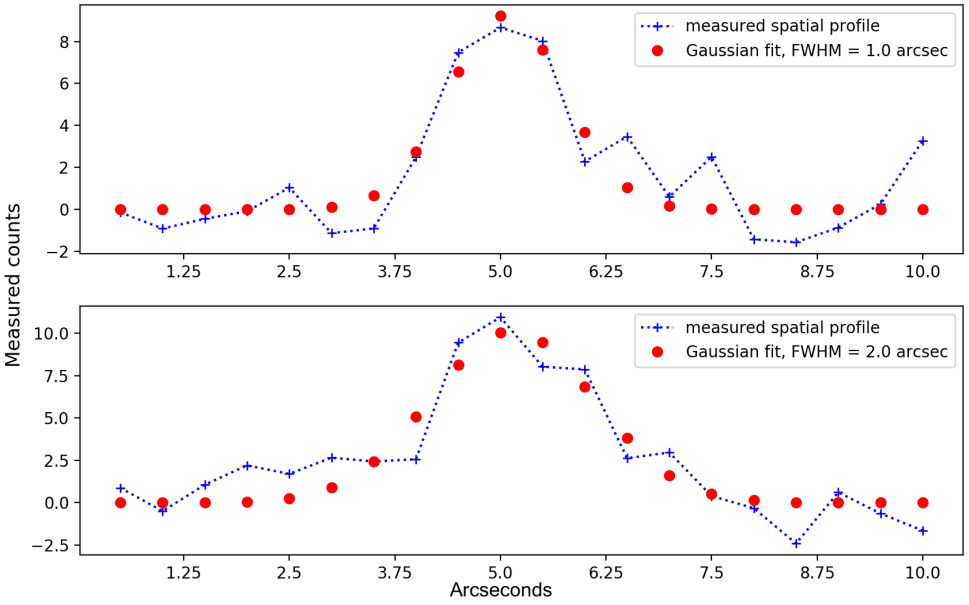

FIGURE 5.46: The spatial profile of the combined source image of IRC +10420 as measured across the centroid in the x-axis (top) and y-axis (bottom).

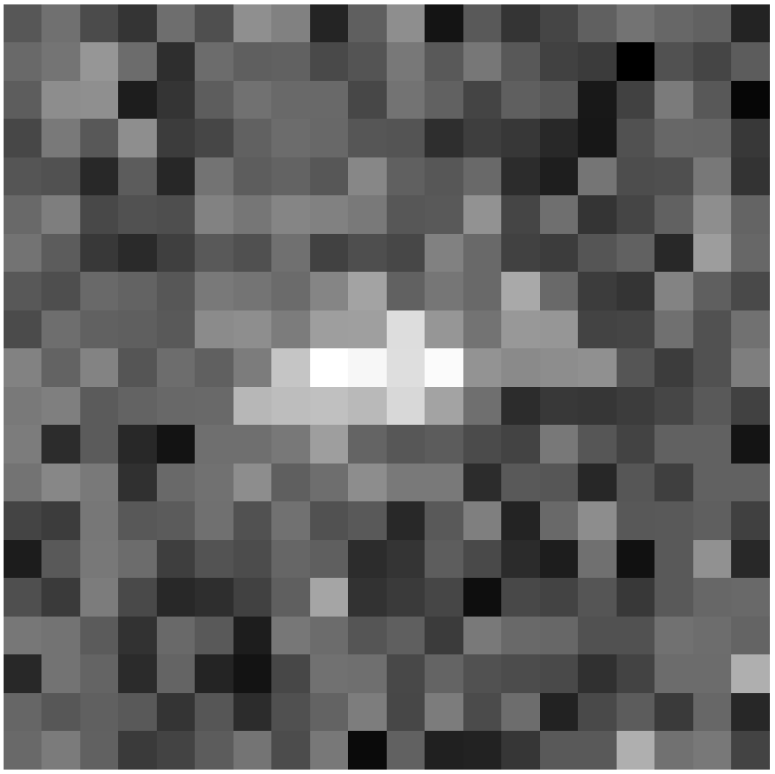

FIGURE 5.47: Combined source image of W Aql.

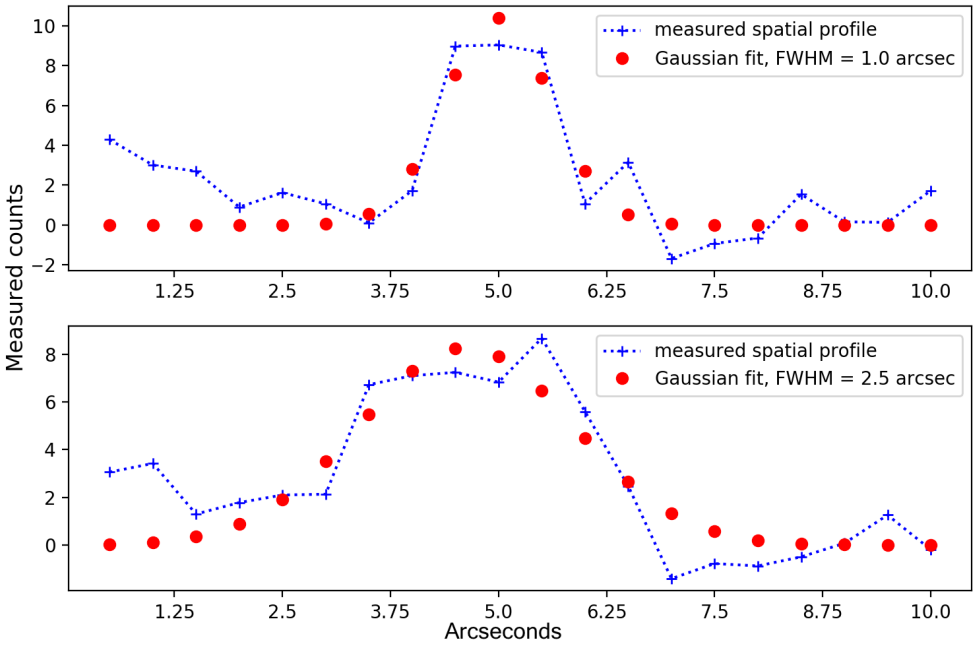

FIGURE 5.48: The spatial profile of the combined source image of W Aql as measured across the centroid in the x-axis (top) and y-axis (bottom).

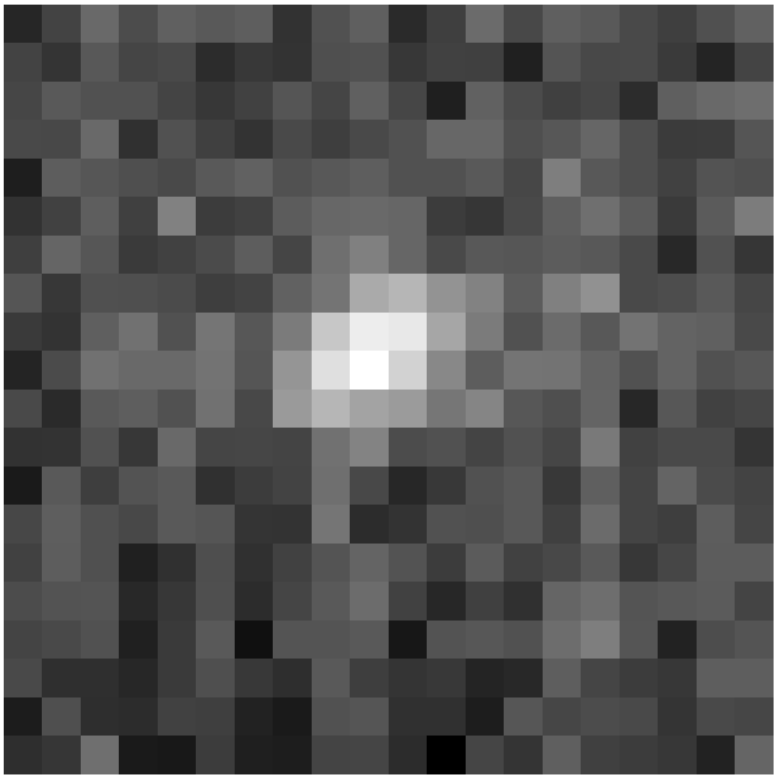

FIGURE 5.49: Combined source image of R Cas.

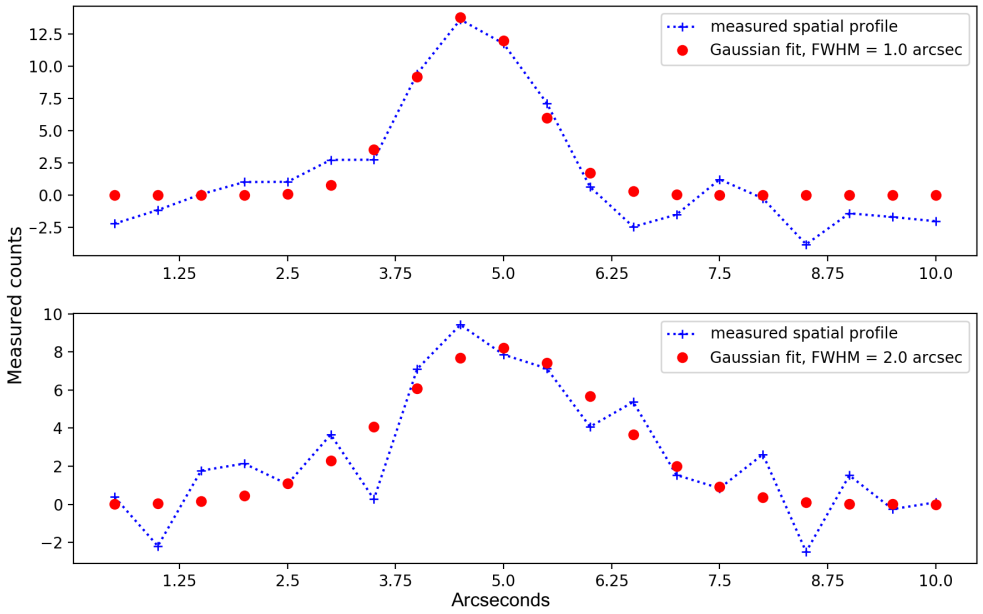

FIGURE 5.50: The spatial profile of the combined source image of R Cas as measured across the centroid in the x-axis (top) and y-axis (bottom).

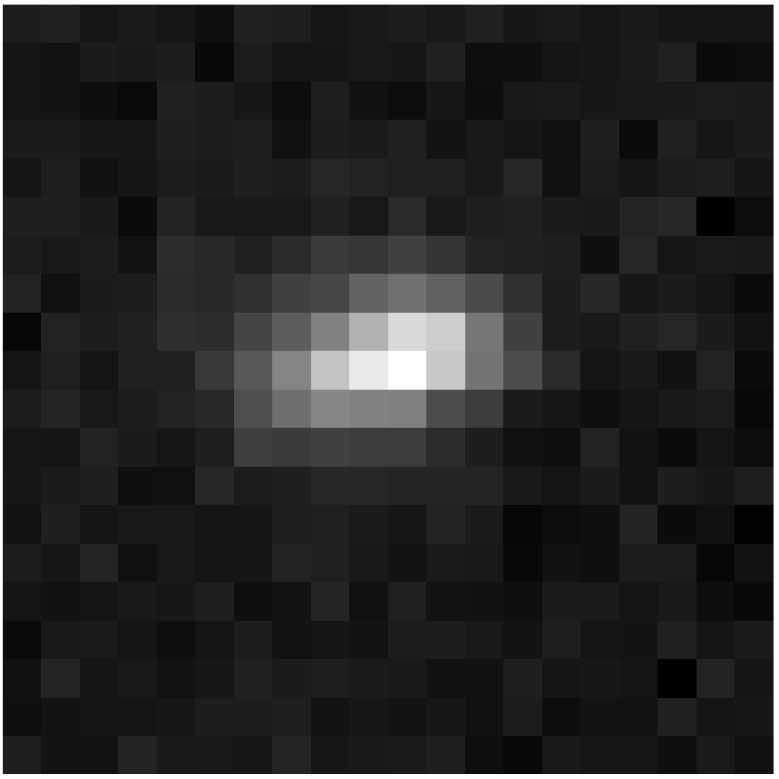

FIGURE 5.51: Combined source image of NML Cyg.

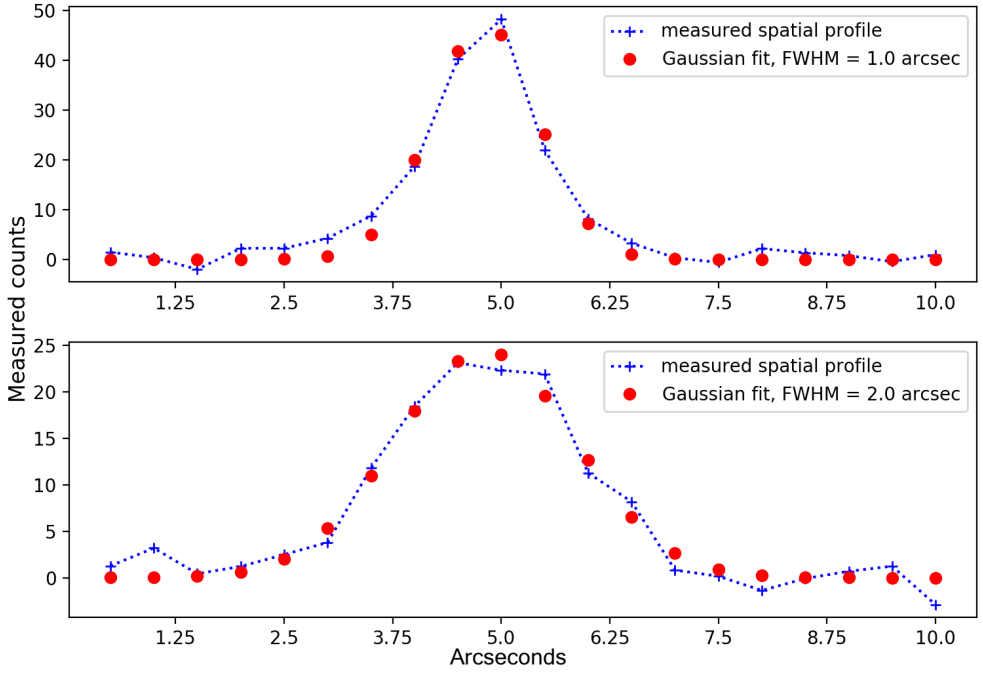

FIGURE 5.52: The spatial profile of the combined source image of NML Cyg as measured across the centroid in the x-axis (top) and y-axis (bottom).

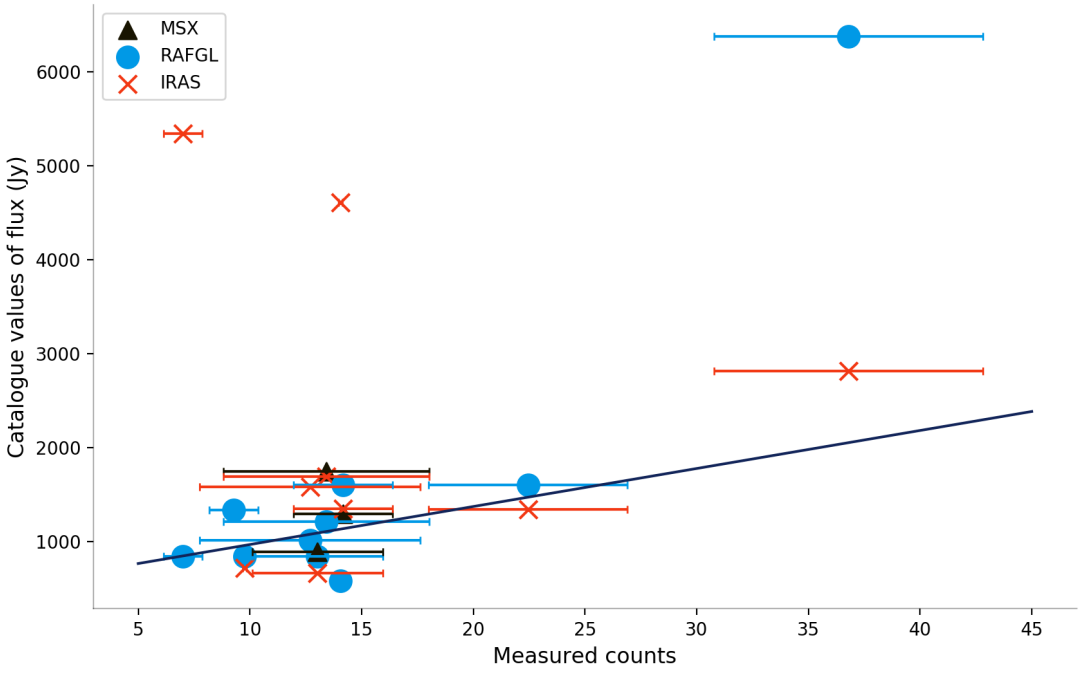

FIGURE 5.53: Counts recorded from reduced observations taken with the instrument plotted against the respective catalogue flux values of each source. Blue dots represent converted RAFGL fluxes, red crosses represent IRAS fluxes and black triangles represent MSX fluxes. Error bars represent ±1 standard deviations. The linear trend line is only fit to sources whose catalogue fluxes are within 30% of each other.

5.4.4 Sensitivity

In chapter 4, we determined that observations of IRC+10216 were at the sensitivity limit of the instrument as no fainter sources were detected. IRC+10216 is a known variable and listed with an RAFGL magnitude of -7.7. However, it was unobservable from the Observatorio del Teide in September 2019, therefore we were unable to make any direct comparisons with the new instrument configuration. The recorded sky background temperatures were similar for observations taken with both telescopes, so it is likely that any improvements to sensitivity are predominantly a result of the chop/nod technique.

Figure 5.53 compares the measured counts of all ten observed sources against their respective catalogue fluxes, with RAFGL magnitudes converted to flux using the conversion factor given by Price et al. (1976). We measured source counts by summing the signal in an aperture for all positive sources present in chop/nod subtracted observations. Aperture size was selected using a curve-of-growth technique to maximise SNR. The horizontal error bars represent ±1 standard deviations. Several of the sources showed significant variability in their catalogue values, so a least-squares linear fit was

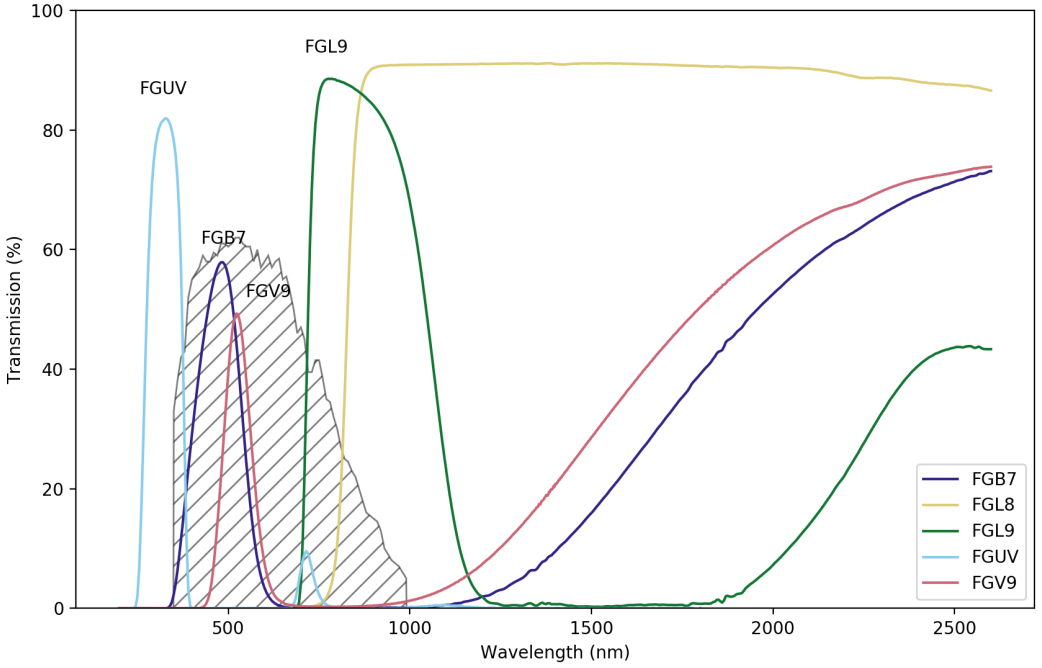

FIGURE 5.54: Transmission curves for the five coloured bandpass filters: FGB7 (435 - 500 nm), FGL9 (721 nm - 1035 nm), FGL830 (830 nm), FGUV11 (275 - 375 nm) and FGV9 (485 - 565 nm). Data provided by Thorlabs. The quantum efficiency of the Thorlabs DCC3240M optical CMOS camera is described by the black hatched region.

made to sources whose catalogue fluxes were within 30% of each other. Although a naive estimate of linearity, based on a select few sources, this positive linear trend indicates the instrument is likely to be functioning as intended. However, a further factor of 10x in sensitivity would be needed to observe typical bright, non-variable standard stars such as Vega, to allow a proper calibration.

5.4.5 Optical system

We were unable to robustly test the performance of the instrument for dual wavelength acquisition due to the time lost for weather. However we found that the optical system proved useful for pointing and we were able to determine the focus of the optical camera and the alignment of the deployable mirror with observations of Saturn in five Thorlabs 25mm diameter, coloured bandpass filters: FGB7 (435 - 500 nm), FGL9 (721 nm - 1035 nm), FGL830 (830 nm), FGUV11 (275 - 375 nm) and FGV9 (485 - 565 nm). The transmission curves of each filter and the quantum efficiency of the camera, plotted from data provided by Thorlabs, can be seen in figure 5.54. Figure 5.55 is a three colour

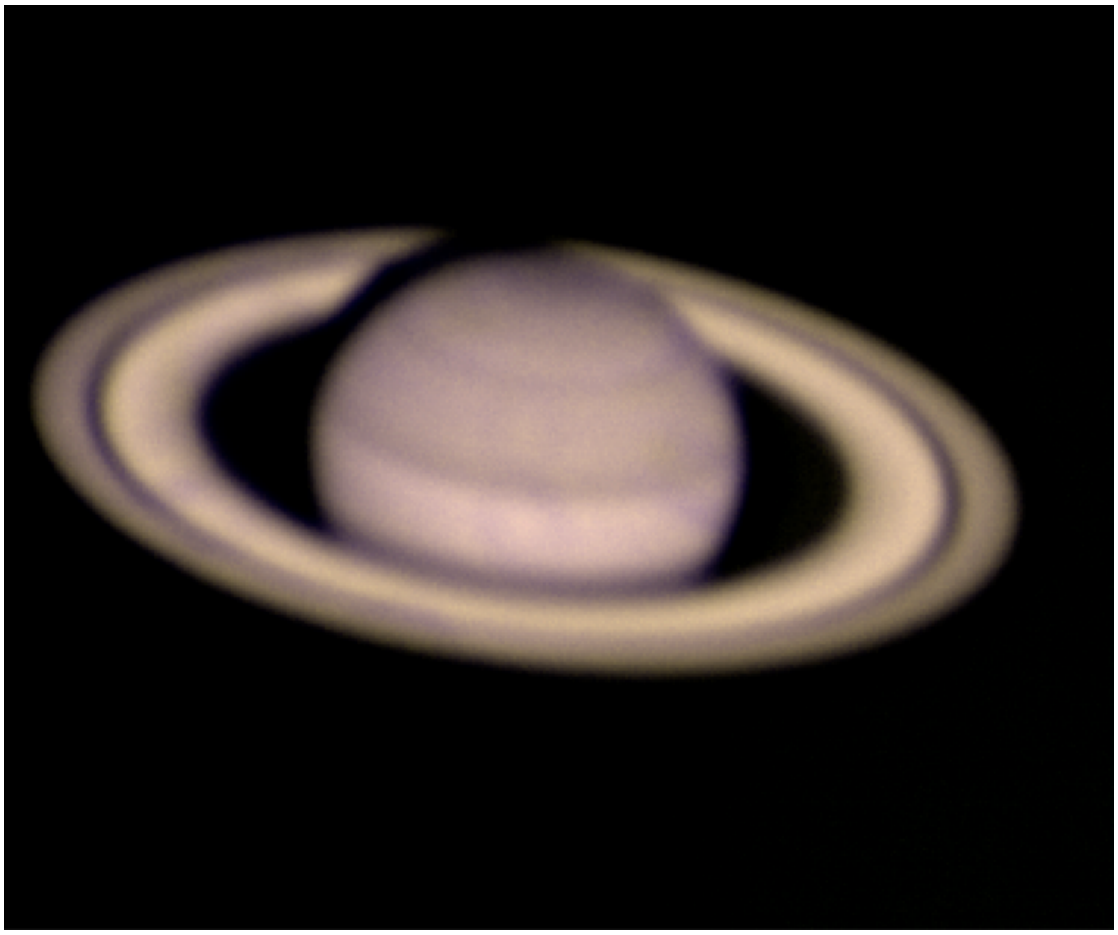

FIGURE 5.55: A three-colour composite of Saturn observations taken with the Thorlabs DCC3240M optical CMOS camera. The filters used to create this image were the Thorlabs FGB7, FGL9 and FGV9.

composite of Saturn observations taken with the FGB7, FGL9 and FGV9 bandpass filters.

5.5 Summary of Chapter

This Chapter describes the further development of the prototype instrument introduced in Chapter 4. To improve on sensitivity, a chopping module wasimplemented into the foreoptics of the system and deployed alongside a telescope nodding routine. This addition was built from commercially available units, at a low cost, much like the rest of the instrument. The instrument was tested on the TCS over 8 nights in 2019 September. A plate scale of $0.5''$ per pixel was recorded on the TCS, indicating that the image is slightly oversampled. Varying nod patterns were tested, with an ABCD pattern being selected as the best fit for the positional accuracy of the telescope and system. After

commissioning, a programme of observations was conducted, with 13 stellar objects selected from the RAFGL catalogue. While ten of these sources were observable with the camera, only four fulfilled the selection criteria of having catalogue values that vary by no more than 30%. The faintest of these sources, according to the values recorded in RAFGL, IRAS and MSX, are V Cyg and IRC +10365, with fluxes in the range of 600 - 900 Jy. This is a vast improvement on previous observations with an unchopped system, as sources $\sim$ 70 times fainter are now observable. The addition of a chop/nod regime puts the system much closer to the previous estimate of a sensitivity limit for the system of 300 Jy for a 60 second integration and is starting to approach that of the bright asteroids ($\sim$ 100 Jy) (Müller & Lagerros, 2002).

The offset speed of the telescope, and the positioning speed of the rotational platform, limited the period at which chopping and nodding could occur. Under these circumstances, the quality of chop/nod background reduction was highly variable, with significant residuals left in several reduced images. Reducing the nod period in particular, to one more in line with those at other infrared facilities, is likely to make some improvements to the sensitivity and quality of data reduction going forward.

Chapter 6

Conclusion and Future work

6.1 Conclusions

In this thesis we provide a three-part analysis of the suitability of uncooled microbolometers in two differing fields; ecology and astronomy. We did so primarily to gain an understanding as to the scientific potential of COTS systems which are readily available and low in cost, unlike most infrared detectors. Referring to the motivating science goals presented in chapter 1.5, this chapter summarises our work, discusses how successful we have been in our aims and presents suggestions on how to build on this work in future studies.

Chapters 1 - 2 provide some context and background for this unusual project. In chapter 2 we introduce the FLIR COTS microbolometer used throughout and present the results from testing three analogous, standard astronomical instrumentation techniques to characterise the random and spatial noise present in the system. These techniques were attempted as a means to optimise the quality of the data for the purpose of application in ecology and astronomy. From flat fielding, stacking and binning we determine that the microbolometer FPA is dominated by large-scale spatial structure noise. We demonstrate how this can be corrected by subtracting median stacks of flat field exposures and determine the in-lab NEdT as $< 60\,\mathrm{mK}$. From this we estimate the minimum change in temperature that can be resolved with the system as $0.2^{\circ}\mathrm{C}$.

In chapter 3, we present an application of the microbolometer system as the primary imager in conservation ecology. We introduce Astro-Ecology, a field that was still in

its infancy at the time of this work, and describe a series of investigations to answer the motivating question: **"How can mid-IR imaging and astronomical data reduction and analysis techniques be applied practically in ecology?"** To answer this question, we determine the feasibility of developing an astronomy-based, fully automated reduction pipeline for mid-IR data collected using UAV technology. During this work we encountered a series of technical challenges when attempting to deploy standard astronomical observing and data-analysis techniques to animal data.

As briefly discussed in section 1.3.1 of the introduction, the mid-IR spectral region is notorious for background-limited observations. Unfortunately, none of the astronomical background reduction techniques would be particularly beneficial for this application, and the effects of detector systematics (as investigated in chapter 2 and section 3.3) can be a limiting factor when attempting to resolve absolute temperature values, often without a standard calibration source. To add to this, UAV technology comes with its own challenges. Namely, restrictive and locally-varying regulations around the time of day and distances that can be flown, and the (although ever improving) limited battery life. From the three field applications described in section 3.5, it can be concluded that each environment comes with its own, potentially unique, set of constraints and restrictions on flying UAVs and collecting mid-IR data. This makes optimising flight strategies for effective data analysis very challenging.

Point source detection in astronomical software relies on three basic principles: thresholding, constraining size and assuming shape (usually that of a 2D Gaussian kernel). Different techniques are deployed for extended source and crowded-field observations, but animal sources in UAV collected data, for even the simplest cases, are significantly more extreme than this. In almost all cases, when applied to mid-IR animal data in section 3.4.1, these three basic principles were observed to fail. Thresholding relies on local temperature maxima, however only in certain environments are animals solely the warmest sources. Environmental features often have comparable or higher surface temperatures, or albedos such that they reflect enough local mid-IR radiation to appear comparable or higher in surface temperature. Fixed size and shape constraints can only be applied to static sources observed without any parallax. Animals are rarely static and change in size and shape depending on viewing angle and body position. Environmental obstruction also contributes to the failure to detect animal sources through constant, fixed size and shape constraints. Any features between the mid-IR detector

and the individual source have the potential to block, absorb or scatter part or parts of the emission from the animal. When data collection is planned for a time at which annual or diurnal ground and ambient air temperatures are such that animals appear warmer than their surroundings, basic astronomy techniques can be used to detect animals. However, applying these principles will always include many erroneous sources (and often will produce multiple detections for a single individual) which require more sophisticated methods to identify and remove.

From section 2.5.4 of chapter 2 we know that, theoretically, temperature changes as low as 0.2°C can be detected, which is beneficial when considering a system that looks for deviations from lateral symmetry, i.e. as a non-invasive diagnostic tool. However, the lack of direct correlation between internal and external body temp, and the scaling of surface body temperatures with local environment make it impossible to predict an absolute temperature for any one individual species. Species identification therefore relies solely on the observed distribution of mid-IR emissions across the body in high resolution imaging. As presented in section 3.4.3, variations in this, what we designate as the 'thermal-profile', arise from individual age, health, body position, viewing angle and environmental obstruction. Although not directly observed, it can also be assumed that the 'thermal-profile' of a given species would also vary with extreme environmental to body temperature gradients, i.e. the variation in emitting regions as a result of homeostasis in very cold and very hot environments where heat loss is either being avoided or actively encouraged. Therefore, to deploy automatic detection and identification to avoid a data analysis bottleneck and to reduce the need for human identification (which is proven to be an unreliable means of detecting animal presence and identifying species in conservation survey data) requires a more complex and specialised algorithm, most likely machine-learning-based, than those used on standard photometric observations in astronomy.

The investigations presented in Chapter 3 will be essential in directing the burgeoning field of Astro-Ecology towards achievable goals that could have a lasting impact on animal conservation ecology. In Section 3.6 we conclude with a more thorough discussion of the goals of the field, and whether they are achievable with the current pipeline framework.

In chapter 4, we present the development of a low-cost instrument for mid-IR, ground

based observing built from a FLIR microbolometer to answer the motivating question: **"How can we develop inexpensive ground-based instruments for mid-IR observations?"** In section 4.3 a 'back of the envelope' feasibility study is described, wherein we make some basic predictions of a -1 mag sensitivity limit for the instrument based on the NEdT determined in Section 2.5.4 and some basic measurements of the emissivity of the LT. This precedes the optical design of the system, described in Section 4.4. Simple adjustable germanium reimaging optics, comprised of a field lens and collimator lens, were used to rescale the plate scale of the LT for the detector. We describe the mechanical design of the system in Section 4.5 and the steps taken to allow remote control of the instrument for use on the LT. We describe an approximate conversion of read-out values into raw counts and the correction of images using Gaussian maps in Section 4.6. These calibration steps were used to correct the large-scale spatial noise, as described in Chapter 2, without any inter-observation background calibration. Using these calibrations, we evaluate the performance of the system, as commissioned on the LT, in Section 4.7. From our observations we confirm the expected plate scale of $0.75''$ per pixel and determine that the instrument has a stability of $\sim 10\%$. We show that, as expected, the instrument performance is limited by the overwhelming, and rapidly varying, mid-IR background. This chapter concludes with section 4.7.4, where we present a short study into the variation in lunar regolith properties, as observed during a total lunar eclipse.

In Chapter 5, we present further development of the instrument to allow for background reduction during observations to answer the motivating question: **"What techniques can we use to improve the performance of these instruments?"** We describe the adjustment to the optical design for use on the TCS to include a chopping mirror in the foreoptics of the system in Section 5.2. We detail the mechanical construction of the instrument from low-cost COTS components, and the inclusion of an optical camera system and deployable dichroic mirror in Section 5.3. We discuss the design of software to trigger data acquisition and control the additional moving platforms in parallel, and outline the software which reduces the chop and nod observations. In Section 5.4 we describe the commissioning and alignment of the instrument on the TCS. We report on the full background subtraction process, where we couple chopping observations using the mirror in the foreoptics with nodding the telescope through 4 different positions, in Section 5.4.1. While an ABBA nod pattern is the standard, we found that the

positional accuracy of the TCS was not sufficient to precisely re-align the A and B positions and in Section 5.4.1.1 we present investigations into two other nod patterns: ABBC and ABCD. All subsequent data, as presented in Section 5.4.3, were taken with an ABCD nod pattern. In Section 5.4.4 we demonstrate a sensitivity improvement of $\sim$ 4 magnitudes as a result of introducing a chopping/nodding regime. We conclude that, while a drastic improvement, the system is still limited to observations of the brightest mid-IR sources and, as estimated in Section 4.3, observing standard calibration sources may be unfeasible given the measured NEdT of the system.

6.2 Future Work

The future of Astro-Ecology is in pairing machine learning and innovative UAV technology to take species survey data, and in coupling RGB imaging with mid-IR imaging. The sensitivity of the system is sufficient that any improvements in the use of COTS microbolometers in this application are more likely to come from improvements in the data collection and analysis methods. As briefly discussed in Chapter 3.6, developing the machine learning component is the primary focus of McWhirter et al. (2019). The development of comprehensive flying strategies, specific for the survey environment, has been identified as an important component of optimising data collection for machine-learning analysis. This has been the subject of ongoing study by Burke et al. (2018a,b, 2019a,b,c), who have continued adapting and developing the field in response to the investigations presented in this thesis. The detection and identification of terrestrial species requires an analysis pipeline that uses movement to distinguish animals from environmental features that may have comparable mid-IR emissions, and takes a statistical approach to recognise behaviours that may be unique to species, e.g. using the fore-knowledge of which species are endemic to the region and how they interact with their environment and each other to aid in identification. To overcome the limitations of using mid-IR imaging to detect and identify species, as presented in this thesis, it has been proposed that RGB imaging should be used in tandem to aid in identifying areas of interest that have been detected in the mid-IR.

At the time of writing, there are many, much-anticipated advancements in ground- and space-based mid-IR observing facilities coming in the next decade, e.g. JWST. Any resulting advancements in mid-IR instrumentation may show a 'trickle down' effect into

COTS systems. For these systems to prove useful in mid-IR observing, a significant improvement to the NEdT of uncooled systems would be necessary to achieve the sensitivities needed to increase the sample size of observable stars and become scientifically useful.

One current example of where current COTS technology could prove useful is the ongoing monitoring of Betelgeuse, which is recorded in the RAFGL catalogue as having an 11μm magnitude of -5.6. Recently, the visual brightness of this red supergiant has been observed to dim significantly, which has been widely theorised as an indicator of imminent core collapse. Gehrz et al. (2020) have used N-band observations to demonstrate that the mid-IR magnitude of Betelgeuse is unchanged and thus, they have attributed the visual dimming to local surface phenomena rather than a change in overall energy output from the star.

However, there are several modifications that could be undertaken to achieve small improvements in sensitivity that could allow for monitoring of bright variable systems and Solar System planetesimals like asteroids. Sensitivity improvements could be made by decreasing the chop and nod period to those more in line with other facilities ($\sim 10 - 50$Hz for chopping and ~ 0.1Hz for nodding). This would require replacing the rotational platform for one with a quicker response/positioning time and commissioning the instrument on a facility optimised for fast nodding. This would also be likely to improve the positional accuracy of the nod and allow a standard ABBA nod pattern to be used.

Zinc Selenide (ZnSe) is a commonly used material for mid-IR optics. When coated it has $\sim>$ 97% transmission over the entire $7.5 - -13.5\,\mu$m wavelength range of the detector. Replacing the germanium optics, which achieves the same transmission but in the reduced spectral window of 8-12μm, with ZnSe and introducing a bandpass filter to limit wavelengths to the range of the detector could limit unwanted background contribution and make minor improvements to sensitivity.

On a manufacturing level, sensitivity improvements could be achieved by cooling the system to the lower end of the operational temperature range (see table 2.1) with the addition of a low-cost ($<$ 100 GBP) thermoelectric cooler (i.e. a cooling system that operates via the Peltier effect). While this wouldn't achieve sensitivity levels comparable

to cryogenically cooled systems, this could reduce the effect of thermal drift and thus decrease the frequency of FFC events.

Theoretically, increasing the aperture of the telescope on which the system is commissioned could also yield a sensitivity improvement by increasing the flux received at the detector. However, scaling up the telescope usually requires scaling up the instrumentation. This re-design of the optics would likely increase the overall cost of the system, with COTS optics suitable for mid-IR transmission only available in sizes up to 50mm and cost increasing drastically for custom pieces.

We have learned a great deal during the work described in this thesis. As discussed in the Introduction, there is great potential in astronomical observing in the mid-IR. Microbolometer technology will never be competitive with the cooled technologies employed at the major, large-aperture facilities. However, it is our hope that employing COTS systems at smaller facilities in future could provide the opportunity to expand at low cost the availability of mid-IR observing and, in particular, provide a key resource to train students and early career researchers on mid-IR observing techniques and data analysis.

Appendix A

Code for Part II.

CODE A.1: Python pipeline for Astro-Ecology. This code applies an adaptive threshold and a size parameter to detect sources in data.

```
#!/usr/bin/env python2.7
# -*- coding: utf-8 -*-

####### Import relevant modules #######
import cv2
import cv2.cv as cv
import os
import numpy as np
import matplotlib.pyplot as plt
import ast
import sys
from progress.bar import IncrementalBar

plt.ion()

########## Replaces non valid data in array with zeros ##############
def numpy_fillna(data):
    # Get lengths of each row of data
    lens = np.array([len(i) for i in data])
    # Mask of valid places in each row
    mask = np.arange(lens.max()) < lens[:,None]
    # Setup output array and put elements from data into masked positions
    out = np.zeros(mask.shape, dtype=np.uint64)
    out[mask] = np.concatenate(data)
    return out

########## Convert from list to array #############
def arrconv(list):
   list = np.asarray(list)
   array = numpy_fillna(list)
   array = array[array!=0]
   return array

########## Returns filelist and directory #############
```

```
def files(directory, type):
    files = [file for file in os.listdir(directory) if file.endswith(type)]
    file_list = np.asarray(files)
    return file_list

########## Asks user to pre-define parameters needed for code #############
def co_param():
    Mi_arr = input('Minimum Size of object (pixels)?')
    Ma_arr = input('Maximum Size of object (pixels)?')
    Per_thr = input('Desired Threshold (%)?')
    return Mi_arr, Ma_arr, Per_thr

########## Changes image from uint16 to uint8 #############
def framegray(image):
    gray = image.copy()
    gray = gray*(1/256.)
    gray = np.uint8(gray)
    return gray

def framefusion(image):
    gray = (image*0.04)-273.14
    gray = np.uint8(gray)
    return gray

########## Thresholds image & produces a mask #############
def mask(grey_image, thresh_per):
    thresh = np.percentile(grey_image.ravel(),thresh_per)
    mask = np.where(grey_image <= thresh)
    resim0 = grey_image.copy()
    resim0[mask] = 0
    return resim0

########## Removes noise & finds contours #############
def cont(masked_img, min_area, max_area):
    kernel = np.ones((10,10),np.uint8)
    resim = cv2.dilate(masked_img,kernel,iterations = 1) # resim0 after dilation
    contours, heirarchy = cv2.findContours(resim,
     cv2.RETR_EXTERNAL,cv2.CHAIN_APPROX_SIMPLE)
```

```
    contours = [contour for contour in contours if
     cv2.contourArea(contour)>=min_area and cv2.contourArea(contour)<=max_area]
    return contours, resim

########## Finds the area of contours & the average temp of pixels within
     contour #############
def param_cont(contours, resim, original):
    arealist_frame = []
    meanlist_frame = []
    cimglist_frame = []
    stdlist_frame = []
    for i in range(len(contours)):
        cimg = np.zeros_like(resim)
        cv2.drawContours(cimg, contours, i, color=255, thickness=-1)
        pts = np.where(cimg == 255)
        area = len(pts[0])
        arealist_frame.append(area)
        meanlist_frame.append(np.mean(original[pts])*0.04)
        stdlist_frame.append(np.std(original[pts])*0.04)
        cimglist_frame.append(cimg)
    return arealist_frame, meanlist_frame, stdlist_frame

########## Draws contour on original frame #############
def draw_cont(image, contours):
    for i in range(len(contours)):
        cv2.drawContours(image, contours, i,(0,0,0), 1)
    return image

########## Displays contours on an RGB frame #############
def show(img_list):
        plt.figure('Track')
        for i in img_list:
            plt.imshow(i)
            plt.axis('off')
            plt.show()
            plt.draw()
            plt.pause(0.001)
            plt.clf()
```

```
        plt.close()

########## Crops original image using contour coordinates #############
def crop(image, coords_array, border):
    min = np.min(coords_array, axis=0)
    max = np.max(coords_array, axis=0)
    min_x, min_y = min[0][0]-border, min[0][1]-border
    max_x, max_y, = max[0][0]+border, max[0][1]+border
    c_img = image[min_y:max_y, min_x:max_x]
    return c_img

########## Showing crops #############
def showcrop(crop_array, coords_array, number):
    x = len(crop_array)
    plt.figure('frame '+ str(number))
    for i,v in enumerate(xrange(x)):
        v = v+1
        plt.subplot(x,1,v)
        plt.xticks([])
        plt.yticks([])
        plt.title('Frame '+ str(number) +' detection '+ str(v))
        plt.imshow(crop_array[i])
    pick = raw_input("Remove which crops [i]?: ") or '42'
    if pick == '42':
        plt.close()
    else:
        li = ast.literal_eval(pick)
        crop_array = np.delete(crop_array, li, axis=0)
        coords_array = np.delete(coords_array, li, axis=0)
        plt.close()
    return crop_array,coords_array

########## Saving Video of Detections #############
def save_vid(detec_array, frame_rate, output_name):
    video = cv2.VideoWriter(output_name,-1,frame_rate,(640,512))
    for i in range(0,len(detec_array)):
        video.write(detec_array[i])
    video.release()
```

```
    return video

########## Initialise directories and empty lists #############
directory = sys.argv[1]
rgb_dir = sys.argv[2]
file_list = files(directory, '.tif')
jpg_list = files(rgb_dir, '.png')
arealist = []
meanlist = []
stdlist = []
framelist = []
croplist = []

bar = IncrementalBar('Processing', max=len(file_list), suffix='%(percent)d%%')
min_arr, max_arr, p_thresh = co_param()

for file_number,file in enumerate(file_list):
    bar.next()
    framecount = file_number
    frame = cv2.imread(directory+'/'+file, -1)
    frame = frame[:, :465]
    jpg = cv2.imread(rgb_dir+'/'+jpg_list[framecount], -1)
    jpg = jpg[:,:640]
    if framecount==0:
        maxframe = jpg.max()
        minframe = jpg.min()
    #gray_img = framegray(frame)
    gray_img = framefusion(frame)
    mask_img = mask(gray_img, p_thresh)
    contour_list, dilate_img = cont(mask_img, min_arr, max_arr)
    crops = [crop(frame, i, 50) for i in contour_list]
    means = []
    area_cont, mean_cont, std_cont = param_cont(contour_list, dilate_img, frame)
    arealist.append(area_cont)
    meanlist.append(mean_cont)
    stdlist.append(std_cont)
    for_show = draw_cont(jpg, contour_list)
    framelist.append(for_show)
```

```
    croplist.append(crops)
bar.finish()
# show(framelist)
# save_vid(framelist, 7)
```

Appendix B

Code for Part III.

CODE B.1: Shell script to initialise data acquisition of the instrument as described in chapter 4. This script wraps the camera control code (see code B.2) and the display code (see code B.3) to ensure they run simultaneously and that any data output is stored in a new directory

```
#run_camera.sh
d=$(date +%d%m%y%H%M%S)
echo $d
mkdir $d
echo made
cd $d
camera_code | python display.py
```

CODE B.2: C++ code to control the instrument as described in chapters 4 and 5. Data acquisition is triggered using the tauRawBitmap library provided with the Thermal Grabber USB OEM. Data are saved to fits files with very basic fits headers and the following naming convention ddmmyy_hhmmss.sss

```
// camera_code.cpp
 #include "thermalgrabber.h"
 #include "stdbool.h"
 #include "cstdlib"
 #include "iostream"
 #include "chrono"
 #include "thread"
 #include "cstdint"
 #include "cstring"
 #include "fitsio.h"
 #include "string"
 #include "unistd.h"
 #include "stdio.h"
 #include "time.h"
 #include "sys/time.h"
 #include "math.h"
 ThermalGrabber* tGr;
int count=0;
 class Test
 {
 public:
     void test();
 };
 void callbackTauImage(TauRawBitmap& tauRawBitmap, void* caller)
 {
   count = count+1;
   std::cout << "updateTauRawBitmap -> w/h: " << tauRawBitmap.width << "/" <<
    tauRawBitmap.height << " min/max: " << tauRawBitmap.min << "/" <<
    tauRawBitmap.max << "time" << tauRawBitmap.pps_timestamp << std::endl;
     unsigned int mWidth = tauRawBitmap.width;
     unsigned int mHeight = tauRawBitmap.height;
```

```
    unsigned int t = tauRawBitmap.pps_timestamp;
    unsigned short* d = tauRawBitmap.data;
    time_t nowbin;
    struct tm *timeinfo;
    char buffer [5000];
    int millisec;
    struct tm* tm_info;
    struct timeval tv;
    gettimeofday(&tv, NULL);
    millisec = lrint(tv.tv_usec/1000.0);
    if (millisec>=1000) {
      millisec -=1000;
      tv.tv_sec++;
    }
    tm_info = localtime(&tv.tv_sec);
    strftime (buffer,5000,"%d%m%y_%H%M%S", tm_info);
    char name [5000];
    sprintf(name, "%s.%03d", buffer, millisec);
    if(count > 15){
    fitsfile *fptr;
    long naxes[2];
    int fits_status=0;
    char s[5000];
    sprintf(s, "%s.fits", name);
    unlink("/tmp/expose");
    symlink(s, "/tmp/expose");
    fits_create_file(&fptr, s, &fits_status);
    naxes[0]=mWidth;
    naxes[1]=mHeight;
    fits_create_img(fptr, SHORT_IMG, 2, naxes, &fits_status);
    fits_write_img(fptr, TSHORT, 1, mWidth*mHeight, d, &fits_status);
    fits_write_key(fptr, TSTRING, "TIME", buffer, "[UTC] Start of obs.",
   &fits_status);
    fits_close_file(fptr, &fits_status);
    }
}
void Test::test()
{
```

```
    std::cout << "Test" << std::endl;
    tGr = new ThermalGrabber(callbackTauImage, this, "FT2K5V70");
    tGr->enableTLinearHighResolution();
    std::this_thread::sleep_for(std::chrono::milliseconds(2000000));
    delete tGr;
}
int main()
{
    std::cout << "main:" << std::endl;
    {
        Test* t = new Test();
        t->test();
        delete t;
    }
    return 0;
}
```

CODE B.3: Python code to display fits files as they are downloaded from the camera, with a < 0.5s delay

```
# display.py
# !/usr/bin/python3

import os
from astropy.io import fits
import matplotlib.pyplot as plt
import time

time.sleep(2)

dst = '/tmp/expose'
imcapture = 0
plt.ion()
plt.figure()
before = 0
while imcapture == 0:
   path = os.readlink(dst)
   if before == path:
      imcapture = 1
   im = fits.open(path)
   image_data = im[0].data
   plt.title(path)
   plt.imshow(image_data)
   plt.xticks([])
   plt.yticks([])
   plt.pause(0.1)
   before = path
plt.close()
```

CODE B.4: Python code to control rotation stage through chop sequence. Timestamps at the beginning and end of each chop throw are written to a csv file

```
#chop.py

import serial
import time
import sys
import numpy as np
import datetime
import os
cwd = os.getcwd()

rotser = serial.Serial(port = "/dev/ttyrot", baudrate = 9600, parity =
    serial.PARITY_NONE, stopbits = serial.STOPBITS_ONE, bytesize =
    serial.EIGHTBITS, timeout = 1, xonxoff = False, rtscts = False, dsrdtr =
    False, writeTimeout = 2)

rotser.close()

try:
   rotser.open()
except Exception as e:
   print(e)
   exit()

f = open(cwd+"/chop_cycles.csv", "w+")
rotser.write("TX 0in")
time.sleep(1.5)
response = rotser.readline()
print(">> " + response)
rotser.write("TX 0ho1")
time.sleep(2)
rotser.write("TX 0ma0000E16E")
time.sleep(1.5)
print('In position')
loop = 0
```

```
while loop == 0:
      f.close()
      cycle = []
      cycle_start = str(datetime.datetime.now())
      rotser.write("TX 0mr0000018E")
      time.sleep(0.25)
      rotser.write("TX 0mrFFFFFE72")
      cycle_end = str(datetime.datetime.now())
      time.sleep(0.8)
      cycle = cycle_start + " ; " + cycle_end
      f = open(cwd+"/chop_cycles.csv", "a+")
      f.write(cycle)
      f.write("\n")
      f.close()
```

CODE B.5: Python code to reduce observations. Observations are read and sorted into chopped and unchopped exposures using the timestamp csv file written in code B.4. Observations that are likely to be taken during motion of the rotational platform are removed. The nth observation in a chopped set is subtracted from the nth observation in the previous unchopped set. The resulting chop subtracted observations are stacked and saved.

```
import sys
import numpy as np
import csv
import os
from astropy.io.fits import getheader
from astropy.io import fits
import scipy.ndimage as ndimage
from scipy.ndimage import gaussian_filter

def fopen(dir, file):
   im = fits.open(dir+'/'+file, memmap=False)
   im = im[0].data
   im = im.astype('float64')
   return im

def save(im, dir, file):
   new = fits.PrimaryHDU(im)
   new = fits.HDUList([new])
   new.writeto(dir+'/'+file)
   return

############################################################
wd = sys.argv[1]
cycles_d = wd+'/chop_cycles.csv'
cycles = []

with open(cycles_d, 'r') as c:
   reader = csv.reader(c)
   for row in reader:
```

```
        start = row[0][11:13]+row[0][14:16]+row[0][17:26]
        end = row[0][40:42]+row[0][43:45]+row[0][46:55]
        j = start,end
        cycles.append(j)


fit_file = [file for file in sorted(os.listdir(wd)) if file.endswith('.fits')]
im_time = [char[7:17] for char in fit_file]

chopped = []
index_chop = []
for x in range(0, len(cycles)):
    inter_chop = []
    un_chop = []
    start = cycles[x][0]
    end = cycles[x][1]
    for y in range(0, len(im_time)):
        if im_time[y] >= start and im_time[y] <= end:
            inter_chop.append(fit_file[y])
            un_chop.append(y)
    chopped.append(inter_chop)
    index_chop.append(un_chop)
os.mkdir(wd+'/subs')
reduced_im = []

for L in range(2,len(index_chop)):
    if len(index_chop[L]) == 0:
        continue
    if len(index_chop[L-1]) == 0:
        continue
    useful_chop_i = index_chop[L][1:-1]
    useful_chop_f = chopped[L][1:-1]

    data = index_chop[L-1][-1]+1, index_chop[L][0]-1
    data_i = np.arange(data[0], data[1]+1, 1)
    useful_data_i = data_i[1:-1]
    if len(index_chop[L]) == len(data_i):
        for G in range(0, len(useful_chop_i)):
```

```
            try:
               u= fopen(wd, fit_file[useful_data_i[G]])
            except Exception as e:
               continue
            try:
               c = fopen(wd, useful_chop_f[G])
            except Exception as e:
               continue
            s = u-c
            reduced_im.append(s)
      if len(index_chop[L]) < len(data_i):
         for H in range(0, len(useful_chop_i)):
            try:
               u= fopen(wd, fit_file[useful_data_i[H]])
            except Exception as e:
               continue
            try:
               c = fopen(wd, useful_chop_f[H])
            except Exception as e:
               continue
            s = u-c
            reduced_im.append(s)
      if len(index_chop[L]) > len(data_i):
         for K in range(0, len(useful_data_i)):
            try:
               u= fopen(wd, fit_file[useful_data_i[K]])
            except Exception as e:
               continue
            try:
               c = fopen(wd, useful_chop_f[K])
            except Exception as e:
               continue
            s = u-c
            reduced_im.append(s)

mean_stack = np.mean(reduced_im, axis=0)
new = fits.PrimaryHDU(mean_stack)
new1 = fits.HDUList([new])
```

```
new1.writeto(wd+'/subs/Meanstack.fits')
```

Bibliography

Absil O., Bakker E., Schöller M., Gondoin P., 2004, Proceedings of SPIE - The International Society for Optical Engineering

Adams J. D., et al., 2012, The Astrophysical Journal, 749, L24

Ancrenaz M., Goossens B., Gimenez O., Sawang A., Lackman-Ancrenaz I., 2004, Animal Conservation, 7, 375–385

Ancrenaz M., et al., 2005, Plos Biology, 3 (1), 30

Armus L., et al., 2007, The Astrophysical Journal, 656, 148

Aryasomayajula S., Reddy Y., 2008, Journal of Physics D: Applied Physics, 41, 195108

Astropy Collaboration et al., 2013, Astronomy & Astrophysics, 558, A33

Bakes E. L. O., Tielens A. G. G. M., 1994, in Cutri R. M., Latter W. B., eds, Astronomical Society of the Pacific Conference Series, Vol. 58, The First Symposium on the Infrared Cirrus and Diffuse Interstellar Clouds. p. 412

Barasona J. A., Mulero-Pázmány M., Acevedo P., Negro J. J., Torres M. J., Gortázar C., Vicente J., 2015, PLOS ONE, 9, 1

Barr E. S., 1961, Infrared Physics, 1, 1,IN1,3,IN3

Barr E. S., 1963, Infrared Physics, 3, 195,IN1,197,IN3,201

Beasor E. R., Davies B., 2016, Monthly Notices of the Royal Astronomical Society, 463, 1269

Beichman C. A., Neugebauer G., Habing H. J., Clegg P. E., Chester T. J., 1988, in Infrared Astronomical Satellite (IRAS) Catalogs and Atlases.Volume 1: Explanatory Supplement..

Benirschke D., Howard S., 2017, Optical Engineering, 56, 1

Bernstein M. P., Sandford S. A., Allamandola L. J., Gillette J. S., Clemett S. J., Zare R. N., 1999, Science, 283, 1135

Bertero M., Boccacci P., Robberto M., 2000, Publications of the Astronomical Society of the Pacific, 112, 1121

Black J. H., van Dishoeck E. F., 1987, The Astrophysical Journal, 322, 412

Boltzmann L., 1884, Annalen der Physik, 258, 291

Bonanno A., Li A., Bernold L., 2015, in Earth and Space: Engineering for Extreme Environments. pp 434–443

Bonnin N., Van Andel A. C., Kerby J. T., Piel A. K., Pintea L., Wich S. A., 2018, Drones, 2 (2), 17

Boss A. P., 2008, The Astrophysical Journal, 677, 607

Bouwman J., Meeus G., de Koter A., Hony S., Dominik C., Waters L. B. F. M., 2001, Astronomy & Astrophysics, 375, 950

Bouwman J., et al., 2008, The Astrophysical Journal, 683, 479

Brande J., Barclay T., Schlieder J. E., Lopez E. D., Quintana E. V., 2020, The Astronomical Journal, 159, 18

Britavskiy N. E., Bonanos A. Z., Mehner A., García-Álvarez D., Prieto, J. L. Morrell N. I., 2014, A&A, 562, A75

Buckland S. T., Anderson D. R., Laake J. L., 2001b, Introduction to Distance Sampling. Oxford University Press.

Buckland S., Anderson D., Burnham K., Laake J., Borchers D., Thomas L., 2001a, Introduction to Distance Sampling: Estimating Abundance of Biological Populations. Oxford University Press, United Kingdom

Buckland S. T., Anderson D. R., Burnham K. P., Laake J. L., Borchers C. L., Thomas L., 2004, Advanced Distance Sampling: Estimating Abundance of Biological Populations.. Oxford University Press.

Buckland S. T., Anderson D. R., Burnham K. P., Laake J. L., Borchers C. L., Thomas L., 2008, 64, 997

Buckland S. T., Plumptre A., Thomas L., Rexstad E. A., 2010, International Journal of Primatology, 31 (5), 833

Bullock M. A., Stoker C. R., McKay C. P., Zent A. P., 1994, Icarus, 107, 142

Burgdorf M., Orton G., van Cleve J., Meadows V., Houck J., 2006, Icarus, 184, 634

Burke C., Rashman M., McAree O., Hambrecht L., Longmore S., Piel A., Wich S., 2018b.

Burke C., Rashman M., Wich S., Symons A., Theron C., Longmore S., 2018a, International Journal of Remote Sensing

Burke C., et al., 2019a, Drones, 3, 23

Burke C., McWhirter P. R., Veitch-Michaelis J., McAree O., Pointon H. A., Wich S., Longmore S., 2019b, Drones, 3, 78

Burke C., Rashman M., Longmore S., McAree O., Glover-Kapfer P., Ancrenaz M., Wich S., 2019c, Journal of Unmanned Vehicle Systems, 7

Burrows A., Hubbard W. B., Lunine J. I., Marley M., Guillot T., Saumon D., Freedman R. S., 1997, in Soderblom D., ed., Astronomical Society of the Pacific Conference Series, Vol. 119, Planets Beyond the Solar System and the Next Generation of Space Missions. p. 9

Cabrit S., Flower D. R., Pineau des Forêts G., Le Bourlot J., Ceccarelli C., 2004, Astrophysics & Space Science, 292, 501

Cameron R. M., 1976, Sky and Telescope, 52, 327

Cami J., Yamamura I., 2001, Astronomy & Astrophysics, 367, L1

Canal D., Mulero-Pázmány M., Negro J. J., Sergio F., 2016, PLOS ONE, 11, 1

Caputi K. I., 2007, arXiv e-prints, p. arXiv:0706.4369

Ceballos G., Ehrlich P. R., Barnosky A. D., García A., Pringle R. M., Palmer T. M., 2015, Science Advances, 1

Chrétien L.-P., Théau J., Ménard P., 2015, International Archives of the Photogrammetry, Remote Sensing and Spatial Information Sciences, XL-1/W4

Chrétien L.-P., Théau J., Ménard P., 2016, Wildlife Society Bulletin, 40, 181

Ciesla F. J., Cuzzi J. N., 2006, Icarus, 181, 178

Clarke A., Rothery P., 2008, Functional Ecology, 22, 58

Cohen M., Walker R. G., Barlow M. J., Deacon J. R., 1992, The Astronomical Journal, 104, 1650

Cohen M., Walker R. G., Carter B., Hammersley P., Kidger M., Noguchi K., 1999, The Astronomical Journal, 117, 1864

Collins K., du Toit J. T., 2016, African Journal of Ecology, 54, 195

Cox A. N., 2000, Allen's Astrophysical Quantities

Crepeau J., 2009, in Proceedings of the ASME Summer Heat Transfer Conference HT2009.

Cruikshank D. P., 1988, Astrophysical Letters and Communications, 27, 97

Dalal N., Triggs B., 2005, in Proceedings of the 2005 IEEE Computer Society Conference on Computer Vision and Pattern Recognition (CVPR'05) - Volume 01. CVPR '05. IEEE Computer Society, pp 886–893

Dempsey J. T., et al., 2013, Monthly Notices of the Royal Astronomical Society, 430, 2534

Deutsch L. K., Hora J. L., Adams J. D., Kassis M., 2003, in Iye M., Moorwood A. F. M., eds, Society of Photo-Optical Instrumentation Engineers (SPIE) Conference Series Vol. 4841, SPIE Conference Proceedings. pp 106–116, doi:10.1117/12.461436

Dole H., et al., 2006, Astronomy & Astrophysics, 451, 417

Dollfus A., 2000, Icarus, 146, 430

Duley W. W., Williams D. A., 1981, Monthly Notices of the Royal Astronomical Society, 196, 269

Duthie A., Skinner J., Robinson T., 1989, Biological Conservation, 47, 195

Egan M. P., Price S. D., 1996, The Astronomical Journal, 112, 2862

Ehrenfreund P., Dartois E., Demyk K., D'Hendecourt L., 1998, Astronomy & Astrophysics, 339, L17

Eikelboom J., Wind J., van de Ven E., Kenana L., Schroder B., de Knegt H., van Langevelde F., Prins H., 2019, Methods in Ecology and Evolution, 10, 1875

Elbaz D., 2002, Astrophysics & Space Science, 281, 449

Elston D. P., Holt H. E., 1967, in , Vol. 57, Geological Society of America

Encrenaz T., 2005, Space Science Reviews, 116, 99

Encrenaz T., 2008, Space Science Reviews, 135, 11

Encrenaz T., et al., 2004, Icarus, 170, 424

Encrenaz T., et al., 2005, Icarus, 179, 43

Ennico K. A., Keller L. D., Mar D. J., Herter T. L., Jaffe D. T., Adams J. D., Greene T. P., 2006, in McLean I. S., Iye M., eds, Vol. 6269, Ground-based and Airborne Instrumentation for Astronomy. SPIE Conference Proceedings, pp 579 – 588

FLIR A., 2015, FLIR AB. URL https://vault.flir.com/file/asset/18320/original?token=8df9f33c-ebf4-43ce-897e-4fdeb4672a18, p. 5

Fabian D., Henning T., Jäger C., Mutschke H., Dorschner J., Wehrhan O., 2001, Astronomy & Astrophysics, 378, 228

Fauchez T. J., et al., 2020, Nature Astronomy, p. 5

Fazio G. G., et al., 1998, in Fowler A. M., ed., Society of Photo-Optical Instrumentation Engineers (SPIE) Conference Series Vol. 3354, SPIE Conference Proceedings. pp 1024–1031

Feuchtgruber H., Helmich F. P., van Dishoeck E. F., Wright C. M., 2000, The Astrophysical Journal Letters, 535, L111

Flagey N., Boulanger F., Verstraete L., Miville Deschenes M. A., Noriega Crespo A., Reach W. T., 2006, in Armus L., Reach W. T., eds, Astronomical Society of the Pacific Conference Series, Vol. 357, The Spitzer Space Telescope: New Views of the Cosmos. p. 85

Fountain W. F., Raine W. L., Fountain J. A., Jones B. P., Watkins J. R., 1976, The Moon, 15, 421

Franklin J., 2010, Mapping Species Distributions: Spatial Inference and Prediction. Cambridge University Press.

Fretwell P. T., et al., 2012, PLOS ONE, 7, 1

Fudali R. F., 1966, Icarus, 5, 536

Fuente A., Martín-Pintado J., Rodríguez-Fernández N. J., Rodríguez-Franco A., de Vicente P., Kunze D., 1999, The Astrophysical Journal Letters, 518, L45

Galliano F., 2006, arXiv e-prints, pp astro–ph/0610852

Galliano F., Dwek E., Chanial P., 2008a, The Astrophysical Journal, 672, 214

Galliano F., Madden S. C., Tielens A. G. G. M., Peeters E., Jones A. P., 2008b, The Astrophysical Journal, 679, 310

Gehrz R. D., Marchetti J., McMillan S., Procter T., Zarling A., Bartlett J., Smith N., 2020, The Astronomer's Telegram, 13518, 1

Gillett F. C., Forrest W. J., 1973, The Astrophysical Journal, 179, 483

Glass I. S., 1999, Handbook of Infrared Astronomy. Cambridge Observing Handbooks for Research Astronomers, Cambridge University Press, doi:10.1017/CBO9780511564949

Glasse A. C., Atad-Ettedgui E. I., Harris J. W., 1997, in Ardeberg A. L., ed., SPIE Conference ProceedingsVol. 2871, Optical Telescopes of Today and Tomorrow. pp 1197–1203

Gonzalez L. F., Montes G. A., Puig E., Johnson S., Mengersen K., Gaston K. J., 2016, Sensors, 16

Gordon M. S., et al., 2018, The Astronomical Journal, 155, 212

Hadi Pfeifer M., Korhonen L., Wheeler C., Rautiainen M., 2017, Remote Sensing of Environment, 201, 314

Hammel H. B., Lynch D. K., Russell R. W., Sitko M. L., Bernstein L. S., Hewagama T., 2006, The Astrophysical Journal, 644, 1326

Hammel H. B., Sitko M. L., Lynch D. K., Orton G. S., Russell R. W., Geballe T. R., de Pater I., 2007, The Astronomical Journal, 134, 637

Hao L., et al., 2005, The Astrophysical Journal Letters, 625, L75

Harris A., Sluss, Jr. J. J., Refai H. H., LoPresti P. G., 2006, Opt. Eng., 45, 086001

Hatchell J., Thompson M. A., Millar T. J., MacDonald G. H., 1998, Astronomy & Astrophysics, 338, 713

Hayward T. L., Miles J. E., Houck J. R., Gull G. E., Schoenwald J., 1993, in Fowler A. M., ed., Society of Photo-Optical Instrumentation Engineers (SPIE) Conference Series Vol. 1946, SPIE Conference Proceedings. pp 334–340, doi:10.1117/12.158686

Hellebrand H. J., Brehme U., Beuche H., Stollberg U., Jacobs H., 2003, Proc., 1st European Conference on Precision Livestock Farming, pp 761–763

Helmich F. P., et al., 1996, Astronomy & Astrophysics, 315, L173

Hemingway B. S., Robie R. A., Wilson W. H., 1973, Lunar and Planetary Science Conference Proceedings, 4, 2481

Herschel W., 1800, Philosophical Transactions of the Royal Society of London Series I, 90, 284

Herter T. L., et al., 2018, Journal of Astronomical Instrumentation, 7, 1840005

Ho L. C., 1998, arXiv e-prints, pp astro–ph/9803307

Ho L. C. W., 2004, in Ho L. C., ed., Carnegie Observatories Astrophysics Series, Vol. 1: Coevolution of Black Holes and Galaxies. p. 292 (`arXiv:astro-ph/0401527`)

Ho L. C., 2008, Annual Review of Astronomy and Astrophysics, 46, 475

Hoffmann W. F., Fazio G. G., Shivanandan K. i., Hora J. L., Deutsch L. K., 1993, in Fowler A. M., ed., Society of Photo-Optical Instrumentation Engineers (SPIE) Conference Series Vol. 1946, SPIE Conference Proceedings. pp 449–460, doi:10.1117/12.158697

Hollenbach D. J., Tielens A. G. G. M., 1999, Reviews of Modern Physics, 71, 173

Hony S., Van Kerckhoven C., Peeters E., Tielens A. G. G. M., Hudgins D. M., Allamandola L. J., 2001, Astronomy & Astrophysics, 370, 1030

Hughes G. O., Thuiller W., Midgley G. F., Collins K., 2008, Biological Conservation, 141, 23

Hunt G. R., Salisbury J. W., Vincent R. K., 1968, Science, 162, 252

Husson S. J., et al., 2008, Orangutans: Geographic Variation in Behavioral Ecology and Conservation. Oxford Scholarship

Imanishi M., Ueno S., 2000, The Astrophysical Journal, 535, 626

Israel M., 2011, International Archives of Photogrammetry and Remote Sensing, Vol XXXVIII-1/C22, 51

Jessen C., 2001, Temperature Regulation in Humans and Other Mammals. Springer-Verlag Berlin Heidelberg

Jones T., 1978, Journal of the British Astronomical Association, 88, 257

Jones G. P., Pearlstine L. G., Percival H. F., 2006, Wildlife Society Bulletin (1973-2006), 34, 750

Kataza H., Okamoto Y., Takubo S., Onaka T., Sako S., Nakamura K., Miyata T., Yamashita T., 2000, in Iye M., Moorwood A. F., eds, Society of Photo-Optical Instrumentation Engineers (SPIE) Conference Series Vol. 4008, SPIE Conference Proceedings. pp 1144–1152, doi:10.1117/12.395433

Kaufman M. J., Wolfire M. G., Hollenbach D. J., Luhman M. L., 1999, The Astrophysical Journal, 527, 795

Kays R., Sheppard J., Mclean K., Welch C., Paunescu C., Want V., Kravit G., Crofoot M., 2018, International Journal of Remote Sensing, 0, 1

Keane J. V., Boonman A. M. S., Tielens A. G. G. M., van Dishoeck E. F., 2001, Astronomy & Astrophysics, 376, L5

Kelley M. S., Wooden D. H., 2009, Planetary Space Science, 57, 1133

Kelley M. S. P., et al., 2016, Publications of the Astronomical Society of the Pacific, 128, 018009

Kessler M. F., et al., 1996, Astronomy & Astrophysics, 500, 493

Kim S. J., Lim G. J., Cho J., 2018, Computers & Industrial Engineering, 117, 291

Kirchhoff G., 1860, The London, Edinburgh, and Dublin Philosophical Magazine and Journal of Science, 20, 1

Knížková I., Kunc P., Gürdil G., Pinar Y., Selvi K., 2007, J. Fac. Agric., 22, 329

Koh L. P., Wich S. A., 2012, Tropical Conservation Science, 5, 121

Kohin M., Butler N. R., 2004, in Andresen B. F., Fulop G. F., eds, Vol. 5406, Infrared Technology and Applications XXX. SPIE, pp 447 – 453

Kühl H., Maisels F., Ancrenaz M., Williamson E., 2008, Best Practice Guidelines for the Surveys and Monitoring of Great Ape Populations. Occasional papers of the IUCN Species Survival Commission, World Conservation Union (IUCN) in collab. with the Center for Applied Biodiversity Science

Lacy J. H., Richter M. J., Greathouse T. K., Jaffe D. T., Zhu Q., Knez C., 2003, in Iye M., Moorwood A. F. M., eds, Society of Photo-Optical Instrumentation Engineers (SPIE) Conference Series Vol. 4841, SPIE Conference Proceedings. pp 1572–1580, doi:10.1117/12.461194

Lagache G., et al., 2004, The Astrophysical Journal Supplement Series, 154, 112

Lagage P. O., Durand G. A., Lyraud C., Rio Y., Pel J. W., de Haas J. C., 2000, in Iye M., Moorwood A. F., eds, SPIE Conference ProceedingsVol. 4008, Optical and IR Telescope Instrumentation and Detectors. pp 1120–1131

Laing S. E., Buckland S. T., Burn R. W., Lambie D., Amphlett A., 2003, Journal of Applied Ecology, 40, 1102

Lambert J. H., 1892, Lamberts Photometrie: Photometria, sive De mensura et gradibus luminus, colorum et umbrae (1760). Vol. 6, W. Engelmann

Lamprey R., Pope F., Ngene S., Norton-Griffiths M., Frederick H., Okita-Ouma B., Douglas-Hamilton I., 2019, Biological Conservation, p. 108243

Larsson B., Liseau R., Men'shchikov A. B., 2002, Astronomy & Astrophysics, 386, 1055

Lawson S. L., Rodger A. P., Henderson B. G., Bender S. C., Lucey P. G., 2003, in Mackwell S., Stansbery E., eds, Lunar and Planetary Science Conference. Lunar and Planetary Science Conference. p. 1761

Le Floc'h E., et al., 2005, The Astrophysical Journal, 632, 169

Leinert C., et al., 2003, Astrophysics & Space Science, 286, 73

Leisawitz D., 2020. American Astronomical Society Meeting Abstracts. p. 171.01

Lhoest S., Linchant J., Quevauvillers S., Vermeulen C., Lejeune P., 2015, International Archives of the Photogrammetry, Remote Sensing and Spatial Information Sciences, XL-3/W3, 355

Linchant J., Lisein J., Semeki J., Lejeune P., Vermeulen C., 2015, Mammal Review, 45

Longair M. S., 2003, Theoretical Concepts in Physics: An Alternative View of Theoretical Reasoning in Physics, 2 edn. Cambridge University Press

Longmore S. N., et al., 2017, International Journal of Remote Sensing, 38, 2623

Low F. J., 1961, J. Opt. Soc. Am., 51, 1300

Low F. J., Rieke G. H., 1974, Methods of Experimental Physics, 12, 415

Lutz D., Spoon H. W. W., Rigopoulou D., Moorwood A. F. M., Genzel R., 1998, The Astrophysical Journal Letters, 505, L103

Lynch D. K., et al., 2007, The Astronomical Journal, 134, 1459

MacKenzie D., 2006, Occupancy estimation and modeling: inferring patterns and dynamics of species occurrence. Academic Press.

Madden S. C., Galliano F., Jones A. P., Sauvage M., 2006, Astronomy & Astrophysics, 446, 877

Maghrabi A. H., , Journal of Geophysical Research: Atmospheres, 117

Malfait K., Waelkens C., Waters L. B. F. M., Vand enbussche B., Huygen E., de Graauw M. S., 1998, Astronomy & Astrophysics, 332, L25

Mallama A., 2007, Icarus, 192, 404

Markwick-Kemper F., Gallagher S. C., Hines D. C., Bouwman J., 2007, The Astrophysical Journal Letters, 668, L107

Marshall A., Meijaard E., 2009, Oryx, 43 (3), 416

Marshall A. R., Lovett J. C., White P. C., 2008, American Journal of Primatology, 70(5), 452

Mason R., Wong A., Geballe T., Volk K., Hayward T., Dillman M., Fisher R. S., Radomski J., 2008, in Brissenden R. J., Silva D. R., eds, SPIE Conference ProceedingsVol. 7016, Observatory Operations: Strategies, Processes, and Systems II. p. 616 627

McCafferty D., Gallon S., Nord A., 2015, Animal Biotelemetry, 3

McMahon C. R., Howe H., van den Hoff J., Alderman R., Brolsma H., Hindell M. A., 2014, PLOS ONE, 9, 1

McWhirter P. R., Veitch-Michaelis J., Burke C., Lam M. C., Longmore S. N., 2019, Saving Endangered Animals with Astro-Ecology. p. 95

Meijerink R., Poelman D. R., Spaans M., Tielens A. G. G. M., Glassgold A. E., 2008, The Astrophysical Journal Letters, 689, L57

Milam S. N., Stansberry J. A., Sonneborn G., Thomas C., 2016, Publications of the Astronomical Society of the Pacific, 128, 018001

Mittermeier R. A., Rylands A. B., Wilson D. E., 2013, Handbook of the Mammals of the World - Volume 3: Primates. Lynx Edicions

Miyata T., Kataza H., Okamoto Y., Tanabé T., Onaka T., Yamashita T., Nakamura K., Shibai H., 1999, Publications of the Astronomical Society of the Pacific, 111, 750

Molster F. J., Waters L. B. F. M., Tielens A. G. G. M., 2002, Astronomy & Astrophysics, 382, 222

Moreno M., Torres Jacome A., Ambrosio R., Kosarev A., 2012, Un-Cooled Microbolometers with Amorphous Germanium-Silicon (a-GexSiy:H) Thermo-Sensing Films, doi:10.5772/32222.

Morrison P. R., Ryser F. A., 1952, Science, 116, 231

Mulero-Pázmány M., Stolper R., van Essen L. D., Negro J. J., Sassen T., 2014, PLOS ONE, 9, 1

Mulero-Pázmány M., Barasona J. A., Acevedo P., Vicente J., Negro J. J., 2015, Ecology and Evolution, 5, 4808

Müller T. G., Lagerros J. S. V., 2002, Astronomy & Astrophysics, 381, 324

Müller T., Lellouch E., Fornasier S., 2020, Trans-Neptunian objects and Centaurs at thermal wavelengths. pp 153–181

Murakami H., et al., 1994, The Astrophysical Journal, 428, 354

Murakami H., et al., 2007, Publications of the Astronomical Society of Japan, 59, S369

Murcray F. H., Murcray D. G., Williams W. J., 1970, Journal of Geophysical Research, 75, 2662

Natta A., Testi L., 2004, in Johnstone D., Adams F. C., Lin D. N. C., Neufeeld D. A., Ostriker E. C., eds, Astronomical Society of the Pacific Conference Series Vol. 323, Star Formation in the Interstellar Medium: In Honor of David Hollenbach. p. 279

Neugebauer G., Leighton R. B., 1969, NASA SP-3047

Neugebauer G., et al., 1984, The Astrophysical Journal Letters, 278, L1

Norwood J., et al., 2016, Publications of the Astronomical Society of the Pacific, 128, 025004

Ohyama Y., et al., 2018, Astronomy & Astrophysics, 618, A101

Olbrycht R., Więcek B., 2015, Quantitative InfraRed Thermography Journal, 12, 184

Packham C., Telesco C. M., Hough J. H., Ftaclas C., 2005, in Hidalgo-Gámez A. M., González J. J., Rodrìguez Espinosa J. M., Torres-Peimbert S., eds, Vol. 24, Revista Mexicana de Astronomia y Astrofisica. pp 7–12

Paige D. A., et al., 2010, Space Science Reviews, 150, 125

Papoular R., 1983, Astronomy & Astrophysics, 117, 46

Payne J., Andau M., 1997, J Wildl Conserv Manag Sabah, 1, 40

Pearson C. P., 2001, Monthly Notices of the Royal Astronomical Society, 325, 1511

Peeters E., Spoon H. W. W., Tielens A. G. G. M., 2004a, The Astrophysical Journal, 613, 986

Peeters E., Mattioda A. L., Hudgins D. M., Allamandola L. J., 2004b, The Astrophysical Journal Letters, 617, L65

Petit dit de la Roche D. J. M., van den Ancker M. E., Kissler-Patig M., Ivanov V. D., Fedele D., 2020, Monthly Notices of the Royal Astronomical Society, 491, 1795

Phillips P. K., Heath J. E., 1995, Journal of Thermal Biology, 20, 281

Pietrow A. G. M., Burtscher L., Brandl B., 2019, Research Notes of the AAS, 3, 42

Planck M., 1900, in , Von Kirchhoff bis Planck. Springer, pp 175–178

Price S. D., Murdock T. L., 1983, AFGL-TR-0208 Environemental Research papers, 161, 0

Price-Whelan A. M., et al., 2018, The Astronomical Journal, 156, 123

Price S., Walker R., Laboratory U. A. F. G., 1976, The AFGL Four Color Infrared Sky Survey: Catalog of Observations at 4.2, 11.0, 19.8, and 27.4 Micrometers. AFGL-TR, Air Force Geophysics Laboratories, Air Force Systems Command, United States Air Force

Price S. D., Mizuno D., Murdock T. L., 2003, Advances in Space Research, 31, 2299

Prinzinger R., PreÃmar A., Schleucher E., 1991, Body temperature in Birds. pp 499–506

Radford W. A., et al., 1999, in Andresen B. F., Strojnik M., eds, Vol. 3698, Infrared Technology and Applications XXV. SPIE, pp 119 – 130

Rashman M. F., Steele I. A., Burke C., Longmore S. N., Wich S., 2018, in Holland A. D., Beletic J., eds, SPIE Conference ProceedingsVol. 10709, High Energy, Optical, and Infrared Detectors for Astronomy VIII. pp 667 – 676

Rayadin Y., Saitoh T., 2009, Am. J. Primatol., 71, 393

Rayleigh L., 1900, The London, Edinburgh, and Dublin Philosophical Magazine and Journal of Science, 49, 539

Régnier C., Achaz G., Lambert A., Cowie R. H., Bouchet P., Fontaine B., 2015, Proceedings of the National Academy of Sciences, 112, 7761

Richter M. J., Dewitt C. N., McKelvey M., Montiel E., McMurray R., Case M. E., 2018, Journal of Astronomical Instrumentation, 7, 1840013

Rieke G. H., et al., 2015, Publications of the Astronomical Society of the Pacific, 127, 584

RodrÃguez A., Negro J. J., Mulero M., RodrÃguez C., HernÃ¡ndez-Pliego J., Bustamante J., 2012, PLOS ONE, 7, 1

Rowan-Robinson M., et al., 2004, Monthly Notices of the Royal Astronomical Society, 351, 1290

Rybicki G. B., Lightman A. P., 1986, Radiative Processes in Astrophysics

Saari J. M., Shorthill R. W., 1963, Icarus, 2, 115

Saari J. M., Shorthill R. W., Deaton T. K., 1966, Icarus, 5, 635

Salisbury J. W., Vincent R. K., Logan L. M., Hunt G. R., 1970, Journal of Geophysical Research, 75, 2671

Sasse D. B., 2003, Wildlife Society Bulletin (1973-2006), 31, 1015

Schaefer A., Cook N., Tessaro S., Deregt D., Desroches G., Dubeski P., Tong A., Godson D., 2004, Canadian Journal of Animal Science, 84, 73

Shaw J., Nugent P., Vollmer M., 2015, Applied Optics, 54

Shenoy D., et al., 2016, The Astronomical Journal, 151, 51

Shorthill R. W., Saari J. M., 1965, Science, 150, 210

Shorthill R. W., Saari J. M., 1972, in KOPAL Z., ed., , Vol. 9, Advances in Astronomy and Astrophysics. Elsevier, pp 149 – 201

Shorthill R. W., Borough H. C., Conley J. M., 1960, Publications of the Astronomical Society of the Pacific, 72, 481

Siebenmorgen R., Haas M., Kruegel E., Schulz B., 2005, Astronomische Nachrichten, 326, 556

Skinner J., Chimimba C., 2005, The Mammals of the South African Sub-Region

Smith J. D. T., et al., 2007, The Astrophysical Journal, 656, 770

Spinoglio L., Malkan M. A., Rush B., Carrasco L., Recillas-Cruz E., 1995, The Astrophysical Journal, 453, 616

Spoon H. W. W., et al., 2006, The Astrophysical Journal, 638, 759

Sprague A. L., 2000, in Sitko M. L., Sprague A. L., Lynch D. K., eds, Astronomical Society of the Pacific Conference Series Vol. 196, Thermal Emission Spectroscopy and Analysis of Dust, Disks, and Regoliths. pp 167–186

Sprague A., Nash D., Witteborn F., Cruikshank D., 1997, Advances in Space Research, 19, 1507

Steele I. A., et al., 2004, in Oschmann Jr. J. M., ed., SPIE Conference ProceedingsVol. 5489, Ground-based Telescopes. pp 679–692

Stefan J., 1879, Akademie der Wissenschaften, 79, S

Sternberg A., Dalgarno A., 1989, The Astrophysical Journal, 338, 197

Stetson P. B., 1987, Publications of the Astronomical Society of the Pacific, 99, 191

Stewart S. M., Johnson R. B., 2016, Blackbody radiation: A history of thermal radiation computational aids and numerical methods. CRC Press

Sturm E., Lutz D., Tran D., Feuchtgruber H., Genzel R., Kunze D., Moorwood A. F. M., Thornley M. D., 2000, Astronomy & Astrophysics, 358, 481

Sturm E., et al., 2005, The Astrophysical Journal Letters, 629, L21

Sund-Levander M., Forsberg C., Wahren L. K., 2002, Scandinavian Journal of Caring Sciences, 16, 122

Swarna Nantha H., Tisdell C., 2008, Economics, Ecology and Environment Working Papers 55318, The Orangutan-oil Palm Conflict: Economic Constraints and Opportunities for Conservation. University of Queensland, School of Economics

Sylvester R. J., 1999, Monthly Notices of the Royal Astronomical Society, 309, 180

Szentkuti A., Skala Kavanagh H., Grazio S., 2011, Infrared thermography and image analysis for biomedical use. Vol. 113

Tan J. C., Beltrán M. T., Caselli P., Fontani F., Fuente A., Krumholz M. R., McKee C. F., Stolte A., 2014, in Beuther H., Klessen R. S., Dullemond C. P., Henning T., eds, Protostars and Planets VI. p. 149

Taylor R., 2005, Australian Veterinary Journal, 83, 444

Taylor N. A., Tipton M. J., Kenny G. P., 2014, Journal of Thermal Biology, 46, 72

Telesco C. M., Pina R. K., Hanna K. T., Julian J. A., Hon D. B., Kisko T. M., 1998, in Fowler A. M., ed., SPIE Conference ProceedingsVol. 3354, Infrared Astronomical Instrumentation. pp 534–544

Tempelhahn A., Budzier H., Krause V., Gerlach G., 2015, Proceedings IRS^2 2015, pp 961–966

Tempelhahn A., Budzier H., Krause V., Gerlac G., 2016, Journal of Sensors and Sensor Systems, 5, 9

Thi W. F., et al., 2001, The Astrophysical Journal, 561, 1074

Tielens A. G. G. M., Hollenbach D., 1985, The Astrophysical Journal, 291, 722

Timmermann R., Bertoldi F., Wright C. M., Drapatz S., Draine B. T., Haser L., Sternberg A., 1996, Astronomy & Astrophysics, 315, L281

Tremblay L., Line M. R., Stevenson K. B., Kataria T., Zellem R. T., Fortney J. J., Morley C. V., 2019, arXiv e-prints, p. arXiv:1912.10939

Tsang C. C. C., Durda1 D. D., Ennico K. A., Less J., Propp T., Olkin C. B., Stern S. A., 2015, 46th Lunar and Planetary Science Conference

Valentijn E. A., van der Werf P. P., de Graauw T., de Jong T., 1996, Astronomy & Astrophysics, 315, L145

Van Andel A. C., Wich S. A., Boesch C., Koh L. P., Robbins M. M., Kelly J., Kuehl H. S., 2015, American Journal of Primatology, 77, 1122

Varga J., Ábrahám P., Chen L., Ratzka T., Gabányi K. É., Kóspál Á., 2020, in Elmegreen B. G., Tóth L. V., Güdel M., eds, IAU Symposium Vol. 345, IAU Symposium. pp 128–131 (`arXiv:2002.05543`)

Vasavada A. R., Bandfield J. L., Greenhagen B. T., Hayne P. O., Siegler M. A., Williams J.-P., Paige D. A., 2012, Journal of Geophysical Research: Planets, 117

Vermeij R., Peeters E., Tielens A. G. G. M., van der Hulst J. M., 2002, Astronomy & Astrophysics, 382, 1042

Visser R., van Dishoeck E. F., Doty S. D., Dullemond C. P., 2009, Astronomy & Astrophysics, 495, 881

Voigt M., et al., 2018, Current Biology, 28, 761

Vollmer M., Möllmann K. P., 2012, European Journal of Physics, 33, 1703

Waelkens C., et al., 1996, Astronomy & Astrophysics, 315, L245

Wenger M., et al., 2000, Astronomy & Astrophysics Supplement Series, 143, 9

Wich S. A., 2015, Drones and aerial observation: new technologies for property rights, human rights, and global development, a primer.. Vol. 63

Wich S., Koh L., 1995, Population estimates and habitat preferences of orang-utans based on line transects of nests. In The neglected ape (Nadler, R.D. et al. eds). Plenum Press.

Wich S., Koh L., 2018, Conservation drones: Mapping and monitoring biodiversity

Wich S. A., et al., 2016, Science Advances, 2 (3)

Wich S., Dellatore D., Houghton M., Ardi R., Koh L., 2017, Journal of Unmanned Vehicle Systems, 4, 45

Wien W., 1897, The London, Edinburgh, and Dublin Philosophical Magazine and Journal of Science, 43, 214

Winter D. F., 1972, in KOPAL Z., ed., , Vol. 9, Advances in Astronomy and Astrophysics. Elsevier, pp 203 – 243

Wolf A., Pezoa J. E., Figueroa M., 2016, Sensors, 16, 1121

Wolfe W. L., 1996, Introduction to infrared system design / William L. Wolfe. SPIE Optical Engineering Press Bellingham, Wash., USA

Wolfe W., of Michigan. Infrared Information E. R. I., Center A., Zissis G., of Naval Research U. S. O., 1985, The Infrared handbook. Press Monographs, Environmental Research Institute of Michigan

Wolfire M. G., Tielens A. G. G. M., Hollenbach D., 1990, The Astrophysical Journal, 358, 116

Wood R. A., Han C. J., Kruse P. W., 1992, in Technical Digest IEEE Solid-State Sensor and Actuator Workshop. pp 132–135

Wooden D. H., 2008, Space Science Reviews, 138, 75

Wright E. L., 1976, The Astrophysical Journal, 210, 250

Wright C. M., van Dishoeck E. F., Black J. H., Feuchtgruber H., Cernicharo J., González-Alfonso E., de Graauw T., 2000, Astronomy & Astrophysics, 358, 689

Wright E. L., et al., 2010, The Astronomical Journal, 140, 1868

Xu C., et al., 1998, The Astrophysical Journal, 508, 576

Yang M., et al., 2018, Astronomy & Astrophysics, 616, A175

de Graauw T., et al., 1996, Astronomy & Astrophysics, 315, L345

de Zotti G., Mandolesi N., Preite-Martinez A., 1989, Memorie della Societa Astronomica Italiana, 60, 333

van Boekel R., 2007, Nature, 447, 535

van Boekel R., Ratzka T., Leinert C., Henning T., Min M., Waters R., 2005, in Protostars and Planets V Posters. p. 8448

van Broekhuizen F. A., Keane J. V., Schutte W. A., 2004, Astronomy & Astrophysics, 415, 425

van Dishoeck E. F., 1998, Faraday Discussions, 109, 31

van Dishoeck E. F., 2004, Annual Review of Astronomy and Astrophysics, 42, 119–167

van den Ancker M. E., Bouwman J., Wesselius P. R., Waters L. B. F. M., Dougherty S. M., van Dishoeck E. F., 2000, Astronomy & Astrophysics, 357, 325